V

Semiconductor Optical Amplifiers (SOAs)

20

Semiconductor Optical Amplifier Fundamentals

Michael J. Connelly

20.1 Introduction

The rapid growth in the development of optical networks requires small, inexpensive, and easy-to-integrate optical amplifiers for use as basic amplifiers (power boosters, in-line amplifiers to compensate for fiber loss, and optical receiver preamplifiers) and also as optoelectronic signal processing devices such as wavelength converters, optical switches, intensity and phase modulators, logic gates, and dispersion compensators.

There are two main classes of optical amplifier: optical fiber amplifiers (OFAs) and semiconductor optical amplifiers (SOAs). OFAs are optical amplifiers that use optical fiber as the gain medium, which in most cases is a glass fiber doped with rare-earth ions such as erbium (for operation in the 1.55-μm telecommunications band). The active dopant is supplied with energy by an external pump laser. OFAs are relatively large devices, with advantages such as wide optical bandwidth (tens of nm), high gain (>20 dB), high saturation output power (>20 dBm), defined as the output signal power at which the gain is half that of the unsaturated gain, low-noise figure, and low polarization sensitivity. When an OFA is used to amplify an optical data signal, its slow gain dynamics (the lifetime of the excited energy levels are typically in the tens of ms range) are a significant advantage as the amplifier only experiences the average power of the data signal. This results in low intersymbol interference and, when used to amplify wavelength division multiplexed signals, low interchannel cross-talk. However, OFA's slow dynamics preclude its use in optical signal processing applications.

To achieve optical gain, an SOA uses an electrically pumped semiconductor material, as is the case for a semiconductor laser, such that a population inversion occurs between the material conduction and valence bands. An incoming light wave is amplified when the resulting stimulated emission exceeds losses due to stimulated absorption and other material or structural losses. By appropriate choice of the gain

material and its bandgap energy, SOAs can be designed to operate in the wavelength region of choice, typically the 1.3- and 1.55-μm optical communication windows (Connelly, 2002a; Dutta and Wang, 2013). Various SOA designs have been shown to achieve gain, noise figure, saturation output power, and optical bandwidths comparable to those for OFAs; however, SOAs can exhibit significant polarization sensitivity. The main advantages of SOAs over fiber amplifiers are their small size and compatibility with photonic integrated circuit (PIC) technology. SOAs have much faster dynamics than OFAs, which can lead to data signal distortion and interchannel cross-talk when operated in the gain-saturated regime. However, high-speed dynamics and nonlinearities can be exploited to realize all-optical signal processing functions.

In this chapter, the basic principles and types of SOA are reviewed followed by descriptions and implementations of relatively simple models that are used to gain insight into important SOA static, dynamic, and nonlinear behavior. The models described are (1) quasi-analytic static model, (2) bulk SOA static model including amplified spontaneous emission (ASE), (3) time-domain model including ASE, which is used to simulate pattern effects and a cross-gain modulation (XGM)-based wavelength converter, (4) pulse amplification analytic model, which is also used to simulate a cross-phase modulation (XPM)-based wavelength converter, and (5) a four-wave mixing (FWM) analytic model. Further chapters describe more detailed descriptions and models of particular types of SOA.

20.2 Basic Principles

The principle of operation of a traveling-wave SOA is shown in Figure 20.1. The amplifier consists of an electrically pumped active waveguide. An incoming light wave is amplified as it propagates through the waveguide. Antireflection (AR) coatings are used to suppress the end facet reflections, which are approximately 32% in uncoated devices. Through the use of AR coatings and optimized waveguide designs (such as using a tilted waveguide geometry), reflectivities as low as 10^{-5} or less can be achieved. The models described in this chapter assume zero facet reflectivities. The input signal experiences a single-pass power gain $G = \exp(gL)$, where g is the gain coefficient at the signal wavelength and L the amplifier length. Although SOA waveguides are designed to be single mode, they support two orthogonal polarization modes, the transverse electric (TE) and transverse magnetic (TM) modes.

The amplification process adds broadband noise (spontaneous emission) to the propagating signal, caused by spontaneous recombination of conduction band electrons to valence band holes. This noise is subsequently amplified, leading to ASE. In the linear operating region, where the gain is constant and the ASE statistics are not affected by the input signal, the output ASE power spectral density (W/Hz) in a single polarization state at the signal energy E_s is given by

$$\rho_{ASE} = n_{sp}E_s(G-1), \tag{20.1}$$

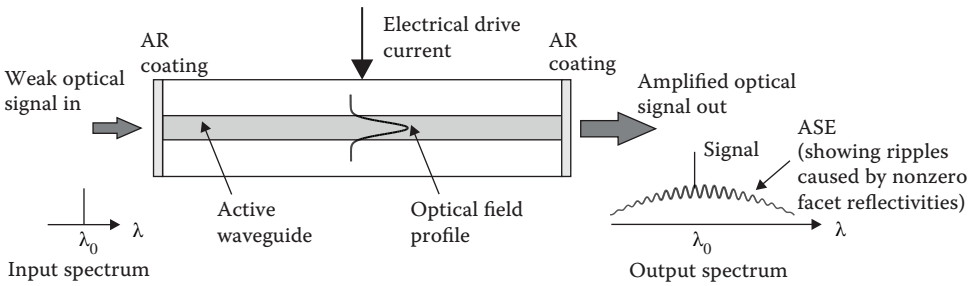

FIGURE 20.1 Semiconductor optical amplifier (SOA) basic structure.

where n_{sp} is the population inversion factor having a maximum possible value of 1. The amplifier noise factor F is defined as the ratio of the amplifier input to output signal-to-noise ratios (SNRs). F quantifies the degradation of the SNR, as determined in terms of the signal and noise levels in the photocurrent of an ideal photodetector placed in the signal path, due to the insertion of the amplifier in a signal transmission system (Baney et al., 2000; Kweon, 2002). The ideal photodetector responsivity $R = e/E$ (having a quantum efficiency equal to 1), where e and E are the electronic charge and light wave photon energy, respectively. Assuming that the input signal is shot-noise limited, the input SNR is equal to $P_s/(2E_sB_e)$, where P_s is the input signal power and B_e the detector electrical bandwidth. In practical receivers, the photodetector is preceded by an optical bandpass filter of bandwidth B_o that passes the signal and greatly reduces the ASE. The average signal and total ASE powers after the optical filter are P_sG and $2\rho_{ASE}B_o$, respectively, with corresponding photodetector shot-noise current variances (A^2), after electrical filtering, of $\sigma^2_{sig} = 2eRGP_sB_e$ and $\sigma^2_{sp} = 2eR\rho_{ASE}B_oB_e$ (Olsson, 1989; Kweon, 2002). Since the photodetector is a square-law type detector, the signal also beats with the ASE giving rise to a signal-spontaneous beat noise current variance $\sigma^2_{s\text{-}sp} = 4R^2GP_s\rho_{ASE}B_e$. The beating of the ASE with itself leads to spontaneous–spontaneous beat noise having a current variance $\sigma^2_{sp\text{-}sp} = 2R^2\rho^2_{ASE}B_e(2B_o - B_e)$. The output SNR, SNR_{out}, is the ratio of the square of the signal photocurrent $(RGP_s)^2$ to the sum of the noise variances. If the optical filter bandwidth is small enough such that $\sigma^2_{sp\text{-}sp}$ and σ^2_{sp} are negligible compared to the other two noise sources (the signal-spontaneous beat noise limit), then

$$SNR_{out} = \frac{(RGP_s)^2}{4R^2GP_s\rho_{ASE}B_e + 2eRGP_sB_e}. \tag{20.2}$$

The noise factor is then

$$F = \frac{2\rho_{ASE}}{GE_s} + \frac{1}{G}. \tag{20.3}$$

The noise figure (NF) is F expressed in decibel units, $NF = 10\log_{10} F$ dB. For large gains, $F \approx 2n_{sp}$. Since the maximum value of n_{sp} is 1, the minimum noise figure possible is 3 dB. Usually, the shot-noise term in Equation 20.3 is much smaller than the signal-spontaneous beat noise term so

$$F = \frac{2\rho_{ASE}}{GE_s}. \tag{20.4}$$

Nonzero reflectivities lead to multiple passes of the signal and ASE, with constructive interference occurring at discrete optical frequencies ν_q that are integer multiples r of the ratio of the speed of light in the amplifier c/n_{eff}, where n_{eff} is the waveguide effective index (defined as the ratio of the propagation constant in the waveguide to the free space propagation constant), to the round-trip distance $2L$. As the latter quantity is much greater than the wavelength, r is very large. The frequency spacing $\Delta\nu$ between adjacent resonances is $\Delta\nu = c/(2n_{eff}L)$. For a typical SOA with $L = 1$ mm and $n_{eff} = 3.5$ and operating in the 1.55-μm region, the wavelength spacing is 1.2 nm. When the effect of nonzero reflectivities is significant, the SOA is termed a Fabry–Pérot SOA (FP-SOA) because of its similarity to a Fabry–Pérot resonator. The signal gain of an FP-SOA at optical frequency ν is given by

$$G_{FP}(\nu) = \frac{(1 - R_1)(1 - R_2)G}{(1 - \sqrt{R_1R_2}G)^2 + 4\sqrt{R_1R_2}G\sin^2[\pi(\nu - \nu_r)/\Delta\nu]}, \tag{20.5}$$

where R_1 and R_2 are the SOA input and output facet reflectivities, respectively. FP resonances cause undesirable ripples in the signal gain and ASE spectrums (Figure 20.1). If the single-pass gain is high enough such that the denominator in Equation 20.5 approaches 0, G_{FP} will become very large and the SOA will begin to oscillate, at which point it behaves as a laser and not as an amplifier.

A reflective semiconductor optical amplifier (RSOA) can be formed by applying an AR coating to the input facet and a highly reflective coating to the opposite facet. RSOAs have applications such as modulators in passive optical networks (Lee et al., 2005).

20.2.1 Typical Bulk SOA Structure

A bulk material SOA operating in the 1550-nm region is shown in Figure 20.2 (Connelly, 2007). The active region is sandwiched between two separate confinement heterostructure (SCH) layers, which have a lower refractive index than the active region, and hence confine the light. The p–n junctions formed by the p-type and n-type InP layers act as current blocks, thereby providing good confinement of the injected carriers in the active region. An important SOA geometrical parameter is the optical confinement factor Γ defined as the fraction of the transverse (to the propagation direction) optical intensity overlapping with the active region. In general, Γ is polarization dependent, so the TE and TM confinement factors Γ_{TE} and Γ_{TM} are unequal. They are only equal in an unstrained bulk material SOA having a square cross-section waveguide. Such SOAs are difficult to fabricate as they require optical confinement in both transverse directions. Most commercial SOAs use rectangular cross-section waveguides and consequently, $\Gamma_{TE} \neq \Gamma_{TM}$. Confinement factors can be determined using formulas (Chuang, 2009) or commercial mode solvers. If $\Gamma_{TE} \neq \Gamma_{TM}$ and the material gain is polarization independent, then the SOA gain will be polarization dependent. In Figure 20.2, the introduction of tensile strain between the active region and SCH layers is used to increase the TM to TE material gain ratio, to compensate for the higher Γ_{TE} value caused by the waveguide asymmetry, and thereby reduce polarization sensitivity. The tapered regions act as mode expanders that couple light from the active waveguide to an underlying passive waveguide, thereby simplifying coupling to external optical fibers.

20.2.2 Quantum Well, Dot and Dash SOAs

SOAs that use bulk materials require high transparency current densities (at which the SOA has unity gain). The active layer in quantum well (QW) SOAs have much smaller thicknesses (~5–10 nm) than in conventional bulk structures (~100 nm). In bulk material, the injected carriers can move in three dimensions whereas in a QW they are confined to two dimensions. The enhanced quantum effects result in a significantly different band structure and material gain compared to bulk material. The small thickness of the QW allows many QWs to be stacked to form a multiple quantum well (MQW) active region. MQW SOAs have a number of advantages compared to bulk SOAs. Because of the small active region volume compared to bulk SOAs, a reduced injection current is sufficient to create a large carrier density in the

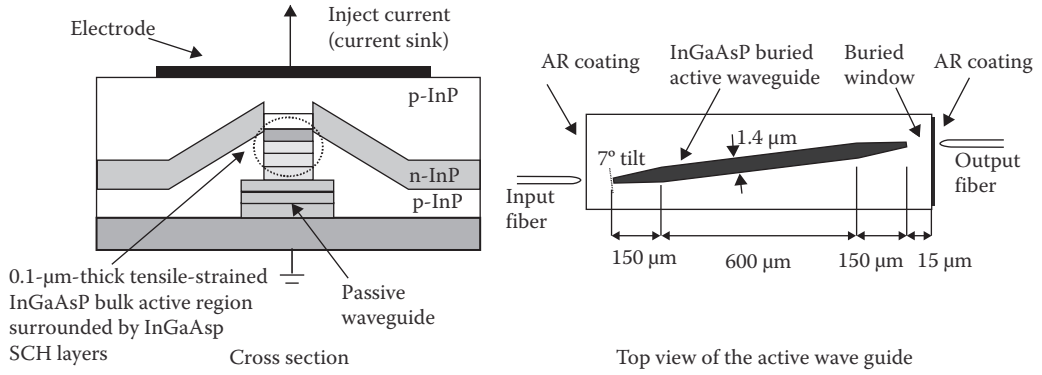

FIGURE 20.2 Typical SOA structure (Connelly, 2007). The buried windows and 7° tilted waveguide (with respect to the end facets) further reduce the effective facet reflectivity.

active region resulting in a broader gain spectrum and shorter carrier lifetime (related to the average time for conduction band electrons to recombine with valence band holes). Shorter carrier lifetimes result in shorter gain recovery times, which is of particular importance in reducing pattern effects when the SOA is used to amplify high-speed data. Furthermore, the loss coefficient in MQW active regions is significantly smaller than that in bulk devices, which leads to an improvement in noise performance. The polarization sensitivity of QW structures can be reduced by using strained QWs. Strain-induced band structure modifications also result in a reduction in loss mechanisms such as Auger recombination and intervalence band absorption (IVBA). The linewidth enhancement factor (LEF) is also reduced, which results in amplified pulses experiencing less spectral broadening, leading to superior high-speed performance as compared to bulk and unstrained QW SOAs. Bulk and QW SOAs have typical gain recovery lifetimes in the range of hundreds of picoseconds; so, when used to amplify data signals, significant pattern effects can be present at baud rates in the region of tens of Gbaud/s. Pattern effects also induce nonlinear phase noise through the self-phase modulation (SPM) effect, which can be a more serious performance degradation factor when advanced modulation formats are used. The amount of SPM is directly related to the LEF.

A quantum dot (QD) is a semiconductor nanostructure with dimensions that typically range from 2 to 10 nm, which confines the motion of injected carriers to all three spatial directions (Akiyama et al., 2007). Compared to bulk and QW SOAs, QD SOAs have been shown to have improved gain bandwidth, noise figure, and saturation output power as well as enhanced nonlinear effects such as FWM. Polarization insensitive QD SOAs have been realized using optimized QD shapes along with close stacking of the QD layers. Of particular significance is the ultrafast gain recovery lifetime, typically of the order of a few picoseconds, a factor of ten lower than that for bulk and QW SOAs so that QD SOAs are capable of amplifying ultrafast data signals with little or no pattern effects (Ben-Ezra et al., 2005). QD SOA LEFs can be much lower than for bulk and QW SOAs and so are particularly suitable for amplifying very high baud rate advanced modulation data signals.

Quantum dash (QDash) SOAs are of interest as an alternative to QD SOAs, since they have some dot-like properties and can more easily be made to operate in the 1.55-μm region, although they also have been shown to have longer gain recovery times in the range of hundreds of picoseconds (Lelarge et al., 2007).

20.3 Quasi-Analytic Static Model

As the input signal power to an SOA is increased, the gain reduces as the electrically pumped conduction band carriers (electrons) in the active material are depleted by stimulated recombination with holes in the valence band. To determine the factors that influence SOA gain at high input powers, a simple traveling-wave-based model can be used (Connelly, 2002a). The carrier density n dependent material gain g_m per unit length at the signal wavelength is assumed to be a linear function $g_m = a(n - n_t)$, where a is the differential of the material gain with respect to n and n_t is the transparency carrier density. The carrier density rate equation is

$$\frac{dn}{dt} = \frac{\eta I}{eV} - \frac{n}{\tau_c} - \frac{\Gamma a(n - n_t)P}{AE_s}, \tag{20.6}$$

where I is the bias current and E_s the signal photon energy. The injection efficiency η is the fraction of the SOA current entering the active region. The active region cross-section area, $A = dW$, where d and W are the active waveguide thickness and width, respectively, and the active region volume $V = AL$. τ_c is the interband carrier lifetime due to nonradiative and radiative spontaneous recombination processes including trap, Auger, and spontaneous emission. The propagation of the signal power P is described by the traveling-wave equation

$$\frac{dP}{dz} = \left[\Gamma a(n - n_t) - \alpha\right] P, \tag{20.7}$$

where z is the propagation direction (along the amplifier axis) measured from the input and α is the loss coefficient. Under steady-state conditions, the time differential in Equation 20.6 is zero, from which

$$n = \left(\frac{\tau_c \eta I}{eV}\right) \frac{P_{sat}}{P + P_{sat}} + n_t \frac{P}{P + P_{sat}}. \tag{20.8}$$

The saturation power P_{sat} is defined as

$$P_{sat} = \frac{AE_s}{\Gamma a \tau_c}, \tag{20.9}$$

Defining the spatially dependent normalized power $p(z) = P(z)/P_{sat}$, the unsaturated carrier density $n_0 = \tau_c \eta I/(eV)$ and the unsaturated gain coefficient $g_0 = \Gamma a (n_0 - n_t)$, Equation 20.8 can be written as

$$n(z) = \frac{n_0}{1 + p} + \frac{n_t p}{1 + p}. \tag{20.10}$$

Inserting Equation 20.10 into Equation 20.7 gives

$$\frac{dp}{dz} = \left(\frac{g_0}{1 + p} - \alpha\right) p. \tag{20.11}$$

The unsaturated gain $G_0 = \exp[(g_0 - \alpha)L]$. Equation 20.11 can be solved numerically, using, e.g., the Runge–Kutta method, with the boundary condition $p(0) = P_{in}/P_{sat}$, where P_{in} is the input signal power. The amplifier gain G is calculated as the ratio of the output power $P_{out} = p(L)P_{sat}$ to the input power. The calculated gain versus output power is shown in Figure 20.3a for various values of G_0 with $\exp(\alpha L) = 10$. The carrier density is calculated using Equation 20.10. For a given SOA, G_0 corresponds to a particular value of bias current. The normalized saturation output power $p_{o,sat}$ is defined as the normalized output power at which the amplifier gain is half the unsaturated gain. From Figure 20.3a, it can be seen that $p_{o,sat} \approx -3.8$ dB for the 20 dB unsaturated gain curve and almost independent of G_0. The saturation output power $P_{o,sat} = p_{o,sat} P_{sat}$, which from the form of Equation 20.9 can be increased by reducing a and τ_c. In real SOAs, these two parameters are not constants but for a given structure and material depend on wavelength and carrier density.

Consider a square cross-section bulk SOA with parameters $W = d = 0.4$ μm, $L = 600$ μm, $\Gamma = 0.45$, $\tau_c = 0.5$ ns, $a = 1 \times 10^{-20}$ m^2, $n_t = 2.5 \times 10^{24}$ m^{-3}, and $\exp(\alpha L) = 10$. If the unsaturated gain is 20 dB at a bias current of 150 mA and assuming 100% injection efficiency, then $n_o = 4.9 \times 10^{24}$ m^{-3}, $g_0 = 1.1 \times 10^4$ m^{-1} and for a signal wavelength of 1550 nm, $P_{sat} = 9.6$ dBm and so $P_{o,sat} = 5.8$ dBm. Figure 20.3b shows the signal power and carrier density distributions for various values of normalized input power. At input powers $\ll P_{sat}$, the carrier density is uniform throughout the amplifier. Models that include ASE show that below saturation, the carrier density is not uniform but is symmetrical with minima at the SOA ends and a maximum at the center. As the level of saturation increases, the carrier distribution becomes less uniform, until the amplifier is highly saturated, at which the carrier density throughout the amplifier approaches its transparency value. As Figure 20.3b shows, the spatial distribution of the carrier density in a SOA can vary greatly. A further disadvantage of this model is that the spontaneous recombination term in Equation 20.4 is assumed to be a linear function of n. In practice, spontaneous recombination is more accurately modeled as a polynomial function of carrier density, so τ_c is actually carrier dependent.

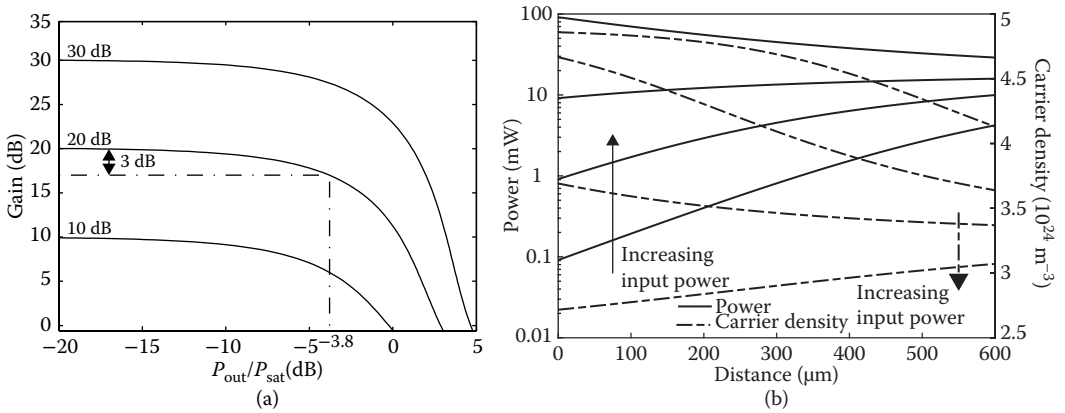

FIGURE 20.3 (a) Gain characteristics for various unsaturated gains. (b) Carrier density and power distributions for normalized input powers of 0.01, 0.1, 1, and 10. The unsaturated gain is 20 dB.

20.4 Bulk SOA Static Model Including ASE

The simple model described above illustrates SOA operational principles, in particular, saturation effects, but it is of limited use in a real SOA analysis. Most importantly, it does not include gain coefficient wavelength dependency or ASE, which contributes to gain saturation and determines the amplifier noise performance. In this section, a modified version of the wideband models for an unstrained bulk SOA that includes ASE (Connelly, 2001, 2007) is considered. The SOA has the same active region geometry and confinement factor as used in the quasi-analytic static model. The bulk material is unstrained, and thereby polarization independent. In the mathematical formulation, Γ_{TE} and Γ_{TM} are assumed to be different but are assumed to be equal in the simulations.

20.4.1 Material Gain

The material gain g_m and spontaneous gain g_{sp} (used to determine the additive spontaneous emission) of the unstrained bulk material are calculated using methods detailed in Jones and O'Reilly (1993) and Connelly (2007). Typical gain spectra are shown in Figure 20.4. The net gain coefficient, at energy E and polarization p (TE or TM), $g_p(n, E) = \Gamma_p g_{m,p} - \alpha_p$ and the loss coefficient $\alpha_p(n) = \alpha_0 + \Gamma_p \alpha_1 n$, where α_0 is the waveguide scattering loss and α_1 the IVBA coefficient loss coefficient (Suematsu and Adams, 1994), with values of 3000 m^{-1} and 7500×10^{-24} m^2, respectively (Connelly, 2001).

20.4.2 Traveling-Wave and Carrier Density Rate Equations

A traveling-wave approach is used to determine signal and the TE and TM ASE photon rates. Transverse variations in the optical field are not considered, and as such, the model has a one-dimensional spatial dependency. The traveling-wave equation for the forward propagating signal photon rate N_s is

$$\frac{dN_s}{dz} = g_s N_s, \tag{20.12}$$

where g_s is the net gain coefficient at the signal polarization and photon energy E_s. The boundary condition at the input $N_s(z = 0) = P_{in}/E_s$, where P_{in} is the input signal power. For a given carrier density spatial

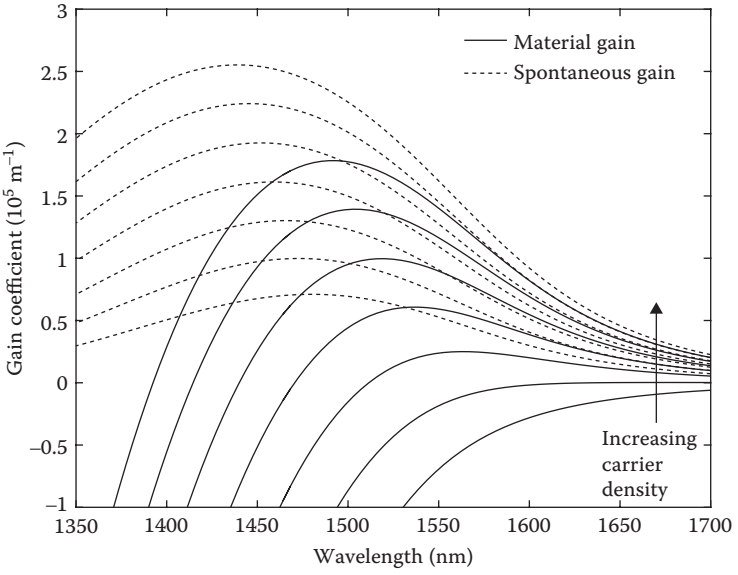

FIGURE 20.4 Unstrained bulk material gain and spontaneous emission gain spectra. The carrier density ranges from 2 to 5×10^{24} m^{-3} in increments of 0.5×10^{24} m^{-3}. The model takes into account intraband relaxation effects and carrier density–dependent bandgap shrinkage. The bandgap wavelength at zero carrier density is 1.55 μm.

distribution, Equation 20.12 has the solution

$$N_s(z) = \frac{P_{in}}{E_s} \exp\left(\int_0^z g_s dz\right), \tag{20.13}$$

which can be calculated using numerical integration. To model ASE, a spectral slicing scheme is used in which the ASE is split into M spectral slices, each of energy width ΔE. The traveling-wave equations for the forward (+) and backward (−) propagating kth spectral slice $N^{\pm}_{p,k}$ with polarization p and centered at energy E_k are given by

$$\frac{dN^{\pm}_{p,k}}{dz} = \pm g_{p,k} N^{\pm}_{p,k} \pm \Gamma_p g_{sp,p,k} \Delta E, \tag{20.14}$$

with boundary conditions $N^{+}_{p,k}(z = 0) = 0$ and $N^{-}_{p,k}(z = L) = 0$. The last term on the right-hand side (RHS) of Equation 20.14 is the additive spontaneous emission into the kth spectral slice. For a given carrier density spatial distribution, Equation 20.14 has the solution

$$N^{+}_{p,k}(z) = \exp\left(-\int_0^z g_{p,k}\, dz\right) \int_0^z \left[\exp\left(\int_0^z g_{p,k}\, dz\right) \Gamma_p\, g_{sp,p,k} \Delta E\right] dz \tag{20.15}$$

$$N^{-}_{p,k}(z) = \exp\left(-\int_z^L g_{p,k}\, dz\right) \int_z^L \left[\exp\left(\int_z^L g_{p,k}\, dz\right) \Gamma_p\, g_{sp,p,k} \Delta E\right] dz, \tag{20.16}$$

which can be calculated using numerical integration. The carrier density rate equation is

$$\frac{\mathrm{d}n}{\mathrm{d}t} = \frac{\eta I}{eV} - R(n) - \frac{1}{\mathrm{d}W}\left[\Gamma_\mathrm{s} g_{\mathrm{m},p} N_\mathrm{s} \; + \sum_{p=\mathrm{TE,TM}} \sum_{k=1}^{M} \Gamma_p \, g_{\mathrm{m},p,k}(N^+_{p,k} + N^-_{p,k})\right]. \tag{20.17}$$

The first term on the RHS of Equation 20.17 is the carrier pumping due to the injected bias current. The injection efficiency η is assumed to be equal to 1. Γ_s is the confinement factor of the signal polarization. The nonstimulated emission recombination rate $R(n)$ is given by

$$R(n) = A_\mathrm{tr} n + R_\mathrm{rad}(n) + Cn^3, \tag{20.18}$$

where A_tr and C are the trap and Auger coefficients, respectively. Trap recombination is mainly caused by Shockley–Read–Hall recombination at defects in the material (Fukuda, 1991). The spontaneous radiative recombination rate $R_\mathrm{rad}(n)$ is commonly assumed to be a bimolecular process approximated by $R_\mathrm{rad} = Bn^2$, where the bimolecular recombination coefficient B is often taken to be a fitting parameter; however, it can be directly calculated from the material gain (Chuang, 2009). For the material under consideration, $B \approx 2.8 \times 10^{-16} - 0.24 \times 10^{-40} \mathrm{n}\ \mathrm{m}^3\mathrm{s}^{-1}$. Auger recombination involves three carriers: an electron and hole, which recombine in a band-to-band transition and give off the resulting energy to another electron or hole (Chuang, 2009). Because SOAs usually operate with high carrier (electron) densities, the hole density is almost equal to the carrier density so the Auger recombination rate is proportional to n^3. The Auger coefficient for a particular material or structure can be calculated from first principles, but this is difficult and there is often a high degree of uncertainty in values quoted in the literature. In most models, typical values are used or it is treated as a fitting parameter. Here, C is taken to be equal to $3 \times 10^{-41}\ \mathrm{m}^6\mathrm{s}^{-1}$. At the high carrier densities present in SOAs and if the defect level is low, trap-induced recombination is often assumed to be negligible compared to the other two processes and can be ignored, as is the case here. The third term on the RHS of Equation 20.17 is the amplified signal-induced carrier density depletion rate. $\Gamma_\mathrm{s} N_\mathrm{s}$ is the photon rate in the active region, which is multiplied by $g_{\mathrm{m},p}$ to obtain the conduction band to valence band carrier recombination rate per unit length. Division by the active region cross-section area results in the carrier density depletion rate. The fourth term on the RHS of Equation 20.17 is the ASE-induced carrier density depletion rate, which is obtained in a similar fashion to that for the amplified signal.

20.4.3 Algorithm and Simulations

Under static conditions, the time differential in Equation 20.17 is equal to zero; the aim of the numerical algorithm is to determine the signal, ASE photon rates, and the carrier density such that this is the case (Connelly, 2007). The model equations cannot be solved analytically, thereby requiring a numerical solution (Connelly, 2001, 2007). Fifty spatial points are used for numerical integration and 150 spectral slices covering a range of 1250–1650 nm. First, the material gain and spontaneous gain are calculated for the spectral slice energies and particular values of carrier density within the expected range. The bimolecular recombination coefficient is calculated for the same carrier density values. Initially, the carrier density in the amplifier is set to some reasonable value (e.g., $3 \times 10^{24}\ \mathrm{m}^{-3}$). The signal intensity and ASE photon rates are then estimated using Equations 20.13, 20.15, and 20.16. An updated value for n at each spatial section is then estimated using Equation 20.17 with the time derivative set to zero, and subsequently the gain and spontaneous recombination rate throughout the amplifier, using interpolation of the full calculations, followed by the signal and ASE photon rates. This process is continued until the values of the ASE photon

rates converge to a suitable tolerance (0.1%). Amplifier characteristics such as gain, ASE spectrum, and noise figure can then be calculated. The polarization-dependent ASE output spectral density (W/Hz) at E_k is given by

$$\rho_{p,k} = \frac{h E_k}{\Delta E} N^+_{p,k}(z = L). \tag{20.19}$$

In the signal-spontaneous beat noise limit, the noise figure spectrum is given by

$$NF_{p,k} = 10 \log_{10} \left(\frac{2\rho_{p,k}}{E_k G_{p,k}} \right), \tag{20.20}$$

where $G_{p,k}$ is the amplifier gain at E_k (Baney et al., 2000; Olsson, 1989). The maximum gain achievable is mainly limited by ASE. The small-signal gain and ASE spectra are shown in Figure 20.5 for bias currents ranging from 40 to 100 mA. The gain and ASE spectrum peaks shift to shorter wavelengths as the bias current increases, an effect which is present in real SOAs, and they both saturate at high bias currents. The 3-dB optical gain bandwidth at a bias of 100 mA is 30.6 nm. The corresponding ASE spectrum has a 3-dB bandwidth of 34.4 nm; in general, the ASE spectral width is a reasonably good measure of the amplifier gain bandwidth. Figure 20.6a shows the small-signal gain and noise figure bias current dependency. The gain begins to saturate at bias currents at which the ASE saturates; the noise figure reaching a limiting value of approximately 11.7 dB. The ASE and carrier density spatial distributions are shown on Figure 20.6b for no input signal. The latter has a symmetrical profile with a maximum at the center, in contrast to the quasi-analytic model, which does not include ASE. The gain, output signal, and ASE powers versus input power characteristics are shown in Figure 20.7a for a bias current of 100 mA at which the unsaturated gain is 23.3 dB and $P_{o,sat} = 4.9$ dBm. The reduction in ASE power is clearly seen as the amplifier is driven into saturation by the input signal. As the input power level is increased, the amplified signal begins to compete for the available gain and the carrier density distribution becomes more asymmetrical, as shown in Figure 20.7b for a moderate saturation level.

The model can be used to investigate the effects of different material and geometrical parameters on SOA performance and is thereby useful in SOA design.

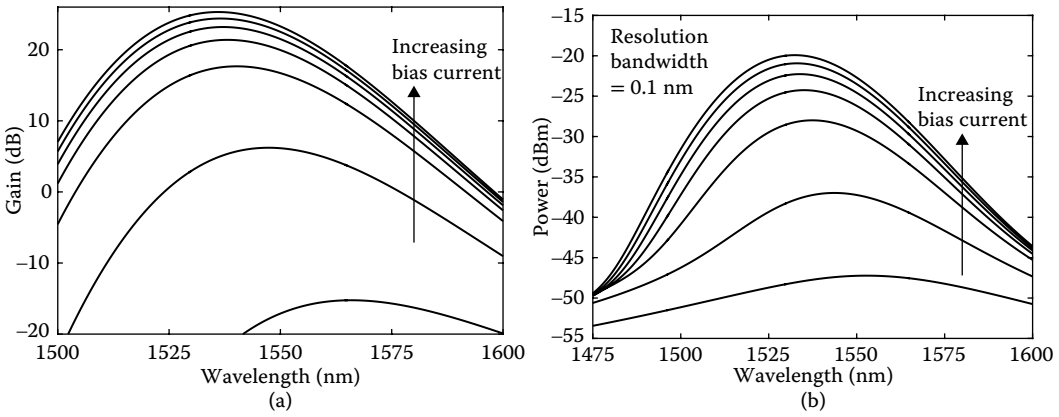

FIGURE 20.5 (a) Gain spectra and (b) amplified spontaneous emission (ASE) spectra (summed over both polarizations) in the absence of an input signal for bias currents of 40–100 mA in increments of 10 mA.

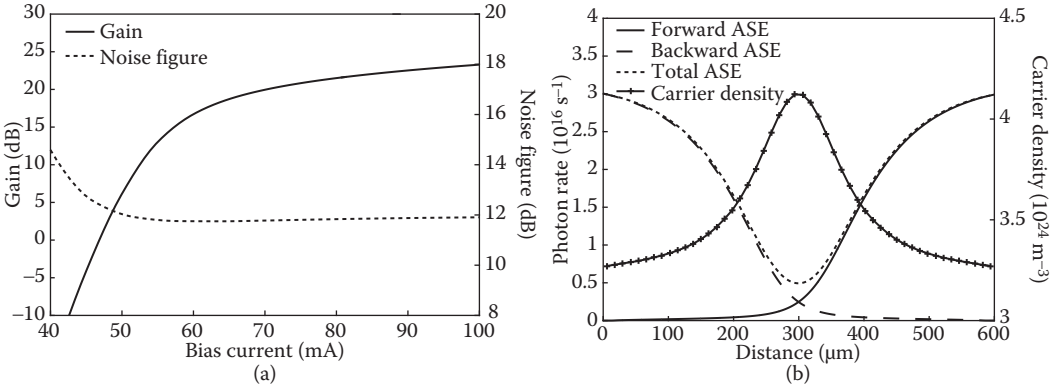

FIGURE 20.6 Small-signal (a) gain and noise figure versus bias current at 1550 nm, (b) ASE and carrier density spatial distributions. The bias current and signal wavelength are 100 mA and 1550 nm, respectively.

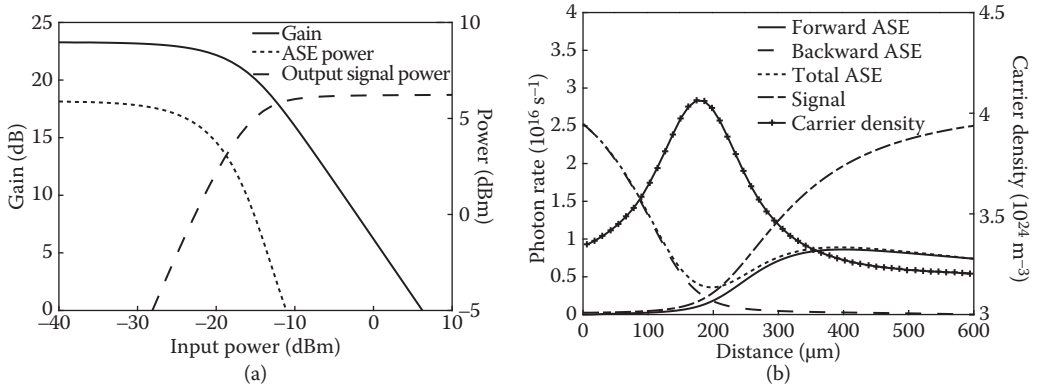

FIGURE 20.7 (a) Gain, output signal and ASE powers versus input power. (b) ASE and carrier density spatial distributions for an input power of −15 dBm, at which the gain has been reduced from its unsaturated value of 23.3–20 dB. The bias current and signal wavelength are 100 mA and 1550 nm, respectively.

20.5 Time-Domain Model Including ASE

The most common application of SOAs is for modulated signal amplification, so it is of interest to model time-domain behavior such as pattern effects, XGM, SPM, and XPM (Obermann et al., 1998; Durhuus et al., 1992; Asghari et al., 1997; Occhi et al., 2003). By including the time differential term in Equation 20.17, the static model described above can be used to model SOA dynamics having timescales as short as hundreds of picoseconds (Connelly, 2002b). The carrier density is initialized to some suitable value and the initial values of the signal and ASE photon rates are set to zero. The carrier density at the next time step is determined by solving Equation 20.17 using the modified Euler method, which is a second-order technique (Press et al., 2007) and for a given time step is significantly more accurate than simply replacing the time differential by a first-order finite difference (Euler method). Nonetheless, an appropriate time-step size must be chosen to prevent stability issues and ensure accuracy. Assuming that the propagation time through the amplifier is much less than the time variation of the optical input and current, the ASE and signal photon rates can be determined using Equations 20.13, 20.15, and 20.16. The new values of the

photon rates are then used in Equation 20.17 to determine the carrier density at the next time step until the time span of interest is completed.

The carrier density rate Equation 20.17 can be expressed as

$$\frac{\mathrm{d}n}{\mathrm{d}t} = \frac{\eta I}{eV} - n\left(\frac{1}{\tau_c} + \frac{1}{\tau_s}\right), \tag{20.21}$$

where the inverse of the nonstimulated emission carrier lifetime τ_c is given by

$$\frac{1}{\tau_c} = \frac{R(n)}{n}, \tag{20.22}$$

and the inverse of the stimulated recombination carrier lifetime τ_s is given by

$$\frac{1}{\tau_s} = \frac{1}{n\,\mathrm{d}W}\left[\Gamma_s g_{m,p} N_s + \sum_{p=\mathrm{TE,TM}} \sum_{k=1}^{M} \Gamma_p g_{m,p,k}(N_{p,k}^{+} + N_{p,k}^{-})\right]. \tag{20.23}$$

The total effective carrier lifetime τ_{eff} is

$$\tau_{eff} = \left(\frac{1}{\tau_c} + \frac{1}{\tau_s}\right)^{-1}, \tag{20.24}$$

which depends on the amplifier operating point and input optical power and also has a strong spatial dependency. The smaller the τ_{eff}, the faster the gain recovery time. Figure 20.8 shows the output power, spatially averaged effective carrier lifetime $\tau_{eff,m}$, and instantaneous gain for an amplified 5-Gb/s non-return-to-zero (NRZ) data stream with high and low powers of 0.1 mW and 0.1 μW, respectively. The bias current, unsaturated gain, and signal wavelength are 100 mA, 23.3 dB, and 1550 nm, respectively. The amplified data distortion is due to the dynamic changes of the carrier and photon distributions causing pattern effects on a timescale approximately given by $\tau_{eff,m}$, which for the simulations shown in Figure 20.8 can vary between 370 and 850 ps. At higher bit rates the severity of pattern effects increases and consequently their effect on system performance.

20.5.1 XGM Wavelength Converter

XGM occurs when an intensity-modulated input data signal (the pump) causes dynamic changes in the carrier density and thereby the gain experienced by a copropagating or counter-propagating light wave (the probe) at a different wavelength to the data signal. Carrier density changes also cause changes in the active region refractive index and thereby the phase of both the pump and probe leading to SPM and XPM. XGM can be used to realize wavelength converters in which data is copied from an input pump data signal to an input continuous wave (CW) probe. An XGM-based 2.5-Gb/s wavelength converter with copropagating pump and probe light waves is shown in Figure 20.9. When the pump power is high, the gain experienced by the probe is reduced and vice versa, hence the inverted pump data is transferred to the probe. The above time-domain model is used to simulate the converter, as shown in Figure 20.9. The performance degrades as the bit rate increases, as the dynamic gain is unable to follow the variations in the input pump power. Because of their superior dynamics, compared to bulk or QW SOAs, QD SOAs can be used as XGM wavelength converters at much higher bit rates.

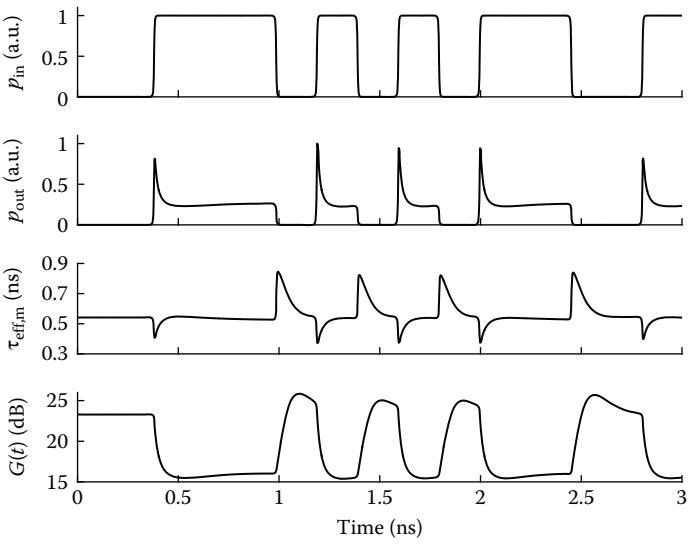

FIGURE 20.8 Simulated SOA output power, spatially averaged effective carrier lifetime, and instantaneous gain for an input NRZ 5-Gb/s data sequence. The data high- and low-level powers are 0.1 mW and 0.1 μW, respectively. The bias current, unsaturated gain, and signal wavelength are 100 mA, 23.3 dB, and 1550 nm, respectively. The simulation time step is 2.5 ps.

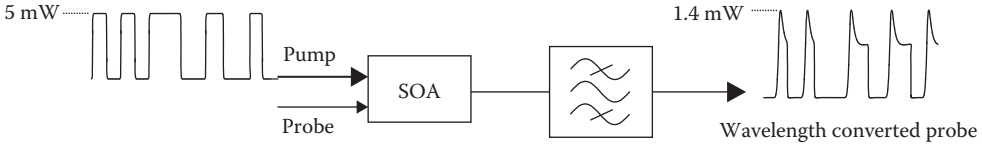

FIGURE 20.9 Cross-gain modulation (XGM)-based wavelength converter and simulated wavelength converted probe output. The bandpass filter is used to select the probe signal. The pump input is a 30-dB extinction ratio NRZ 2.5-Gb/s data sequence with a peak power and wavelength of 5 mW and 1550 nm, respectively. The input probe power and wavelength are 10 μW and 1560 nm, respectively. The bias current is 100 mA.

20.6 Pulse Amplification Analytic Model

Because SOAs have wide optical bandwidths and fast gain recovery lifetimes, they can be used to amplify optical pulses with full width at half-maximum (FWHM) pulse widths in the picosecond range. By exploiting SOA nonlinearities using materials with intrinsically faster gain recovery times, it is possible to amplify femtosecond pulses. Many pulse amplification models are described in the literature; here a simple model (Agrawal and Olsson, 1989), which does not include ASE, is described. The model is applicable to pulse widths greater than the intraband relaxation time (typically <0.1 ps). The amplifier is assumed to be polarization independent. The optical field can be written as $A(t) = \sqrt{P(t)}\,\exp[j\varphi(t)]$, where P and φ are the temporal power and phase. The gain coefficient g at the signal wavelength is modeled as $g = \Gamma a\,(n - n_{tr})$. The power, phase, and gain coefficient dynamics are determined by solving

$$\frac{\partial P}{\partial z} = (g - \alpha)P \tag{20.25}$$

$$\frac{\partial \varphi}{\partial z} = -\frac{1}{2}\alpha_H g \tag{20.26}$$

$$\frac{\partial g}{\partial \tau} = \frac{(g - g_0)}{\tau_c} - \frac{gP}{E_{sat}}. \tag{20.27}$$

τ is the pulse local time measured with respect to a time frame moving with the pulse. The temporal dependence of g, induced by the propagating pulse power, leads to dynamic changes in the pulse phase, i.e., SPM. τ_c is the interband carrier lifetime, which is typically the order of hundreds of picoseconds in bulk and QW SOAs, and α_H is the LEF—a proportionality factor relating phase changes to changes in the gain (Henry, 1982). α_H is often taken to be a constant, but for a given material is carrier density and wavelength dependent. The saturation energy $E_{sat} = E_s Wd/(\Gamma a)$. To determine the evolution of the pulse shape and phase, a numerical solution of Equations 20.25 through 20.27 is required. However, if it is assumed that $\alpha << g$ then Equations 20.23 through 20.25 can be solved to obtain a closed-set of equations for the output pulse power and phase given by

$$P_{out}(\tau) = G(\tau)P_{in}(\tau) \tag{20.28}$$

$$\varphi_{out}(\tau) = \varphi_{in}(\tau) - \frac{\alpha_H}{2}h(\tau), \tag{20.29}$$

where the instantaneous gain $G(\tau) = \exp[h(\tau)]$. If the input FWHM pulse width $\tau_p << \tau_c$, then the integrated gain $h(\tau)$ is given by

$$h(\tau) = -\ln\left\{1 - \left(1 - \frac{1}{G_0}\right)\exp\left[-\frac{U_{in}(\tau)}{E_{sat}}\right]\right\}, \tag{20.30}$$

where $G_0 = \exp(g_0 L)$ is the unsaturated gain, g_0 is the unsaturated gain coefficient, and

$$U_{in}(\tau) = \int_{-\infty}^{\tau} P_{in}(\tau')\,d\tau'. \tag{20.31}$$

The output pulse frequency chirp, defined as the time derivative of its instantaneous phase divided by 2π, is given by

$$\Delta\nu_{out}(\tau) = \Delta\nu_{in}(\tau) + \frac{\alpha(G_0 - 1)}{4\pi G_0}\frac{P_{out}(\tau)}{E_{sat}}\exp\left[\frac{-U_{in}(\tau)}{E_{sat}}\right], \tag{20.32}$$

where $\Delta\nu_{in}$ is the input pulse chirp. The model is applicable to pulse widths of the order of picoseconds to tens of picoseconds. For pulse widths >1 ps, nonlinear intraband processes such as carrier heating (CH) and spectral hole burning (SHB) that have characteristic time constants in the subpicosecond range are important; so, models that take such effects into account are required (Hong et al., 1994; Mecozzi and Mork, 1997). Once the output pulse power and phase are known, its power spectrum can be calculated. To show the effects of an SOA on an amplified pulse consider an unchirped zero phase Gaussian input pulse,

$$P_{in}(\tau) = \frac{E_{in}}{\tau_0\sqrt{\pi}}\exp\left[-\left(\frac{\tau}{\tau_0}\right)^2\right], \tag{20.33}$$

where E_{in} is the pulse energy. τ_o is related to τ_p by $\tau_p \approx 1.665\tau_0$. Simulated amplified pulse shape, chirp, and spectrum are shown in Figure 20.10. The amplified pulse is asymmetric because the leading edge of

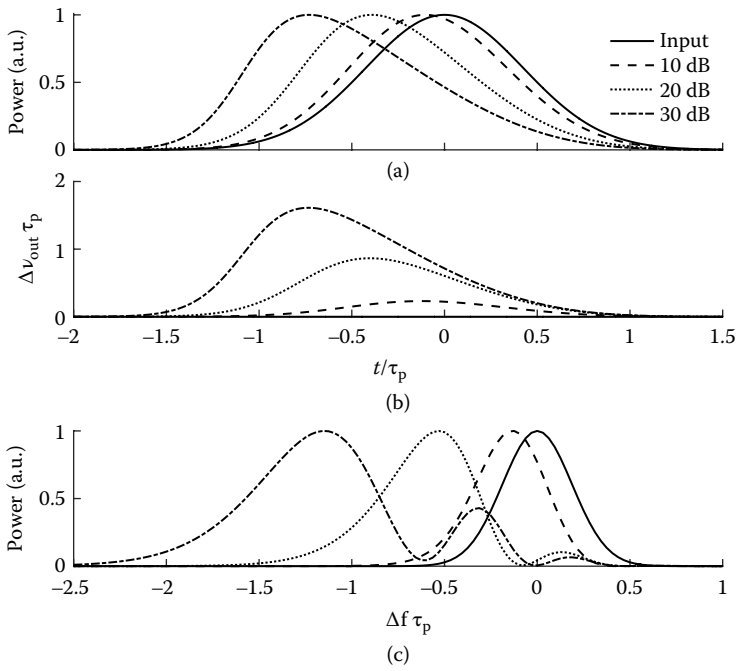

FIGURE 20.10 Amplified pulse; (a) power, (b) chirp, and (c) spectrum. Δf is the frequency deviation from the input light wave center frequency. The input is a zero-chirp Gaussian pulse with $E_{in}/E_{sat} = 0.1$. The parameter is the unsaturated gain and $\alpha_H = 5$.

the pulse experiences a larger gain than the trailing edge. The amplified pulse is chirped and its spectrum is broader than the input spectrum. At high gains, the amplified pulse spectrum exhibits a multipeak structure caused by SPM-induced frequency chirp.

20.6.1 SOA XPM Mach–Zehnder Wavelength Converter

XGM-based wavelength converters suffer from the disadvantage that high-input pump powers are required to obtain the large SOA gain modulation depth necessary to achieve a large converted signal extinction ratio. The associated high-carrier depletion rates lead to a significant increase in the gain recovery lifetime, which limits the data rates at which such converters can operate. To overcome the trade-off between speed and modulation depth SOA XPM can be used (Asghari et al., 1997). XPM occurs when an intensity-modulated input data signal (the pump) causes dynamic changes in the carrier density and, consequently, the active region refractive index and thereby the phase of a copropagating or counter-propagating probe signal at a different wavelength to the pump. In an SOA XPM-based wavelength converter, the probe phase changes are converted into amplitude changes by incorporating one or two SOAs in an interferometric structure such as the Mach–Zehnder interferometer (MZI) shown in Figure 20.11. If sufficient phase shift is achieved with a low-gain modulation index, and the interferometer visibility is high, then the XPM converter performance will be superior to XGM-based converters. An optical delay line is used to adjust the relative delay between the modulated input pump pulses reaching each SOA. The interferometer output probe power, assuming that destructive interference occurs between the recombining probe light waves when their relative phases are equal, is given by

$$p(t) = \frac{P_{probe}}{4}\left[G_1(t) + G_2(t) - 2\sqrt{G_1(t)G_2(t)}\cos\left(\varphi_1(t) - \varphi_2(t)\right)\right], \tag{20.34}$$

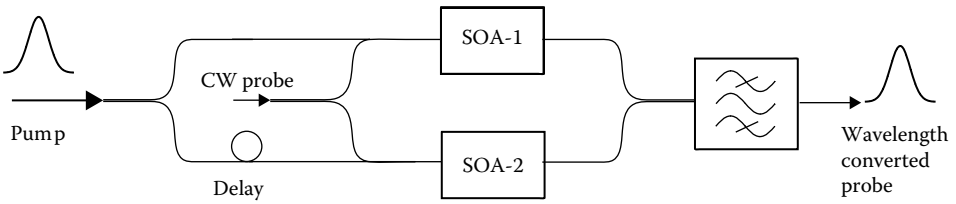

FIGURE 20.11 SOA Mach–Zehnder interferometer (MZI) wavelength converter.

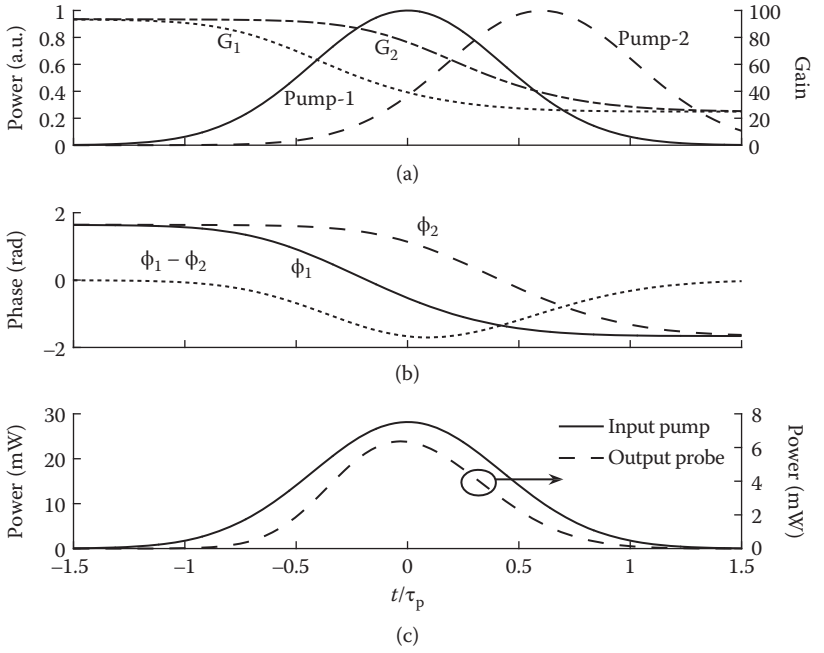

FIGURE 20.12 SOA MZI wavelength converter simulations. (a) SOA input pump powers and dynamic gains, (b) induced SOA probe phase shifts and difference, (c) comparison between the input pump and converted probe pulse shapes.

where P_{probe} is the input CW probe power, $G_1(t)$, $\varphi_1(t)$, $G_2(t)$, and $\varphi_2(t)$ are the gain and phase changes of the SOA in the upper and lower interferometer arms, respectively. The couplers have splitting and coupling ratios of 3 dB. The pulse amplification model described above can also be used to model XPM in the case where the input pump pulse width is much less than the intraband lifetime and assuming that the gain has fully recovered since the previous pulse. Including the effects of relatively slow interband processes requires a numerical solution. In the following simulations, an MZI with two identical SOAs having gains of 20 dB and $\alpha_H = 5$ is considered. The input pump is a zero-chirp Gaussian pulse with $E_{in}/E_{sat} = 0.03$. The CW input probe power is −10 dBm. The delay between the pump pulses entering SOA-1 and SOA-2 is equal to 0.6 of the input pump pulse width. These settings were chosen to obtain a converted probe pulse shape similar to the input pump pulse, as shown in Figure 20.12. The input pump pulse causes dynamic gain saturation and associated probe phase shifts. In the unsaturated state, the phase difference between the probe light waves in the interferometer arms is zero, leading to total destructive interference and thereby a zero output probe signal. The arrival of the pump pulses in the SOAs creates a window in which the magnitude of the phase difference increases, leading to constructive interference and thereby a nonzero converted probe signal pulse.

20.7 FWM Analytic Model

FWM is a *coherent* nonlinear process that can occur in an SOA between two copolarized input optical fields, a strong pump and a weaker probe at angular frequencies ω_0 and $\omega_0 - \Omega$, where Ω is the pump and probe detuning Agrawal (1988). Beating between the optical fields results in the establishment of gain and refractive index pulsations in the SOA at the detuning frequency. In most practical applications of FWM, in particular wavelength conversion, the detuning is much larger than the inverse of the interband carrier lifetime (typically in the nanosecond range) and the pulsations are caused by fast intraband processes, in particular CH and SHB. The gain and index pulsations result in nondegenerate FWM, in which energy from the pump and probe is coupled into a new copropagating field at frequency $\omega_0 + \Omega$, called the conjugate, so termed because its dynamic phase is the opposite of the signal phase.

SHB is caused by the injected pump signal creating a hole in the *intraband* carrier distribution. This modulates the occupation probability of carriers within a band leading to fast gain modulation. CH is caused by stimulated emission and free carrier absorption. Stimulated emission subtracts carriers that are cooler than average while free carrier absorption moves carriers to higher-energy levels in the band. The resulting increase in temperature decreases the gain. Two characteristic times are associated with CH: the carrier–phonon scattering time τ_1, which is the average time carriers require to cool down to the semiconductor lattice temperature, and the carrier–carrier scattering time τ_2, which is the average time taken by the carrier population to reach a heated equilibrium from the initial nonheated equilibrium. The latter time constant is also associated with SHB. The characteristic times are of the order of tens to hundreds of femtoseconds, so FWM-based wavelength converters can operate with detuning frequencies as high as hundreds of GHz. A comprehensive analysis of FWM in SOAs requires a numerical solution to a set of coupled-mode equations Agrawal (1988). The electric field in the SOA can be expressed as

$$E(z,t) = E_1 \exp\left\{j[k_1 z - (\omega_0 - \Omega)t]\right\} + E_0 \exp\left[j(k_0 z - \omega_0 t)\right] + E_2 \exp\left\{j[k_2 z - (\omega_0 + \Omega)t]\right\}, \quad (20.35)$$

where the copropagating and copolarized pump, probe, and conjugate field amplitudes are E_0, E_1, and E_2, respectively, with corresponding frequencies of ω_0, $\omega_0 - \Omega$, and $\omega_0 + \Omega$, and propagation coefficients k_0, k_1, and k_2. If it is assumed that the conjugate power is small relative to the copropagating input pump and probe powers, then an analytic model can be used to predict the SOA FWM characteristics (Mecozzi et al., 1995). In this model, the FWM conversion efficiency η defined as the ratio of the output conjugate to input probe powers is given by

$$\eta = G\left|G_1\right|^2. \quad (20.36)$$

G is the saturated amplifier gain, which can be calculated using Equation 20.11, where p is taken to be the sum of the pump and probe powers. The unsaturated gain $G_0 = \exp[(g_0 - \alpha)L]$, where g_0 and α are the unsaturated gain and loss coefficients, respectively.

$$G_1 = \frac{-1 + j\alpha_H}{\alpha_H} \exp\left[-\frac{1}{2}\sigma F_{cd}(\Omega)\right] \sin\left[\frac{\alpha_H}{2}\sigma F_{cd}(\Omega)\right] - \frac{1}{2}\varepsilon_{sh} P_{sat} H_{sh}(\Omega)\,\sigma F_{sh} - \frac{1}{2}\varepsilon_{ch} P_{sat} H_{ch}(\Omega)\,\sigma F_{ch} \quad (20.37)$$

$$F_{cd}(\Omega) = \frac{1}{1 - j\Omega\tau_c\,\zeta}\left[\ln\left(\frac{1 + GP_T/P_{sat} - j\Omega\tau_c}{1 + P_T/P_{sat} - j\Omega\tau_c}\right) + \zeta \ln\left(\frac{G_0}{G}\right)\right] \quad (20.38)$$

$$F_{ch} = -\frac{1}{\zeta}\left[\frac{P_T}{P_{sat}}(G-1) - \ln\left(\frac{G_0}{G}\right)\right] \quad (20.39)$$

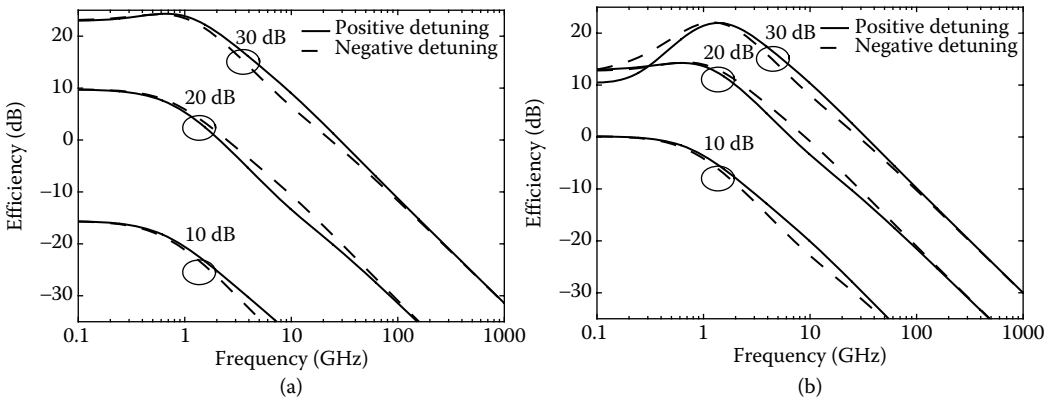

FIGURE 20.13 Four-wave mixing (FWM) efficiency versus absolute value of frequency detuning for input pump and probe powers of (a) 200 and 20 μm, and (b) 20 and 2 μm, respectively.

$$F_{sh} = \ln\left(\frac{G_0}{G}\right) \tag{20.40}$$

$$S(0) = P_{sat}\left(\frac{1-\zeta}{\zeta}\right)\frac{1-(G/G_0)^{\zeta}}{G-(G/G_0)^{\zeta}} \tag{20.41}$$

$$\sigma = \frac{P_0}{P_0+P_1}. \tag{20.42}$$

ε_{ch} and ε_{sh} are parameters characterizing the strengths of CH and SHB processes, respectively, and $\zeta = \alpha/g_0$. P_0 and P_1 are the input pump and probe powers, respectively, and the total input power $P_T = P_0 + P_1$. The Fourier transforms H_{ch} and H_{sh} of the nonlinear gain responses due to CH and SHB, respectively, are given by

$$H_{ch}(\Omega) = \frac{1}{(1-j\Omega\tau_1)(1-j\Omega\tau_2)} \tag{20.43}$$

$$H_{sh}(\Omega) = \frac{1}{1-j\Omega\tau_2}. \tag{20.44}$$

The spatial dependence of the saturated gain G can be determined using Equation 20.9, where p is taken to be the sum of the normalized pump and probe powers. Figure 20.13 shows the calculated efficiency for different values of amplifier unsaturated gain and input pump/probe powers with model parameters: $P_{sat} = 10$ mW, $\alpha_H = 4.0$, $\tau_c = 0.25$ ns, $\tau_1 = 750$ ps, $\tau_2 = 15$ ps, $\varepsilon_{sh} = 10.0$ W^{-1}, $\varepsilon_{ch} = 2.5$ W^{-1}, and $\exp(\alpha L) = 5$ dB. The efficiency characteristics are asymmetric and show a more peaked structure as the amplifier gain is increased. The efficiency can be greater than unity for frequencies up to hundreds of GHz, i.e., frequency conversion with gain, so FWM-based SOA wavelength converters are of particular importance in wavelength division multiplexed systems with wide wavelength channel spacing.

20.8 Conclusion

SOAs have many uses in optical networks, not only as basic amplifiers but also as fundamental components in all-optical signal processing applications. Although SOAs have been investigated for many years, the development of new SOA structures and incorporation in PICs, advanced materials such as QDs, and exploitation of ultrafast nonlinearities make SOA research and development an exciting field of study.

The successful advancement of SOA technology requires the development of accurate models, which can be a significant challenge requiring a deep knowledge and understanding of many diverse areas such as photonic materials, device design, optoelectronic nonlinearities, noise modeling, and communication systems design. This chapter has given an overview of SOA basics and used relatively simple models to explain important SOA characteristics and applications. Further chapters consider more advanced models applied to particular types of SOAs.

References

Agrawal, A. P. 1988. Population pulsations and nondegenerate four-wave mixing in semiconductor lasers and amplifiers. *J. Opt. Soc. Am. B* 5:147–159.

Agrawal, A. P. and Olsson, A. 1989. Self-phase modulation and spectral broadening of optical pulses in semiconductor laser amplifiers. *IEEE J. Quantum Electron*. 25:2297–2306.

Akiyama, T., Sugawara, M. and Arakawa, Y. 2007. Quantum-dot semiconductor optical amplifiers. *Proc. IEEE* 95:1757–1766.

Asghari, M., White, I. H. and Penty, R. V. 1997. Wavelength conversion using semiconductor optical amplifiers. *J. Lightwave Technol*. 15: 1181–1190.

Baney, D. M., Gallion, P. and Tucker, R. S. 2000. Theory and measurement techniques for the noise figure of optical amplifiers. *Opt. Fiber Technol*. 6:122–154.

Ben-Ezra, Y., Haridim, M. and Lembrikov, B. I. 2005. Theoretical analysis of gain-recovery time and chirp in QD-SOA. *IEEE Photonics Technol. Lett*. 17:1803–1805.

Chuang, S. L. 2009. *Physics of Optoelectronic Devices*. New York, NY: Wiley.

Connelly, M. J. 2001. Wide-band semiconductor optical amplifier steady-state numerical model. *IEEE J. Quant. Electron*. 37:439–447.

Connelly, M. J. 2002a. *Semiconductor Optical Amplifiers*. Boston, MA: Springer.

Connelly, M. J. 2002b. Wideband dynamic numerical model of a tapered buried ridge stripe semiconductor optical amplifier gate. *IEE Proc. Circ. Dev. Syst*. 149:173–178.

Connelly, M. J. 2007. Wide-band steady-state numerical model and parameter extraction of a tensile-strained bulk semiconductor optical amplifier. *IEEE J. Quant. Electron*. 43:47–56.

Durhuus, T., Mikkelsen, B. and Stubkjaer, K. E. 1992. Detailed dynamic model for semiconductor optical amplifiers and their crosstalk and intermodulation distortion. *J. Lightwave Technol*. 10:1056–1065.

Dutta, N. K. and Wang, Q. 2013. *Semiconductor Optical Amplifiers*. Singapore: World Scientific Publishing.

Fukuda, M. 1991. *Reliability and Degradation of Semiconductor Lasers and LEDs*. Boston, MA: Artech House.

Henry, C. H. 1982. Theory of the linewidth of semiconductor lasers. *IEEE J. Quant. Electron*. 18:259–264.

Hong, M. Y., Chang, Y. H., Dienes, A., Heritage, J. P. and Delfyett, P. J. 1994. Subpicosecond pulse amplification in semiconductor laser amplifiers: Theory and experiment. *IEEE J. Quant. Electron*. 30:1122–1131.

Jones, G. and O'Reilly, E. P. 1993. Improved performance of long-wavelength strained bulk-like semiconductor lasers. *IEEE J. Quant. Electron*. 29:1344–1345.

Kweon, G. 2002. Noise figure of optical amplifiers. *J. Korean Phys. Soc*. 41:617–628.

Lee, W., Park, M. Y., Cho, S. H., Lee, J., Kim, B. W., Jeong, G. and Kim, B. W. 2005. Bidirectional WDM-PON based on gain-saturated reflective semiconductor optical amplifiers. *IEEE Photon. Technol. Lett*. 17:2460–2462.

Lelarge, F., Dagens, B., Renaudier, J., Brenot, R., Accard, A., van Dijk, F., Make, D., Le Gouezigou, O., Provost, J. G., Poingt, F. and Landreau, J. 2007. Recent advances on InAs/InP quantum dash based semiconductor lasers and optical amplifiers operating at 1.55 μm. *IEEE J. Sel. Top. Quantum Electron*. 13:111–124.

Mecozzi, A. and Mork, J. 1997. Saturation induced by picosecond pulses in semiconductor optical amplifiers. *J. Opt. Soc. Am. B* 14:761–770.

Mecozzi, A., Scotti, S., D'Ottavi, A., Iannone, E. and Spano, P. 1995. Four-wave mixing in traveling-wave semiconductor optical amplifiers. *IEEE J. Quant. Electron*. 31:689–699.

Obermann, K., Kindt, S., Breuer, D. and Petermann, K. 1998. Performance analysis of wavelength converters based on cross-gain modulation in semiconductor-optical amplifiers. *J. Lightwave Technol*. 16:78–85.

Occhi, L., Schares, L. and Guekos, G. 2003. Phase modeling based on the α-factor in bulk semiconductor optical amplifiers. *IEEE J. Sel. Top. Quantum Electron*. 9:788–797.

Olsson, N. A. 1989. Lightwave systems with optical amplifiers. *J. Lightwave Technol*. 7:1071–1082.

Press, W. H., Teukolsky, S. A., Vetterling, W. T. and Flannery, B. P. 2007. *Numerical Recipes: The Art of Scientific Computing*, 3rd ed. New York, NY: Cambridge University Press.

Suematsu, Y. and Adams, A. R. 1994. *Handbook of Semiconductor Lasers and Photonic Integrated Circuits*. London: Chapman & Hall.

21

Traveling-Wave and Reflective Semiconductor Optical Amplifiers

Angelina Totović
and
Dejan Gvozdić

21.1 Introduction

Eras in modern human history have often been labeled by their most significant and widely adopted technological achievements. It is no wonder that the last several decades proudly bear the name "The Information Age." Information, in its many forms, is an invaluable asset and its dissemination, collection, storage, and analysis have been the primary focus of researchers in numerous fields. Ever-increasing hunger for information exchange has driven supporting technologies to new levels. The transition from electric to optical domain has proved to be one of the most significant milestones of modern communications. According to TeleGeography and Huawei Marine Networks, as of early 2017, it has been estimated that close to 1.1 million kilometers of submarine optical cables exist, each bearing several optical fibers, and approximately 99% of all international telecommunications traffic is carried over this infrastructure. Starting from the overloaded backbone links, optical technology was gradually implemented in the lower levels of network hierarchy, with the ultimate goal of reaching individual users in the foreseeable future. Decreasing attenuation, eliminating electromagnetic interference, reducing the power consumption, and

diminishing the possibility of eavesdropping are just some of the advantages the new technology has realized (Ramaswami, 2002). With advantages also come challenges, as we are gravitating toward increased efficiency, which includes increased capacity over larger distances with decreased signal degradation and power consumption, and aggregation of fixed and mobile networks into a single network architecture (Carapellese et al., 2014). Aside from information exchange, information processing and storage in the optical domain remain in focus as we pursue all-optical solutions to mitigate unnecessary electro-optic and opto-electric conversion (Ramaswami, 2002; Sygletos et al., 2008). Many steps have already been taken, both in the physical layer, where new materials and production technologies significantly influenced performance, and in the higher levels of abstraction, where new modulation formats and protocols have been introduced (Ramaswami, 2002; Gladisch et al., 2006; Sygletos et al., 2008). Devices that are simple, but can perform multiple functions, have always been highly regarded. One example is the semiconductor optical amplifier (SOA)—a photonic device that under adequate conditions can amplify the input optical signal. SOAs have been extensively studied and perfected over the past three decades. Similar to laser diodes, they are compact and easy to produce and integrate with other photonic devices on a single chip (Xing et al., 2004). Wide amplification spectrum makes them suitable for use in wavelength-division multiplexed (WDM) optical networks (Mecozzi and Wiesenfeld, 2001; Zimmerman and Spiekman, 2004; Kani, 2010). SOAs consume relatively little power (Xing et al., 2004; Sygletos et al., 2008; Koenig et al., 2014), they are transparent to the optical signal modulation format (Schmuck et al., 2013; Koenig et al., 2014), and they can be designed to be polarization insensitive (Mathur and Dapkus, 1992; Carlo et al., 1998; Michie et al., 2006).

Aside from being used as standalone amplifiers, SOAs can be used for numerous other important functions (Olsson, 1989; Mecozzi and Wiesenfeld, 2001), such as switching (Stabile and Williams, 2011; Figueiredo et al., 2015), modulation/remodulation (Totović et al., 2011; Pham, 2014), wavelength conversion (Joergensen et al., 1997; Dailey and Koch, 2009), signal regeneration (Sygletos et al., 2008), all-optical flip-flops (Pitris et al., 2015), and all-optical random access memory (RAM) cells (Vyrsokinos et al., 2014), to name just a few.

21.2 General Structure and Operation Principles of TW- and R-SOA

Although SOAs come in many different forms, they all share several common features. Each SOA consists of an active region and a cladding and can have either highly reflective or antireflective facets, or a combination of the two, as shown in Figure 21.1. The two most commonly used SOA structures are the traveling-wave (TW) SOA and the reflective (R) SOA.

In the TW-SOA, both facets are coated with an antireflective layer, and the optical signal travels only once through the active region. In other words, input and output ports of TW-SOA are on opposite sides. This is preferable configuration for using SOA as a standalone amplifier, whether as a booster, in-line, or preamplifier (Olsson, 1989; Xing et al., 2004). On the other hand, the R-SOA has one antireflective and one highly reflective facet, which causes the signal to be reflected and travel through the active region twice. Both input and output ports are on the same side, namely at the antireflective facet. The rear facet can be made semitransparent, rather than highly reflective, which is usually the case if the interface between the cleaved semiconductor facet and air is responsible for reflection. This may be a useful feature, since now two output signals can be used, one at the rear and one at the front facet. An SOA with both facets highly reflective is the Fabry–Pérot (FP) SOA (Adams et al., 1985; Thylén, 1988). Due to the feedback loop provided by the highly reflective facets, the FP-SOA closely resembles a laser diode, although it is not typically used to generate coherent signal by itself (Yariv and Yeh, 2007). Nevertheless, its spectrum does exhibit pronounced resonances and antiresonances, unlike TW- and R-SOAs, where ripples in spectrum are much more subtle and are the result of residual reflectivity of the antireflective facets (Yariv and Yeh, 2007).

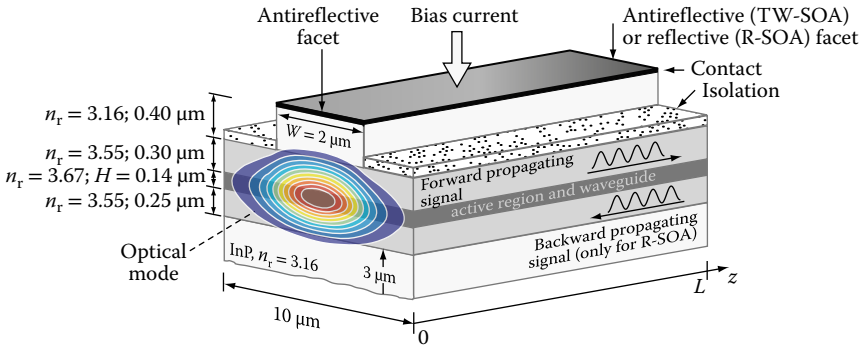

FIGURE 21.1 Schematic representation of the semiconductor optical amplifier (SOA), with relevant geometrical parameters and signals denoted. The active region is based on the unstrained bulk $In_{0.53}Ga_{0.47}As$ and designed to be polarization insensitive. (R-SOA, reflective SOA; TW-SOA, traveling-wave SOA.)

The active region is responsible for the signal amplification through the mechanism of stimulated emission, where the electric bias current is used to achieve population inversion. The purpose of the built-in waveguide is to confine the optical signal that propagates along the SOA and prevent its leaking into the cladding. The output signal of any SOA should ideally be an amplified replica of the input signal, although, in practice, a certain amount of noise is always superimposed, due to the always-present spontaneous emission. Aside from the photons initially generated through the process of spontaneous emission, noise propagation leads to its amplification, which finally results in amplified spontaneous emission (ASE) noise. Although the noise is typically regarded as the unwanted by-product of the device operation, there are numerous examples of using the noise either to generate or deliberately modify the optical signal (Yamatoya and Koyama, 2004; de Oliveira Ribeiro et al., 2005; Kang et al., 2006; Gebrewold et al., 2015), or enhance the overall SOA performance (Valiente et al., 1996).

SOAs can also be classified based on the material used for the active region, where each material has advantages and disadvantages. The simplest choice is bulk semiconductor (Michie et al., 2006; Connelly, 2007; Mazzucato et al., 2015; Totović et al., 2015). However, due to the several drawbacks of bulk SOA, such as high recovery time (Zilkie et al., 2007), and broad ASE spectrum (Totović et al., 2013), other solutions have emerged.

Depending on the desired improvement, different materials with a higher degree of confinement can be used (Zilkie et al., 2007), starting from multiple quantum well (MQW) (Nagarajan et al., 1992; Keating et al., 1999; Qin et al., 2012), and continuing to quantum dash (QDash) (Gioannini, 2004; Reithmaier et al., 2005; Qasaimesh, 2013) and quantum dot (QD) materials (Berg et al., 2001; Qasaimesh, 2003; Kim et al., 2009). SOAs with the active region based on these materials usually exhibit better performance in one or more aspects, at the expense of increased complexity and production cost. For example, QD SOA has fast recovery time, which is crucial for ultrafast signal processing, but due to the dot size distribution, it has moderate material gain and wide ASE spectrum, with full-width at half-maximum (FWHM) reaching double the values reported for MQW and QDash SOAs (Zilkie et al., 2007). On the other hand, QDash SOA has high differential gain and requires much lower driving currents in comparison with other active region types and outperforms bulk SOA in terms of time needed for gain recovery (Reithmaier et al., 2005).

21.3 Modeling of Material and Structural Parameters

Before proceeding to the SOA analysis, it is necessary to understand the physical principles responsible for its operation and quantify them through the parameters typically used for description of photon–electron

interaction in the active media. In addition, the waveguide should be optimized to provide polarization-insensitive operation, and the parameters describing it should also be studied.

21.3.1 Material Gain, Radiative Spontaneous Recombination, and Refractive Index Variation

Some of the most important optical properties of an SOA's active layer, determining its functional performance and parameters, are material gain, radiative spontaneous recombination (spontaneous emission) rate, and refractive index. Material gain, or gain per unit length, together with several other structural parameters, is responsible for defining the transmission (device) gain, i.e., the ratio of powers of the output and input optical signals, which is a figure of merit for the amplifier's capability to amplify the input optical signal by stimulated emission of photons (Connelly, 2002). Radiative spontaneous recombination rate and its spectral distribution represent the defining parameters that sculpt ASE spectrum and the SOA's noise (Silver et al., 2000; Connelly, 2002), whereas the refractive index variation directly affects the SOA linewidth enhancement factor (LEF) (Wang et al., 2007), further influencing the SOA's performance in cross-phase modulation (XPM) systems and optical switching.

In SOAs, stimulated emission has interband character, meaning that it occurs between the conduction band (CB) and the valence band (VB) of the semiconductor. Since these electronic bands consist of dispersed energy levels with different density per unit energy and occupation probability, the material gain significantly differs from gain in other solid-state or gas optically active media, which have a few (usually three or four) energy levels involved in the process of stimulated emission and its provisioning. The spreading of energy levels in the bands leads to a broad spectrum of material gain, which increases with the increase of injected carrier density or, equivalently, the current density. The radiative stimulated recombination rate is generally proportional to material gain (Chuang, 1995; Coldren et al., 2012), similar to the radiative spontaneous recombination rate (Chuang, 1995; Coldren et al., 2012). The material gain, as well as the radiative spontaneous recombination rate and the refractive index change, is, generally speaking, the function of three quantities: the joint density of states, electron/hole occupation probability, and a constant corresponding to a single optical transition between the two energy levels, one in CB and the other in VB.

The model of material gain, and the other two parameters, depends on the degree of carrier confinement in the active region of the SOA and the semiconductor strain introduced by the confinement. However, the models may differ with respect to degree of accuracy, i.e., approximations adopted in the model. The common framework for calculating optical properties of semiconductor bulk and quantum confined structures is the envelope function approximation (Meney et al., 1994). Within this framework, a relatively simple, so-called "two-band" model is used for material gain calculation (Chuang, 1995). It is based on the assumption of parabolic band dependence $E(k)$, where E is the energy and k is the wave vector of electron (hole) in the conduction (valence) band. Each band is treated separately by the effective mass Schrödinger equation (Chuang, 1995). More sophisticated multiband envelope function models account for the VB mixing effect, which essentially means that the character of sub-bands is a mixture of heavy hole (HH), light hole (LH), and split-off (SO) band. This effect occurs as a result of quantum confinement and becomes more prominent as the degree of confinement increases.

The most common multiband envelope function models are the Luttinger–Kohn (LK) 4×4 (Chuang, 1991) and 6×6 models (Chao and Chuang, 1992). The former model (LK 4×4) accounts for HH and LH band mixing, whereas the latter (LK 6×6) includes SO band, in addition to HH and LH bands. A more advanced multiband approach is based on the 8×8 $\mathbf{k} \cdot \mathbf{p}$ model (Meney et al., 1994; Liu and Chuang, 2002; Gvozdić and Ekenberg, 2006), which comprises all three VBs and the CB. In addition to nonparabolicity of VB, this model accounts for nonparabolicity of CB as well. However, its fundamental drawback is the occurrence of the spurious solutions, which can be avoided to some extent by various techniques (Foreman, 1997; Cartoixa et al., 2003; Kolokolov et al., 2003; Veprek et al., 2007).

21.3.1.1 Two-Band Model

Although relatively rough, the two-band model might be used in case of bulk, and even other types of quantum confined structures, but with modest accuracy. It is suitable for the unstrained bulk active region since the optical matrix element is isotropic in this case (Chuang, 1995), which means that material gain is the same for any direction of the amplified light polarization. Contrarily, in case of quantum confined semiconductor structures, material gain is polarization dependent. Nevertheless, the two-band model can still be implemented even in the case of quantum wells. If the optical dipole matrix element is averaged over the azimuthal angle corresponding to the plane of the quantum well, it is possible to derive its angular dependence with respect to the confinement direction of the quantum well (Chuang, 1995).

Here, the detailed expressions for material gain g, spontaneous emission rate per unit energy r_{sp} and refractive index variation Δn_r are presented for the unstrained bulk active region, according to the two-band model (Chuang, 1995). They are all functions of photon energy $\hbar\omega$ and carrier density n, which is included in expressions through the carrier-dependent quasi-Fermi levels:

$$g(n,\hbar\omega) = C_g \frac{M_b^2}{4\pi^2} \sum_{i=\mathrm{HH,LH,SO}} \left(\frac{2\mu_i}{\hbar^2}\right)^{3/2} \int_{E_{g,i}}^{\infty} \frac{\gamma}{\pi} \frac{\sqrt{x-E_{g,i}}}{(x-\hbar\omega)^2+\gamma^2} \left(f_{FD}^{c} - f_{FD}^{v}\right) \mathrm{d}x, \tag{21.1}$$

$$r_{sp}(n,\hbar\omega) = \frac{8\pi n_r^2 (\hbar\omega)^2}{h^3 c^2} C_g \frac{M_b^2}{4\pi^2} \sum_{i=\mathrm{HH,LH,SO}} \left(\frac{2\mu_i}{\hbar^2}\right)^{3/2} \int_{E_{g,i}}^{\infty} \frac{\gamma}{\pi} \frac{\sqrt{x-E_{g,i}}}{(x-\hbar\omega)^2+\gamma^2} f_{FD}^{c} \cdot \left(1 - f_{FD}^{v}\right) \mathrm{d}x, \tag{21.2}$$

$$\Delta n_r(n,\hbar\omega) = \frac{q^2\hbar^2}{n_r \varepsilon_0 m_0^2} \frac{M_b^2}{2\pi^2} \sum_{i=\mathrm{HH,LH,SO}} \left(\frac{2\mu_i}{\hbar^2}\right)^{3/2} \int_{E_{g,i}}^{\infty} \frac{(x-\hbar\omega)\sqrt{x-E_{g,i}}}{x(x+\hbar\omega)\left[(x-\hbar\omega)^2+\gamma^2\right]} \left(f_{FD}^{v} - f_{FD}^{c}\right) \mathrm{d}x. \tag{21.3}$$

In previous equations, $C_g = \pi q^2/(n_r c \varepsilon_0 m_0^2 \omega)$, where q is the absolute electron charge, m_0 is the free-electron mass, n_r is the refractive index of the active region, c is the speed of light in vacuum, ε_0 is the vacuum permittivity, $\omega = 2\pi\nu$ is the angular photon frequency, with ν being its frequency, and $\hbar = h/(2\pi)$ is the reduced Planck's constant, with h being the Planck's constant. In Equations 21.1 through 21.3, $M_b^2 = m_0 E_p/6$ stands for the bulk momentum matrix element squared, where E_p is the interband matrix element, $\mu_i = (m_e^{-1} + m_i^{-1})^{-1}$ and $E_{g,i}$ are the reduced effective mass and the energy gap between the CB bottom E_c and the VB top $E_{v,i}$, respectively, where i stands for the HH, LH, and SO band. With $f_{FD}^{c}(E) = f_{FD}^{c}[E_c + \mu_i/m_e \cdot (x - E_{g,i})]$ and $f_{FD}^{v}(E) = f_{FD}^{v}[E_{v,i} - \mu_i/m_i \cdot (x - E_{g,i})]$ we denote the Fermi–Dirac distribution $f_{FD}^{(j)}(E) = \{1 + \exp[(E - E_f^{(j)}/k_B T)]\}^{-1}$ for the CB ($j = c$) and the VB ($j = v$), characterized by the corresponding quasi-Fermi levels $E_f^{(j)}$, where k_B is the Boltzmann constant and T is the temperature. The half linewidth of the Lorentzian function is denoted by γ.

21.3.1.2 Multiband Model

The LK 4 × 4 and 6 × 6 Hamiltonians are usually implemented in the analysis of quantum confined structures. However, this approach can be very useful in the calculation of gain of strained bulk material (Connelly, 2007), which is polarization dependent in this case. As shown by Connelly (2007), and Mazzucato et al. (2015), eigenvectors of multiband Hamiltonian can be used to find the components of the optical matrix elements along the directions corresponding to polarizations of incoming light.

Totović et al. (2013) present an analysis of the material gain, radiative spontaneous recombination rate spectrum, and refractive index variation in MQWs based on the 8 × 8 **k·p** method (Liu and Chuang, 2002; Gvozdić and Ekenberg, 2006). The analysis is done for an MQW active region consisting of six

coupled 0.13% tensile-strained $In_{0.516}Ga_{0.484}As$ quantum wells, which are strain-compensated by the $In_{0.9}Ga_{0.1}As_{0.3}P_{0.7}$ 0.26% compressively strained barriers. The well thickness is $L_w = 19$ nm, while the barriers between the wells are $L_b = 10$ nm thick, making the total thickness of the structure $L_z = 6L_w + 5L_b = 164$ nm. The electronic band structure calculation accounts for Burt–Foreman Hermitianization (Foreman, 1993) and biaxial strain generated by lattice-mismatched growth of the well-barrier layers. By using an appropriate basis set, the 8×8 Hamiltonian is decoupled into two 4×4 Hamiltonians (H_U and H_L) corresponding to the upper (U) and lower (L) block Hamiltonians (Liu and Chuang, 2002). In calculating the band structure, the finite difference method (FDM) is employed. For determining g, r_{sp}, and Δn_r, the following relations are used (Chuang, 1995; Liu et al., 2001; Liu and Chuang, 2002):

$$g(n,\hbar\omega) = \frac{q^2\pi}{n_r c\varepsilon_0 m_0^2 \omega L_z} \sum_{\eta=U,L}\sum_{\sigma=U,L}\sum_{n,m}\int \left|\mathbf{e}\cdot\mathbf{M}_{nm}^{\eta\sigma}\right|^2 \frac{\gamma}{\pi}\frac{f_{\eta n}^{c} - f_{\sigma m}^{v}}{\left(E_{nm}^{\eta\sigma}-\hbar\omega\right)^2+\gamma^2}\frac{k_t dk_t}{2\pi}, \tag{21.4}$$

$$r_{sp}(n,\hbar\omega) = \frac{q^2 n_r \omega}{\pi\hbar c^3\varepsilon_0 m_0^2 L_z} \sum_{\eta=U,L}\sum_{\sigma=U,L}\sum_{n,m}\int \left|M_{sp}\right|^2 \frac{\gamma}{\pi}\frac{f_{\eta n}^{c}\cdot\left(1-f_{\sigma m}^{v}\right)}{\left(E_{nm}^{\eta\sigma}-\hbar\omega\right)^2+\gamma^2}\frac{k_t dk_t}{2\pi}, \tag{21.5}$$

$$\Delta n_r(n,\hbar\omega) = \frac{q^2\hbar^2}{n_r\varepsilon_0 m_0^2 L_z} \sum_{\eta=U,L}\sum_{\sigma=U,L}\sum_{n,m}\int \left|\mathbf{e}\cdot\mathbf{M}_{nm}^{\eta\sigma}\right|^2 \frac{E_{nm}^{\eta\sigma}-\hbar\omega}{E_{nm}^{\eta\sigma}\cdot\left(E_{nm}^{\eta\sigma}+\hbar\omega\right)}\frac{f_{\eta n}^{v} - f_{\sigma m}^{c}}{\left(E_{nm}^{\eta\sigma}-\hbar\omega\right)^2+\gamma^2}\frac{k_t dk_t}{2\pi}, \tag{21.6}$$

where η and σ stand for one of the two 4 × 4 Hamiltonians (H_U or H_L) and corresponding to the nth conduction and the mth valence sub-band, respectively, and k_t is the in-plane wave vector, while $f_{\eta n}^{c}(k_t)$ and $f_{\sigma m}^{v}(k_t)$ are the Fermi–Dirac distributions for CB and VB, respectively. In these relations, $E_{nm}^{\eta\sigma} = E_{nm}^{\eta\sigma}(k_t)$ is the energy difference between the eigenenergy of the nth conduction sub-band corresponding to the η-Hamiltonian and mth valence sub-band of the σ-Hamiltonian, whereas $\mathbf{M}_{nm}^{\eta\sigma} = \mathbf{M}_{nm}^{\eta\sigma}(k_t)$ is the corresponding momentum matrix element vector (Liu and Chuang, 2002). Depending on the unit polarization vector $\mathbf{e}$, the components of the $\mathbf{M}_{nm}^{\eta\sigma}$ vector correspond to the transverse-electric (TE) mode ($\mathbf{e} = \mathbf{x}$ or $\mathbf{z}$) or the transverse-magnetic (TM) mode ($\mathbf{e} = \mathbf{y}$). In the calculation of r_{sp}, the average matrix element for the three polarization directions is used, i.e., $|M_{sp}(k_t)|^2 = (2|\mathbf{M}_{TE}(k_t)|^2 + |\mathbf{M}_{TM}(k_t)|^2)/3$.

The spectral dependencies of material gain, radiative spontaneous recombination rate, and refractive index variation are shown in Figure 21.2. In Figure 21.2a through c, the results are given for the bulk unstrained $In_{0.53}Ga_{0.47}As$ active region, calculated using the two-band model and the parameters listed in Table 21.1. In Figure 21.2d through f, the same quantities, calculated using the multiband model, are given for an MQW active region consisting of six coupled 0.13% tensile-strained $In_{0.516}Ga_{0.484}As$ quantum wells, which are strain-compensated by the $In_{0.9}Ga_{0.1}As_{0.3}P_{0.7}$ 0.26% compressively strained barriers. The spectral dependencies for the MQW active region are given only for TE polarization and are determined based on the parameters given in Table 21.2.

In addition to bulk and QWs, the SOA's active region often comprises self-assembled QDs. The calculation of the optical properties of QDs can be based on sophisticated **k·p** models, such as 8 × 8 **k·p** model (Grundmann et al., 1995; Stier et al., 1999). However, due to the statistical nature of the QD size, very precise calculation is usually meaningless. Therefore, some simple methods can also be sufficiently effective as in the two-band model (Kim and Chuang, 2006; Kim et al., 2008).

21.3.2 Waveguide Design and Polarization Insensitivity

In addition to high transmission gain, high optical output power, low-noise, and low-energy consumption, in many SOA applications polarization insensitivity of modal gain is required. This demand can be difficult to fulfill since polarization dependence of modal gain is caused by SOA's waveguide geometry, through confinement factor, and material choice, through the optical transitions. Therefore, careful analysis and design of the waveguide structure and material gain are needed (Labukhin and Li, 2006). Numerical

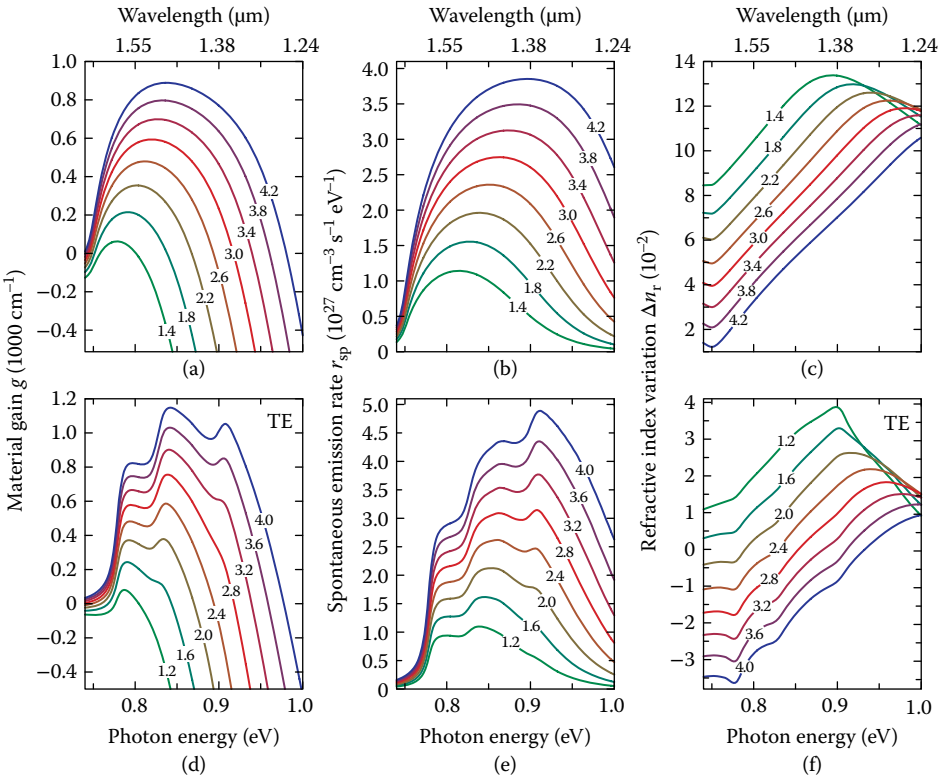

FIGURE 21.2 Spectral dependency of (a, d) material gain, (b, e) radiative spontaneous recombination rate per unit energy, and (c, f) refractive index variation for different carrier densities n (10^{18} cm^{-3}) for (a) through (c) bulk and (d) through (f) multiple quantum well (MQW) active region.

TABLE 21.1 Material Parameters Used for Band Calculation for Bulk SOA

Symbol	Quantity	$In_{0.53}Ga_{0.47}As$	$In_{0.76}Ga_{0.24}As_{0.52}P_{0.48}$
E_g	Energy gap CB–VB (HH, LH)	748 meV	1001 meV
$E_{g,SO}$	Energy gap CB–VB (SO)	1115 meV	1246 meV
Δ_{SO}	SO energy	367 meV	245.3 meV
E_p	Interband matrix element	24.93 eV	23.26 eV
m_e^*	Electron effective mass	0.0389 m_0	0.0541 m_0
m_{HH}^*	HH effective mass	0.3410 m_0	0.4069 m_0
m_{LH}^*	LH effective mass	0.0567 m_0	0.0889 m_0
m_{SO}^*	SO effective mass	0.1393 m_0	0.1709 m_0

SOA, semiconductor optical amplifier; LH, light hole; HH, heavy hole; SO, split-off; CB, conduction band; VB, valence band.

modeling of the active region's susceptibility, the real and imaginary parts of which correspond to refractive index and material gain, in combination with the calculation of the waveguide propagation constant and confinement factor is an inevitable and important step in the quest for the optimal, polarization-insensitive design of SOA. Waveguide polarization sensitivity comes from significant disproportion of its cross-section dimensions, where the width is usually one order of magnitude larger than its thickness, raising the difference in TE and TM wave propagation and the corresponding confinement factors. Moreover, as shown in

TABLE 21.2 Material Parameters Used for Band Calculation for MQW SOA

Symbol	Quantity	$In_{0.516}Ga_{0.484}As$	$In_{0.9}Ga_{0.1}As_{0.3}P_{0.7}$
E_g	Energy gap	765.2 meV	1107.3 meV
$E_{v,av}$	Average VB position	−6.6689 eV	−6.8986 eV
Δ_{SO}	SO energy	366.3 meV	189.2 meV
E_p	Interband matrix element	25.03 eV	21.91 eV
m_e^*	Electron effective mass	0.0395 m_0	0.0617 m_0
γ_1	Luttinger parameters	10.1534	6.0906
γ_2		3.6114	1.9545
γ_3		4.5580	2.6785
c_{11}	Elastic stiffness constants	1020.7 GPa	996.79 GPa
c_{12}		507.48 GPa	536.03 GPa
a_c	CB deformation potential	−6.091 eV	−5.941 eV
a_v	VB deformation potential	−1.077 eV	−0.802 eV
b	Shear deformation	−1.897 eV	−1.918 eV

SOA, semiconductor optical amplifier; MQW, multiple quantum well; SO, split-off; CB, conduction band; VB, valence band.

Section 21.3.1, quantum-confined and stressed bulk semiconductors in active region exhibit polarization-dependent dipole optical matrix elements, leading to additional variation of TE and TM modes. An unstrained bulk material is polarization isotropic and in this case square waveguide cross-section may provide SOA polarization insensitivity (Connelly, 2001; Michie et al., 2006). Unfortunately, such waveguide design is technologically very demanding (Connelly, 2001; Michie et al., 2006). Moreover, it leads to large far-field divergence and consequently to poor coupling efficiency from the SOA to optical fiber (Connelly, 2002). This can be overcome by tapering the active waveguide near the amplifier facets (Connelly, 2002; Michie et al., 2006).

Nevertheless, there are other solutions for polarization-insensitive operation of SOA proposed in the literature. The majority of these proposals concern MQW SOA and rely on any of the following concepts: MQWs with tensile barriers (Magari et al., 1991, 1994), tensile-strained QWs (Ito et al., 1998; Carrère et al., 2010), tensile-strained QWs with compressive barriers (Godefroy et al., 1995; Zhang and Ruden, 1999), alternation of tensile and compressive QWs (Mathur and Dapkus, 1992; Joma et al., 1993; Tiemeijer et al., 1993; Tishinin et al., 1997; Silver et al., 2000), and the delta-strained QW (Carlo et al., 1998; Cho and Choi, 2001). The concept based on MQWs with tensile barriers (Magari et al., 1991, 1994) essentially relies on considerable increase of barrier refractive index for TM mode in comparison with TE mode, as a consequence of LH band contribution, which modifies the bandgap and shifts the wavelength toward the longer wavelength side due to the tensile strain. The approach based on tensile-strained MQWs with compressive barriers, proposed by Zhang and Ruden (1999), involves the barrier width optimization such that the HH sub-bands are grouped tightly and the LH sub-bands are widely separated in energy. The uppermost valence sub-bands, which have large occupation probability and strongly contribute to the gain, consist of a single LH sub-band and a group of coupled HH sub-bands, giving rise to balanced gains for the TE and TM polarizations. The method of alternation of separate tensile and compressive QWs (Silver et al., 2000) requires thick QWs (around 14 nm) and with high strain (around −0.8%). Due to the thick tensile layers, the difference in density of states of the two types of wells leads to significant charge redistribution within the active region. The space charge modifies the band profile and forces holes to move from the tensile well to the compressive well, increasing TE gain. In order to compensate for hole redistribution, the number of tensile wells can be increased so that they outnumber the compressive wells.

Otherwise, the thickness of the compressive wells can be increased to minimize the charge redistribution effects.

In unstrained MQWs, HH band sub-bands are usually higher than those of LH band, resulting in higher TE gain than the TM one. In delta-strained QWs (Cho and Choi, 2001), the delta layer introduces larger VB discontinuity for HH bands than LH bands, and the quantized energy levels for HH bands experience a shift downward, in contrast to those corresponding to LH bands, which shift upward. As a consequence, the TM transition strength for the transition between the first conduction sub-band and the top LH-like valence sub-band is much larger than the TE transition strength.

In addition to polarization insensitivity, SOA has to provide as high as possible transmission gain. Totović et al. (2013), presented a case study, where both design criteria have been implemented: high device gain and polarization insensitivity. The study analyzes two types of SOA waveguides, with active regions described in Section 21.3.1: unstrained bulk and tensile-strained MQWs, which are strain compensated by compressively strained barriers. In order to satisfy the first design criterion, the upper limit of the confinement factor is set to approximately 30%, thereby preventing the strong influence of ASE on SOA saturation (de Valicourt, 2012). Due to the gain isotropy, polarization-insensitive operation of bulk SOA requires equal confinement factors for both polarizations ($\Gamma_{TE} = \Gamma_{TM}$) (Connelly, 2001; Labukhin and Li, 2006; Michie et al., 2006). This requires optimization of the waveguide structure since confinement factor Γ_{TE} is usually larger than Γ_{TM} (Connelly, 2002; Labukhin and Li, 2006; Michie et al., 2006). Instead of using the unstrained, it is possible to implement a tensile-strained bulk active region, which leads to the polarization and gain anisotropy (Michie et al., 2006; Connelly, 2007). If the difference between the confinement factors is sufficiently small, a carefully chosen amount of tensile strain (Michie et al., 2006; Connelly, 2007) may compensate for the difference in the confinement factors Γ_{TE} and Γ_{TM} without the waveguide optimization. This can provide an efficient way for polarization-insensitive operation of bulk SOAs.

Similarly, tensile-strained MQWs in the active region, for which TM gain dominates over TE gain, may compensate for the difference in confinement factors Γ_{TE} and Γ_{TM}, leading to balanced modal gains for both polarizations, $\Gamma_{TE}g_{TE} = \Gamma_{TM}g_{TM}$, in the wavelength range of interest. The design of the MQW active region and the waveguide as a whole can be performed by a self-consistent iterative procedure involving calculation of the confinement factors and material gain, which ultimately, should provide optimized well/barrier dimensions, strain, number of wells, and waveguide cladding. The self-consistent procedure becomes important if the calculation of the confinement factor accounts for the refractive index variation of the active region, associated with variation of the material gain, and caused by carrier injection into the MQW structure (Totović et al., 2013). For the MQW active region from Section 21.3.1, the procedure leads to the confinement factor ratio $\Gamma_{TM}/\Gamma_{TE} = 0.806$, with $\Gamma_{TE} = 22\%$. The same procedure is applied in the optimization of the waveguide for unstrained bulk SOA. The optimization is performed for 1.55 μm and an average carrier density of 2×10^{18} cm^{-3}, for both bulk and MQW SOAs. The modal gains for TE and TM polarization of the optimized MQW active region are compared in Figure 21.3 for a range of photon energies and carrier densities.

It should be brought to attention that the temperature variation can significantly affect the refractive index and consequently the confinement factor. If efficient heat sink is not available for SOA, temperature effects should be accounted for in the design of the waveguide. More details on temperature effects will be given in Section 21.4.3.4.

The proposed design of the MQW waveguide is similar to those described by Wünstel et al. (1996) and Wolfson (2001) in both optical confinement and layer thicknesses. A rigorous treatment of the confinement factor should take into account the variation of the refractive index imaginary part, i.e., gain, in the active region (Visser et al., 1997). However, in this case study, the focus was set only on the variation of the real part of refractive index Δn_r due to the carrier injection. Although for other carrier densities and photon energies confinement factors somewhat detune from the optimal values and ratio, they partially compensate for the material gain ratio detuning, toning down the difference in modal gains for the TE and TM modes.

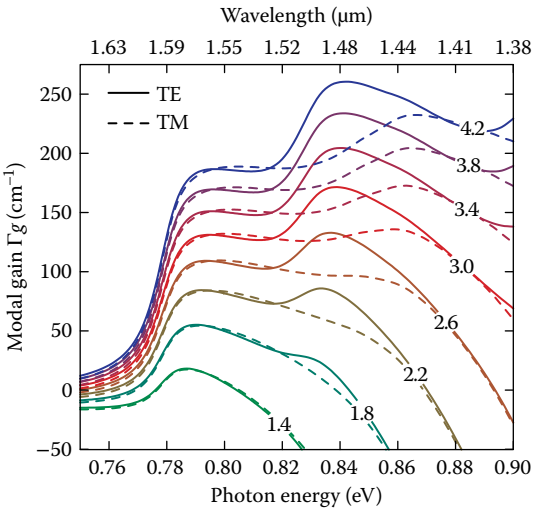

FIGURE 21.3 Spectral dependency of modal gain for polarization insensitive multiple quantum well (MQW) active region for the transverse-electric (TE) (solid lines) and transverse-magnetic (TM) (dashed lines) modes, for different carrier densities n (10^{18} cm^{-3}).

Distribution of the transversal components of the electric $\mathbf{E}(x, y)$ and magnetic $\mathbf{H}(x, y)$ fields is determined by a system of Helmholtz equations (Kawano and Kitoh, 2001):

$$\nabla_{\perp}^2 \mathbf{E}(x,y) + \left[\left(n_{\mathrm{r}} + \Delta n_{\mathrm{r}} \right)^2 k_0^2 - \beta^2 \right] \mathbf{E}(x,y) = 0, \tag{21.7}$$

$$\left(n_{\mathrm{r}} + \Delta n_{\mathrm{r}} \right)^2 \nabla_{\perp} \left[\frac{1}{\left(n_{\mathrm{r}} + \Delta n_{\mathrm{r}} \right)^2} \nabla_{\perp} \mathbf{H}(x,y) \right] + \left[\left(n_{\mathrm{r}} + \Delta n_{\mathrm{r}} \right)^2 k_0^2 - \beta^2 \right] \mathbf{H}(x,y) = 0, \tag{21.8}$$

where $\Delta n_{\mathrm{r}} = \Delta n_{\mathrm{r}}(n, \hbar\omega)$ is the refractive index variation, which is nonzero only in the active region of SOA, k_0 is the wave vector, $\beta = n_{\mathrm{eff}} k_0$ is the wave propagation constant, and n_{eff} is the effective index of refraction, also dependent on n and $\hbar\omega$. Equations are solved using the finite element method (FEM), with all boundaries set to the Neumann boundary conditions, except for the top ridge, which is set to the Dirichlet boundary condition.

Confinement factors for TE and TM polarizations are defined as (Kawano and Kitoh, 2001)

$$\Gamma_{\mathrm{TE}} = \int_{\mathrm{a.r.}} \left| \mathbf{E}(x,y) \right|^2 \mathrm{d}x\mathrm{d}y \Big/ \int_{-\infty}^{+\infty} \left| \mathbf{E}(x,y) \right|^2 \mathrm{d}x\mathrm{d}y, \tag{21.9}$$

$$\Gamma_{\mathrm{TM}} = \frac{1}{n_{\mathrm{a.r.}}^2} \int_{\mathrm{a.r.}} \left| \mathbf{H}(x,y) \right|^2 \mathrm{d}x\mathrm{d}y \Big/ \sum_i \frac{1}{n_i^2} \int_i \left| \mathbf{H}(x,y) \right|^2 \mathrm{d}x\mathrm{d}y, \tag{21.10}$$

where a.r. stands for the active region and i stands for each subdomain of the waveguide, including the active region. It should be noted that the background part of the refractive index $n_{\mathrm{r},i}$, with excluded Δn_{r} for the active region, is derived from Adachi's interpolation formulas (Adachi, 1989), and it is consequently a function of photon energy, i.e., $n_{\mathrm{r},i} = n_{\mathrm{r},i}(\hbar\omega)$. Since this dependence has abrupt changes, quantities shown in Figure 21.4 cannot exhibit smooth behavior.

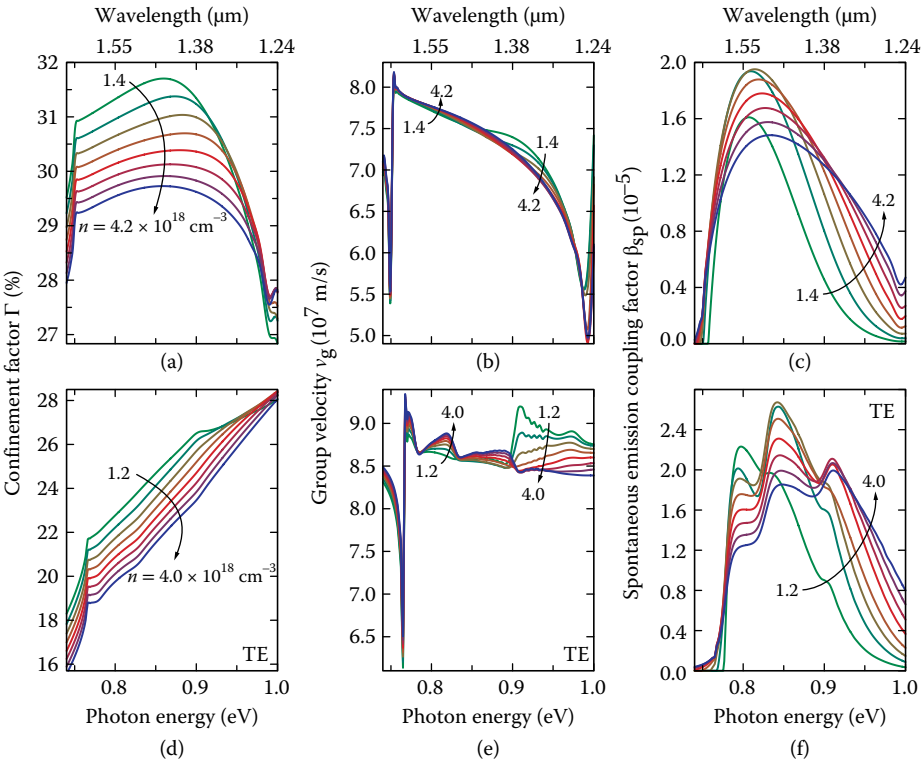

FIGURE 21.4 Spectral dependency of (a, d) confinement factor, (b, e) group velocity, and (c, f) spontaneous emission coupling factor for different carrier densities n (10^{18} cm^{-3}) for (a) through (c) bulk and (d) through (f) multiple quantum well (MQW) active region.

Another important parameter for ASE noise modeling in SOAs is the spontaneous emission coupling factor $\beta_{sp}(n, \hbar\omega)$, which is defined as the spontaneous emission rate coupled to the one optical mode, relative to the total spontaneous emission rate, $R_{sp}(n) = \int r_{sp}(n, \hbar\omega)\mathrm{d}(\hbar\omega)$, and can be calculated according to the following expression (Coldren et al., 2012):

$$\beta_{sp} = \frac{\Gamma v_g}{V} \frac{g n_{sp}}{R_{sp}}, \tag{21.11}$$

where V is the active region volume and Γ and g are the averaged values of confinement factor and material gain over polarizations, respectively, obtained in the same way as the average optical matrix element for radiative recombination rate. Here, $n_{sp}(n, \hbar\omega)$ is the population inversion factor defined by (Coldren et al., 2012)

$$n_{sp} = \left[1 - \exp\left(\frac{\hbar\omega - \Delta E_f}{k_B T}\right)\right]^{-1}, \tag{21.12}$$

where $\Delta E_f = E_f^{(c)} - E_f^{(v)}$ is the difference between the quasi-Fermi levels of CB and VB. In order to calculate β_{sp}, in addition to confinement factor, it is necessary to calculate the group velocity of the light $v_g(n, \hbar\omega)$:

$$v_g = \frac{\partial\omega}{\partial\beta} = \frac{1}{\hbar} \cdot \left[\frac{\partial\beta}{\partial(\hbar\omega)}\right]^{-1}. \tag{21.13}$$

Spectral dependencies of the confinement factor, group velocity, and spontaneous emission coupling factor are shown in Figure 21.4, for both bulk and the MQW active region, optimized to be polarization insensitive. Therefore, the quantities for the MQW active region are given only for TE polarization.

21.4 Rate Equations

In order to analyze the SOA's performance, it is first necessary to identify the main physical processes underlying its operation, which are related to the interaction mechanisms between photons and carriers. These are then typically presented in the form of a coupled system of differential equations denoted as the rate equation system. Optical signal can be described either in terms of complex electric field or in terms of photon density and phase. On the other hand, carriers are modeled either via carrier density (Dailey and Koch, 2007; Totović et al., 2013) or material gain (Shtaif et al., 1998), or, in some cases, using the integrated material gain along the direction of signal propagation (Agrawal and Olsson, 1989; Cassioli et al., 2000; Antonelli and Mecozzi, 2013).

For TW-SOA, it usually suffices to analyze only the forward-propagating optical signal, with respect to the longitudinal axis. However, for R-SOA, both forward and backward-propagating optical signals need to be accounted for. Although the model's complexity increases when counterpropagating optical signals are analyzed, it is often good practice to develop the generalized model since it can easily be customized to account for any SOA type by simply changing the power reflectivity coefficient of the front and/or rear facet.

21.4.1 Basic Rate Equations

During the decades of SOA study, a variety of models of different complexity emerged. Some of them are based on signal power (Agrawal and Olsson, 1989), intensity (Adams et al., 1985), or photon density analysis (Totović et al., 2014), which may or may not include a separate phase equation, whereas the others treat the optical signal using the complex electric field envelope (Melo and Petermann, 2008; Schrenk, 2011; Antonelli and Mecozzi, 2013). In its basic form, the SOA model describes the interaction between the carrier density $n(z, t)$ and the two counterpropagating optical signals, forward (+) and backward (−), with respect to the longitudinal z-axis, all of which are dependent on both time t and the z-coordinate. For SOA operation, it is necessary to achieve population inversion, which is done using the electric (bias) current I. When the bias current is low, carriers are mainly drained by spontaneous recombination, which can be nonradiative, yielding phonons (Ghafouri-Shiraz, 2004), or radiative, which produces noncoherent spectrally wide optical signal, regarded as noise. As the current increases beyond the transparency value, enough carriers exist in the active region to make the stimulated emission the dominant process and the input signal can be amplified during propagation. For the simplest case of bulk SOA, carrier dynamics can be described as follows (Coldren et al., 2012; Totović et al., 2013):

$$\frac{\mathrm{d}n}{\mathrm{d}t} = \frac{I}{qV} - \left[An + R_{\mathrm{sp}}(n) + Cn^3\right] - R_{\mathrm{st}}(n). \tag{21.14}$$

The first term on the right-hand side (RHS) of Equation 21.14 describes the rate at which the carriers are "pumped" into the active region, where q is the elementary charge, and $V = WHL$ is the active region volume, dependent on the active region width W, height H, and length L. The second term accounts for the loss of carriers through spontaneous recombination, where $R_{\mathrm{sp}}(n)$ is the total radiative spontaneous recombination rate, and A and C are the Shockley–Read–Hall and Auger coefficients, respectively, related to nonradiative spontaneous recombination (Coldren et al., 2012). In some instances, carrier loss due to radiative and nonradiative spontaneous recombination is modeled as n/τ, where τ is the carrier lifetime, which is treated either as constant (Thylén, 1988; Shtaif et al., 1998; Totović et al., 2016) or dependent on

carrier density (Melo and Petermann, 2008; Xia and Ghafouri-Shiraz, 2016). Finally, the last term on the RHS of Equation 21.14, $R_{st}(n)$, accounts for the loss of carriers due to stimulated emission, either through the amplification of the signal alone or the signal and noise combined.

21.4.1.1 Electric Field Envelope Model

Each optical signal can be represented by its electric field, which can be separated into the carrier signal and the slowly varying envelope along the propagation direction. The complex envelope can then be analyzed either as is (Loudon et al., 2005), or, more commonly, it can be normalized such that its squared magnitude represents photon density (Connelly, 2007; Totović et al., 2011), power (Agrawal and Olsson, 1989; Cassioli et al., 2000), or intensity (Henry, 1982). Regardless of the choice for normalization, the system of equations remains the same since the underlying spatiotemporal dependence is unmodified by the normalization constants. The evolution of electric field envelopes $E_{\pm}(z,t)$, normalized such that their square magnitude represents photon densities, $|E_{\pm}(z,t)|^2 = S_{\pm}(z,t)$, propagating forward (+) and backward (−) along the longitudinal z-axis, is governed by the following system of equations (Agrawal and Olsson, 1989):

$$\pm\frac{\partial E_{\pm}}{\partial z} + \frac{1}{v_g}\frac{\partial E_{\pm}}{\partial t} = \frac{1}{2}\left(\Gamma g - \alpha_i\right) E_{\pm}. \tag{21.15}$$

Here, v_g is the group velocity, Γ stands for the optical confinement factor, which determines the portion of the signal propagating through the active region relative to the total photon density, and g is the material gain of the active region, all given at the signal frequency ω. These quantities can be derived from the models given in Section 21.3, and in Figures 21.2 and 21.4, by interpolation at the signal central energy $\hbar\omega$. With $\alpha_i = K_0 + \Gamma K_1 n$ active region loss is denoted (Connelly, 2001), where K_0 and K_1 stand for the carrier-independent and carrier-dependent loss coefficients, respectively, which take into account the intrinsic material loss and the free-carrier and inter-VB absorption (Dailey and Koch, 2009; Schrenk, 2011). It should be noted that, in general, all parameters appearing in Equation 21.15, namely v_g, Γ, g, and α_i, depend on carrier density n, and implicitly on t and z. This dependence notation is omitted from Equation 21.15 and the equations that will follow for compactness and clarity. Nevertheless, it is common to treat v_g and/or Γ as constants (Jin et al., 2003; Totović et al., 2014), which simplifies the model at the expense of accuracy.

Input optical signal, given by its normalized envelope E_0, is assumed to be entering the device at the front facet ($z = 0$), with the amplitude reflection coefficient r_1, and transmission coefficient t_1, as shown in Figure 21.5. The front facet is usually coated with the antireflective layer, and it is a common practice to neglect any residual reflectivity and assume $r_1 = 0$ and $t_1 = 1$, especially if the analytical or semianalytical solution is sought (Antonelli and Mecozzi, 2013; Totović et al., 2014). On the other hand, the rear facet ($z = L$) has the amplitude reflection coefficient r_2, which can be neglected for TW-SOA, but needs to be accounted for in the case of an R-SOA. If the cleaved facet is used as a high-reflecting one, the amplitude reflection coefficient can be determined as $r_2 = (1 - n_r)/(1 + n_r)$ under the assumption of TE polarization,

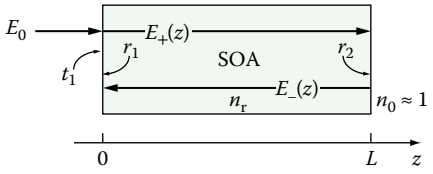

FIGURE 21.5 Semiconductor optical amplifier (SOA) structure with relevant optical signals, refractive indices, and reflection and transmission coefficients denoted.

where n_r is the refractive index of the active region. Boundary conditions according to Figure 21.5 read (Adams et al., 1985, Jin et al., 2003)

$$\begin{aligned} E_+(0) &= t_1 E_0 + r_1 E_-(0), \\ E_-(L) &= r_2 E_+(L). \end{aligned} \tag{21.16}$$

It is common practice to introduce the LEF α in Equation 21.15, which accounts for the phase modulation due to variation of real and imaginary parts of susceptibility χ (Henry, 1982; Agrawal and Olsson, 1989; Dailey and Koch, 2009; Antonelli and Mecozzi, 2013). This variation can be induced by injection of carriers, α_N, and carrier heating (CH), α_{CH} (Occhi et al., 2003). The total phase change will be the sum of these two contributions since they can be treated as uncorrelated. Carrier-induced LEF is defined as (Osinski and Buus, 1987; Occhi et al., 2003)

$$\alpha_N = -\frac{\partial Re\{\chi\}/\partial n}{\partial Im\{\chi\}/\partial n} = -2k_0 \frac{\partial n_r/\partial n}{\partial g/\partial n}, \tag{21.17}$$

where $k_0 = 2\pi\nu/c$ is the wave vector. For a small change in carrier density, which usually is the case, the derivatives in Equation 21.17 can be replaced with finite differences, which leads to (Henry, 1982; Osinski and Buus, 1987)

$$\alpha_N = -2k_0 \frac{\Delta n_r}{\Delta g}, \tag{21.18}$$

where Δn_r and Δg are the differential change in refractive index and material gain, respectively, induced by carrier density variation (Henry, 1982; Osinski and Buus, 1987; Agrawal, 1990). The deviation Δn_r is a result of several different mechanisms, including dipole band-to-band transition (Dailey and Koch, 2009; Qin et al., 2012), band-filling (Burstein–Moss effect), bandgap shrinkage, and free-carrier absorption (plasma effect) (Bennett et al., 1990). Band-filling is related to the decrease in absorption for photon energies slightly above nominal bandgap, caused by low density of states in CB that are easily filled, and is mostly pronounced for heavily doped semiconductors (Moss et al., 1973). Bandgap shrinkage is related to large concentrations of electrons at the bottom of CB, which repel one another due to Coulomb force, leading to the lowering of the energy of CB (Bennett et al., 1990). Finally, free-carrier absorption describes transition of free carriers to the higher-energy level due to photon absorption, and the change in refractive index can be described using the Drude model (Moss et al., 1973; Dailey and Koch, 2009; Qin et al., 2012). These four effects are assumed to be independent, and the total refractive index deviation can be found as a sum of their respective contributions.

Another contribution to LEF, caused by carrier temperature variation, is defined as (Occhi et al., 2003)

$$\alpha_{CH} = -2k_0 \frac{\partial n_r/\partial T}{\partial g/\partial T}. \tag{21.19}$$

However, this contribution is often neglected in SOA models, and LEF is assumed to be $\alpha \approx \alpha_N$. Equation 21.15 now becomes

$$\pm\frac{\partial E_\pm}{\partial z} + \frac{1}{v_g}\frac{\partial E_\pm}{\partial t} = \frac{1}{2}\left[\Gamma g(1 - i\alpha) - \alpha_i\right] E_\pm. \tag{21.20}$$

It should be stressed that, depending on the sign convention adopted for the α-parameter, there may be variation in the literature in the sign prefixing α in Equation 21.20.

Having defined the equations which govern spatiotemporal electric field envelope distribution of the counterpropagating optical signals, it is possible to devise the stimulated emission rate in Equation 21.14, which is proportional to the total photon density in the amplifier's active region, S_Σ:

$$R_{\mathrm{st}}(n) = v_{\mathrm{g}} g S_\Sigma = v_{\mathrm{g}} g \left| E_+ + E_- \right|^2 . \tag{21.21}$$

It can be seen from Equation 21.21 that the interference between the two counterpropagating optical signals will cause the spatial grating in the carrier density distribution. However, characteristic grating length will be of the order of the signal's wavelength λ, and it will be easily washed out by the diffusion (Yacomotti et al., 2004; Serrat and Masoller, 2006; Totović et al., 2013). This justifies neglecting of all high-frequency terms, keeping only the sum of the squared electric field magnitudes, i.e., photon densities, $S_\Sigma = |E_+|^2 + |E_-|^2 = S_+ + S_-$. Depending on the model complexity, S_Σ can also include ASE noise.

21.4.1.2 Photon Density Model

By expressing the electric field envelope in terms of photon densities, $S_\pm$, and phase, $\varphi_\pm$:

$$E_\pm(z,t) = \sqrt{S_\pm(z,t)} \exp\left[i\varphi_\pm(z,t) \right], \tag{21.22}$$

Equation 21.20 can be reduced to the system of coupled TW equations for forward and backward propagation directions, written with respect to photon densities (Qin et al., 2012):

$$\pm \frac{\partial S_\pm}{\partial z} + \frac{1}{v_{\mathrm{g}}} \frac{\partial S_\pm}{\partial t} = \left(\Gamma g - \alpha_{\mathrm{i}} \right) S_\pm, \tag{21.23}$$

and phase (Agrawal and Olsson, 1989):

$$\pm \frac{\partial \varphi_\pm}{\partial z} + \frac{1}{v_{\mathrm{g}}} \frac{\partial \varphi_\pm}{\partial t} = -\frac{1}{2} \Gamma g \alpha. \tag{21.24}$$

Using the definition of LEF, Equation 21.24 can be written in yet another form that emphasizes the underlying cause of phase variation (Agrawal, 1990; Dailey and Koch, 2007; Qin et al., 2012):

$$\pm \frac{\partial \varphi_\pm}{\partial z} + \frac{1}{v_{\mathrm{g}}} \frac{\partial \varphi_\pm}{\partial t} = k_0 \Gamma \Delta n_{\mathrm{r}}. \tag{21.25}$$

If the signal is assumed to preserve its coherence during propagation, both Equations 21.23 and 21.25 are required; otherwise, it is sufficient to use only Equation 21.23 in modeling an SOA. Appending the phase equation to the model is important especially if the input signal carries information encoded in its phase, which is the case for many advanced modulation formats, such as phase shift keying (PSK), quadrature amplitude modulation (QAM), and quadrature phase shift keying (QPSK), to name a few (Schmuck et al., 2013; Koenig et al., 2014).

Assuming that the signal entering the device at the front facet ($z = 0$) is $E_0 = \sqrt{S_0} \exp(i\varphi_0)$, boundary conditions given by Equation 21.16 can now be rewritten using Equation 21.22. Additionally, amplitude reflection and transmission coefficients can be written as functions of the power reflectivity coefficients R_1 and R_2, corresponding to front and rear facets, respectively. The input signal does not change the propagation direction during transmission through the front facet, so no phase change is present, and $t_1 = \sqrt{(1 - R_1)}$ (Adams et al., 1985). On the other hand, during reflection at any facet, the signal being reflected does change the propagation direction, and a phase change of π needs to be accounted for. This can also be inferred from the definition of the amplitude reflection coefficient r_2 for the cleaved

facet, which is negative. Finally, amplitude reflection coefficients can be written as $r_1 = \sqrt{R_1}\exp(i\pi)$ and $r_2 = \sqrt{R_2}\exp(i\pi)$. Substituting amplitude reflection and transmission coefficients in Equation 21.16, and expressing electric fields in terms of photon densities and phase, yields:

$$\begin{aligned}\sqrt{S_+(0)}\exp[i\varphi_+(0)] &= \sqrt{1-R_1}\sqrt{S_0}\exp(i\varphi_0) + \sqrt{R_1}\exp(i\pi)\sqrt{S_-(0)}\exp[i\varphi_-(0)],\\ \sqrt{S_-(L)}\exp[i\varphi_-(L)] &= \sqrt{R_2}\exp(i\pi)\sqrt{S_+(L)}\exp[i\varphi_+(L)].\end{aligned} \tag{21.26}$$

By multiplying previous set of equations with their corresponding complex conjugates, the boundary conditions for photon densities can be derived:

$$\begin{aligned}S_+(0) &= (1-R_1)S_0 + R_1S_-(0) - 2\sqrt{(1-R_1)S_0}\sqrt{R_1S_-(0)}\cos[\varphi_0 - \varphi_-(0)],\\ S_-(L) &= R_2S_+(L).\end{aligned} \tag{21.27}$$

Equating the arguments of the left-hand side (LHS) and RHS of Equation 21.26, the following boundary conditions for phases can be found (Totović et al., 2013):

$$\begin{aligned}\varphi_+(0) &= \arctan\left[\frac{\sqrt{(1-R_1)S_0}\sin\varphi_0 - \sqrt{R_1S_-(0)}\sin\varphi_-(0)}{\sqrt{(1-R_1)S_0}\cos\varphi_0 - \sqrt{R_1S_-(0)}\cos\varphi_-(0)}\right],\\ \varphi_-(L) &= \varphi_+(L) + \pi.\end{aligned} \tag{21.28}$$

Typically, the input optical signal is given in terms of power rather than photon density. For the input optical power P_0, the photon density can be determined as $S_0 = \Gamma P_0/(\hbar\omega v_g WH)$, where $\hbar\omega$ is the signal energy.

21.4.1.3 Signal Spectral Dependence

Most of the parameters figuring in Equations 21.23 and 21.25 do exhibit spectral dependence, as shown in Figures 21.2 and 21.4. When working with photon densities, signal is assumed to be infinitely spectrally narrow and centered at the energy corresponding to the maximum spectral photon density, $\hbar\omega_0$. This assumption justifies the usage of a simplified model where the parameter values are given at the signal central energy, as is the case with Equation 21.23. In practice, signal will always have a finite spectral width, which is not necessarily narrow and cannot always be neglected. This is especially important if SOAs are used in WDM systems, where multiple signals at different wavelengths travel through the active region. In order to correctly model the signal propagation in this case, Equation 21.23 is rewritten in terms of spectral photon density, $s_\pm(\hbar\omega, z, t)$, for forward and backward propagation (Totović et al., 2013):

$$\pm\frac{\partial s_\pm}{\partial z} + \frac{1}{v_g}\frac{\partial s_\pm}{\partial t} = \left(\Gamma g - \alpha_i\right)s_\pm. \tag{21.29}$$

It should be stressed that now v_g, Γ, g, and α_i are spectrally dependent. Additionally, two more changes to the model are required. The first is related to the carriers consumed by stimulated emission in Equation 21.14, which can be determined using

$$R_{st}(n) = \int_0^\infty v_g g s_\Sigma \mathrm{d}(\hbar\omega), \tag{21.30}$$

where $s_\Sigma = s_+ + s_-$. The second is related to the boundary conditions given in Equation 21.27, which are now written with respect to $s_\pm$ instead of $S_\pm$. Finally, if no reflection coating is used for the R-SOA's rear facet, the reflection coefficient R_2 also becomes spectrally dependent through $n_r(\hbar\omega)$.

21.4.2 Amplified Spontaneous Emission

Spontaneous recombination can usually be viewed as an undesirable side effect of SOA operation, from several viewpoints. First, the carriers that should be reserved for signal amplification are indefinitely lost, meaning that the higher bias currents are required to achieve the same material gain. Second, the random nature of spontaneous recombination induces fluctuations in carrier density, which in turn causes the material gain and refractive index to change. This leads to fluctuations in both intensity and phase of the amplified signal (Ghafouri-Shiraz, 2004). Finally, radiative spontaneous recombination generates wideband signal with random phase, polarization, and spatial orientation. Once these photons are generated, they become impossible to separate from the signal, so they travel jointly through the active region and become amplified. Even if the signal is filtered at the SOA's output, a certain amount of noise will always be present in the narrow band around the signal central energy (Yariv and Yeh, 2007). An additional drawback is that the noise will have higher optical power when the input signal is vague since more carriers will be available for spontaneous recombination (Talli and Adams, 2003; Totović et al., 2013; Koenig et al., 2014). As the signal becomes more amplified, fewer carriers remain, and the ASE contribution becomes less important in terms of power.

The process of spontaneous emission is at its core stochastic, and, within the framework of the semiclassical approach, it can be modeled statistically in terms of its probability, similarly to the shot noise present in electronic devices (Ghafouri-Shiraz, 2004). The nature of ASE noise led to the development of numerous models of different degree of complexity, which can be roughly divided into two categories: deterministic, which do not require any random generators (Talli and Adams, 2003; Totović et al., 2013), and stochastic, which require random sources with certain probability density functions (Marcuse, 1984; Cassioli et al., 2000; Park et al., 2005; Melo and Petermann, 2008; Totović et al., 2011). In the semiclassical framework, ASE is usually treated as white Gaussian noise process, or as Poisson process (Park et al., 2005), whereas in the quantum mechanical formalism the noise is treated using the set of appropriate quantum noise operators, including spontaneous emission process, internal absorption, and vacuum field fluctuations (Shtaif et al., 1998). It has been shown by Shtaif et al. (1998) that the semiclassical results are essentially the same as the ones obtained using quantum description, with the exception of the shot noise term, which needs to be explicitly added to the semiclassical intensity. However, for sufficiently small bandwidths, the shot noise term can be ignored (Shtaif et al., 1998).

21.4.2.1 Deterministic Approach

It has already been pointed out that signal and noise travel together, which would justify modification of the photon density equation, either Equation 21.23 or Equation 21.29, to include another term modeling the rate with which the spontaneous photons are generated (Park et al., 2005; Dailey and Koch, 2007; Zhou et al., 2007; Totović et al., 2015). However, from the standpoint of detailed device analysis, it may be useful to separate noise and signal equations, allowing them to be coupled through the carrier rate equation since these two processes are uncorrelated (Ghafouri-Shiraz, 2004). ASE is known to have wide spectrum; therefore, it is more appropriate to use spectral photon densities, $a_\pm(\hbar\omega, z, t)$, rather than photon densities, for its description. The system of equations for two counterpropagating ASE signals reads (Talli and Adams, 2003; Melo and Petermann, 2008; Totović et al., 2013):

$$\pm\frac{\partial a_\pm}{\partial z} + \frac{1}{v_g}\frac{\partial a_\pm}{\partial t} = \left(\Gamma g - \alpha_i\right) a_\pm + \frac{1}{2v_g}\Gamma\beta_{sp} r_{sp}, \tag{21.31}$$

where r_{sp} is the radiative spontaneous recombination rate per unit energy, given by Equation 21.2 or Equation 21.5, depending on the active region type, and β_{sp} is the spontaneous emission coupling factor

given by Equation 21.11. Boundary conditions for noise are $a_+(0) = R_1 a_-(0)$ and $a_-(L) = R_2 a_+(L)$. Phase is not analyzed since it is random and can be averaged to zero. In other words, under the usual operating conditions, i.e., if no resonant cavity is present, ASE does not exhibit coherent behavior.

In order to have the complete model, it is necessary to include ASE together with the signal when calculating total spectral photon density, $s_\Sigma = s_+ + s_- + a_+ + a_-$, which further influences $R_{st}(n)$, given by Equation 21.30.

It should be noted that many other deterministic approaches for ASE analysis exist. The choice depends on the desired model complexity and the tradeoff between accuracy and computational resource consumption. These approaches include the photon statistic master equation method (Mukai and Yamamoto, 1982), field beating (Olsson, 1989), the equivalent circuit model (Berglind and Gillner, 1994; Ghafouri-Shiraz, 2004), the semiclassical wave theory model (Donati and Giuliani, 1997).

21.4.2.2 Resonant Properties of the SOA Cavity

In the previous pages, during the discussion of facet's power reflectivities and boundary conditions, it was assumed that all antireflective facets have zero reflectivity. Although this assumption can be helpful for model simplification, it can also mask some of the processes present in SOAs (Thylén, 1988; Zhou et al., 2007). Residual reflectivity, which always has some finite value, provides a feedback loop that acts as a filter, giving rise to resonances and antiresonances (Adams et al., 1985; Schrenk, 2011). This effect has been reported in both experimental (Olsson, 1989) and theoretical SOA analyses (Zhou et al., 2007; Totović et al., 2013), mostly related to ASE noise. An example of the output spectrum of the signal and noise combined, with visible resonant footprint of the cavity, calculated using the model presented by

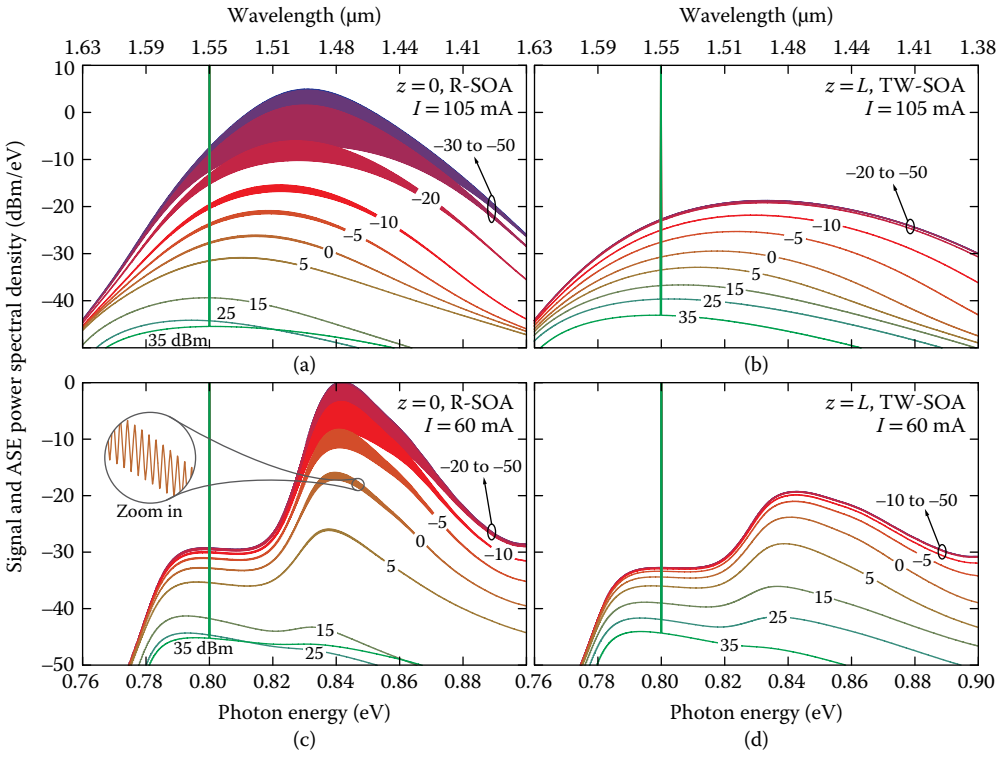

FIGURE 21.6 Total power spectral density at the semiconductor optical amplifier's (SOA's) output for different input optical powers in the case of (a, c) reflective (R) SOA at $z = 0$, and (b, d) traveling wave (TW) SOA at $z = L$, for (a, b) bulk and (c, d) multiple quantum well (MQW) active region.

Totović et al. (2013), is given in Figure 21.6. It can be seen that R-SOA, Figure 21.6a and c, exhibits more pronounced resonances and antiresonances in comparison with TW-SOA, Figure 21.6b and d, which is a consequence of the highly reflective rear facet. The ASE noise spectrum profoundly depends on the optical power of the input signal and resonant pattern washes out as the input optical power increases. This is to be expected since the strong signal easily depletes the carriers and suppresses the noise, consequently reducing the effect of multiple round trips within the cavity on its spectrum. The difference between the output spectrums for distinct active region types, bulk, Figure 21.6a and b, and MQW, Figure 21.6c and d, is a result of different spectrums of radiative spontaneous emission rate and material gain, given in Figure 21.2.

In order to develop the model capable of capturing ripples in the ASE output spectrum, two approaches can be used. One would require an equation for ASE phase evolution in addition to Equation 21.31, which describes ASE spectral photon density. This would enable us to account for interference, and subsequently filtering property of the SOA cavity. However, due to the random nature of the ASE noise phase, this approach would require a random number generator (Park et al., 2005) and could essentially be categorized as a stochastic model. Another approach is based on spectrum slicing and analysis of photon density corresponding to each resonance, or mode, followed by photon redistribution over the energy range between the two antiresonances according to the cavity transfer function. This has been shown to be equivalent to the analysis of the electric field or the spectral photon density and phase (Adams et al., 1985). The phase equation will be included implicitly during the assessment of resonant and antiresonant frequencies of the mth cavity mode, ω_m^{r}, and ω_m^{a}, respectively. These can be derived by equating the phase accumulation during the cavity round trip to $2m\pi$ for resonant, or $(2m-1)\pi$ for antiresonant frequencies, where m is an integer. The single-pass phase shift, Φ, will be the same for either propagation direction and can be found from Equation 21.25 as

$$\Phi = \int_0^L \frac{\partial \varphi_+}{\partial z}\mathrm{d}z = \int_0^L \left(-\frac{1}{v_{\mathrm{g}}}\frac{\partial \varphi_+}{\partial t} + k_0 \Gamma \Delta n_{\mathrm{r}} \right) \mathrm{d}z = \frac{\omega}{v_{\mathrm{g}}} L + k_0 \int_0^L \Gamma \Delta n_{\mathrm{r}} \mathrm{d}z. \tag{21.32}$$

Here, $\omega / v_{\mathrm{g}} = n_{\mathrm{eff},0} k_0 = \beta_0$ is the wave propagation constant for zero carrier density, where $n_{\mathrm{eff},0}$ is the effective index of refraction for zero carrier density or the background index of refraction. Resonant and antiresonant frequencies are calculated from

$$2\frac{\omega}{c}\left(n_{\mathrm{eff},0} L + \int_0^L \Gamma \Delta n_{\mathrm{r}} \mathrm{d}z \right) = \begin{cases} 2m\pi, & \text{for } \omega_m^{\mathrm{r}} \\ (2m-1)\,\pi, & \text{for } \omega_m^{\mathrm{a}} \end{cases}. \tag{21.33}$$

Since both Γ and Δn_{r} depend on photon energy, $\hbar\omega$, resonant and antiresonant frequencies cannot be expressed in a closed analytical form. Additionally, we can conclude that ω_m^{r} and ω_m^{a} depend on carrier density through the second term in the LHS of Equation 21.33 since both Γ and Δn_{r} depend on n. This implies that the spectral output of either TW- or R-SOA will not be static; rather the frequencies corresponding to resonances and antiresonances will be shifted in the presence of the optical signal (Schrenk, 2011; Totović et al., 2013). However, comparing to the first term in the LHS of Equation 21.33, the contribution of the second term is usually small and can be justifiably neglected.

By integrating Equation 21.31 over the energy between each of the two antiresonances, ω_m^{a} and $\omega_{m+1}^{\mathrm{a}}$, a system of equations can be developed, written with respect to noise photon densities of the mth mode, $A_{\pm}^m(z,t)$, for forward (+) and backward (−) propagation directions (Schrenk, 2011; Totović et al., 2013):

$$\pm\frac{\partial A_{\pm}^m}{\partial z} + \frac{1}{v_{\mathrm{g}}}\frac{\partial A_{\pm}^m}{\partial t} = \left(\Gamma_m g_m - \alpha_{\mathrm{i}}^m \right) A_{\pm}^m + \frac{1}{2 v_{\mathrm{g}}^m} \Gamma_m \beta_{\mathrm{sp}}^m R_{\mathrm{sp}}^m, \tag{21.34}$$

where the index m denotes the parameter values corresponding to the mth cavity resonance, and R_{sp}^{m} stands for the fraction of radiative spontaneous recombination rate injected into the mth mode. This approach, relying on separating amplification and filtering properties of the amplifier cavity, reduces time, memory, and processing resource consumption during simulation.

The filtering function of the amplifier is given in the form of an Airy function corresponding to the FP cavity (Adams et al., 1985):

$$G_m(\hbar\omega) = \frac{\left(1-R_1\right)\left(1-R_2\right)G_s^m}{\left(1-G_s^m\sqrt{R_1R_2}\right)^2 + 4G_s^m\sqrt{R_1R_2}\sin^2\Phi(\hbar\omega)}, \tag{21.35}$$

where Φ is the single-pass phase shift, defined by Equation 21.32, and G_s^m stands for the single-pass gain at resonant energy $\hbar\omega_m^r$:

$$G_s^m = \exp\left[\int_0^L \left(\Gamma_m g_m - \alpha_i^m\right) \mathrm{d}z\right]. \tag{21.36}$$

The transmittance given by Equation 21.35 accounts for the signal amplification, so care should be exercised when using it with Equation 21.34. Prior to photon filtering, the transmittance needs to be normalized to unity over the mth mode energy range since the noise amplification has already been accounted for using Equation 21.34, and only photon redistribution is required. The normalized filtering function $T_m(\hbar\omega)$ can be found as

$$T_m(\hbar\omega) = \frac{G_m(\hbar\omega)}{\left(\hbar\omega_{m+1}^a - \hbar\omega_m^a\right)^{-1}\int_{\hbar\omega_m^a}^{\hbar\omega_{m+1}^a} G_m(\hbar\omega)\,\mathrm{d}(\hbar\omega)}, \tag{21.37}$$

which is equivalent to

$$T_m(\hbar\omega) = \frac{G_m(\hbar\omega)}{\pi^{-1}\int_0^{\pi} G_m(\Phi)\,\mathrm{d}\Phi} = \frac{\sqrt{1+\gamma_m}}{1+\gamma_m\sin^2\Phi}, \tag{21.38}$$

where the γ-parameter is defined as follows:

$$\gamma_m = \frac{4G_s^m\sqrt{R_1R_2}}{\left(1-G_s^m\sqrt{R_1R_2}\right)^2}. \tag{21.39}$$

The validity of the previous model can be easily checked by analysis of the corner case where any of R_1 or R_2 is equal to zero. This would yield $\gamma_m = 0$, and $T_m = 1$, which corresponds to the case of uniformly distributed photons. This result is to be expected since for zero reflectivity no feedback loop exists.

Finally, the spectral photon densities of the noise at the SOA's output can be found using (Totović et al., 2013)

$$\begin{aligned} a_-(0,\hbar\omega) &= \sum_m \left[\left(\hbar\omega_{m+1}^a - \hbar\omega_m^a\right)^{-1} A_-^m(0)\,T_m(\hbar\omega)\right], \\ a_+(L,\hbar\omega) &= \sum_m \left[\left(\hbar\omega_{m+1}^a - \hbar\omega_m^a\right)^{-1} A_+^m(L)\,T_m(\hbar\omega)\right], \end{aligned} \tag{21.40}$$

where the summation is done over the modes m from 1 to the total number of accounted modes M.

In order to increase the efficiency of numerical calculations related to noise, an approach based on grouping of several adjacent modes into clusters was proposed by Totović et al. (2013). Although this degrades the accuracy to a certain point, the small intermodal space between resonances, which is of the order of $\Delta\nu = 70$ GHz, or $\Delta\lambda = 0.54$ nm for the active region length of 800 μm, ensures that no significant changes for any spectrally dependent parameter exist within the cluster. The proposed optimal number of modes within one cluster is 5, based on the fact that material gain and stimulated emission rate do not change more than 2% for bulk and 3% for MQW active region, within the cluster's range of frequencies, for the most part of the spectrum. In addition, the grouping of modes need not be uniform. In other words, clusters can comprise a lower number of modes in the frequency range close to the signal central frequency and maximum spontaneous emission rate and that number can be increased approaching the edges of spontaneous emission spectrum.

21.4.2.3 Stochastic Approach

Implementing any stochastic process relies on random number generators, or sources, meaning that only numerical analysis is possible in this case. Nonetheless, this approach can be very useful for investigating statistical properties of noise and signals. As both amplitude and phase of noise signal are random, it is suitable to use the equation written with respect to the normalized electric field envelope Equation 21.20, modified such that it includes a noise generator:

$$\pm\frac{\partial E_{\pm}}{\partial z} + \frac{1}{\nu_{\mathrm{g}}}\frac{\partial E_{\pm}}{\partial t} = \frac{1}{2}\left[\Gamma g\left(1 - i\alpha\right) - \alpha_{\mathrm{i}}\right]E_{\pm} + \mu_{\pm}. \tag{21.41}$$

Here, the complex term $\mu_{\pm}(z,t)$ stands for the random noise source, also known as the Langevin noise source (Henry, 1986; Coldren et al., 2012), which can be modeled as the Poisson or Gaussian phase-independent spatially uncorrelated white noise process (D'Ottavi et al., 1995; Cassioli et al., 2000; Park et al., 2005), based on the fluctuation-dissipation theorem (Shtaif et al., 1998). This implies that the mean value of $\mu_{\pm}(z,t)$ is zero, whereas the autocorrelation function satisfies the following condition:

$$\left\langle\left\langle \mu_{\pm}\left(z,t\right)\mu_{\pm}^{*}\left(z-z',t-t'\right)\right\rangle\right\rangle = \frac{1}{\nu_{\mathrm{g}}^{2}}\Gamma\beta_{\mathrm{sp}}R_{\mathrm{sp}}L\delta\left(z'\right)\delta\left(t'\right). \tag{21.42}$$

Recalling that Equation 21.20 does not include spectrally dependent parameters, it can be seen that the noise source defined in this manner has infinite bandwidth and consequently infinite power due to neglected spectral dependence of material gain (Cassioli et al., 2000). In practice, material gain will have finite bandwidth and will limit the noise power to a finite value. This effect can be included by passing $\mu_{\pm}(z,t)$ through the bandpass filter, which will result in

$$\left\langle\left\langle \mu_{\mathrm{F}\pm}\left(z,t\right)\mu_{\mathrm{F}\pm}^{*}\left(z-z',t-t'\right)\right\rangle\right\rangle = \frac{1}{\nu_{\mathrm{g}}^{2}}\Gamma\beta_{\mathrm{sp}}R_{\mathrm{sp}}LB_{\mathrm{F}}\delta\left(z'\right), \tag{21.43}$$

where $\mu_{\mathrm{F}\pm}(z,t)$ is the band-limited noise source and B_{F} is the noise equivalent bandwidth (D'Ottavi et al., 1995; Cassioli et al., 2000). If the segmentation along the spatial coordinate is small enough, such that the carrier density can be considered constant, in numerical simulations the Dirac delta function can be replaced with the inverse step size Δz (Marcuse, 1984):

$$\left\langle\left\langle \mu_{\mathrm{F}\pm}\left(z,t\right)\mu_{\mathrm{F}\pm}^{*}\left(z-z',t-t'\right)\right\rangle\right\rangle = \frac{1}{\nu_{\mathrm{g}}^{2}}\Gamma\beta_{\mathrm{sp}}R_{\mathrm{sp}}LB_{\mathrm{F}}\frac{1}{\Delta z}. \tag{21.44}$$

Now the noise source can be expressed as follows (Marcuse, 1984; Cassioli et al., 2000; Melo and Petermann, 2008):

$$\mu_{F\pm}(z,t) = \frac{1}{v_g}\sqrt{\Gamma\beta_{sp}R_{sp}B_F\frac{L}{\Delta z}}x_e, \tag{21.45}$$

where x_e is the complex Gaussian random variable. According to the sampling theorem, the sampling period, which is equivalent to the simulation time-step Δt, needs to be less than or equal to $1/(2B_F)$. The complex Gaussian random variable can be expressed in terms of its real and imaginary parts, which finally gives

$$\mu_{F\pm}(z,t) = \sqrt{\frac{1}{2v_g}\Gamma\beta_{sp}R_{sp}\frac{L}{v_g}\frac{1}{\Delta t\Delta z}}\frac{x_1+ix_2}{\sqrt{2}}, \tag{21.46}$$

where x_1 and x_2 are independent and identically distributed numerically generated Gaussian random variables with zero mean and unit variance (Melo and Petermann, 2008). Similarly, x_e can be expressed in terms of magnitude and phase, also distributed according to the Gaussian statistics, with zero mean and unit variance.

21.4.2.4 Noise Figure

The usual method of quantifying the noise is by determining the noise figure (NF). It can be shown (Simon et al., 1989) that the intrinsic NF of an SOA can be obtained using

$$NF_{dB} = 10\log_{10}\left[\frac{1}{G} + 2\frac{(G_s-1)(1+R_1G_s)}{G_s(1-R_1)}n_{sp}\frac{\Gamma g}{\Gamma g-\alpha_i}\right], \tag{21.47}$$

where G stands for the device (transmission) gain and G_s for the single pass gain, defined by Equation 21.36.

21.4.3 Extended Rate Equation Model

Previous discussion on SOA modeling covered the most important aspects of the photon–carrier interaction dynamics. Nevertheless, many more upgrades to the model are possible, and the choice of the model complexity mainly depends on the intended SOA usage. Whenever possible, it is good practice to simplify the model and exclude the effects that bear little to no improvement to the results, in order to reduce resource consumption during computation. Some of the upgrades are listed in the following pages, but many more do exist, e.g., separate analysis of polarization components (Pillai et al., 2006; Melo and Petermann, 2008), inclusion of nonlinearities, etc.

21.4.3.1 Carrier Diffusion

Although often omitted from consideration, carrier diffusion plays an important role in SOA modeling. It provides the means for washing out the spatial grating in carrier density distribution caused by the interference between the electric fields of the counterpropagating optical signals (Yacomotti et al., 2004; Serrat and Masoller, 2006; Totović et al., 2013). In this manner, its effects are implicitly accounted for by neglecting the high frequency terms in carrier density spatial distribution and replacing $|E_+ + E_-|^2$ with $|E_+|^2 + |E_-|^2$. This approach, however, has its limitations. It has been shown that only "fast" spatial grating, coming from counterpropagating fields of the same mode, can be neglected, whereas the "slow" one, resulting from interference effects of the different longitudinal modes, remains to a certain degree (Yacomotti et al., 2004; Serrat and Masoller, 2006). In order to encompass all possible cases, the SOA model can be generalized by

modifying the carrier density rate Equation 21.14 to include the term describing diffusion (Agrawal and Olsson, 1989; Serrat and Masoller, 2006):

$$\frac{\partial n}{\partial t} = D\frac{\partial^2 n}{\partial z^2} + \frac{I}{qV} - \left[An + R_{\mathrm{sp}}(n) + Cn^3\right] - R_{\mathrm{st}}(n), \tag{21.48}$$

where D stands for the diffusion coefficient and $R_{\mathrm{st}}(n)$ includes the square magnitude of the sum of both signal and noise counterpropagating electric fields.

21.4.3.2 Nonlinear Gain Suppression

The two most important effects that can influence material gain on a short-term scale are spectral hole burning (SHB) (Ahn and Chuang, 1990) and CH (Willatzen et al., 1991). The former represents formation of frequency selective dip in the gain spectrum as a consequence of stimulated emission, whereas the latter describes the fact that the temperature of carriers and lattice may differ. Both can be phenomenologically accounted for by introducing the nonlinear gain suppression factor, ε, which causes gain reduction proportional to the photon density in the active region (Willatzen et al., 1991; Totović et al., 2013). Instead of using the so-called linear gain g, which is dependent only on photon energy and carrier density, equations should be modified such that nonlinear gain is used $g_{\mathrm{NL}} = g/(1 + \varepsilon S_\Sigma)$, which also accounts for gain dependence on photon density. The complete set of equations for wideband SOA modeling can now be written in the following form (Totović et al., 2013):

$$\frac{\mathrm{d}n}{\mathrm{d}t} = \frac{I}{qV} - \left(An + R_{\mathrm{sp}} + Cn^3\right) - \frac{R_{\mathrm{st}}}{1 + \varepsilon S_\Sigma}, \tag{21.49}$$

$$\pm\frac{\partial s_\pm}{\partial z} + \frac{1}{v_{\mathrm{g}}}\frac{\partial s_\pm}{\partial t} = \left(\frac{\Gamma g}{1 + \varepsilon S_\Sigma} - \alpha_{\mathrm{i}}\right) s_\pm, \tag{21.50}$$

$$\pm\frac{\partial \varphi_\pm}{\partial z} + \frac{1}{v_{\mathrm{g}}}\frac{\partial \varphi_\pm}{\partial t} = \frac{k_0 \Gamma \Delta n_{\mathrm{r}}}{1 + \varepsilon S_\Sigma}, \tag{21.51}$$

$$\pm\frac{\partial a_\pm}{\partial z} + \frac{1}{v_{\mathrm{g}}}\frac{\partial a_\pm}{\partial t} = \left(\frac{\Gamma g}{1 + \varepsilon S_\Sigma} - \alpha_{\mathrm{i}}\right) a_\pm + \frac{1}{2v_{\mathrm{g}}}\Gamma\beta_{\mathrm{sp}} r_{\mathrm{sp}}. \tag{21.52}$$

Presence of the nonlinear gain suppression also modifies the position of resonant and antiresonant frequencies, given by Equation 21.33, and the new condition can be derived from Equation 21.51:

$$2k_0\left(n_{\mathrm{eff},0}L + \int_0^L \frac{\Gamma\Delta n_{\mathrm{r}}}{1 + \varepsilon S_\Sigma}\mathrm{d}z\right) = \begin{cases} 2m\pi, & \text{for } \omega_m^{\mathrm{r}} \\ (2m-1)\pi, & \text{for } \omega_m^{\mathrm{a}} \end{cases}. \tag{21.53}$$

21.4.3.3 Carrier Transport Model for MQW and QD SOAs

As previously discussed, materials with higher levels of confinement can outperform bulk SOAs in many aspects. The most common choice of active regions aside from bulk are the ones based on MQWs or QDs. Due to the different carrier dynamics, these devices usually require a more elaborate model of carrier rate equations than the one introduced for bulk SOA.

The MQW region in lasers and SOAs is usually embedded into the separate confinement heterostructure (SCH) region. Injected carriers from the outer edges of the SCH region diffuse across the region, leading to the subsequent capture and emission of carriers by the quantum wells.

Figure 21.7 shows a typical SCH MQW active region. Carrier transport effects in MQW SOA can be modeled by rate equations written with respect to the carrier density in the barrier (continuum) states,

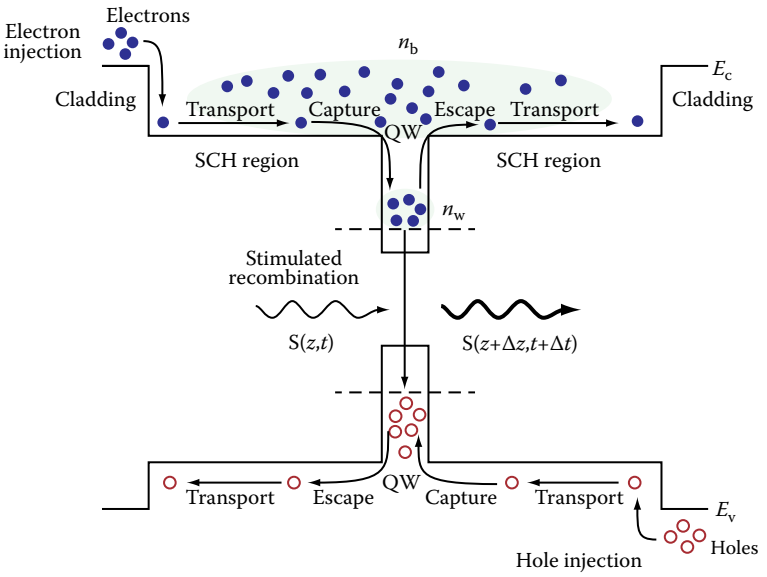

FIGURE 21.7 Band diagram of the multiple quantum well (MQW) semiconductor optical amplifier's (SOA's) active region and schematics showing carrier injection, transport, capture, escape and signal amplification by stimulated emission. (SCH, separate confinement heterostructure; QW, quantum well.)

including the SCH region and active layers, n_b, and the carrier density in the bound states of the well region, n_w, similar to SCH MQW lasers (Nagarajan et al., 1992; Keating et al., 1999; Totović et al., 2012). This model is referred to as the reservoir model (Nagarajan et al., 1992; Keating et al., 1999) and is equivalent to models that incorporate additional effects such as diffusive transport. Coupling of the carrier density in the barrier states above the MQWs to the carrier density in the MQWs is modeled by two terms representing carrier capture and escape into and from the wells, respectively:

$$\frac{dn_b}{dt} = \eta_{inj}\frac{I}{qV_b} - \frac{n_b}{\tau_b} - \frac{n_b}{\tau_{bw}} + \frac{n_w}{\tau_{wb}}\frac{V_w}{V_b}, \tag{21.54}$$

$$\frac{dn_w}{dt} = \frac{n_b}{\tau_{bw}}\frac{V_b}{V_w} - \frac{n_w}{\tau_w} - \frac{n_w}{\tau_{wb}} - \frac{R_{st}}{1+\varepsilon S_\Sigma}. \tag{21.55}$$

Here, η_{inj} is the injection efficiency, V_b is the volume of the SCH and active region, V_w is the volume of the well region, τ_b and τ_w are the carrier recombination lifetimes in the barrier and in the well region, respectively, τ_{bw} is the effective carrier diffusion across the SCH region and capture time by the wells, and τ_{wb} is the thermionic emission and carrier diffusion time from the well to the barrier states.

The TW equations for the counterpropagating optical photon densities retain the same form as in the case of the bulk SOA, with the exception of material gain and internal loss of the active region, which now dominantly depend on carrier density in the bound states of the well, n_w:

$$\pm\frac{\partial S_\pm}{\partial z} + \frac{1}{v_g}\frac{\partial S_\pm}{\partial t} = \left(\frac{\Gamma g}{1+\varepsilon S_\Sigma} - \alpha_i\right) S_\pm. \tag{21.56}$$

A more detailed model of the MQW active region's carrier dynamics may comprise additional rate equations for the reservoir model. For example, in addition to barrier states, well states may be divided into the excited state (ES) and the ground state (GS) (Qin et al., 2012). An even more elaborate approach

is required for asymmetric MQW structures, where the tunneling effect of carriers through the barriers needs to be accounted for (Lysak et al., 2005, 2006).

The basic rate equations for QD SOA are essentially the same as for the detailed model of the MQW active region (Qin et al., 2012). The discrete energy levels in the well of QDs include the GS level and the ES level, which is doubly degenerated. The populations of these two levels are described by separate carrier densities, n_G and n_E, respectively, which are normalized with respect to the total dot volume V_D. Dots are interconnected by the wetting layer (WL), described by the carrier density, n_W, which is normalized to the WL volume, V_W. It can be assumed that the carriers are injected directly from the contacts into the WL and the barrier dynamics is thus ignored in the model (Berg et al., 2001; Qasaimesh, 2003). The rate equations describing the carrier dynamics read

$$\frac{dn_W}{dt} = \frac{I}{qV_W} + \frac{n_E}{\tau_e^E}\frac{V_D}{V_W}f'_W - \frac{n_W}{\tau_c}f'_E - \frac{n_W}{\tau_{sp}}, \tag{21.57}$$

$$\frac{dn_E}{dt} = \frac{n_W}{\tau_c}\frac{V_D}{V_W}f'_E + \frac{n_G}{\tau_e^G}f'_E - \frac{n_E}{\tau_e^E}f'_W - \frac{n_E}{\tau_0}f'_G - \frac{n_E}{\tau_{sp}}, \tag{21.58}$$

$$\frac{dn_G}{dt} = \frac{n_E}{\tau_0}f'_G - \frac{n_G}{\tau_e^G}f'_E - \frac{n_G}{\tau_{sp}} - \frac{R_{st}}{1+\varepsilon S_\Sigma}. \tag{21.59}$$

Here, τ_e^E is the escape time of carriers from the ES level to WL, τ_c is the capture time of carriers from the WL to the ES level, τ_{sp} is the spontaneous recombination time, which is assumed to be identical for all levels, τ_e^G is the excitation time of carriers from the GS level to the ES level, and τ_0 is the intradot relaxation time. In Equations 21.57 through 21.59, $f'_{W,E,G} = 1 - f_{W,E,G}$ denote the probabilities of finding an empty carrier state at the WL band edge, the ES and GS levels, respectively, which are closely related to the carrier densities of the corresponding levels (Berg et al., 2001). Finally, material gain is now dependent on carrier density in the GS state. A similar model can be implemented in the case of active regions based on QDashes.

Last, when QDs are embedded into the QW region, it is necessary to extend the model with an additional rate equation that deals with the QW dynamics. Each additional state in QDs also requires a separate rate equation (Kim et al., 2009).

21.4.3.4 Carrier Heating

During the discussion on effects that cause material gain to behave nonlinearly, CH was introduced. Moreover, CH is responsible for phase variation, through Equation 21.19. Depending on the SOA regime of operation, CH might be accounted for phenomenologically, using the nonlinear gain suppression factor, ε, and LEF, α_{CH}, or, in the case of ultrafast applications, a more elaborate model can be used. The temperature dynamics in SOAs can be described using the carrier temperature rate equation (Dailey and Koch, 2007, 2009; Xia and Ghafouri-Shiraz, 2015):

$$\frac{dT}{dt} = \frac{1}{\partial U/\partial T}\left(\frac{dU}{dt} - \frac{\partial U}{\partial n}\frac{dn}{dt}\right) - \frac{T - T_0}{\tau}, \tag{21.60}$$

where T is the carrier temperature, T_0 is the lattice temperature, U is the total carrier plasma energy density, and τ is the electron–phonon interaction time. In this model, electron and hole plasmas are assumed to be equal in both temperature, T, and density, n (Dailey and Koch, 2007). The rate of energy density change can be found to be (Xia and Ghafouri-Shiraz, 2015)

$$\begin{aligned}\frac{dU}{dt} = &-v_g\sum_l\left(\hbar\omega_l - E_g\right)g_l\left(S_+^l + S_-^l\right) + v_g\Gamma K_1 n\sum_l\hbar\omega_l\left(S_+^l + S_-^l\right)\\ &- v_g\sum_m\left(\hbar\omega_m - E_g\right)g_m\left(A_+^m + A_-^m\right) + v_g\Gamma K_1 n\sum_m\hbar\omega_m\left(A_+^m + A_-^m\right),\end{aligned} \tag{21.61}$$

where summations are done over each mode l of the two counterpropagating signal photon densities $S_{\pm}^{l}$, and each mode m of the two counterpropagating ASE noise photon densities $A_{\pm}^{m}$. The free-carrier and intravalence absorption is captured in ΓK_1. The remaining derivatives, namely, $\partial U/\partial T$ and $\partial U/\partial n$, can be determined from the energy density distribution function (Xia and Ghafouri-Shiraz, 2015), given as (Dailey and Koch, 2009; Coldren et al., 2012)

$$U = \frac{2}{\sqrt{\pi}} k_B T \left(N_c F_{3/2}^{c} + N_v F_{3/2}^{v} \right), \tag{21.62}$$

where N_c and N_v stand for the effective densities of states for CB and VB, respectively, and $F_{3/2}^{c}$ and $F_{3/2}^{v}$ are the Fermi–Dirac integrals of order 3/2 for CB and VB, respectively. Having determined the rate of temperature change, it is possible to account for its variation in calculating the material gain, radiative spontaneous recombination rate, and variation of index of refraction, which are all temperature dependent through the Fermi–Dirac functions, Equations 21.1 through 21.3, or Equations 21.4 through 21.6, depending on the active region type. The analysis by Xia and Ghafouri-Shiraz (2015) confirms that the difference in carrier density and material gain caused by CH does influence the signal amplification in the picosecond regime of SOA operation.

21.4.3.5 Distributed Bias Current

It is common practice to assume that the driving current of SOA gets instantaneously uniformly distributed along the active region. In practice, this lumped electrode model is not always appropriate. Electric current does require a finite amount of time to travel from the contact to the edges of the electrode, and modeling it as a traveling microwave (TMW) might be more suitable in some cases, especially when the time delay is a significant fraction of the modulation period (Tauber et al., 1994; Mørk et al., 1999; Totović et al., 2015). This distributed nature of the current can have important implications on the results when SOAs are directly modulated at high bitrates (Tauber et al., 1994; Wu et al., 1995; Liljeberg and Bowers, 1997). Moreover, the microwave will be attenuated during the propagation, and the loss can sometimes be very high at typical modulation frequencies (Tauber et al., 1994). An additional point worth noting is that the microwave can be reflected at the end of an electrode, depending on the load impedance. When the microwave reflection coefficient differs from zero, two counterpropagating microwaves will exist (Totović et al., 2015):

$$I(z,t) = \bar{I} + \Delta I_F(z) \exp\left[i\left(2\pi f t - \beta_e z\right)\right] + \Delta I_B(z) \exp\left[i\left(2\pi f t + \beta_e z\right)\right]. \tag{21.63}$$

Here $\bar{I}$ is the stationary value of bias current, ΔI_F and ΔI_B are the small-signal bias current amplitudes for forward (F) and backward (B) propagation with respect to z-axis, which are defined by the spatially variable voltage across the electrode, f is the modulation frequency, $\beta_e = 2\pi f/v_e$ is the microwave propagation constant, $v_e = c/n_e$ is the microwave velocity, and n_e is the effective electric refractive index. Bias current will induce carrier density change through the carrier rate Equation 21.49, which will lead to change in all carrier-dependent parameters.

21.5 Overview of Steady-State and Dynamic TW- and R-SOA Models

Both TW- and R-SOA have found their application niches within the optical networks and photonic circuits. In order to make the optimal choice regarding the SOA material and geometric properties, as well as operating conditions, it is necessary to analyze their performance, in both the steady-state and dynamic regimes. This can be done either experimentally or theoretically, using any of the models presented in this section. Essentially, two borderline approaches can be used depending on required precision, available

time, and computational resources. The first one is largely exploited in commercially available software for optical network analysis and relies on a significant number of approximations that either allow for analytical or semianalytical solutions or a relatively simple numerical approach using efficient numerical methods. The second one includes a detailed and comprehensive analysis and is mostly used in SOA design and optimization.

Modeling of steady-state and dynamic properties of SOAs essentially reduces to efficient and accurate self-consistent solving of coupled rate equations written with respect to the counterpropagating signals and noise, and carrier density, with imposed boundary and initial conditions. In the case of TW-SOA, the equation system usually comprises only the forward-propagating TW equation, whereas in the case of R-SOA both forward and backward TW equations are needed. The number of rate equations describing the carrier density depends on the material used for the active region and anticipated model accuracy. A self-consistent approach is required since the carrier depletion in the active region is caused by the stimulated amplification of the input optical signal, and this in turn modifies the material gain and, consequently, further amplification of the signal. If the carrier depletion is weak and the carrier density is approximately uniformly distributed along the active region, the TW equation for the forward-propagating signal (Equation 21.23) can be analytically solved. In the case of the continuous wave (CW), i.e., stationary input optical signal $S_{\text{in}} = S_+(z = 0)$, the output photon density $S_{\text{out}} = S_+(z = L)$ is given by

$$S_{\text{out}} = G_{\text{s}} S_{\text{in}} = S_{\text{in}} \exp\left[\left(\Gamma g - \alpha_{\text{i}}\right) L\right], \tag{21.64}$$

where G_{s} is the single pass gain. An analogous relation can be written for the electric field, where the factor 1/2 should be accounted for in the argument of exponential function: $\exp[(\Gamma g - \alpha_{\text{i}})L/2])$, or $G_{\text{s}}^{1/2}$. In the case of the time-dependent (nonstationary) input optical signal, the solution of Equation 21.23 for the forward-propagating photon density reads

$$S_{\text{out}}(t) = S_{\text{in}}\left(t - \frac{L}{v_{\text{g}}}\right) \exp\left[\left(\Gamma g - \alpha_{\text{i}}\right) L\right]. \tag{21.65}$$

Here, a reference frame traveling with the signal is used, and therefore the temporal dependence of the input signal, $S_{\text{in}}(t)$, is replaced with $S_{\text{in}}(t - L/v_{\text{g}})$. It can be seen that in both cases the output photon density is proportional to G_{s}.

The above relations can be generalized and may also be applied for an SOA section in which the carrier density is uniformly distributed. In this case, S_{in} and S_{out} represent the section's input and output photon densities, ${S_+}^{k-1} = S_+(z_{k-1})$ and ${S_+}^{k} = S_+(z_k)$ for forward propagation, and ${S_-}^{k} = S_-(z_k)$ and ${S_-}^{k-1} = S_-(z_{k-1})$ for backward propagation, respectively, as shown in Figure 21.8. The decrease of the section length makes the assumption of the uniform carrier distribution more justified. This fact represents the basis for the development of various methods, which can provide efficient stationary and time-domain modeling of TW- and R-SOA.

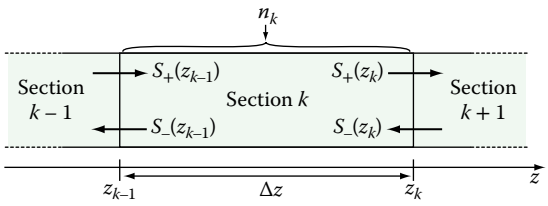

FIGURE 21.8 Schematic representation of the semiconductor optical amplifier (SOA) section with the relevant carrier and photon densities.

21.5.1 Steady-State Models

One of the oldest methods used in modeling of SOAs, optical waveguides, and semiconductor lasers is the transfer matrix method (TMM) (Chu and Ghafouri-Shiraz, 1994), which has long been regarded as an efficient and powerful numerical tool. The robustness and simplicity of its implementation on computer platforms are the major reasons for its success and popularity in using it to analyze complex photonics structures. The method assumes that the entire amplifier is divided into p sections, each with a length of $\Delta z = L/p$, where L is the amplifier length. Each section is labeled such that the kth section extends from $(k-1)\Delta z$ to $k\Delta z$. The value of Δz is small enough such that the carrier density, material gain, and modal gain can be assumed as uniform along each section. If only the forward-propagating wave is of interest, as in TW-SOA, the output photon densities of subsequent sections, S_+^{k-1} and S_+^k, satisfy the relation that is a generalized form of Equation 21.64

$$S_+^k = G_k S_+^{k-1} = S_+^{k-1} \exp\left[\left(\Gamma g_k - \alpha_{i,k}\right)\Delta z\right], \tag{21.66}$$

where g_k and $\alpha_{i,k}$ are the material gain and active region loss corresponding to section k, respectively, and G_k stands for the single pass gain of the kth section. In the case of bidirectional propagation (forward and backward), as in R-SOA or FP-SOA, the matrix relating $(k-1)$th and the kth section may be written in the following form, based on Equation 21.66:

$$\begin{bmatrix} S_+^k \\ S_-^k \end{bmatrix} = \begin{bmatrix} G_k & 0 \\ 0 & G_k^{-1} \end{bmatrix} \begin{bmatrix} S_+^{k-1} \\ S_-^{k-1} \end{bmatrix}. \tag{21.67}$$

Same method can be applied when the TW equation is written with respect to the electric field envelope (Equation 21.15) instead of photon density, intensity, or power. In this case, the transfer matrix may comprise the information about phase (Chu and Ghafouri-Shiraz, 1994):

$$\begin{bmatrix} E_+^k \\ E_-^k \end{bmatrix} = \begin{bmatrix} G_k^{1/2} \exp(i\beta\Delta z) & 0 \\ 0 & G_k^{-1/2} \exp(i\beta\Delta z) \end{bmatrix} \begin{bmatrix} E_+^{k-1} \\ E_-^{k-1} \end{bmatrix}. \tag{21.68}$$

By using input parameters, namely, bias current I and injected optical power P_0, or electric field $E_0 = S_0^{1/2} \exp(i\varphi_0)$, along with boundary conditions and transfer matrices, the carrier density for each section can be found from the Equation 21.14. In the case of R-SOA, the carrier rate equation will be converted into a p-dimensional system of transcendental equations with respect to carrier densities corresponding to all sections (Totović et al., 2014). Once the carrier density in each section is known, the transfer matrices can be used in the evaluation of the photon density or the corresponding electric field envelope in each of the SOA sections.

In this consideration, it is assumed that the photon density, or the corresponding envelope of the electric field, represents the signal. Most of the steady-state models do not account for the noise contribution to the signal, assuming that its phase is uncorrelated to the signal's phase. Therefore, some models neglect the noise (Chu and Ghafouri-Shiraz, 1994), while others use separate TW equations for the signal and the ASE (Jin et al., 2003; de Valicourt et al., 2010), which means that the signal and noise are generally treated separately. However, coupling between the signal and noise is provided by the carrier rate equation that accounts for both contributions, which finally affects the carrier density in the active region and all carrier dependent parameters, and consequently, the photon density. In the case of steady-state analysis, it is possible to solve the TW equation for ASE (Equation 21.31) on domain Δz of section k, and use it in the TMM. The solution is given by

$$a_+^k = G_k a_+^{k-1} + \sigma_k \frac{G_k - 1}{\ln G_k}, \tag{21.69}$$

where a_+^{k-1} and a_+^k represent ASE spectral photon densities at the input and the output of the kth section, respectively, whereas $\sigma_k = 1/(2v_g)\Gamma\beta_{sp}r_{sp}^k\Delta z$ is the contribution of the radiative spontaneous recombination rate spectral density in section k. If the ASE spectrum is uniform over an optical noise bandwidth B_N, the photon density corresponding to ASE can be obtained by multiplying Equation 21.69 by B_N. Otherwise, the total ASE photon density can be found by integrating Equation 21.69 over the ASE bandwidth. The above result can be generalized for both propagation directions (de Valicourt et al., 2010) and written in the following matrix form:

$$\begin{bmatrix} a_+^k \\ a_-^k \end{bmatrix} = \begin{bmatrix} G_k & 0 \\ 0 & G_k^{-1} \end{bmatrix} \begin{bmatrix} a_+^{k-1} \\ a_-^{k-1} \end{bmatrix} + \frac{\sigma_k}{\ln G_k} \begin{bmatrix} G_k - 1 \\ G_k^{-1} - 1 \end{bmatrix}. \tag{21.70}$$

This matrix form does not strictly fit into the standard transfer matrix form due to additional vector representing the ASE contribution of the kth section. However, a considerable number of time-domain multisection methods accounts for ASE by using the form defined by Equation 21.70 (Durhuus et al., 1992; Davis and O'Dowd, 1994; Kim et al., 1999; Occhi et al., 2003; Park et al., 2005; Mathlouthi et al., 2006; Morel and Sharaiha, 2009). Since these methods are not essentially different from TMM, they can be referred to as TMMs.

Although TMM is simple for implementation, it requires a significant number of matrix multiplications, increasing linearly with the number of sections. A large number of multiplications may cause error accumulation and inaccuracy in the evaluation of photon density or the corresponding electric field envelope. The TW equations can be solved by implementation of the FDM rather than the TMM (Connelly, 2001, 2002). Forward differences are used for forward-propagating TWs, and backward differences for backward-propagating TWs. The carrier rate equation in each mesh point is used for determining the carrier density value. Since the self-consistent method implementation is required, the process of calculation of carrier and photon densities relies on iterative procedure, with adjustment of at least one variable in each iteration step, usually the carrier density. However, the carrier density variation along the amplifier is rather small even for a wide range of the signal input powers (Totović et al., 2013). On the other hand, the photon density varies significantly, up to several orders of magnitude. Therefore, the control of the iteration process by the carrier density adjustments, as proposed by Connelly (2001, 2002), makes the process very sensitive since the small variation of the carrier density leads to a large variation of the photon density. It is shown by Jin et al. (2003) that iterations based on photon density may provide faster convergence and increased stability of the iteration process.

21.5.2 Dynamic Models

Due to its simplicity and popularity, TMM has been modified and implemented in the development of the large-signal dynamic model (Davis and O'Dowd, 1994; Kim et al., 1999). The model is bidirectional, which makes it suitable for both TW- and R-SOA time-domain simulations. Similar multisection time-domain models, based on the time-dependent version of Equation 21.67 or Equations 21.68 and 21.70, can also be found in the literature (Occhi et al., 2003; Park et al., 2005; Mathlouthi et al., 2006; Kim et al., 2009). It has been shown by Park et al. (2005) that only the "fullwave" model, which accounts for the intensity and phase of the superimposed electric fields of the signal and noise, provides accurate results. The model based solely on photon densities of signal and noise (or their optical powers) overestimates the influence of the noise on the signal (Park et al., 2005). On the other hand, the model in which the signal is represented by the electric field, and spontaneous emission noise by the photon density, underestimates the effect of noise on the signal (Park et al., 2005).

Another time-domain multisection, wideband, and bidirectional method has been derived using the inverse Fourier transform of the frequency-domain propagation equation (Durhuus et al., 1992). It is essentially a type of TMM, comprising complex time delay. Due to included wideband spectral dependence, it is suitable for simulation of multichannel amplification. A similar method proposed by Morel and Sharaiha

(2009) is implemented in a commercially available software, Advanced Design System from Keysight Technologies (www.keysight.com), after conversion of transfer matrices, including complex time delay, into an equivalent SOA circuit. Another recently developed equivalent circuit model, more precisely transmission line model (TLM), was presented by Xia and Ghafouri-Shiraz (2016). A multisection wideband time-domain method based on the finite-impulse response (FIR) filter scheme has been proposed by Toptchiyski et al. (1999) and Runge et al. (2010). The method is based on two computational steps in each section. The first step includes calculation of local gain with its linear and nonlinear components, as well as the local nonlinear phase change. Then, the propagation equations for the forward- and backward-traveling fields are solved by accounting for the spectral profile of the gain through the implementation of an FIR filter. The FDM can also be applied in time-domain simulations of SOAs. A comprehensive improved finite-difference beam propagation model (IFD-BPM) (Razaghi et al., 2009) has been used for modeling of temporal and spectral properties of copropagating and counterpropagating picosecond optical pulses with different wavelengths. The aforementioned model includes the following effects: interband gain and refractive index dynamics, CH, SHB, two-photon absorption (TPA), ultrafast nonlinear refraction (UNR), gain dispersion, gain peak shift with carrier density variation, and group velocity dispersion (GVD). Due to numerous linear and nonlinear effects, the forward and backward TW equations become essentially nonlinear propagation equations, and are named modified nonlinear Schrödinger equations. Solving these equations is based on coordinate transformation, which can be successfully done by trapezoidal integration and central difference technique. The same method has been also used in the development of the R-SOA pulse propagation model (Connelly, 2012). An interesting method for modeling of SOA time-domain response and four-wave mixing (FWM) was proposed by Mecozzi and Mørk (1997) and Cassioli et al. (2000). The method assumes a relatively small variation of carrier density along the amplifier and consequently a small gain variation. It is based on the analytical integration of material gain over the entire SOA length. This eliminates the spatial coordinate dependence and allows for the amplifier dynamics to be described by solving a set of ordinary differential equations for the complex gain. The ASE noise is modeled by an equivalent noise source with appropriate statistical properties. When the internal loss is included, the method's complexity increases. The SOA simulator is implemented in the Simulink® software, based on the MATLAB® engine and routines for numerical calculations, because of its capability to deal with time-domain analysis of dynamical systems. A similar approach, based on the delayed differential equation, has been used in the derivation of R-SOA's time-domain transmission function, which is then implemented in the semianalytical analysis of FWM in R-SOA (Antonelli and Mecozzi, 2013). The fundamental condition for the method implementation is that the round-trip time of the pulse is small compared to its duration. An improved version of this, the so-called reduced model, is proposed by Dúill and Barry (2015), where the improvement is achieved by the inclusion of the internal losses.

If the dynamic effects of interest occur on a much larger time scale than the time required for the signal to travel along the active region, a simplification to the dynamic model can be introduced by assuming instantaneous propagation of signals across the SOA length (Connelly, 2014, 2015). This assumption significantly simplifies the model by reducing the TW equations to their steady-state form, which can then be solved using the corresponding finite differences for each propagation direction. In this manner, spatial distributions of photon and carrier densities are calculated at each point in time, under the quasi-steady-state conditions. This approach might be helpful as a basis for the simple TW- and R-SOA models; however, a detailed model does require accounting for the finite time needed for wave propagation. In this case, the system of coupled partial differential TW equations may be solved numerically using a first-order upwind scheme based on the FDM (Totović et al., 2011) in order to obtain a full spatiotemporal distribution of all relevant quantities.

21.5.3 Case Study: Steady-State Wideband Self-Consistent Numerical Model

In order to fully understand the mechanisms underlying SOA operation, the model needs to be designed such that it accounts for spectral dependencies of all relevant parameters discussed in Section 21.3 and

given in Figures 21.2 through 21.4. These models, typically referred to as wideband, are required to operate not with photon densities, but rather their spectral distributions. Additionally, it is good practice to generalize the model such that it supports any facet reflectivity. This makes the model transparent to the SOA type and it can be further used to analyze TW-, FP-, or R-SOA simply by adjusting the facet reflectivities to the desired value. For TW-SOA, the values can be chosen to be either zero, or, if higher precision is required, some small, but finite value, in the range of 10^{-3}–10^{-5}. In the case of FP- or R-SOA, the reflectivity of a highly reflective facet is usually chosen to be equal to the reflectivity of the interface between cleaved semiconductor and air, $R_2 = (n_r - 1)^2/(n_r + 1)^2$, but it can be set to another value if reflective layers are used.

The full system of equations for a steady-state wideband model can be derived from Equations 21.49 through 21.52 by setting the time derivatives of carrier density and spectral photon densities to zero:

$$\frac{\mathrm{d}n}{\mathrm{d}t} = \frac{I}{qV} - \left(An + R_{\mathrm{sp}} + Cn^3\right) - \frac{R_{\mathrm{st}}}{1 + \varepsilon S_\Sigma} = 0, \tag{21.71}$$

$$\pm \frac{\mathrm{d}s_\pm}{\mathrm{d}z} = \left(\frac{\Gamma g}{1 + \varepsilon S_\Sigma} - \alpha_{\mathrm{i}}\right) s_\pm, \tag{21.72}$$

$$\pm \frac{\mathrm{d}\varphi_\pm}{\mathrm{d}z} = \beta_0 + k_0 \frac{\Gamma \Delta n_r}{1 + \varepsilon S_\Sigma}, \tag{21.73}$$

$$\pm \frac{\mathrm{d}a_\pm}{\mathrm{d}z} = \left(\frac{\Gamma g}{1 + \varepsilon S_\Sigma} - \alpha_{\mathrm{i}}\right) a_\pm + \frac{1}{2v_{\mathrm{g}}} \Gamma \beta_{\mathrm{sp}} r_{\mathrm{sp}}, \tag{21.74}$$

where

$$S_\Sigma(n) = \int_0^\infty \left(s_+ + s_- + a_+ + a_-\right) \mathrm{d}(\hbar\omega), \tag{21.75}$$

$$R_{\mathrm{st}}(n) = \int_0^\infty v_{\mathrm{g}} g \left(s_+ + s_- + a_+ + a_-\right) \mathrm{d}(\hbar\omega). \tag{21.76}$$

Boundary conditions for the signal can be derived from Equations 21.27 and 21.28 and are given by the following set of equations at the front facet:

$$s_+(0) = \left(1 - R_1\right) s_0 + R_1 s_-(0) - 2\sqrt{\left(1 - R_1\right) s_0}\sqrt{R_1 s_-(0)} \cos\left[\varphi_0 - \varphi_-(0)\right], \tag{21.77}$$

$$\varphi_+(0) = \arctan\left[\frac{\sqrt{\left(1 - R_1\right) s_0} \sin\varphi_0 - \sqrt{R_1 s_-(0)} \sin\varphi_-(0)}{\sqrt{\left(1 - R_1\right) s_0} \cos\varphi_0 - \sqrt{R_1 s_-(0)} \cos\varphi_-(0)}\right], \tag{21.78}$$

and by $s_-(L) = R_2 s_+(L)$, and $\varphi_-(L) = \varphi_+(L) + \pi$ at the rear facet. The input signal is assumed to have Gaussian power spectral distribution $\sigma_{\mathrm{G}}(\hbar\omega)$, with FWHM of 0.1 nm, which is a good approximation of the signal generated by the distributed feedback (DFB) laser. Given the input optical power P_0, input signal spectral density can be found by multiplying the input signal photon density, S_0, by the Gaussian function normalized to unity with respect to energy:

$$s_0(\hbar\omega) = \frac{\Gamma(\hbar\omega) P_0}{\hbar\omega v_{\mathrm{g}}(\hbar\omega) WH} \sigma_{\mathrm{G}}(\hbar\omega). \tag{21.79}$$

In analysis of ASE noise, phase is not included explicitly, and therefore no interference exists at either facet, giving $a_+(0) = R_1 a_-(0)$ and $a_-(L) = R_2 a_+(L)$.

In order to account for the resonant properties of the SOA cavity, the procedure described in Section 21.4.2 for deriving Equation 21.34 from Equation 21.31 can be employed, and Equation 21.74 can be transformed into a system of steady-state equations written with respect to the noise photon densities corresponding to each mode m:

$$\pm \frac{\mathrm{d}A_{\pm}^{m}}{\mathrm{d}z} = \left(\Gamma_m g_m - \alpha_{\mathrm{i}}^{m}\right) A_{\pm}^{m} + \frac{1}{2v_{\mathrm{g}}^{m}} \Gamma_m \beta_{\mathrm{sp}}^{m} R_{\mathrm{sp}}^{m}, \tag{21.80}$$

with boundary conditions $A_+^m(0) = R_1 A_-^m(0)$ and $A_-^m(L) = R_2 A_+^m(L)$. The system given by Equation 21.80 represents the steady-state form of Equation 21.34. Introducing the mode photon densities $A_{\pm}^{m}$ also implies that modification of Equations 21.75 and 21.76 is required, where the integral over energies for ASE noise now becomes a sum over modes m:

$$S_{\Sigma}(n) = \int_0^{\infty} \left(s_+ + s_-\right) \mathrm{d}(\hbar\omega) + \sum_m \left(A_+^m + A_-^m\right), \tag{21.81}$$

$$R_{\mathrm{st}}(n) = \int_0^{\infty} v_{\mathrm{g}} g \left(s_+ + s_-\right) \mathrm{d}(\hbar\omega) + \sum_m v_{\mathrm{g}}^m g_m \left(A_+^m + A_-^m\right). \tag{21.82}$$

In this manner, signal amplification will be accounted for by TW Equation 21.80 and the photons will be subsequently redistributed within the mode frequency range using the filtering function (Equation 21.38). The resonant and antiresonant frequencies are found by equating the noise phase accumulation to $2m\pi$ and $(2m-1)\pi$, respectively, the same as in Equation 21.33:

$$2k_0 \left(n_{\mathrm{eff},0} L + \int_0^L \frac{\Gamma \Delta n_{\mathrm{r}}}{1 + \varepsilon S_{\Sigma}} \mathrm{d}z \right) = \begin{cases} 2m\pi, & \text{for } \omega_m^{\mathrm{r}} \\ (2m-1)\pi, & \text{for } \omega_m^{\mathrm{a}} \end{cases}. \tag{21.83}$$

In the pursuit of increased efficiency, several adjacent modes can be grouped into clusters of $2l+1$ mode, spanning between two antiresonances, from $\hbar\omega_{m-l}^{\mathrm{a}}$ to $\hbar\omega_{m+l+1}^{\mathrm{a}}$, where l stands for a small nonnegative integer. All photons corresponding to one cluster are now treated with a single pair of photon densities $A_{\pm}^{m}$, centered at the mth mode resonance, $\hbar\omega_m^{\mathrm{r}}$, where the values of all spectrally dependent parameters in Equations 21.80 through 21.82 are given at $\hbar\omega_m^{\mathrm{r}}$. In this manner, the number of equation pairs (comprising one equation for each propagation direction) required for modeling the ASE noise is reduced from the number of modes N to the number of clusters $M = N/(2l+1)$. This method effectively reduces the time and resource consumption at the cost of a modest decrease in accuracy. The error in calculating the photon density corresponding to a cluster will be pronounced in the portions of the spectrum where the ASE noise photon count reaches high values. Since the photon count depends on both the radiative spontaneous recombination rate and the material gain among other parameters, this error can be alleviated by nonuniform clustering of modes; the clusters can comprise only one mode in the vicinity of the signal central frequency, where the material gain and stimulated emission rate are high and the number of modes within the cluster can be increased further away in the spectrum.

21.5.3.1 Implementation of the Self-Consistent Method

As discussed earlier, the system of equations describing SOA needs to be solved in a self-consistent manner due to the coupling between the signal and noise though the carrier rate equation. Numerical solving of

the system requires discretization of the space-spectrum domain into a two-dimensional (2D) mesh, where each point represents a unique pair of position along the longitudinal axis z_i and energy $\hbar\omega_j$. The size of the spectral domain should be chosen such that it covers the region where material gain is positive since in the remaining regions spontaneously emitted photons will be attenuated during propagation and their contribution to the ASE spectrum can be neglected. Step size along the spectral axis should be smaller than the difference between two adjacent resonances of the cavity, which can roughly be estimated from Equation 21.83 as $\Delta(\hbar\omega) = \pi\hbar c/(n_{\text{eff},0}L)$, whereas for the longitudinal axis no particular constraints exist and the smaller step size simply enables a more accurate spatial distribution calculation. The choice of 1001 equidistant points z_i along the longitudinal axis, where i spans from 0 ($z = 0$) to 1000 ($z = L$), provides a quasi-continuous spatial domain, with the step length equal to $\Delta z = L/1000$. An example of such 2D mesh is given in Figure 21.9.

The derivatives over the z-coordinate in Equations 21.72 and 21.73 and Equation 21.80 can now be replaced with finite differences. Depending on the propagation direction of signal and ASE noise, forward or backward, appropriate finite differences are used, forward in the former, and backward in the latter case. This approach allows for successive calculation of the variable values in the next point in space based on the values from the previous one. For forward propagation, the equations can be written in the following generalized form:

$$f_+\left(z_{i+1}\right) = f_+\left(z_i\right) + F_+\left(z_i\right)\Delta z, \tag{21.84}$$

where f_+ stands for any forward-propagating variable, s_+, φ_+, or A_+^m, whereas F_+ denotes the RHS of the corresponding equations, evaluated at the ith point in space, z_i. For backward propagation, using the same generalized notation, the equations can be reduced to

$$f_-\left(z_{i-1}\right) = f_-\left(z_i\right) + F_-\left(z_i\right)\Delta z, \tag{21.85}$$

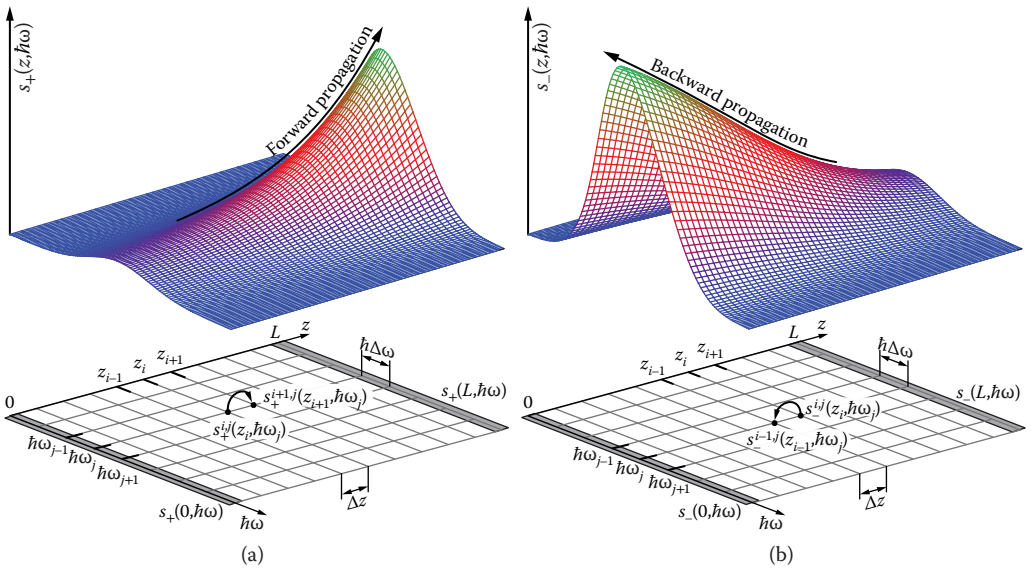

FIGURE 21.9 Illustration of the two-dimensional space-spectrum mesh used in the wideband steady-state self-consistent numerical method for modeling semiconductor optical amplifiers (SOAs). The example includes spectral photon density distribution for (a) forward and (b) backward propagations.

where f_- stands for any backward-propagating variable, s_-, φ_-, or A_-^m, whereas F_- denotes the RHS of the corresponding equations, evaluated at the ith point in space, z_i. The coupling between Equations 21.84 and 21.85 is provided by the boundary conditions at $z = 0$ and $z = L$. Carrier density in each point in space can be found as a solution of the transcendental Equation 21.71, which is then followed by calculation of resonant and antiresonant frequencies, using Equation 21.83.

The system given by Equations 21.71 through 21.73, 21.80, and 21.83 represents the basis of one iteration step in the self-consistent numerical method (SCNM). Starting from the arbitrarily chosen carrier density distribution, signal and noise for both propagation directions can be determined and subsequently used for calculating the new carrier distribution. Assuming that the newly calculated carrier density distribution converges to the steady-state distribution, repeating this process should give improved results with each iteration step. The process can be stopped when the difference between the values calculated within two consecutive iteration steps reaches the tolerance point. Although this simplified algorithm is useful for conceptualization of iterative procedure, in practice it suffers from severe instability, and rarely converges. The instability is caused by significant changes in photon spectral densities, up to several orders of magnitude, for subtle changes in carrier density. An approach typically used to alleviate this issue relies on self-consisting tuning of the carrier density (Connelly, 2001) or photon density (Jin et al., 2003) by its averaging over the current and previous iteration step, with proper weight coefficients. Although these approaches have shown to be successful in modeling TW-SOA, in the case of an R-SOA they still diverge for high driving currents and high input signal optical powers. Choosing to simultaneously tune all variables of interest, namely $s_\pm$, $A_\pm^m$, and n, instead of just one, does increase stability, but not sufficiently enough to provide a reliable algorithm. The main issue comes from the interplay between counterpropagating signals and noise, where the backward-propagating ones are the delayed replicas of their forward-propagating counterparts. This "echoing," present whenever either facet reflectivity is nonzero, destabilizes the algorithm and raises the need for restraining the variables through the fading memory of previous iteration steps. Instead of averaging the variables over the current and previous iteration steps, the generalized algorithm assumes inclusion of k previous iteration steps, where $k \geq 1$. In this manner, sudden changes are prevented, and the system steadily converges toward the solution. The contribution of each iteration step can be adjusted using the set of weight coefficients w_i, with a sum of unity, which ponder the results of the ith iteration step during the averaging process. The updated (averaged) iteration variable that is passed to the next iteration step, x_{i+1}, can be found as

$$x_{i+1} = w_i x_i + w_{i-1} x_{i-1} + \ldots + w_{i-k} x_{i-k}. \tag{21.86}$$

The optimal number of iteration steps included will depend on the device's properties, mainly on the front and rear facet reflection coefficients. It has been shown by Totović et al. (2013) that $k = 3$ previous iteration steps, in addition to the current one, suffice to provide a stable algorithm, with a set of weight coefficients $\{w_i, w_{i-1}, w_{i-2}, w_{i-3}\} = \{0.4, 0.3, 0.2, 0.1\}$. The choice of weight coefficients depends on desired robustness of the algorithm and the convergence speed. By using higher pondering values for the current iteration step relative to the previous ones, the iteration process becomes more time efficient at the cost of an increased risk for divergence. Inclusion of several previous iteration steps is required in modeling FP- and R-SOA but can be relaxed to $k = 1$ for TW-SOA.

Prior to entering the iteration procedure, the maximum tolerable relative error $\delta_{\max}$ needs to be defined. The error δ between the two consecutive iteration steps is calculated as a maximum value of relative errors among all monitored variables, for each point in the mesh $(z_i, \hbar\omega_j)$:

$$\delta = \max\left\{\delta(n), \delta\left(s_\pm\right), \delta\left(A_\pm^m\right), \delta\left(\hbar\omega_m^{\mathrm{r}}\right)\right\}. \tag{21.87}$$

The iteration procedure is stopped once the value of the current relative error δ drops below the defined tolerance $\delta_{\max}$. The meticulousness with which the iteration error δ is calculated during each iteration step

ensures that all results consistently need to converge in order for the iteration procedure to end. Setting δ_{max} to 10^{-3} imposes very strict convergence requirements for all variables.

Aside from the input and control parameters, i.e., I, P_0, weight coefficients, and δ_{max}, SCNM requires a set of initial guess values (IGVs) for all variables. Since the spectral photon density of the input signal, s_0, depends on the confinement factor as shown in Equation 21.79, its IGV is calculated for an arbitrary carrier density between the transparency value n_{tr} and the maximum allowed value, n_{max}, governed by the bias current. The transparency value of the carrier density is determined by equating material gain to zero, whereas the maximum allowed value can be found from Equation 21.71, under the assumption of zero photon density in the active region:

$$\frac{I}{qV} - \left[An_{max} + R_{sp}\left(n_{max}\right) + Cn_{max}^3\right] = 0. \tag{21.88}$$

The IGV of spectral photon density for the forward-propagating signal, s_+, is then set to the input signal spectral photon density s_0, whereas the IGV for s_- is set either to zero, for TW-SOA, or to s_0, for FP- and R-SOA. The IGV for phase in both propagation directions, $\varphi_\pm$, is chosen to be zero. Before setting IGVs for ASE noise, it is necessary to determine the number of analyzed modes and the type of clustering. For a device length between 500 and 1000 μm, the intermodal space is of the order of 0.5 nm, and $N = 600$ modes covers the portion of the spectrum where ASE is expected to be pronounced. For the 100 modes around the signal central frequency, clusters of 1 mode have been chosen, whereas in the rest of the spectrum, clusters consist of 5 modes. This gives a total of $M = 200$ clusters to be analyzed. The ASE noise is usually orders of magnitude lower than the signal, therefore IGVs for all clusters $A_\pm^m$ are set to zero. The IGV for carrier density is calculated based on the IGVs for signal and noise photon densities by solving the transcendental Equation 21.71 with respect to n at each point z_i along the discretized longitudinal axis. Using Equation 21.83, IGVs for resonant and antiresonant frequencies are determined. Finally, using the appropriate expressions depending on the active region type, bulk or MQW, all material parameters dependent on carrier density can be determined. These include material gain (Equation 21.1 or Equation 21.4), radiative spontaneous recombination rate (Equation 21.2 or Equation 21.5), refractive index variation (Equation 21.3 or Equation 21.6), confinement factor (Equation 21.9), group velocity (Equation 21.13), and spontaneous emission coupling factor (Equation 21.11). Once all IGVs are defined, the iteration procedure can be initialized.

As discussed earlier, the iteration procedure essentially relies on repeating one iteration step and updating variable values according to the current and k previous iteration steps using Equation 21.86. It should be noted that until the number of completed iteration steps reaches k, corresponding IGVs are used as a replacement for the missing previous iteration values. The iteration step starts with solving Equations 21.72, 21.73, and 21.80, for forward propagation and determining s_+, φ_+, and A_+^m, based on the initial conditions at $z = 0$. This is followed by adjusting the variable values by averaging them over previous iteration steps and applying boundary conditions at $z = L$. Next, using Equations 21.72, 21.73, and 21.80, backward propagation is simulated and s_-, φ_-, and A_-^m are determined, and subsequently adjusted by averaging their values over k previous iteration steps. The total photon density in the active region, S_Σ, and the rate of stimulated emission, R_{st}, are found from Equations 21.81 and 21.82, respectively, which gives the basis for determining carrier density distribution using Equation 21.71. After adjusting n by averaging it over previous iteration steps, all parameters dependent on carrier density can be calculated. Finally, at the end of the iteration step, the maximum relative error between two consecutive iteration steps is calculated using Equation 21.87 and compared with the tolerance δ_{max}. If the tolerance is satisfied, the iteration process has successfully converged to the solution; otherwise the iteration process continues. The algorithm described for SCNM is summarized in Figure 21.10.

When the iteration process successfully converges to the steady-state solution, normalized filtering function of the cavity $T_m(\hbar\omega)$ can be found from Equation 21.38, and the ASE noise spectral photon

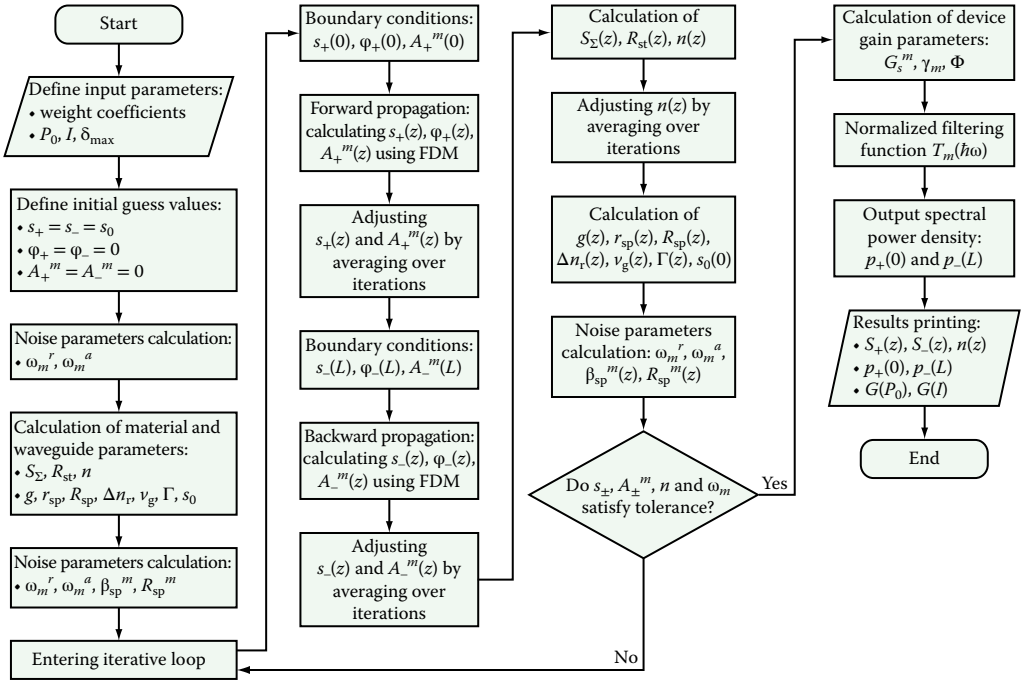

FIGURE 21.10 Flowchart of the steady-state wideband self-consistent numerical method (SCNM). FDM, finite difference method.

densities determined using

$$a_+(L,\hbar\omega) = \sum_{m=1}^{M}\left[\left(\hbar\omega_{m+l+1}^{a} - \hbar\omega_{m-l}^{a}\right)^{-1} A_+^m(L)\, T_m(\hbar\omega)\right], \tag{21.89}$$

$$a_-(0,\hbar\omega) = \sum_{m=1}^{M}\left[\left(\hbar\omega_{m+l+1}^{a} - \hbar\omega_{m-l}^{a}\right)^{-1} A_-^m(0)\, T_m(\hbar\omega)\right]. \tag{21.90}$$

Finally, the output spectral power densities of signal and noise combined are calculated as

$$p_+(L,\hbar\omega) = \left[1 - R_2(\hbar\omega)\right]\left[s_+(L,\hbar\omega) + a_+(L,\hbar\omega)\right] v_g(\hbar\omega)\, WH\hbar\omega \Big/ \Gamma(\hbar\omega), \tag{21.91}$$

$$p_-(0,\hbar\omega) = \left[1 - R_1(\hbar\omega)\right]\left[s_-(0,\hbar\omega) + a_-(0,\hbar\omega)\right] v_g(\hbar\omega)\, WH\hbar\omega \Big/ \Gamma(\hbar\omega), \tag{21.92}$$

where the signal spectral distribution is calculated using Equations 21.84 and 21.85, whereas the noise spectral distribution is determined from Equations 21.89 and 21.90. It should be noted that, if reflectivities of both facets are chosen to be zero, which is an idealized case of TW-SOA, the previous algorithm can be simplified. After determining and adjusting the forward-propagating variables, the following step, related to backward propagation, can be reduced to calculation and adjusting of only A_-^m since the backward-propagating signal will not exist.

One of the most valuable figures of merit for SOA characterization is the device (transmission) gain G. Strictly speaking, it is defined as the ratio of the signal's output and input photon density, or their corresponding powers, i.e., $G = 10\log_{10}(P_{out}/P_0)$. However, as the signal output photon density cannot be separated from ASE noise in the signal's wavelength range, the output photon density usually includes a small fraction of ASE, which has a negligible effect on G, as long as the input optical power P_0 is sufficiently high (above −40 dBm). For TW-SOA, the output photon density is recorded at the rear facet ($z = L$), $P_{out} = \int p_+(L,\hbar\omega)\mathrm{d}(\hbar\omega)$,

whereas for the R-SOA, at the front facet ($z = 0$), $P_{out} = \int p_{-}(0, \hbar\omega)\mathrm{d}(\hbar\omega)$. For FP-SOA, either facet can be regarded as the output one, depending on system configuration. In the case when the SOA model bundles up signal and the whole ASE noise spectrum into one quantity, the above definition of device gain G is meaningful for somewhat larger input powers, which can be recognized by the relatively flat dependence of G versus P_0. For insufficient input powers P_0, the device gain tends to increase more rapidly as the input optical power decreases, ultimately reaching the infinite value for the zero-input signal.

21.5.3.2 Results and Discussion

Based on the wideband self-consistent numerical model presented in earlier section, a full analysis of TW- and R-SOA is carried out under the steady-state operation regime. The list of parameters used in the analysis is given in Table 21.3. The remaining parameters, which are both carrier and energy dependent, including g, r_{sp}, Δn_r, Γ, v_g, and β_{sp}, are determined using the models presented in Section 21.3 and are given in Figures 21.2 and 21.4. Both bulk and MQW-based active regions are optimized to be polarization insensitive, as shown in Figure 21.3, so only TE polarization is analyzed.

21.5.3.2.1 Steady-State Signal and Carrier Densities Spatial Distribution

Figures 21.11 and 21.12 show spatial distribution of carrier densities, $n(z)$, and photon densities of forward and backward-propagating signal and ASE noise combined, $\int[s_{+}(z, \hbar\omega) + a_{+}(z, \hbar\omega)]\mathrm{d}(\hbar\omega)$, and $\int[s_{-}(z, \hbar\omega) + a_{-}(z, \hbar\omega)]\mathrm{d}(\hbar\omega)$, respectively, for different input optical powers P_0. In Figure 21.11, the distributions are shown for the active region based on the unstrained bulk $In_{0.53}Ga_{0.47}As$, with the parameters listed in Table 21.1, whereas in Figure 21.12, the results are given for MQW consisting of six coupled 0.13% tensile-strained $In_{0.516}Ga_{0.484}As$ quantum wells, which are strain-compensated by the $In_{0.9}Ga_{0.1}As_{0.3}P_{0.7}$ 0.26% compressively strained barriers, with the parameters given in Table 21.2. In both active region types, carrier dynamics is treated using Equation 21.71. Although this is a somewhat simplified model for MQW SOA, its usage is justified when the volumes of the well and barrier regions do not differ significantly. Namely, the carrier recombination time in the barrier, τ_b, figuring in the full system of carrier rate equations describing MQW active region, Equations 21.54 and 21.55, is of the order of nanoseconds, unlike the capture time by the wells τ_{bw}, which has the value between 25 and 55 ps (Keating et al., 1999). On the other hand, it has been shown by Tsai et al. (1995) that the escape time from the wells, τ_{wb}, is one to two orders of magnitude higher in comparison with τ_{bw}. Assuming that the volumes of the well and barrier regions, V_w and V_b, respectively, are similar, the most significant contribution to $\mathrm{d}n_b/\mathrm{d}t$ comes from the first and the third terms on the RHS of Equation 21.54, whereas the second and fourth terms can be neglected. In

TABLE 21.3 SOA Material and Geometric Parameters

Symbol	Quantity	Value
W	Active region width	2 μm
H	Bulk active region height	140 nm
L_w	MQW well thickness	19 nm
L_b	MQW barrier thickness	10 nm
H	MQW active region height for six QWs	114 nm
L	Active region length	600 μm
K_0	Carrier independent loss coefficient	62 cm^{-1}
K_1	Carrier dependent loss coefficient	7.5×10^{-17} cm^2
A	Shockley–Read–Hall coefficient	$1.1 \times 10^{8}\mathrm{s}^{-1}$
C	Auger coefficient	5.82×10^{-29} cm^6/s
ε	Nonlinear gain suppression factor	1.5×10^{-17} cm^3
$\hbar\omega_0$	Signal central energy	0.8 eV
R_1	Antireflective facet power reflectivity	5×10^{-5}

SOA, semiconductor optical amplifier; MQW, multiple quantum well.

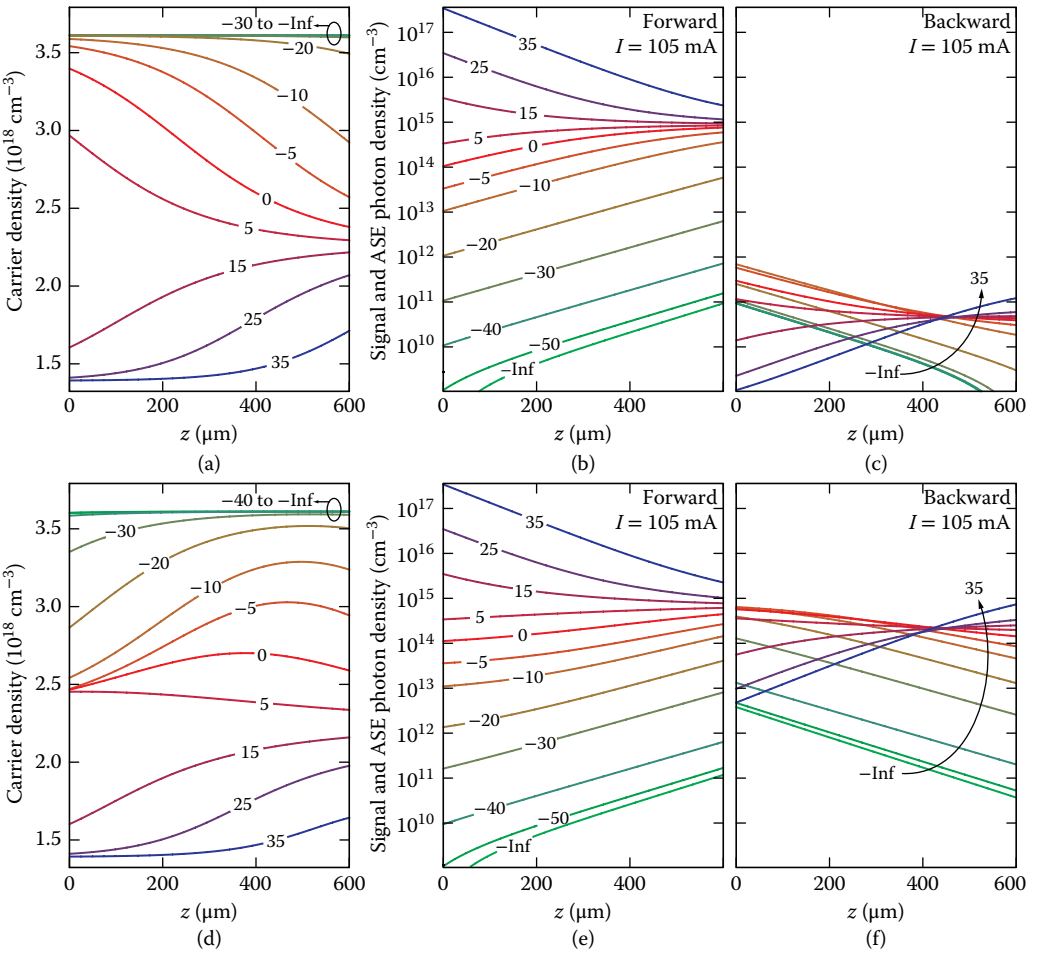

FIGURE 21.11 Spatial distribution of (a), (d) carrier density, and total photon density (signal and amplified spontaneous emission [ASE]) for (b), (e) forward, and (c), (f) backward propagation for different input signal optical powers (given in dBm) in the case of (a) through (c) traveling-wave semiconductor optical amplifier (TW-SOA), and (d) through (f) reflective (R)-SOA, both with the active region based on the unstrained bulk material.

this manner, the generation term $\eta_{inj} I/(qV_b)$ directly influences the carrier density in the barrier states, n_b, which is further reflected in the first term of Equation 21.55. This effect becomes even more pronounced if the capture time is short and the steady-state value of n_b is quickly reached.

It can be seen that for low input optical powers, up to −30 dBm, the carrier density has values close to the maximum allowed by the available bias current, n_{max}, due to the low consumption by vague optical signals. As P_0 increases, it dumps the carrier density overall and leads to its nonuniform spatial distribution caused by the intensified consumption of carriers. For both SOA types, forward-propagating photon densities have similar values and spatial distributions, as shown in Figure 21.11b and e. The signals are exponentially amplified for low to moderate input optical powers, up to 5 dBm. A further increase of P_0 leads to significant carrier depletion close to the front facet, Figure 21.11a and d, and consequently exponential signal attenuation. The backward-propagating photon densities, Figure 21.11c and f, are orders of magnitude lower for TW-SOA than for R-SOA, which is expected due to very low residual reflectivity of the rear facet. However, spatial distributions are qualitatively similar, and resemble the reversed forward-propagating ones, exponentially amplified for low P_0, and attenuated as P_0 increases. The existence of strong backward-propagating signal in the case of R-SOA leads to a different distribution of $n(z)$

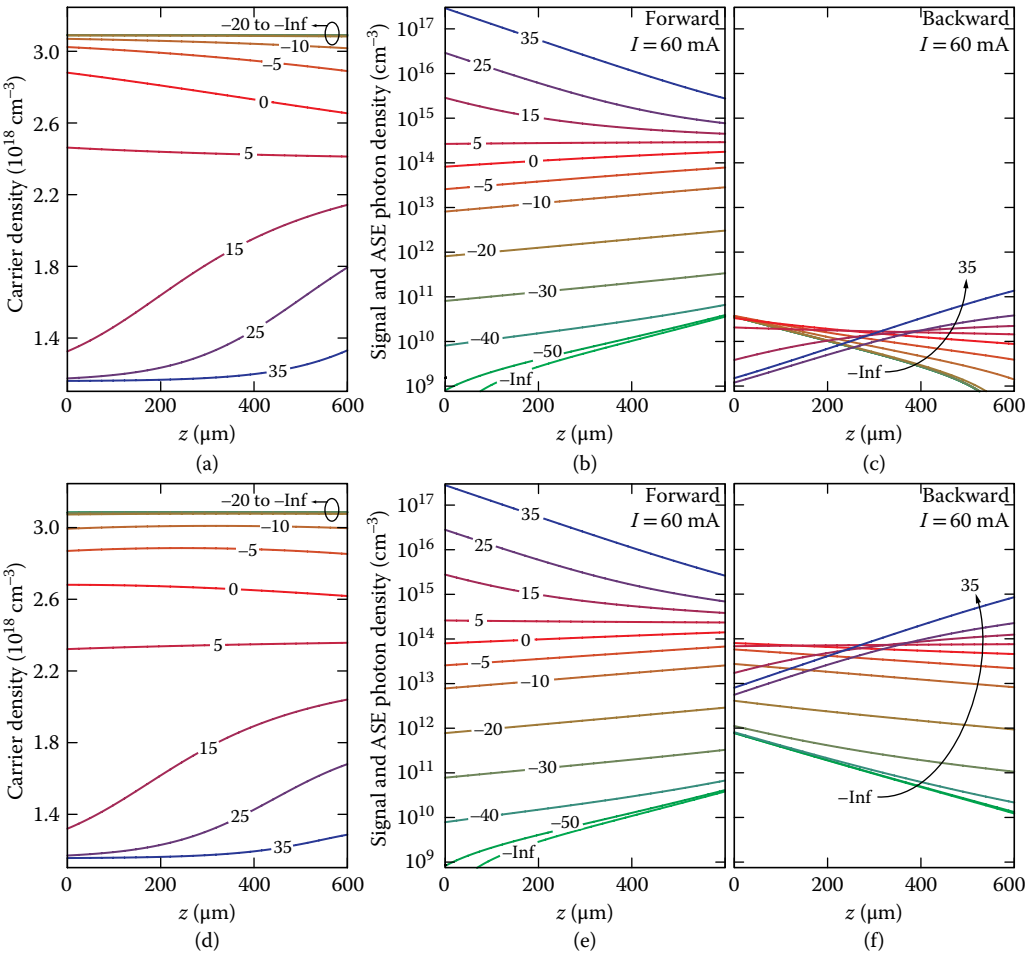

FIGURE 21.12 Spatial distribution of (a, d) carrier density, and total photon density (signal and amplified spontaneous emission [ASE]) for (b, e) forward and (c, f) backward propagation for different input signal optical powers (given in dBm) in the case of (a) through (c) traveling-wave semiconductor optical amplifier (TW-SOA), and (d) through (f) reflective (R)-SOA, both with the active region based on the tensile-strained quantum wells, which are strain-compensated by the compressively strained barriers.

for moderate P_0, between −20 and 5 dBm, in comparison to TW-SOA. The carrier density is more severely depleted closer to the front facet, by the amplified $S\_(z)$, as shown in Figure 21.11d, and has a maximum close to the rear facet, caused by the interplay of the counterpropagating signals.

Spatial distributions of carrier and photon densities for MQW-based SOAs, as shown in Figure 21.12, resemble the ones shown for bulk SOAs, as shown in Figure 21.11, and same qualitative analysis can be applied. The main difference comes from lower carrier density, and material gain, due to the polarization-insensitive design and lower bias current. This leads to the more uniform carrier spatial distribution, as shown in Figure 21.12c and d, and somewhat lower device gain, which can be inferred from the values of the output photon densities, at $z = L$ for TW-SOA, and $z = 0$ for R-SOA.

21.5.3.2.2 Steady-State Device Gain

One of the most valuable figures-of-merit for SOA is its steady-state device (transmission) gain. As defined in earlier section, it is the ratio of the output and input optical powers, or photon densities. Figures 21.13 and 21.14 show the dependence of device gain on operating conditions, i.e., bias current I, and input optical power P_0, for bulk, and MQW active region types, respectively, for both TW- and R-SOA.

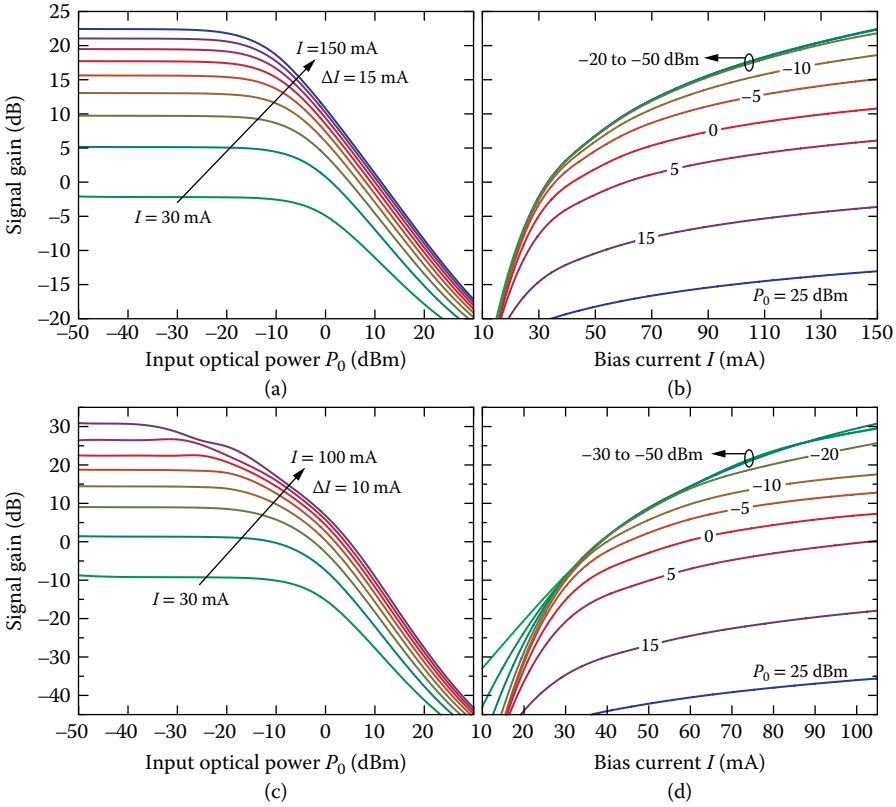

FIGURE 21.13 Device (transmission) gain for bulk active region versus (a), (c) input optical power, and (b), (d) bias current, for (a), (b) traveling-wave semiconductor optical amplifier (TW-SOA), and (c), (d) reflective (R)-SOA.

Figure 21.13 shows that the increase in bias current leads to the higher gain in both SOA types since more carriers are available to provide signal amplification, whereas the increase in P_0 leads to the gain decrease due to excessive carrier consumption. For low to moderate P_0, up to approximately −10 dBm, the device gain does not change significantly with input power and is limited by the length of the active region that is responsible for amplification. Additionally, R-SOA exhibits higher gain, Figure 21.13c and d in comparison with TW-SOA, Figure 21.13a and b, for bias currents beyond 50 mA. In contrast, for the currents below 50 mA, the gain is lower in R-SOA compared with TW-SOA. This comes from double signal propagation through the active region in the case of R-SOA, which emphasizes either amplification, when carrier density is high, or attenuation, when n is low. The maximum operating current of SOA is limited either by maximum bias current density, which provides long-term stable operation, or by the threshold for stimulated emission. In the latter case, the threshold material gain g_{th} can be determined from (Coldren et al., 2012)

$$\Gamma g_{th} - \left(K_0 + \Gamma K_1 n_{th}\right) = \frac{1}{2L} \ln \frac{1}{R_1 R_2}. \tag{21.93}$$

Having the value for g_{th}, it is possible to determine n_{th}, and using Equation 21.71, the corresponding threshold current value. Since the product of the two reflectivities is higher for R-SOA than for TW-SOA, the g_{th} will be lower, and, therefore, the current threshold value will also be lower.

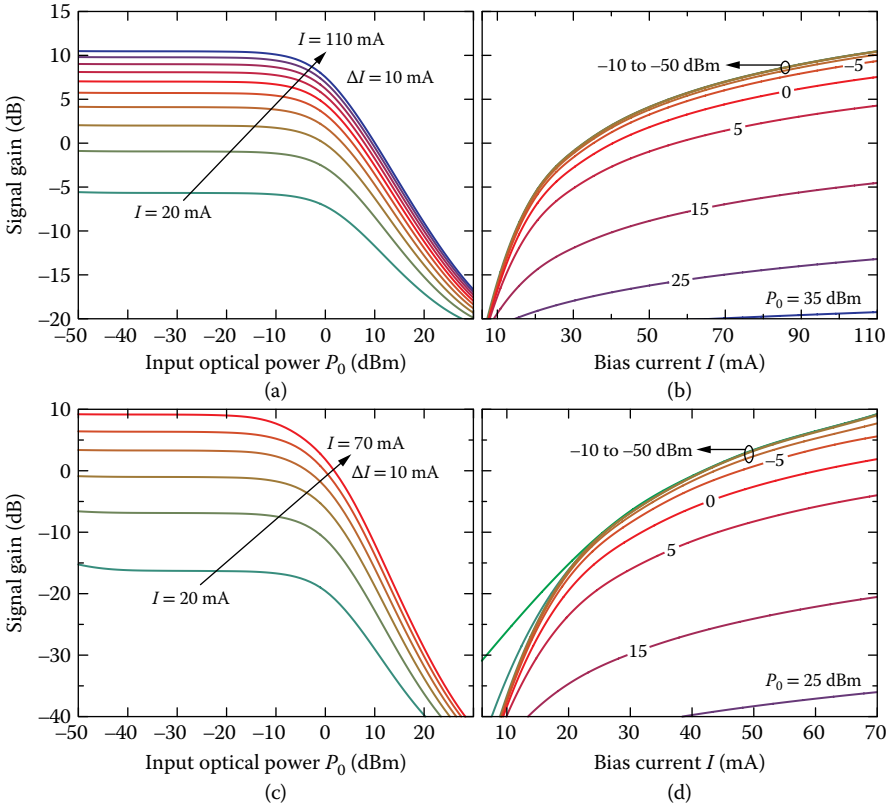

FIGURE 21.14 Device (transmission) gain for the multiple quantum well (MQW) active region versus (a), (c) input optical power, and (b), (d) bias current, for (a), (b) traveling-wave semiconductor optical amplifier (TW-SOA), and (c), (d) reflective (R)-SOA.

An interesting feature in the R-SOA's gain dependence on input optical power can be observed for high bias currents, as shown in Figure 21.13c. As the saturation regime of operation approaches, when the gain begins to decrease, an overshoot in device gain is visible. This effect has already been reported (Schrenk, 2011; Totović et al., 2013) and can be explained by the trade-off between a sudden decrease in the spontaneous emission and ASE with the decrease of carrier density and the corresponding relatively slow decrease in the material gain at the signal wavelength (Totović et al., 2013).

Figure 21.14 shows that MQW SOA provides somewhat lower gain in comparison with bulk, for the same operating conditions. This can be attributed to the lower modal gain, coming from lower confinement factor at the signal central frequency, as shown in Figure 21.4, which is a consequence of the polarization-insensitive design. Nevertheless, qualitatively, the two active regions give similar results, where the device gain increases with bias current increase. For low input optical powers, gain does not vary with P_0, and as the input optical power increases and carrier consumption becomes prominent, the device enters the saturation regime, and gain begins to decrease.

21.5.4 Case Study: Steady-State Semianalytical Model

When simulation time and computational resources are the priority, another approach can be used in SOA analysis. The main underlying idea of the semianalytical approach is to harvest the insightfulness of analytical methods and the versatility of numerical methods to reach a fast and computationally efficient model.

It essentially relies on carefully chosen approximations that can reduce the model complexity but still keep the accuracy at as high a level as possible. Since the carrier density usually does not vary significantly across the active region, it is common practice to model it as a constant, or a piecewise constant function. This approximation is extensively used in TMM, and, as previously discussed, presents the basis for many different SOA models. Choosing a fixed value for $n(z)$ simplifies TW equations to the point where an analytical solution can be found, either in closed form, e.g., Equation 21.64, or in the form of a transcendental equation. The carrier density's spatial distribution can also be approximated by a linear function, but this approach may give an analytical solution for photon densities only when nonlinear gain suppression is neglected (Totović et al., 2014).

Unlike carrier density, signal and noise photon densities can vary up to several orders of magnitude during the propagation from one SOA facet to the other. This implies that small variations in n can build up to significant changes in signal and noise, and special attention is required in selecting the adequate carrier density value. For example, choosing the value at the front or rear facet, $n_0 = n(z = 0)$ or $n_L = n(z = L)$, respectively, can significantly over- or underestimate material gain and spontaneous emission rate and lead to noticeable error in the output photon density, and, consequently, device gain. In order to alleviate this discrepancy, an average value of these two carrier densities can be chosen, $\bar{n} = (n_0 + n_L)/2$, and thus the error caused by neglecting the spatial dependence of n can be partially compensated.

The requirements for increased model efficiency can be met by yet another model approximation, where the signal and noise spectral dependences are neglected and the total spontaneous emission and signal are assigned to a single wavelength corresponding to signal peak, providing model analysis in terms of photon densities rather than spectral photon densities. Since no spectral analysis is present, TW equations written with respect to signal and noise can be wrapped up into a single equation that accounts for both spontaneous and stimulated emission of photons. This equation can be derived as a sum of Equations 21.72 and 21.74, integrated over the whole spectrum, resulting in

$$\pm\frac{\mathrm{d}S_{\pm}}{\mathrm{d}z} = \left[\frac{\Gamma g}{1+\varepsilon\left(S_{+}+S_{-}\right)} - \alpha_{\mathrm{i}}\right] S_{\pm} + \frac{1}{2v_{\mathrm{g}}}\Gamma\beta_{\mathrm{sp}}R_{\mathrm{sp}}, \tag{21.94}$$

where $S_{\pm}$ now stands for the photon density of the signal and noise combined, at the signal central frequency ω_0. All parameters that are dependent on carrier density and photon energy in Equation 21.94, namely, $\Gamma, g, \alpha_{\mathrm{i}}, v_{\mathrm{g}}$, and β_{sp}, are now replaced with the corresponding numerical dependencies on n, interpolated from the full spectral and carrier dependent model presented in Figures 21.2 and 21.4, for the energy of $\hbar\omega_0$. Additionally, for parameters that do not vary significantly with n, i.e., $\Gamma, \alpha_{\mathrm{i}}, v_{\mathrm{g}}$, and β_{sp}, as shown in Figure 21.4, a fixed value can be used, interpolated for an average carrier density, n_{av}, between the transparency, n_{tr}, and maximum allowed value, n_{max}, given by Equation 21.88. The carrier density at transparency will depend only on material gain, and not on operating conditions, whereas the maximum allowed value for carrier density n_{max} will depend on the value of bias current. In order to choose the adequate value of n_{av} for parameter interpolation, it is useful to determine n_{max} for maximum allowed bias current I_{max}. The value of I_{max} can be calculated as $I_{\mathrm{max}} = J_{\mathrm{max}}WL$, for a cross-section area defined by the active region's width W and length L, given in Table 21.3, where J_{max} is the maximum allowed bias current density for the long-term stable operation, which is in the range of 25–35 kA/cm^2. Under the listed conditions, the chosen values for bulk and MQW-SOA are $n_{\mathrm{av}} = 2.5 \times 10^{18}$ cm^{-3} and $n_{\mathrm{av}} = 2.1 \times 10^{18}$ cm^{-3}, respectively. The interpolated values of $\Gamma, v_{\mathrm{g}}, \beta_{\mathrm{sp}}$, and additional parameters are listed in Table 21.4 for bulk and MQW at the signal central energy of $\hbar\omega_0 = 0.8$ eV.

If a simpler model is used, particularly if an analytical solution is sought, it proves to be impractical to use numerical dependencies of g and R_{sp} on n (Figure 21.2). Rather, numerical results can be fitted to analytical functions, which further simplifies calculation. The most common choice for $g(n)$ dependence is a linear one, $g(n) = \alpha(n - n_{\mathrm{tr}})$, where α is the differential gain (Thylén, 1988; Shtaif et al., 1998; Mørk et al., 1999). This approximation is justified if the bias current is low enough to prevent a significant increase in carrier

TABLE 21.4 Interpolated Parameter Values for Bulk and Multiple Quantum Well (MQW) Active Region at the Signal Central Energy $\hbar\omega_0 = 0.8$ eV and for the Average Carrier Density of $n_{av} = 2.5 \times 10^{18}$ cm^{-3} for Bulk and $n_{av} = 2.1 \times 10^{18}$ cm^{-3} for MQW

Symbol	Quantity	Bulk	MQW
Γ	Optical confinement factor	30.44%	21.62%
v_g	Group velocity	7.76×10^7 m/s	8.73×10^7 m/s
k_0	Wave vector	4.05×10^6 m^{-1}	4.05×10^6 m^{-1}
n_r	Index of refraction	3.660	3.597
Δn_r	Variation of index of refraction	0.071	7.44×10^{-4}
$n_{eff,0}$	Effective index of refraction for zero carrier density	3.405	3.291
n_{eff}	Effective index of refraction	3.490	3.291
β_0	Wave propagation constant for zero carrier density	1.38×10^7 m^{-1}	1.33×10^7 m^{-1}
R_2	Highly reflective facet power reflectivity	0.3258	0.3192
n_{sp}	Inversion factor	1.035	1.055
β_{sp}	Spontaneous emission coupling factor	1.842×10^{-5}	1.869×10^{-5}

All values given are for transverse electric (TE) polarization.

TABLE 21.5 Bulk and Multiple Quantum Well (MQW) Active Region Fitting Parameters at the Signal Central Energy $\hbar\omega_0 = 0.8$ eV for Material Gain and Spontaneous Emission Rate to the two-Parameter Logarithmic and Second-Degree Polynomial Function of Carrier Density, Respectively

Symbol	Quantity	Bulk	MQW
g_0	Material gain fitting parameter	742.182 cm^{-1}	669.205 cm^{-1}
n_{tr}	Carrier density at transparency	1.38×10^{18} cm^{-3}	1.15×10^{18} cm^{-3}
B_0	Spontaneous emission fitting parameter	-8.375×10^{25} cm^{-3}/s	-1.351×10^{26} cm^{-3}/s
B_1	Spontaneous emission fitting parameter	1.344×10^8 s^{-1}	1.975×10^8 s^{-1}
B_2	Spontaneous emission fitting parameter	2.790×10^{-11} cm^3/s	2.146×10^{-11} cm^3/s

density. However, a more suitable model relies on a two-parameter (g_0, n_{tr}) logarithmic dependence (Coldren et al., 2012), which provides gain saturation with carrier density increase, $g(n) = g_0 \ln(n/n_{tr})$, where g_0 is the material gain fitting parameter and n_{tr} is the carrier density at transparency. It should be noted that, although the two-parameter logarithmic gain does provide reasonably good results, for more linear-like dependencies of gain on carrier density, such as for bulk materials, another model may be employed, which includes a third parameter, n_s. This model, $g(n) = g_0 \ln[(n + n_s)/(n_{tr} + n_s)]$, prevents infinite gain value for zero carrier densities, and in the limiting case of $n_s \to 0$ reduces to the purely logarithmic model, whereas for $n_s \to \infty$ reduces to purely linear model (Coldren et al., 2012). The model used in this case study is a two-parameter logarithmic gain since it fits well on numeric results.

The radiative spontaneous recombination rate is usually modeled via the quadratic function (Chu and Ghafouri-Shiraz, 1994; Melo and Petermann, 2008). Although this function fits actual dependence quite well, a more detailed model would include a second-degree polynomial function, $R_{sp}(n) = B_0 + B_1 n + B_2 n^2$, where B_0, B_1, and B_2 are the spontaneous emission rate fitting parameters. Table 21.5 shows a list of fitting parameters at wavelength $\lambda = 1.55$ μm ($\hbar\omega_0 = 0.8$ eV), for active regions based on the unstrained bulk $In_{0.53}Ga_{0.47}As$, and the MQW consisting of six coupled 0.13% tensile-strained $In_{0.516}Ga_{0.484}As$ quantum wells, which are strain-compensated by the $In_{0.9}Ga_{0.1}As_{0.3}P_{0.7}$ 0.26% compressively strained barriers.

In a steady-state analysis, the input signal carries no information encoded in its amplitude or phase, so the phase equation may be omitted from the model, in attempting to reduce the model's complexity. This simplification is additionally supported by the fact that the carrier diffusion will wash out the spatial grating in the carrier density produced by the interference between two counterpropagating optical fields.

For all antireflective facets, residual reflectivity can be neglected and equated with zero. Since the noise power is usually several orders of magnitude lower than the signal power, zero reflectivity implies that in the case of TW-SOA, the signal can be assumed to travel only once through the active region in the forward direction. On the other hand, in the case of R-SOA, the signal will pass through the active region twice, forward and backward, as a consequence of reflection at the rear facet. In other words, no multiple reflections are present, and the cavity does not exhibit resonant behavior. The boundary conditions for the signal at the front and rear facets are $S_+(0) = S_0$ and $S_-(L) = R_2 S_+(L)$, respectively, where S_0 is the input signal photon density. Depending on the SOA type, reflectivity of the rear facet can have either some finite value, for R-SOA, or it can be zero, for TW-SOA, which essentially simplifies the boundary condition to $S_-(L) = 0$.

The steady-state carrier density rate equation can be derived from Equations 21.71, 21.75, and 21.76, under the previously listed assumptions:

$$\frac{I}{qV} - \left(An + R_{\text{sp}} + Cn^3\right) - \frac{v_g g\left(S_+ + S_-\right)}{1 + \varepsilon\left(S_+ + S_-\right)} = 0. \tag{21.95}$$

This equation can be used for R-SOA modeling as is, whereas in the case of TW-SOA, it can be simplified by neglecting the backward-propagating noise contribution and setting the photon density of the backward-propagating signal to zero ($S_- = 0$). The system of coupled equations given by Equations 21.94 and 21.95 cannot be solved analytically unless the approximation regarding the carrier density's spatial distribution is introduced. Different approximations require different analytical treatments and implementations, which are further discussed.

21.5.4.1 The Fundamentals of the Semianalytical Models

The starting point of semianalytical treatment is replacement of the carrier density spatial distribution with a fixed value, equal to the arithmetic mean of the carrier density values at the edges of the SOA structure, or the edges of its sections, namely, $n(z) = \bar{n} = (n_0 + n_L)/2$. These carrier densities are deduced by solving the carrier rate Equation 21.95, where photon density distributions are expressed as functions of the fixed carrier density $\bar{n}$. In other words, once the analytical dependence of $S_\pm(\bar{n}, z) = S_\pm(n_0, n_L, z)$ is determined, it can be substituted in Equation 21.95 at $z = 0$ and $z = L$, which results in a system of two coupled transcendental equations written with respect to n_0 and n_L. The difference between these two carrier density equations comes from the spontaneous emission term $R_{sp}(n)$ and material gain $g(n)$, which for $z = 0$ depend on n_0, and for $z = L$ depend on n_L. Solving these equations provides the numerical value of $\bar{n}$, which is then returned to $S_\pm(\bar{n}, z)$, and the output photon density can be evaluated.

The same method can be applied to an SOA section of length $\Delta z = L/p$, given in Figure 21.15, where p is the number of analyzed sections, and the method can be generalized to the piecewise constant carrier density spatial distribution. The advantage of this approach over the TMM is the choice of the kth section carrier density value, $\bar{n}_k$, as the mean value between the carrier densities at the section interfaces, $\bar{n}_k = (n_{k-1} + n_k)/2$. In this manner, a higher degree of accuracy is provided for a smaller number of sections, compared to the choice of carrier density at the edge of a section.

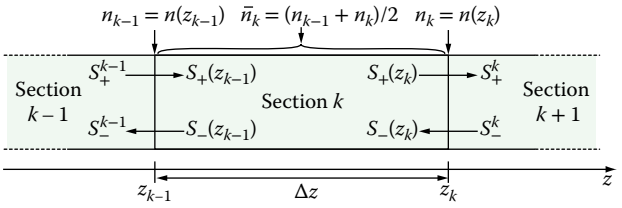

FIGURE 21.15 Schematic representation of the kth section in the segmented semiconductor optical amplifier structure with the relevant carrier and photon densities.

Assuming that the carrier density has a known, fixed value $\bar{n}_k$ at the kth section of an R-SOA, Equation 21.94 needs to be solved analytically for both propagation directions, with initial conditions imposed by the photon densities entering the kth section, which can be determined by solving Equation 21.94 at section $k-1$ for forward, and $k+1$ for backward propagation. However, the analytical solution of Equation 21.94 cannot be obtained for R-SOA without additional approximations, due to the nonlinear coupling of S_+ and S_-. In the case of TW-SOA, only the forward-propagating photon density S_+ is included in Equation 21.94, providing an analytical solution and the corresponding initial conditions for all sections along TW-SOA.

21.5.4.2 Approximate Solutions of Counterpropagating Photon Density Distributions and Implementation of the Semianalytical Algorithm

In order to derive the photon density spatial distributions, S_+ and S_-, corresponding to R-SOA, the system of Equation 21.94 needs to be decoupled, which can be done in two ways.

First, the nonlinear gain suppression can be neglected by setting $\varepsilon = 0$, which results in a linear decoupled system with respect to S_+ and S_-:

$$\pm\frac{dS_\pm}{dz} = \left(\Gamma g - \alpha_i\right) S_\pm + \frac{1}{2\nu_g}\Gamma\beta_{sp}R_{sp}. \tag{21.96}$$

This assumption greatly simplifies the system, and, for the bias currents and input optical powers that are not too high, it does not degrade the model accuracy significantly. The solution of Equation 21.96 for each section can be found in closed analytical form, corresponding to the matrix form (Equation 21.70) used in description of noise by TMM:

$$S_+^k = S_+^{k-1}G_k + \sigma_{sp}^k\left(G_k - 1\right)/\ln G_k, \tag{21.97}$$

$$S_-^{k-1} = S_-^k G_k + \sigma_{sp}^k\left(G_k - 1\right)/\ln G_k, \tag{21.98}$$

where $G_k = G(\bar{n}_k) = \exp\{[\Gamma g(\bar{n}_k) - \alpha_i(\bar{n}_k)]\Delta z\}$ is the single-pass gain of the kth section and $\sigma_{sp}^k = \sigma_{sp}(\bar{n}_k) = 1/(2\nu_g)\Gamma\beta_{sp}R_{sp}(\bar{n}_k)\Delta z$ is the single-pass generated spontaneous emission within the kth section. Due to the cascading nature of sections, the output photon density of the $(k-1)$th section, $S_+^{k-1} = S_+(z_{k-1})$, is the input photon density of the kth one for forward propagation, whereas for backward propagation, the output photon density of the $(k+1)$th section, $S_-^k = S_-(z_k)$, is the input photon density of the kth one, as shown in Figure 21.15. This chaining, along with the form of Equations 21.97 and 21.98, suggests that the photon densities at section interfaces are calculated by recursion. The base cases in a recursive method for forward and backward propagation are defined by the boundary conditions at the front ($k=1$) and rear ($k=p$) facets, respectively, $S_+^0 = S_0$ and $S_-^p = R_2 S_+^p$. The forward-propagating signal exiting the kth section will depend on carrier densities of all preceding sections, $S_+^k = S_+(z_k, \bar{n}_1, \ldots, \bar{n}_k) = S_+(z_k, n_0, \ldots, n_k)$, whereas the backward-propagating signal will depend on carrier densities in all sections, $S_-^k = S_-(z_k, \bar{n}_1, \ldots, \bar{n}_p) = S_-(z_k, n_0, \ldots, n_p)$, due to the imposed initial condition at the rear facet, which assumes reflection of $S_+(z_p, n_0, \ldots, n_p)$. These analytical expressions can now be returned to the carrier rate Equation 21.95 at each section interface located at z_k

$$f_k = 0 = \frac{I}{qV} - \left[An_k + R_{sp}\left(n_k\right) + Cn_k^3\right] - \nu_g g\left(n_k\right)\left[S_+\left(z_k, n_0, ..., n_k\right) + S_-\left(z_k, n_0, ..., n_p\right)\right], \tag{21.99}$$

which forms a system of $p+1$ transcendental equations, all of which are dependent on $p+1$ carrier densities, from n_0 to n_p. This system cannot be solved analytically, so a numerical procedure is required. An example of such a procedure, given by Totović et al. (2014), relies on numerically assisted elimination of variables, where, in an iterative approach, the range of carrier densities in which the solution n_k is expected to be found is narrowed simultaneously for all k from 0 to p. The initial range for carrier densities at all

interfaces is bounded by the carrier density at transparency, n_{tr}, and the maximum carrier density, n_{max}, limited by the available current (Equation 21.88). In each iteration step, the corresponding range of each n_k is reduced to one fifth of its previous size by the appropriate algorithm, still including the solution n_k. After a predefined number of iteration steps, the values for n_k can be determined by evaluating the RHS of the system (Equation 21.99) for the carrier densities in the narrowed ranges, giving a function $f_k(n)$, and subsequent interpolation of the function $f_k(n)$ in search for n_k which returns 0, i.e., the LHS value of Equation 21.99. Usually, four iteration steps suffice for the error coming from neglected gain suppression to prevail over the error coming from the iteration process. Having the values for carrier densities at all interfaces, it is possible to evaluate the photon densities at each z_k using Equations 21.97 and 21.98, and subsequently determine the device gain. Since this model treats the propagation of the signal and ASE noise combined through Equation 21.96, or more generally Equation 21.94, the device gain is defined as the ratio of the output signal power, along with the total ASE noise, and the input signal power. This definition implies that in the limiting case of zero input signal, the device gain will asymptotically approach infinity due to division by zero.

Another approach that can be used for the decoupling of Equation 21.94 with respect to $S_\pm(z,n)$ is to assume that the opposite-propagating photon density is spatially independent, i.e., $S_\mp(z,n) = S_\mp^{cst}(n)$. Unlike the carrier density, which varies modestly across the active region, photon density exhibits exponential increase or decrease from one section edge to the other, so a choice of geometric mean is a more suitable one, which gives $S_\mp^{cst,k}(n) = [S_\mp^{k-1}(n)S_\mp^k(n)]^{1/2}$. The term $1+\varepsilon(S_+ + S_-)$ in Equation 21.94, which is responsible for equation coupling, can now be replaced with $1+\varepsilon(S_\pm + S_\mp^{cst})$, or, more generally, with a sum of the spatially independent, and spatially dependent functions, $\theta_\pm + \varepsilon S_\pm$, where $\theta_\pm = 1 + \varepsilon S_\mp^{cst}$. In the case of TW-SOA, no backward-propagating signal exists and $\theta_\pm = 1$. Equation 21.94 now reads

$$\pm\frac{dS_\pm}{dz} = \left(\frac{\Gamma g}{\theta_\pm + \varepsilon S_\pm} - \alpha_i\right) S_\pm + \frac{1}{2\nu_g}\Gamma\beta_{sp}R_{sp}, \tag{21.100}$$

and its solution for the kth section can be found in the implicit form from the transcendental equation

$$2\alpha_i^k\Delta z = \left(\frac{1}{T_\pm^k} - 1\right)\ln\left|\frac{\theta_\pm^k + \varepsilon S_\pm^{out,k} - \left(1-T_\pm^k\right)/\mu_\pm^k}{\theta_\pm^k + \varepsilon S_\pm^{in,k} - \left(1-T_\pm^k\right)/\mu_\pm^k}\right| - \left(\frac{1}{T_\pm^k} + 1\right)\ln\left|\frac{\theta_\pm^k + \varepsilon S_\pm^{out,k} - \left(1+T_\pm^k\right)/\mu_\pm^k}{\theta_\pm^k + \varepsilon S_\pm^{in,k} - \left(1+T_\pm^k\right)/\mu_\pm^k}\right|, \tag{21.101}$$

where the auxiliary parameters $\mu_\pm^k$ and $T_\pm^k$ are defined as follows:

$$\mu_\pm^k = \frac{2\alpha_i^k}{\Gamma g_k + \alpha_i^k\theta_\pm^k + \varepsilon\Gamma\beta_{sp}R_{sp}^k\Big/\left(2\nu_g\right)}, \tag{21.102}$$

$$\left(T_\pm^k\right)^2 = 1 - \left(\mu_\pm^k\right)^2\Gamma g_k\theta_\pm^k\Big/\alpha_i^k. \tag{21.103}$$

In Equation 21.101, $S_\pm^{in,k}$ and $S_\pm^{out,k}$ denote the input and output photon densities into and from the kth section, respectively. For forward propagation, $S_+^{in,k} = S_+^{k-1}$ and $S_+^{out,k} = S_+^k$, whereas in the case of backward propagation, $S_-^{in,k} = S_-^k$ and $S_-^{out,k} = S_-^{k-1}$, according to Figure 21.15. Equation 21.101 is solved with respect to $S_\pm^{out,k}$ recursively, using the previously determined $S_\pm^{in,k}$, with the base cases in a recursive method defined by the boundary conditions in sections $k=1$ and $k=p$, for forward and backward propagation, respectively. Just as in the previous model, where the nonlinear gain suppression was neglected, the solutions of Equation 21.101 will depend either on carrier densities in all preceding sections for forward propagation, $S_+^{out,k} = S_+(z_k, \bar{n}_1, \ldots, \bar{n}_k) = S_+(z_k, n_0, \ldots, n_k)$, or on all carrier densities in the case of backward propagation, $S_-^{out,k} = S_-(z_{k-1}, \bar{n}_1, \ldots, \bar{n}_p) = S_-(z_{k-1}, n_0, \ldots, n_p)$. Substituting these dependencies

into the carrier rate Equation 21.95 at each section interface, z_k, gives the system of $p + 1$ transcendental equations:

$$f_k = 0 = \frac{I}{qV} - \left[An_k + R_{\text{sp}}\left(n_k\right) + Cn_k^3\right] - \frac{v_g g\left(n_k\right)\left[S_+\left(z_k, n_0, ..., n_k\right) + S_-\left(z_k, n_0, ..., n_p\right)\right]}{1 + \varepsilon\left[S_+\left(z_k, n_0, ..., n_k\right) + S_-\left(z_k, n_0, ..., n_p\right)\right]}. \quad (21.104)$$

Unlike the previous model, for $\varepsilon = 0$, where the photon density dependencies on n_k could be expressed in closed analytical form, the solutions are now given in implicit form (Equation 21.101), which essentially requires a numerical method. Moreover, in order to employ a numerical method, the values for carrier densities in all sections need to be known. This raises the need for a self-consistent numerical approach in solving the system given by Equations 21.101 and 21.104. The numerical method should comprise two distinct steps. First, the IGVs need to be generated for carrier and photon densities at all section interfaces, which is done using the model for $\varepsilon = 0$. Next, an iterative procedure is used, where carrier and photon densities are alternately calculated, and carrier densities are subsequently updated based on the values from the current and previous iteration steps until the predefined tolerance is satisfied. The maximum relative error between two consecutive iteration steps, δ, is calculated as the maximum relative error for all monitored variables, at all interfaces, i.e., $\delta = \max\{\delta(n_k), \delta(S_+^k), \delta(S_-^k)\}$, and the tolerance is chosen to be $\delta_{\max} = 10^{-6}$. The updating of n_k is done using a set of weight coefficients with a sum of unity for the current and previous iteration steps, $\{w_i, w_{i-1}\} = \{0.1, 0.9\}$. The weight coefficients are chosen such that they give balance between the stability and speed of convergence, and usually no more than 100 iteration steps are required for the procedure to reach a self-consistent solution. It should be noted that due to the nature of the algorithm, the system of equations given by Equation 21.104 is not coupled since $S_+(z_k, n_0, \ldots, n_k)$ and $S_-(z_k, n_0, \ldots, n_p)$ are calculated for the carrier values from the previous iteration step and can be treated as parameters. In other words, the current iteration variable n_k is included in Equation 21.104 through the spontaneous emission terms and material gain.

It has been shown by Totović et al. (2014) that depending on the number of chosen sections and the level of approximation, the semianalytical model can be up to two orders of magnitude faster in comparison to the numerical model based on SCNM. Meanwhile, the maximum absolute mismatch in the device gain calculated by the numerical and semianalytical models does not exceed 1.6 dB even for only one section, and neglected nonlinear gain suppression, whereas this mismatch drops to a maximum of 0.11 dB for three sections with included gain suppression for a bulk R-SOA.

21.5.5 Case Study: Dynamic Propagation Model

When the input signal carries information encoded either in its amplitude, or phase, or both, a dynamic approach in SOA modeling is required. The same model needs to be applied for modulation or remodulation purposes, when the bias current is time dependent. The most general dynamic model, suitable for both large- and small-signal modulation, includes spatiotemporal and spectral dependency of both forward- and backward-propagating signals and noise, given by Equations 21.50 through 21.52, and, depending on the active region type, one or several equations describing spatiotemporal carrier density distribution. For bulk SOA, carrier density evolution can be described by Equation 21.49, for the MQW active region by Equations 21.54 and 21.55, and for the QD-SOA by Equations 21.57 through 21.59. Due to the ampleness and complexity of three-dimensional (3D) mesh (time-space-spectrum) implementation in the numerical algorithms, whenever the input signal is spectrally narrow, it is common practice to simplify the model and perform the analysis for photon densities and not their spectral distributions. Similar to Section 21.5.4, material gain and spontaneous emission rate can be approximated with the two-parameter logarithmic and second-order polynomial function, respectively, $g(n) = g_0 \ln(n/n_{\text{tr}})$ and $R_{\text{sp}}(n) = B_0 + B_1 n + B_2 n^2$, where the fitting parameters are given in Table 21.5 for the bulk and MQW active region, at the signal central

wavelength of 1.55 μm. All other parameters, which are dependent on photon energy and carrier density, can be approximated by the corresponding fixed values given in Table 21.4, interpolated for the photon energy of $\hbar\omega_0 = 0.8$ eV and an average carrier density n_{av}, which depends on the active region type. Under these assumptions, the signal can be described by the equation similar to Equation 21.23, with the addition of nonlinear gain suppression:

$$\pm\frac{\partial S_\pm}{\partial z} + \frac{1}{v_g}\frac{\partial S_\pm}{\partial t} = \left(\frac{\Gamma g}{1+\varepsilon S_\Sigma} - \alpha_i\right) S_\pm. \tag{21.105}$$

The phase evolution for both propagating directions is given by Equation 21.51:

$$\pm\frac{\partial \varphi_\pm}{\partial z} + \frac{1}{v_g}\frac{\partial \varphi_\pm}{\partial t} = \frac{k_0 \Gamma \Delta n_r}{1+\varepsilon S_\Sigma}. \tag{21.106}$$

ASE noise is treated with a separate equation, resembling Equation 21.105, with the addition of the spontaneous emission rate contribution:

$$\pm\frac{\partial A_\pm}{\partial z} + \frac{1}{v_g}\frac{\partial A_\pm}{\partial t} = \left(\frac{\Gamma g}{1+\varepsilon S_\Sigma} - \alpha_i\right) A_\pm + \frac{1}{2v_g}\Gamma\beta_{sp}R_{sp}. \tag{21.107}$$

It should be noted that by using Equation 21.107, spectral dependence of ASE is neglected and all noise photons are treated at the single frequency. Boundary conditions are defined by the input signal, described by its photon density $S_0(t)$ and phase $\varphi_0(t)$, and front and rear facet reflectivities, R_1 and R_2, respectively. For antireflective facets, zero reflectivity can be assumed, whereas for the highly reflective ones, the reflectivity coefficient can be calculated as $R_2 = (n_r - 1)^2/(n_r + 1)^2$, if no reflective layer is placed. At the front facet, which is antireflective, the boundary conditions read $S_+(0) = S_0, \varphi_+(0) = \varphi_0, A_+(0) = 0$, and for the rear facet, which can be either highly- or antireflective, $S_-(L) = R_2 S_+(L), \varphi_-(L) = \varphi_+(L) + \pi$, and $A_-(L) = R_2 A_+(L)$. In the case of TW-SOA, rear facet reflectivity R_2 will be zero, and no backward-propagating signal will exist. However, since the noise is generated within the SOA, with equal probability of photon traveling in any direction, backward-propagating noise will exist, both for TW- and R-SOA.

Carrier density distribution is described by Equation 21.49, where the current I can be time dependent:

$$\frac{dn}{dt} = \frac{I}{qV} - \left(An + R_{sp} + Cn^3\right) - \frac{v_g g S_\Sigma}{1+\varepsilon S_\Sigma}. \tag{21.108}$$

In Equations 21.105 through 21.108, S_Σ stands for the total photon density in the SOA's active region, including both signal and noise, $S_\Sigma = S_+ + S_- + A_+ + A_-$.

The system given by Equations 21.105 through 21.108 cannot be analytically solved, and several numerical approaches are described in Section 21.5.2. Although TMM is widely used due to its simplicity, coarse segmentation along the longitudinal axis might lead to an error in calculating the photon density distribution. Moreover, this error can be accumulated during matrix multiplication and can be even more pronounced when two counterpropagating signals exist.

21.5.5.1 Upwind Scheme Numerical Implementation

In order to mitigate potential errors, a first-order upwind scheme numerical method based on FDM can be developed, where the space and time axis are treated as quasi-continuous through fine segmentation. After choosing the number of points along the longitudinal axis, P, which define the section length, $\Delta z = L/(P-1)$, segmentation of the temporal axis is done, such that $\Delta t \leq \Delta z/v_g$, according to the Courant–Friedrichs–Lewy stability condition. Depending on the length of the analyzed time interval, T, the number

of points along the temporal axis is determined as $Q = \lceil T/\Delta t \rceil + 1$. All derivatives in Equations 21.105 through 21.108 are replaced with finite differences, such that for temporal derivatives forward differences are used:

$$\frac{\mathrm{d}f}{\mathrm{d}t} \approx \frac{f\left(t_{j+1}\right) - f\left(t_j\right)}{\Delta t}, \tag{21.109}$$

where f is any time-dependent variable, i.e., $S_{\pm}, \varphi_{\pm}, A_{\pm}, n$, and for spatial derivatives, the choice is made based on the propagation direction. For forward propagation

$$\frac{\mathrm{d}f_{+}}{\mathrm{d}z} \approx \frac{f_{+}\left(z_i\right) - f_{+}\left(z_{i-1}\right)}{\Delta z}, \tag{21.110}$$

where f_+ denotes any of the following variables S_+, φ_+, A_+, whereas for backward propagation

$$\frac{\mathrm{d}f_{-}}{\mathrm{d}z} \approx \frac{f_{-}\left(z_{i+1}\right) - f_{-}\left(z_i\right)}{\Delta z}, \tag{21.111}$$

where f_- denotes any of the following variables: S_-, φ_-, A_-. Using Equations 21.109 through 21.111, a set of coupled partial differential equations describing signal and noise propagation along the SOA, Equations 21.105 through 21.107, can be transformed into the set of coupled linear algebraic equations, for forward

$$f_{+}\left(z_i, t_{j+1}\right) = f_{+}\left(z_i, t_j\right) + \Delta t v_{\mathrm{g}}\left[F_{+}\left(z_i, t_j\right) - \frac{f_{+}\left(z_i, t_j\right) - f_{+}\left(z_{i-1}, t_j\right)}{\Delta z}\right], \tag{21.112}$$

and backward propagation

$$f_{-}\left(z_i, t_{j+1}\right) = f_{-}\left(z_i, t_j\right) + \Delta t v_{\mathrm{g}}\left[F_{-}\left(z_i, t_j\right) + \frac{f_{-}\left(z_{i+1}, t_j\right) - f_{-}\left(z_i, t_j\right)}{\Delta z}\right], \tag{21.113}$$

where $f_{\pm}$ stands for any variable $S_{\pm}, \varphi_{\pm}$, or $A_{\pm}$, whereas $F_{\pm}$ stands for the RHS of the corresponding equation evaluated at point (z_i, t_j) in the 2D spatiotemporal mesh. For carrier density equation, the transformation yields

$$n\left(z_i, t_{j+1}\right) = n\left(z_i, t_j\right) + \Delta t F\left(z_i, t_j\right), \tag{21.114}$$

where F stands for the RHS of Equation 21.108, evaluated at point (z_i, t_j) in the 2D spatiotemporal mesh. Forward differences for temporal derivatives enable calculation of all variables in the next point in time, t_{j+1}, based on the values from the current one t_j, as shown in Equations 21.112 through 21.114, and illustrated in Figure 21.16.

The numerical implementation of the discretized system (Equations 21.112 through 21.114) essentially requires two distinctive iteration processes: one for the temporal and another for spatial evolution. For every point j along the temporal axis, spatial distribution of carrier density for the next temporal point $(j + 1)$ is determined using Equation 21.114, which is followed by simulation of forward and subsequently

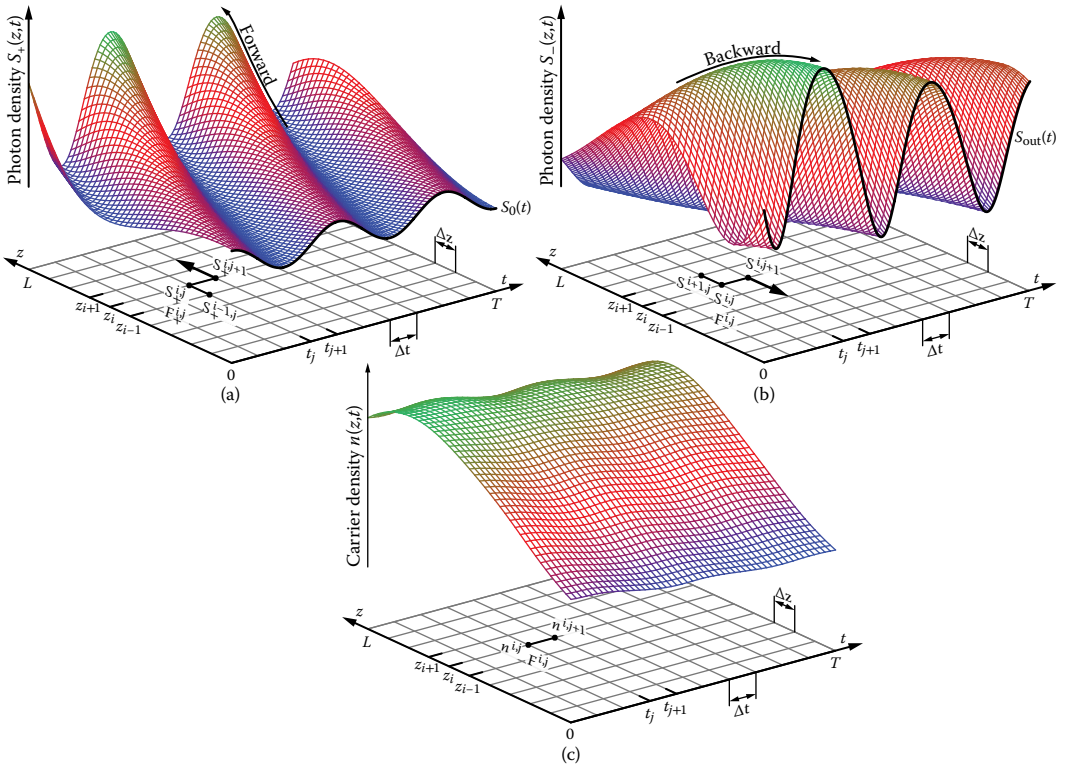

FIGURE 21.16 Illustration of two-dimensional (2D) spatiotemporal mesh with denoted relevant points for calculation of (a) forward- and (b) backward-propagating signal photon densities by upwind finite differences scheme, and (c) carrier densities by the forward finite differences method. The same upwind scheme can be applied to the phase, or noise photon density calculation. The example includes spatiotemporal distribution for (a) forward signal, (b) backward signal, and (c) carrier density.

backward propagation of signal and noise along the SOA's active region using Equations 21.112 and 21.113. This process is repeated until the end of the temporal axis is reached, incrementing j by one, up to Q. Since the results in the $(j+1)$th point in time are dependent on the values from the previous jth point, initial conditions for spatial distributions of all variables are required (for $j = 0$), in order to start the iteration process over time by calculating the values in the point $j = 1$. Initial values will depend on the assumed SOA state before the initialization of the simulation. If no input signal is present before $t = 0$, it can be assumed that both $S_{\pm}(z,0)$ and $\varphi_{\pm}(z,0)$ are zero. The noise will exist regardless of the signal's presence, so stationary distributions can be assumed for $A_{\pm}(z,0)$. Based on these values, using Equation 21.108, stationary distribution for carrier density can also be determined and associated with $n(z,0)$. Within the nested loop, for a fixed j, system (Equations 21.112 through 21.114) is solved for every point z_i, from 1 to P for forward-propagation, and P − 1 to 0 for backward propagation. The algorithm is summarized in the flowchart given in Figure 21.17.

21.5.6 Case Study: TMW Small-Signal Model

A very valuable figure-of-merit in using SOA for modulation purposes is its electro-optical (E/O) small-signal −3dB modulation bandwidth Ω_{3dB}. It is defined as the frequency of the modulation signal, i.e., electric current, for which the output SOA small signal, i.e., photon density or optical power, drops

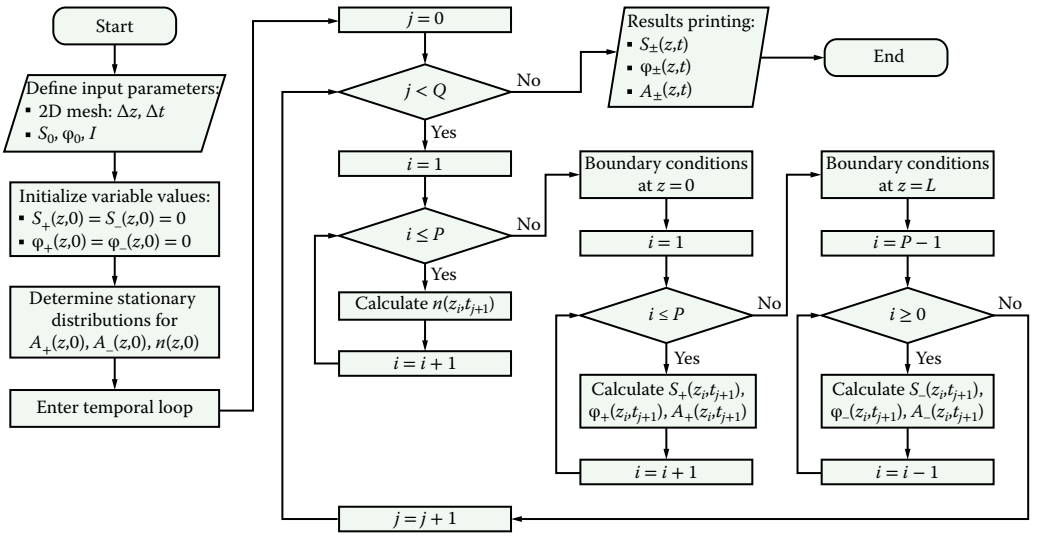

FIGURE 21.17 Flowchart of the upwind finite differences algorithm for the calculation of carrier and photon density spatiotemporal distributions, for both signal and noise.

to the half of its zero-frequency value. Knowing the influence of different structural and material parameters, as well as operating conditions, on Ω_{3dB}, provides the means for optimization of the modulation response and increasing the bandwidth. Under the assumption that the input signal is spectrally narrow, the analysis is based on photon densities for forward and backward propagation, which include both signal and noise. The TW equations have the form similar to Equation 21.105, with the addition of the term describing spontaneous emission, as in Equation 21.107:

$$\pm\frac{\partial S_{\pm}}{\partial z}+\frac{1}{v_g}\frac{\partial S_{\pm}}{\partial t}=\left(\frac{\Gamma g}{1+\varepsilon S_{\Sigma}}-\alpha_i\right)S_{\pm}+\frac{1}{2v_g}\Gamma\beta_{sp}R_{sp}, \tag{21.115}$$

where $S_{\Sigma}=S_{+}+S_{-}$. Since the intensity modulation is of interest, the analysis of the signal phase is not necessary. The carrier rate equation has the same form as Equation 21.108:

$$\frac{\mathrm{d}n}{\mathrm{d}t}=\frac{J}{qH}-\left(An+R_{sp}+Cn^3\right)-\frac{v_g g S_{\Sigma}}{1+\varepsilon S_{\Sigma}}, \tag{21.116}$$

where current density $J=I/(WL)$ is used instead of current I. This choice stems from the fact that modulation current I depends on device length, and the current density proves to be a more suitable parameter for benchmarking the performance of SOAs with different active region lengths. Generally, bias current density will consist of the stationary component and a small signal, which will, through Equation 21.116, lead to the carrier density modulation, and consequently to modulation of all carrier-dependent parameters, namely, g, R_{sp}, α_i, and $S_{\pm}$. From this point onward, all stationary values will be denoted by an overline, whereas all small-signals will be prefixed with Δ.

For the stationary value of bias current density, $\bar{J}$, all temporal derivatives will diminish from Equations 21.115 and 21.116, and the system will reduce to its steady-state form, given by Equations 21.94 and 21.95. In order to determine the steady-state values of $\bar{n}$ and $\bar{S}_{\pm}$, any of the previously discussed methods for steady-state analysis, given in Sections 21.5.1, 21.5.3, and 21.5.4, can be used. It is assumed that the CW input signal enters the device at the front facet, giving $S_{+}(z=0,t)=\bar{S}_{+}(z=0)=S_0$. The boundary

condition for the backward-propagating signal at the rear facet is given by $S_-(z = L, t) = R_2 S_+(z = L, t)$, where R_2 can have either a finite value, for R-SOA, or it can be zero, for TW-SOA.

The typical approach in small-signal analysis is to assume that the small-signal values are approximately lower by an order of magnitude or more, in comparison to the stationary values, and can be treated as perturbation. This assumption enables linearization of the system given by Equations 21.115 and 21.116 with respect to the small-signal quantities. As discussed in Section 21.4.3.5, bias current cannot instantaneously reach a uniform spatial distribution across the electrode and should be treated as a harmonic TMW with finite velocity, v_e. Moreover, due to reflection at the end of microstrip electrode, the microwave will propagate in both directions with respect to the longitudinal axis (Totović et al., 2015). This model becomes very important for the frequencies exceeding $v_e/(2\pi L)$, when an entire electric pulse is accommodated in the SOA's active region. A general model of the small-signal bias current density with sinusoidal waveform, defined by the spatially variable voltage across the electrode, can be written in the following form based on Equation 21.63:

$$\begin{aligned} J(z,t) &= \bar{J} + \Delta J(z) \exp(i\Omega t) \\ &= \bar{J} + \Delta J_{\mathrm{F}}(z) \exp\left[i\left(\Omega t - \beta_e z\right)\right] + \Delta J_{\mathrm{B}}(z) \exp\left[i\left(\Omega t + \beta_e z\right)\right], \end{aligned} \tag{21.117}$$

where $\Delta J(z)$ is the total small-signal bias current density spatial distribution, comprising both forward (F)- and backward (B)-propagating microwaves, $\Omega = 2\pi f$ is the angular frequency, with f being the frequency of the TMW, and β_e is the microwave propagation constant.

21.5.6.1 Derivation of the Small-Signal Model

Modulation of the bias current density leads to the modulation of carrier density n, and all carrier-dependent parameters, g, R_{sp}, α_i, and $S_\pm$, commonly denoted ξ, which will also have sinusoidal form

$$\begin{aligned} \xi(z,t) &= \bar{\xi}(z) + \Delta\xi(z) \exp(i\Omega t) \\ &= \bar{\xi}(z) + \Delta\xi_{\mathrm{F}}(z) \exp\left[i\left(\Omega t - \beta_e z\right)\right] + \Delta\xi_{\mathrm{B}}(z) \exp\left[i\left(\Omega t + \beta_e z\right)\right], \end{aligned} \tag{21.118}$$

where $\Delta\xi(z)$ is the total small-signal spatial distribution of the corresponding quantities. For known dependencies of material gain, and spontaneous emission rate, on carrier density, $g(n) = g_0 \ln(n/n_{tr})$, and $R_{sp}(n) = B_0 + B_1 n + B_2 n^2$, respectively, it is possible to express small-signal values of $\Delta g^{\mathrm{F/B}}$ and $\Delta R_{sp}^{\mathrm{F/B}}$ via $\Delta n^{\mathrm{F/B}}$ using the first derivatives of the corresponding functions, evaluated for the steady-state carrier density. This gives

$$\Delta g^{\mathrm{F/B}} = \left(\mathrm{d}g/\mathrm{d}n\right)\Big|_{n=\bar{n}} \Delta n^{\mathrm{F/B}} = \left(g_0/\bar{n}\right) \Delta n^{\mathrm{F/B}}, \tag{21.119}$$

$$\Delta R_{sp}^{\mathrm{F/B}} = \left(\mathrm{d}R_{sp}/\mathrm{d}n\right)\Big|_{n=\bar{n}} \Delta n^{\mathrm{F/B}} = \left(B_1 + 2B_2\bar{n}\right) \Delta n^{\mathrm{F/B}}. \tag{21.120}$$

Substituting Equations 21.117 through 21.120 into Equation 21.116, and separating the stationary, and small signals, gives a system comprising a steady-state rate equation, given by Equation 21.95, and small-signal equations for forward and backward TMW propagation. In order to linearize the small-signal equations, two approximations are required. The first one is related to the term describing the stimulated emission in Equation 21.116, namely, $v_g g S_\Sigma/(1 + \varepsilon S_\Sigma)$, which is nonlinear due to the presence of the small-signal photon densities both in numerator and denominator. The function

$$\left(1 + \varepsilon S_\Sigma\right)^{-1} = \left[1 + \varepsilon\bar{S}_\Sigma + \varepsilon\left(\Delta S_+^{\mathrm{F}} + \Delta S_-^{\mathrm{F}}\right) e^{i(\Omega t - \beta_e z)} + \varepsilon\left(\Delta S_+^{\mathrm{B}} + \Delta S_-^{\mathrm{B}}\right) e^{i(\Omega t + \beta_e z)}\right]^{-1} \tag{21.121}$$

can be rephrased as

$$\left(1+\varepsilon S_{\Sigma}\right)^{-1}=\frac{1}{1+\varepsilon\bar{S}_{\Sigma}}\left[1+\frac{\varepsilon\left(\Delta S_{+}^{\mathrm{F}}+\Delta S_{-}^{\mathrm{F}}\right)}{1+\varepsilon\bar{S}_{\Sigma}}e^{i(\Omega t-\beta_{e}z)}+\frac{\varepsilon\left(\Delta S_{+}^{\mathrm{B}}+\Delta S_{-}^{\mathrm{B}}\right)}{1+\varepsilon\bar{S}_{\Sigma}}e^{i(\Omega t+\beta_{e}z)}\right]^{-1}. \tag{21.122}$$

The second term in the product of the RHS of Equation 21.122 can be treated as $(1+x)^{-1}$, where $x \ll 1$, and therefore approximated with $1-x$, which leads to

$$\left(1+\varepsilon S_{\Sigma}\right)^{-1}\approx\frac{1}{1+\varepsilon\bar{S}_{\Sigma}}-\frac{\varepsilon\left(\Delta S_{+}^{\mathrm{F}}+\Delta S_{-}^{\mathrm{F}}\right)}{\left(1+\varepsilon\bar{S}_{\Sigma}\right)^{2}}e^{i(\Omega t-\beta_{e}z)}-\frac{\varepsilon\left(\Delta S_{+}^{\mathrm{B}}+\Delta S_{-}^{\mathrm{B}}\right)}{\left(1+\varepsilon\bar{S}_{\Sigma}\right)^{2}}e^{i(\Omega t+\beta_{e}z)}. \tag{21.123}$$

The following step in linearization is applying the first-order approximation, i.e., neglecting of all small-signal terms of the order higher than one. This gives the following system of small-signal rate equations for forward and backward TMW propagation

$$i\Omega\Delta n^{\mathrm{F/B}}=\frac{\Delta J^{\mathrm{F/B}}}{qH}-\left(A+B_{1}+2B_{2}\bar{n}+3C\bar{n}^{2}\right)\Delta n^{\mathrm{F/B}}-\left[\frac{g_{0}}{\bar{n}}\frac{v_{\mathrm{g}}\bar{S}_{\Sigma}}{1+\varepsilon\bar{S}_{\Sigma}}\Delta n^{\mathrm{F/B}}+v_{\mathrm{g}}\frac{g_{\mathrm{eff}}}{\Gamma}\left(\Delta S_{+}^{\mathrm{F/B}}+\Delta S_{-}^{\mathrm{F/B}}\right)\right], \tag{21.124}$$

where $g_{\mathrm{eff}}=\Gamma\bar{g}/(1+\varepsilon\bar{S}_{\Sigma})^{2}$. The previous system can be solved with respect to the small-signal carrier densities resulting from forward (F)- and backward (B)-propagating microwaves:

$$\Delta n^{\mathrm{F/B}}=\frac{\Delta J^{\mathrm{F/B}}\big/(qH)-v_{\mathrm{g}}g_{\mathrm{eff}}\left(\Delta S_{+}^{\mathrm{F/B}}+\Delta S_{-}^{\mathrm{F/B}}\right)\Big/\Gamma}{A+B_{1}+2B_{2}\bar{n}+3C\bar{n}^{2}+\dfrac{g_{0}}{\bar{n}}\dfrac{v_{\mathrm{g}}\bar{S}_{\Sigma}}{1+\varepsilon\bar{S}_{\Sigma}}+i\Omega}. \tag{21.125}$$

Substituting Equations 21.118 through 21.120 and Equation 21.125 into Equation 21.115, followed by the linearization process, leads to the system of two steady-state TW equations given by Equation 21.94, and four small-signal TW equations written with respect to the small-signal photon densities propagating in any of the two directions (denoted by subscript sign $\Delta S_{\pm}$) and resulting from any of the microwave propagation directions (denoted by the superscript $\Delta S^{\mathrm{F/B}}$):

$$\pm\frac{\mathrm{d}\Delta S_{\pm}^{\mathrm{F}}}{\mathrm{d}z}=\frac{\Gamma\gamma_{\pm}}{qHv_{\mathrm{g}}}\Delta J_{\mathrm{F}}-\left(\varepsilon\bar{S}_{\pm}+\gamma_{\pm}\right)g_{\mathrm{eff}}\Delta S_{\mp}^{\mathrm{F}}+\left[g_{\mathrm{eff}}\left(1+\varepsilon\bar{S}_{\mp}-\gamma_{\pm}\right)-\bar{\alpha}_{\mathrm{i}}-i\left(\frac{\Omega}{v_{\mathrm{g}}}\mp\beta_{\mathrm{e}}\right)\right]\Delta S_{\pm}^{\mathrm{F}}, \tag{21.126}$$

$$\pm\frac{\mathrm{d}\Delta S_{\pm}^{\mathrm{B}}}{\mathrm{d}z}=\frac{\Gamma\gamma_{\pm}}{qHv_{\mathrm{g}}}\Delta J_{\mathrm{B}}-\left(\varepsilon\bar{S}_{\pm}+\gamma_{\pm}\right)g_{\mathrm{eff}}\Delta S_{\mp}^{\mathrm{B}}+\left[g_{\mathrm{eff}}\left(1+\varepsilon\bar{S}_{\mp}-\gamma_{\pm}\right)-\bar{\alpha}_{\mathrm{i}}-i\left(\frac{\Omega}{v_{\mathrm{g}}}\pm\beta_{\mathrm{e}}\right)\right]\Delta S_{\pm}^{\mathrm{B}}, \tag{21.127}$$

where

$$\gamma_{\pm}=\frac{v_{\mathrm{g}}\left(\dfrac{g_{0}/\bar{n}}{1+\varepsilon\bar{S}_{\Sigma}}-K_{1}\right)\bar{S}_{\pm}+\dfrac{1}{2}\beta_{\mathrm{sp}}\left(B_{1}+2B_{2}\bar{n}\right)}{A+B_{1}+2B_{2}\bar{n}+3C\bar{n}^{2}+\dfrac{g_{0}}{\bar{n}}\dfrac{v_{\mathrm{g}}\bar{S}_{\Sigma}}{1+\varepsilon\bar{S}_{\Sigma}}+i\Omega}. \tag{21.128}$$

The γ-parameter is dimensionless, complex, and spatially and frequency dependent. It is responsible for frequency dependence of small-signal photon density distributions and their sensitivity to the frequency change for all other parameters fixed. In the case of zero frequency, $\gamma_{\pm}$ becomes purely real, whereas for high frequencies, such as the ones close to the modulation bandwidth and beyond, its imaginary part becomes dominant over the real one.

Since Equations 21.126 and 21.127 are derived from Equation 21.115, the boundary conditions for small-signal equations are inherited from the ones corresponding to Equation 21.115. The input signal is assumed to be CW, so $\Delta S_{+}^{F/B}(0) = 0$. At the rear facet, the boundary conditions are conditioned by the power reflectivity coefficient, $\Delta S_{-}^{F/B}(L) = R_2 \Delta S_{+}^{F/B}(L)$.

21.5.6.2 Numerical Implementation

In order to determine the −3dB bandwidth, $f_{3dB} = \Omega_{3dB}/(2\pi)$, it is necessary to calculate the output small-signal photon density for a range of modulation frequencies, $\Delta S_{out}(\Omega)$, and determine the one for which the condition $|\Delta S_{out}(\Omega_{3dB})/\Delta S_{out}(0)| = 1/2$ is satisfied. In the case of TW-SOA, the output signal will be recorded at the rear facet, $\Delta S_{out} = \Delta S_{+}(L) = \Delta S_{+}^{F}(L)\exp(-i\beta_e L) + \Delta S_{+}^{B}(L)\exp(i\beta_e L)$, whereas for R-SOA, at the front facet, $\Delta S_{out} = \Delta S_{-}(0) = \Delta S_{-}^{F}(0) + \Delta S_{-}^{B}(0)$. These signals can be found by solving the boundary value problem given by Equations 21.126 and 21.127. In the case of an R-SOA, this system comprises four coupled differential equations of the first order, with functional coefficients, and can be solved using any of the available numerical algorithms for boundary value problems, e.g., the FDM that implements the three-stage Lobatto IIIA formula (Hairer and Wanner, 1996). For a TW-SOA, backward-propagating signals can be neglected due to zero power reflectivity, and very low contribution of the spontaneous emission, so the system reduces to two noncoupled equations which can be solved with numerical integration.

Prior to solving system of Equations 21.126 and 21.127, it is necessary to calculate spatial distributions of the steady-state variables, $\bar{n}$ and $\bar{S}_{\pm}$, and auxiliary parameters, g_{eff} and $\gamma_{\pm}$. As previously discussed, steady-state values can be calculated by any of the models presented in earlier sections.

After the output small-signal variables are calculated, the −3dB bandwidth can be determined by interpolating the function $|\Delta S_{out}(\Omega)/\Delta S_{out}(0)|$ in search of the value Ω_{3dB} which gives 1/2 as a solution. For rare, special cases, Ω_{3dB} might be found in analytical form. In order to do this, usually a significant number of approximations is required, and the resulting analytical expression might be very complex (Antonelli et al., 2015), or the expression has a simpler form, but is valid under limited conditions.

21.5.6.3 Results and Discussion

Implementing the algorithm described in the previous pages provides the dependence of −3dB bandwidth, f_{3dB}, on the operating conditions, given in Figure 21.18.

The analysis is done for the microwave velocity of $v_e = 4.6\times10^7$ m/s (Tauber et al., 1994), and under the assumption that the load and characteristic impedances of the transmission line, Z_L and Z_C, respectively, are matched, which results in the microwave reflection coefficient $\Gamma_L = (Z_L - Z_C)/(Z_L + Z_C) = 0$. The small signal bias current density, ΔJ, is assumed to be equal to $0.1\bar{J}$.

Comparing the two SOA types, TW-SOA, Figure 21.18a and b, and R-SOA, Figure 21.18c and d, it can be concluded that, not only does the R-SOA provide higher bandwidths, but it does so for a much wider range of input optical powers. Both SOA types exhibit an increase in f_{3dB} with the increase of steady-state bias current density, but the behavior with P_0 variation differs significantly. In the case of TW-SOA, the bandwidth generally increases with the increase of P_0, reaching its maximum for deep saturation, and input optical powers between 20 and 25 dBm. Contrarily, R-SOA shows two maxima, providing the choice between two operation regimes, one for the low input optical powers and high device gain, and one for the deep saturation. It should be noted that −3dB bandwidth significantly depends on device length (Totović et al., 2015), which can be optimized to achieve maximum values of f_{3dB}. Aside from changes in values of f_{3dB} with the length variation, the prominence of low- and high-power maxima in R-SOA can also be

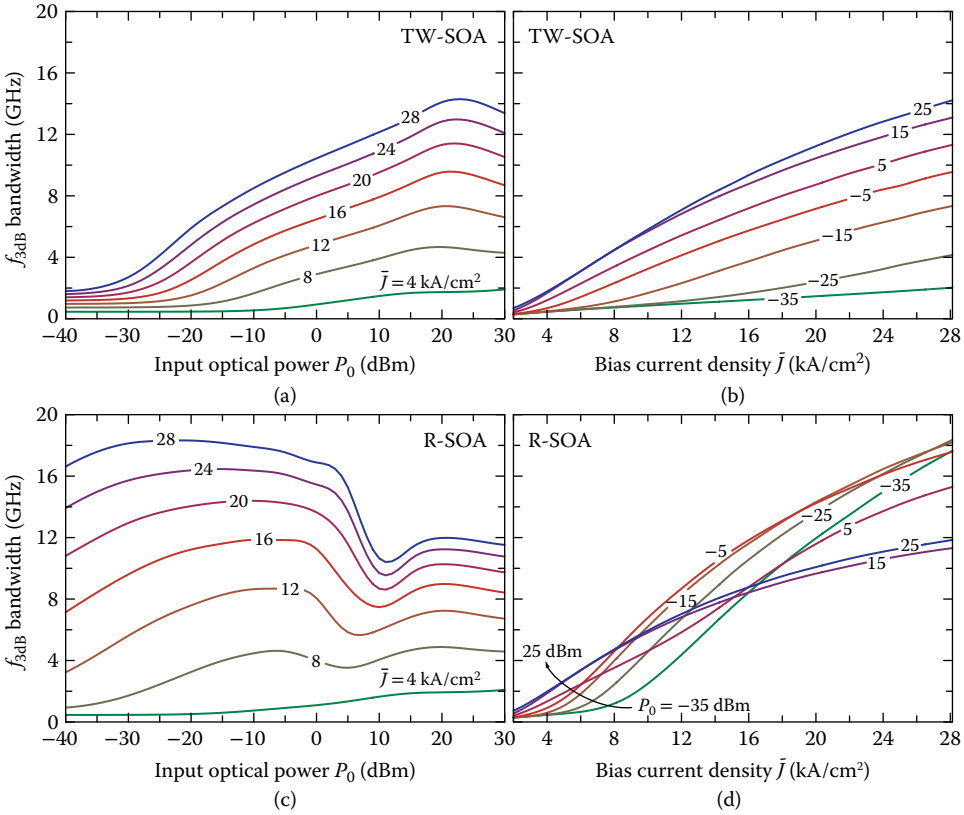

FIGURE 21.18 Bandwidth dependence on (a, c) the continuous wave (CW) input optical power P_0 (dBm) and (b, d) the bias current density $\bar{J}$ (kA/cm^2) for (a), (b) traveling-wave semiconductor optical amplifier (TW-SOA), and (c), (d) reflective (R)-SOA in the case of $L = 800$ μm.

interchanged. It should be noted that calculated bandwidth is intrinsic, and that inclusion of parasitic effects of the supporting circuit may modify the modulation response.

21.5.7 Case Study: Small-Signal Model for Transparent SOA

Transparent SOA has been repeatedly analyzed as a characteristic example of operating conditions under which the analytical expression for −3dB E/O bandwidth may be obtained (Mørk et al., 1999; Antonelli et al., 2015; Totović et al., 2016). By transparency, it is assumed that the steady-state modal gain is equal to the loss of the amplifier cavity, $\Gamma\bar{g} = \bar{\alpha}_i$, and therefore the steady-state photon density remains unchanged during its propagation. However, even under these circumstances, an analytical expression cannot be obtained without a number of approximations which simplify the system.

21.5.7.1 Framework for the Small-Signal Analysis

In this case study, the expressions will be derived under the following assumptions (Totović et al., 2016):

1. Nonlinear gain suppression is neglected, $\varepsilon\bar{S}_\Sigma \ll 1$.
2. Contribution of ASE noise to the signal is neglected, $\beta_{sp} = 0$.
3. Carrier loss due to the spontaneous emission is modeled via carrier lifetime, τ_s.

4. Current is assumed to reach uniform distribution along the electrode instantaneously, i.e., small-signal current density is assumed to be spatially independent, $\Delta J(z) = \Delta J$.

Within this framework, the system of equations governing signal and carrier dynamics can be derived from Equations 21.115 and 21.116, and reads

$$\pm \frac{\partial S_{\pm}}{\partial z} + \frac{1}{v_g} \frac{\partial S_{\pm}}{\partial t} = \left(\Gamma g - \alpha_i\right) S_{\pm}, \tag{21.129}$$

$$\frac{dn}{dt} = \frac{J}{qH} - \frac{n}{\tau_s} - v_g g S_{\Sigma}. \tag{21.130}$$

Assuming that the bias current has the general form given by Equation 21.117, $J(z,t) = J(t) = \bar{J} + \Delta J \exp(i\Omega t)$, the system (Equations 21.129 and 21.130) can be decoupled to the steady-state and small-signal equations. After linearization, small-signal carrier density has the form similar to Equation 21.125:

$$\Delta n = \frac{\Delta J/(qH) - v_g \bar{g}\left(\Delta S_+ + \Delta S_-\right)}{1/\tau_s + v_g g_0/\bar{n} \cdot \bar{S}_{\Sigma} + i\Omega}, \tag{21.131}$$

and the system of equations written with respect to small-signal photon densities reads

$$\pm \frac{d\Delta S_{\pm}}{dz} = \frac{\Gamma \gamma_{\pm}}{qHv_g} \Delta J + \left(\Gamma \bar{g} - \bar{\alpha}_i - i\frac{\Omega}{v_g}\right) \Delta S_{\pm} - \Gamma \bar{g} \gamma_{\pm} \left(\Delta S_{\pm} + \Delta S_{\mp}\right), \tag{21.132}$$

where

$$\gamma_{\pm} = \frac{v_g \left(g_0/\bar{n} - K_1\right)}{1/\tau_s + v_g g_0/\bar{n} \cdot \bar{S}_{\Sigma} + i\Omega} \bar{S}_{\pm} \tag{21.133}$$

has a meaning similar to the γ-parameter defined by Equation 21.128. Although the system given by Equation 21.132 is analytically solvable, the complexity of the solution undermines its benefit, and prevents us from determining the analytical solution for Ω_{3dB}.

21.5.7.2 Employing the Transparency Condition

Choosing the transparency as the operating regime defines the steady-state values of carrier and photon densities. From the condition $\Gamma \bar{g} = \bar{\alpha}_i$, the value for carrier density can be determined:

$$\bar{n} = -\frac{g_0}{K_1} W_L \left[-\frac{K_1 n_{tr}}{g_0} \exp\left(\frac{K_0}{\Gamma g_0}\right)\right], \tag{21.134}$$

where $W_L(x)$ stands for the Lambert W (product-logarithm) function. Introducing the transparency condition in the steady-state form of Equation 21.129 results in $dS_{\pm}/dz = 0$, meaning that the steady-state photon density is not spatially dependent and is defined by the boundary conditions. For both TW- and R-SOA, the forward-propagating steady-state photon density $\bar{S}_+$ will be equal to the input photon density S_0, whereas the backward-propagating photon density will either be zero, for TW-SOA, or $\bar{S}_- = R_2 \bar{S}_+ = R_2 S_0$, for R-SOA. Substituting $\bar{S}_{\pm}$ in the steady-state form of Equation 21.130 gives correlation between the stationary bias current density and the input photon density, for which the transparency condition is met:

$$S_0 = \frac{1}{v_g g_0 \ln\left(\bar{n}/n_{tr}\right)\left(1 + R_2\right)} \left(\frac{\bar{J}}{qH} - \frac{\bar{n}}{\tau_s}\right). \tag{21.135}$$

Aside from the maximum value of bias current density, dictated by the long-term stable SOA operation, Equation 21.135 gives a limit for the minimal value of $\bar{J}_{\min} = qH\bar{n}/\tau_s$ since the input photon density cannot be negative.

Introducing the transparency condition in Equation 21.132 gives

$$\pm\frac{\mathrm{d}\Delta S_{\pm}}{\mathrm{d}z} = \frac{\Gamma\gamma_{\pm}}{qHv_g}\Delta J - i\frac{\Omega}{v_g}\Delta S_{\pm} - \Gamma\bar{g}\gamma_{\pm}\left(\Delta S_{\pm} + \Delta S_{\mp}\right). \tag{21.136}$$

Moreover, having a fixed value for $\bar{n}$ reduces the γ-parameter to a spatially independent value, meaning that Equation 21.136 is the system of differential equations of the first order with fixed coefficients. The output small-signal photon density of TW-SOA has the following form

$$\Delta S_{+}(L) = \frac{\Gamma}{qHv_g}\Delta J\frac{\gamma_{+}}{\Gamma\bar{g}\gamma_{+} + i\Omega/v_g}\left\{1 - \exp\left[-\left(\Gamma\bar{g}\gamma_{+} + i\frac{\Omega}{v_g}\right)L\right]\right\}, \tag{21.137}$$

whereas the output small-signal photon density of an R-SOA reads

$$\Delta S_{-}(0) = 2R_2\frac{\Gamma\gamma_{+}}{qHv_g}\Delta J \times \left\{\frac{1+3R_2}{2}\Gamma\bar{g}\gamma_{+} + i\frac{\Omega}{v_g} + \sqrt{\left(\frac{1-R_2}{2}\Gamma\bar{g}\gamma_{+}\right)^2 + \left[\left(1+R_2\right)\Gamma\bar{g}\gamma_{+} + i\frac{\Omega}{v_g}\right]i\frac{\Omega}{v_g}}\right.$$
$$\left.\times\coth\left[L\sqrt{\left(\frac{1-R_2}{2}\Gamma\bar{g}\gamma_{+}\right)^2 + \left[\left(1+R_2\right)\Gamma\bar{g}\gamma_{+} + i\frac{\Omega}{v_g}\right]i\frac{\Omega}{v_g}}\right]\right\}^{-1}. \tag{21.138}$$

21.5.7.3 Analytical Formulae for Modulation Bandwidth

As previously discussed, the γ-parameter influences the SOA's small-signal modulation response through its dependence on Ω. For zero frequency, $\gamma_{\pm}$ becomes purely real, whereas for high frequencies, close to $\Omega_{3\mathrm{dB}}$ and beyond, it can be approximated with purely imaginary parameter

$$\gamma_{\pm}\big|_{\Omega\to\Omega_{3\mathrm{dB}}} \approx v_g\left(g_0/\bar{n} - K_1\right)\bar{S}_{\pm}\Big/(i\Omega). \tag{21.139}$$

In addition, during the derivation of the analytical expression for $\Omega_{3\mathrm{dB}}$, all trigonometric functions that are encountered, namely $\sin(x)$ for $x \to 0$ in case of TW-SOA and $\coth(x)$ for $x \to 0$ in the case of R-SOA, are approximated by the first term of their respective Maclaurin series expansion, $\sin(x) \approx x$ and $\coth(x) \approx 1/x$, respectively. This leads to the simpler form of Equations 21.137 and 21.138 in the vicinity of $\Omega_{3\mathrm{dB}}$. For TW-SOA, the output small-signal photon density is

$$\left|\Delta S_{+}(L)\right|\big|_{\Omega\to\Omega_{3\mathrm{dB}}} \approx \frac{\Gamma\Delta J}{qH}\left(\frac{g_0}{\bar{n}} - K_1\right)L\frac{S_0}{\Omega}, \tag{21.140}$$

and for R-SOA

$$\left|\Delta S_{-}(0)\right|\big|_{\Omega\to\Omega_{3\mathrm{dB}}} \approx 2R_2\frac{\Gamma\Delta J}{qH}\left(\frac{g_0}{\bar{n}} - K_1\right)L\frac{S_0}{\Omega}. \tag{21.141}$$

Finally, from the condition $|\Delta S_{out}(\Omega_{3dB})/\Delta S_{out}(0)| = 1/2$, the −3dB bandwidth can be found, under the transparency regime. For TW-SOA, it is given by

$$\Omega_{3dB} = \Gamma g_0 \ln\frac{\bar{n}}{n_{tr}} L v_g \left(\frac{g_0}{\bar{n}} - K_1\right) S_0 \left\{1 + \coth\left[\Gamma g_0 \ln\frac{\bar{n}}{n_{tr}} \frac{L}{2} \frac{v_g\left(g_0/\bar{n} - K_1\right) S_0}{1/\tau_s + v_g g_0/\bar{n} \cdot S_0}\right]\right\}, \tag{21.142}$$

and for R-SOA it has the form

$$\Omega_{3dB} = 2\left[\frac{1}{\tau_s} + v_g \frac{g_0}{\bar{n}}\left(1 + R_2\right) S_0\right] + \left(1 + 3R_2\right) \Gamma g_0 \ln\frac{\bar{n}}{n_{tr}} L v_g \left(\frac{g_0}{\bar{n}} - K_1\right) S_0. \tag{21.143}$$

21.6 Conclusion

SOAs have been extensively studied ever since WDM networks became widely adopted. In order to enable massive deployment of optical access networks, optical technologies, including SOAs, have expanded toward the lower levels of network hierarchy, aiming to relieve first/last mile bottleneck. Due to their versatility, SOAs are the key components in many of these levels. R-SOA has recently become one of the most promising candidates for the next-generation wavelength division multiplexed passive optical networks (WDM-PONs), representing the new Fiber-to-the-Home paradigm. Moreover, it is on its way to become a crucial component in Worldwide Interoperability for Microwave Access (WiMAX) and Wireless-Fidelity (Wi-Fi) Radio-over-Fiber (RoF) access network architecture. TW- and R-SOAs are devices of choice for many nonlinear applications, including those related to FWM, wavelength conversion, and all optical signal processing in general.

The choice of the SOA type for a specific purpose does not necessarily require better overall performance but usually better performance in one or several aspects. Therefore, both TW- and R-SOA have found their applications. However, optimization of the devices themselves, as well as the system as a whole, should always be performed in order for the SOAs to reach their full potential. The optimization of the device includes the choice of material, device geometry, and operating conditions, whereas the system analysis involves many more aspects that need to be addressed. This process requires an elaborate, but efficient SOA model, which accounts for all relevant effects. In Section 21.5, various models have been presented for both the steady-state and dynamic operating regimes. All models are built starting from the rate equations describing SOA dynamics, which can include multiple levels of approximation, as discussed in Section 21.4. The basic model recognizes only the essential processes present in the SOAs, i.e., carrier injection, stimulated and spontaneous recombination, and signal amplification. More realistic models comprise additional effects, such as wideband ASE noise, carrier transport, nonlinear gain suppression, temperature effects, and distributed bias current, all of which are discussed in detail. Moreover, in order for the model to accurately represent the SOA's performance, a detailed analysis of the optical properties of materials used for the active region and the waveguide geometry should be performed, which can be done using the models presented in Section 21.3. This includes calculation of the full spectral profile of material gain, radiative spontaneous recombination rate, refractive index variation, and optical confinement factor, among other parameters.

For SOA optimization in the steady-state operating regime, the wideband model, based on the self-consistent iterative method, given in Section 21.5.3, can provide detailed results, but does consume a significant amount of computational resources. This method is mainly designed for the characterization and optimization of the device itself. On the other hand, for quick assessment of the SOA's performance, especially in more complex network architectures, the semi-analytical model, presented in Section 21.5.4, proves to be time and resource efficient, at the expense of somewhat decreased precision. In the dynamic operating regime, the upwind scheme finite difference model can be used, as shown in Section 21.5.5, which

is transparent to the modulation type, and designed to support even advanced modulation formats. For SOAs used in direct E/O modulation, −3dB bandwidth is a good indicator of the SOAs' performance, and can be determined and optimized based on the detailed numerical model given in Section 21.5.6. When resources are limited, and the SOA operates in the transparency regime, simple analytical solutions, derived in Section 21.5.7, can be used for the same purpose.

The overview of various steady-state and dynamic models, as well as the case studies presented, provides insight into the methods for numerically accurate and efficient simulations of standalone and system-embedded SOAs. These methods can help in the development of computational tools which can be used for the optimization of SOA design based on the dependence of its performance on technological parameters and operating conditions. It should be noted that advanced SOA models, which deal with nonlinear effects, are usually built upon the models which simulate standard SOA amplification regime.

References

Adachi S (1989) Optical dispersion relations for GaP, GaAs, GaSb, InP, InAs, InSb, $Al_xGa_{1-x}As$, and $In_{1-x}Ga_xAs_yP_{1-y}$. *Journal of Applied Physics*. 66:6030–6040.

Adams MJ, Collins JV, Henning ID (1985) Analysis of semiconductor laser optical amplifiers. *IEEE Proceedings Journal—Optoelectronics*. 132:58–63.

Agrawal GP (1990) Effect of gain and index nonlinearities on single-mode dynamics in semiconductor lasers. *IEEE Journal of Quantum Electronics*. 26:1901–1909.

Agrawal GP, Olsson NA (1989) Self-phase modulation and spectral broadening of optical pulses in semiconductor laser amplifiers. *IEEE Journal of Quantum Electronics*. 25:2297–2306.

Ahn D, Chuang SL (1990) Optical gain and gain suppression of quantum-well lasers with valence band mixing. *IEEE Journal of Quantum Electronics*. 26:13–24.

Antonelli C, Mecozzi A (2013) Reduced model for the nonlinear response of reflective semiconductor optical amplifiers. *IEEE Photonics Technology Letters*. 25:2243–2246.

Antonelli C, Mecozzi A, Zhefeng H, Santagiustina M (2015) Analytic study of the modulation response of reflective semiconductor optical amplifiers. *Journal of Lightwave Technology*. 33:4367–4376.

Bennett BR, Soref RA, del Alamo JA (1990) Carrier-induced change in refractive index of InP, GaAs and InGaAsP. *IEEE Journal of Quantum Electronics*. 26:113–122.

Berg TW, Bischoff S, Magnusdottir I, Mørk J (2001) Ultrafast gain recovery and modulation limitations in self-assembled quantum-dot devices. *IEEE Photonics Technology Letters*. 13:541–543.

Berglind E, Gillner L (1994) Optical quantum noise treated with classical electrical network theory. *IEEE Journal of Quantum Electronics*. 30:846–853.

Carapellese N, Tornatore M, Pattavina A (2014) Energy-efficient baseband unit placement in a fixed/mobile converged WDM aggregation network. *IEEE Journal on Selected Areas in Communications*. 32:1542–1551.

Carlo AD, Reale A, Tocca L, Lugli P (1998) Polarization-independent-strained semiconductor optical amplifiers: A tight-binding study. *IEEE Journal of Quantum Electronics*. 34:1730–1739.

Carrère H, Truong VG, Marie X, Brenot R, De Valicourt G, Lelarge F, Amand T (2010) Large optical bandwidth and polarization insensitive semiconductor optical amplifiers using strained InGaAsP quantum wells. *Applied Physics Letters*. 97:121101.

Cartoixa X, Ting DZY, McGill TC (2003) Numerical spurious solutions in the effective mass approximation. *Journal of Applied Physics*. 93:3974–3981.

Cassioli D, Scotti S, Mecozzi A (2000) A time-domain computer simulator of the nonlinear response of semiconductor optical amplifiers. *IEEE Journal of Quantum Electronics*. 36:1072–1080.

Chao CYP, Chuang SL (1992) Spin-orbit-coupling effects on the valence-band structure of strained semiconductor quantum wells. *Physical Review B*. 46:4110–4122.

Cho YS, Choi WY (2001) Analysis and optimization of polarization-insensitive semiconductor optical amplifiers with delta-strained quantum wells. *IEEE Journal of Quantum Electronics*. 37:574–579.

Chu CYJ, Ghafouri-Shiraz H (1994) Analysis of gain and saturation characteristics of a semiconductor laser optical amplifier using transfer matrices. *Journal of Lightwave Technology*. 12:1378–1386.

Chuang SL (1991) Efficient band-structure calculations of strained quantum wells. *Physical Review B*. 43:9649–9661.

Chuang SL (1995) *Physics of Optoelectronic Devices*. New York, NY: Wiley-Interscience.

Coldren LA, Corzine SW, Mašanović ML (2012) *Diode Lasers and Photonic Integrated Circuits*. New York, NY: Wiley-Interscience.

Connelly MJ (2001) Wideband semiconductor optical amplifier steady-state numerical model. *IEEE Journal of Quantum Electronics*. 37:439–447.

Connelly MJ (2002) *Semiconductor Optical Amplifiers*. Norwell, MA: Kluwer.

Connelly MJ (2007) Wide-band steady-state numerical model and parameter extraction of a tensile-strained bulk semiconductor optical amplifier. *IEEE Journal of Quantum Electronics*. 43:47–56.

Connelly MJ (2012) Reflective semiconductor optical amplifier pulse propagation model. *IEEE Photonics Technology Letters*. 24:95–97.

Connelly MJ (2014) Reflective semiconductor optical amplifier modulator dynamic model. *14th International Conference on Numerical Simulation of Optoelectronic Devices (NUSOD)*. 2014:41–42.

Connelly MJ (2015) Reflective semiconductor optical amplifier electrode voltage based phase shifter model. *International Conference on Numerical Simulation of Optoelectronic Devices (NUSOD)*. 2015:39–40.

D'Ottavi A, Iannone E, Mecozzi A, Scotti S, Spano P, Dall'Ara R, Eckner J, Guekos G (1995) Efficiency and noise performance of wavelength converters based on FWM in semiconductor optical amplifiers. *IEEE Photonics Technology Letters*. 7:357–359.

Dailey JM, Koch TL (2007) Impact of carrier heating on SOA transmission dynamics for wavelength conversion. *IEEE Photonics Technology Letters*. 19:1078–1080.

Dailey JM, Koch TL (2009) Simple rules for optimizing asymmetries in SOA-based Mach–Zehnder wavelength converters. *Journal of Lightwave Technology*. 27:1480–1488.

Davis MG, O'Dowd RF (1994) A transfer matrix method based large-signal dynamic model for multielectrode DFB lasers. *IEEE Journal of Quantum Electronics*. 30:2458–2466.

de Oliveira Ribeiro R, Pontes MJ, Giraldi MTMR, Carvalho MCR (2005) Characterisation of all-optical wavelength conversion by cross-gain modulation of ASE on a SOA. International Conference on Microwave and Optoelectronics (SBMO/IEEE MTT-S) 2005:218–221.

de Valicourt G (2012) Next generation of optical access network based on reflective-SOA, Ch. 1. In *Selected Topics on Optical Amplifiers in Present Scenario*, edited by S. K. Garai. Rijeka, Croatia: InTech.

de Valicourt G, Violas MA, Wake D, Van Dijk F, Ware C, Enard A, Make D, Liu Z, Lamponi M, Duan GH, Brenot R (2010) Radio-over-fiber access network architecture based on new optimized RSOA devices with large modulation bandwidth and high linearity. *IEEE Transactions on Microwave Theory and Techniques*. 58:3248–3258.

Donati S, Giuliani G (1997) Noise in an optical amplifier: Formulation of a new semiclassical model. *IEEE Journal of Quantum Electronics*. 33:1481–1488.

Dúill SPÓ, Barry LP (2015) Improved reduced models for single-pass and reflective semiconductor optical amplifiers. *Optics Communications*. 334:170–173.

Durhuus T, Mikkelsen B, Stubkjaer KE (1992) Detailed dynamic model for semiconductor optical amplifiers and their crosstalk and intermodulation distortion. *Journal of Lightwave Technology*. 10:1056–1065.

Figueiredo RC, Ribeiro NS, Gallep CM, Conforti E (2015) Frequency- and time-domain simulations of semiconductor optical amplifiers using equivalent circuit modeling. *Optical Engineering*. 54:114107.

Foreman BA (1993) Effective-mass Hamiltonian and boundary conditions for the valence bands of semiconductor microstructures. *Physical Review B*. 48:4964–4967.

Foreman BA (1997) Elimination of spurious solutions from eight-band k.p theory. *Physical Review B*. 56:12748–12751.

Gebrewold SA, Bonjour R, Barbet S, Maho A, Brenot R, Chanclou P, Brunero M, Marazzi L, Parolari P, Totovic A, Gvozdic D, Hillerkuss D, Hafner C, Leuthold J (2015) Self-seeded RSOA-fiber cavity lasers vs. ASE spectrum-sliced or externally seeded transmitters—A comparative study. *Applied Sciences*. 5:1922–1941.

Ghafouri-Shiraz H (2004) *The Principles of Semiconductor Laser Diodes and Amplifiers*. London Imperial College Press.

Gioannini M (2004) Numerical modeling of the emission characteristics of semiconductor quantum dash materials for lasers and optical amplifiers. *IEEE Journal of Quantum Electronics*. 40:364–373.

Gladisch A, Braun RP, Breuer D, Ehrhardt A, Foisel HM, Jaeger M, Leppla R, Schneiders M, Vorbeck S, Weiershausen W, Westphal F (2006) Evolution of terrestrial optical system and core network architecture. *Proceedings of the IEEE*. 94:869–891.

Godefroy A, Le Corre A, Clerot F, Salaan S, Loualiche S, Simon JC, Henry L, Vaudry C, Keromnes JC, Joulie G, Lamouler P (1995) 1.55-μm polarization-insensitive optical amplifier with strain-balanced superlattice active layer. *IEEE Photonics Technology Letters*. 7:473–475.

Grundmann M, Stier O, Bimberg D (1995) InAs/GaAs pyramidal quantum dots: Strain distribution, optical phonons, and electronic structure. *Physical Review B*. 52:11969–11981.

Gvozdić DM, Ekenberg U (2006) Superefficient electric-field-induced spin-orbit splitting in strained p-type quantum wells. *Europhysics Letters*. 73:927–933.

Hairer E, Wanner G (1996) *Solving Ordinary Differential Equations II: Stiff and Differential-Algebraic Problems*. Berlin: Springer-Verlag.

Henry CH (1982) Theory of the linewidth of semiconductor lasers. *IEEE Journal of Quantum Electronics*. 18:259–264.

Henry CH (1986) Theory of spontaneous emission noise in open resonators and its application to lasers and optical amplifiers. *Journal of Lightwave Technology*. 4:288–297.

Ito T, Yoshimoto N, Magari K, Sugiura H (1998) Wide-band polarization-independent tensile-strained InGaAs MQW-SOA gate. *IEEE Photonics Technology Letters*. 10:657–659.

Jin CY, Guo WH, Huang YZ, Yu LJ (2003) Photon iterative numerical technique for steady-state simulation of gain-clamped semiconductor optical amplifiers. *IEEE Proceedings—Optoelectronics*. 150:503–507.

Joergensen C, Danielsen SL, Stubkjaer KE, Schilling M, Daub K, Doussiere P, Pommerau F, Hansen PB, Poulsen HN, Kloch A, Vaa M, Mikkelsen B, Lach E, Laube G, Idler W, Wunstel K (1997) All-optical wavelength conversion at bit rates above 10 Gb/s using semiconductor optical amplifiers. *IEEE Journal of Selected Topics in Quantum Electronics*. 3:1168–1180.

Joma M, Horikawa H, Xu CQ, Yamada K, Katoh Y, Kamijoh T (1993) Polarization insensitive semiconductor laser amplifier with tensile strained InGaAsP/InGaAsP multiple quantum well structure. *Applied Physics Letters*. 62:121–122.

Kang JM, Lee SH, Kwon HC, Han SK (2006) WDM-PON with broadcasting function using direct ASE modulation of reflective SOA. *European Conference on Optical Communications (ECOC)*. 2006: 24–28.

Kani J-I (2010) Enabling technologies for future scalable and flexible WDM-PON and WDM/TDM-PON systems. *IEEE Journal of Selected Topics in Quantum Electronics*. 16:1290–1297.

Kawano K, Kitoh T (2001) *Introduction to Optical Waveguide Analysis: Solving Maxwell's Equations and the Schrödinger Equation*. New York, NY: Wiley-Interscience.

Keating T, Jin X, Chuang SL, Hess K (1999) Temperature dependence of electrical and optical modulation responses of quantum-well lasers. *IEEE Journal of Quantum Electronics*. 35:1526–1534.

Kim J, Chuang SL (2006) Theoretical and experimental study of optical gain, refractive index change, and linewidth enhancement factor of p-doped quantum-dot lasers. *IEEE Journal of Quantum Electronics*. 42:942–952.

Kim J, Laemmlin M, Meuer C, Bimberg D, Eisenstein G (2008) Static gain saturation model of quantum-dot semiconductor optical amplifiers. *IEEE Journal of Quantum Electronics*. 44:658–665.

Kim J, Laemmlin M, Meuer C, Bimberg D, Eisenstein G (2009) Theoretical and experimental study of high-speed small-signal cross-gain modulation of quantum-dot semiconductor optical amplifiers. *IEEE Journal of Quantum Electronics*. 45:1658–1666.

Kim Y, Lee H, Kim S, Ko J, Jeong J (1999) Analysis of frequency chirping and extinction ratio of optical phase conjugate signals by four-wave mixing in SOA's. *IEEE Journal of Selected Topics in Quantum Electronics*. 5:873–879.

Koenig S, Bonk R, Schmuck H, Poehlmann W, Pfeiffer Th, Koos C, Freude W, Leuthold J (2014) Amplification of advanced modulation formats with a semiconductor optical amplifier cascade. *Optics Express*. 22:17854–17871.

Kolokolov KI, Li J, Ning CZ (2003) k·p Hamiltonian without spurious-state solution. *Physical Review B*. 68:161308.

Labukhin D, Li X (2006) Polarization insensitive asymmetric ridge waveguide design for semiconductor optical amplifiers and super luminescent light-emitting diodes. *IEEE Journal of Quantum Electronics*. 42:1137–1143.

Liljeberg T, Bowers JE (1997) Velocity mismatch limits in semiconductor lasers and amplifiers. *IEEE Conference Proceedings: 10th Annual Meeting Lasers and Electro-Optics Society Annual Meeting (LEOS '97)*. 1:341–342.

Liu G, Chuang SL (2002) Modeling of Sb-based type-II quantum cascade lasers. *Physical Review B*. 65:165220.

Liu G, Jin X, Chuang SL (2001) Measurement of linewidth enhancement factor of semiconductor lasers using an injection-locking technique. *IEEE Photonics Technology Letters*. 13:430–432.

Loudon R, Ramoo D, Adams MJ (2005) Theory of spontaneous emission noise in multisection semiconductor lasers. *Journal of Lightwave Technology*. 23:2491–2504.

Lysak VV, Kawaguchi H, Sukhoivanov IA, Katayama T, Shulika AV (2005) Ultrafast gain dynamics in asymmetrical multiple quantum-well semiconductor optical amplifiers. *IEEE Journal of Quantum Electronics*. 41:797–807.

Lysak VV, Sukhoivanov IA, Shulika OV, Safonov IM, Lee YT (2006) Carrier tunneling in complex asymmetrical multiple-quantum-well semiconductor optical amplifiers. *IEEE Photonics Technology Letters*. 18:1362–1364.

Magari K, Okamoto M, Noguchi Y (1991) 1.55-μm polarization insensitive high-gain tensile-strained-barrier MQW optical amplifier. *IEEE Photonics Technology Letters*. 3:998–1000.

Magari K, Okamoto M, Suzuki Y, Sato K, Noguchi Y, Mikami O (1994) Polarization-insensitive optical amplifier with tensile-strained-barrier MQW structure. *IEEE Journal of Quantum Electronics*. 30:695–701.

Marcuse D (1984) Computer simulation of laser photon fluctuations: Theory of single-cavity laser. *IEEE Journal of Quantum Electronics*. 20:1139–1148.

Mathlouthi W, Lemieux P, Salsi M, Vannucci A, Bononi A, Rusch LA (2006) Fast and efficient dynamic WDM semiconductor optical amplifier model. *Journal of Lightwave Technology*. 24:4353–4365.

Mathur A, Dapkus PD (1992) Polarization insensitive strained quantum well gain medium for lasers and optical amplifiers. *Applied Physics Letters*. 61:2845–2847.

Mazzucato S, Carrère H, Marie X, Amand T, Achouche M, Caillaud C, Brenot R (2015) Gain, amplified spontaneous emission and noise figure of bulk InGaAs/InGaAsP/InP semiconductor optical amplifiers. *IET Optoelectronics*. 9:52–60.

Mecozzi A, Mørk J (1997) Saturation effects in nondegenerate four-wave mixing between short optical pulses in semiconductor laser amplifiers. *IEEE Journal of Selected Topics in Quantum Electronics*. 3:1190–1207.

Mecozzi A, Wiesenfeld JM (2001) The roles of semiconductor optical amplifiers in optical networks. *Optics & Photonics News*. 12:36–42.

Melo AM, Petermann K (2008) On the amplified spontaneous emission noise modeling of semiconductor optical amplifiers. *Optics Communications*. 281:4598–4605.

Meney AT, Gonul B, O'Reilly EP (1994) Evaluation of various approximations used in the envelope-function method. *Physical Review B*. 50:10893–10904.

Michie C, Kelly AE, McGeough J, Armstrong I, Andonovic I, Tombling C (2006) Polarization-insensitive SOAs using strained bulk active regions. *Journal of Lightwave Technology*. 24:3920–3927.

Morel P, Sharaiha A (2009) Wideband time-domain transfer matrix model equivalent circuit for short pulse propagation in semiconductor optical amplifiers. *IEEE Journal of Quantum Electronics*. 45:103–116.

Mørk J, Mecozzi A, Eisenstein G (1999) The modulation response of a semiconductor laser amplifier. *IEEE Journal of Selected Topics in Quantum Electronics*. 5:851–860.

Moss TS, Burrell GJ, Ellis B (1973) *Semiconductor Opto-Electronics*. London: Butterworth & Co.

Mukai T, Yamamoto Y (1982) Noise in an AlGaAs semiconductor laser amplifier. *IEEE Transactions on Microwave Theory and Techniques*. 30:410–421.

Nagarajan R, Ishikawa M, Fukushima T, Geels RS, Bowers JE (1992) High speed quantum-well lasers and carrier transport effects. *IEEE Journal of Quantum Electronics*. 28:1990–2008.

Occhi L, Schares L, Guekos G (2003) Phase modeling based on the α-factor in bulk semiconductor optical amplifiers. *IEEE Journal of Selected Topics in Quantum Electronics*. 9:788–797.

Olsson NA (1989) Lightwave systems with optical amplifiers. *Journal of Lightwave Technology*. 7:1071–1082.

Osinski M, Buus J (1987) Linewidth broadening factor in semiconductor lasers—An overview. *IEEE Journal of Quantum Electronics*. 23:9–29.

Park J, Li X, Huang WP (2005) Comparative study of mixed frequency-time-domain models of semiconductor laser optical amplifiers. *IEE Proceedings—Optoelectronics*. 152:151–159.

Pham QT (2014) Highly effective crosstalk mitigation method using counter-propagation in semiconductor optical amplifier for remodulation WDM-PONs. *Journal of Photonics*. 2014:610967.

Pillai BSG, Premaratne M, Abramson D, Lee KL, Nirmalathas A, Lim C, Shinada S, Wada N, Miyazaki T. (2006) Analytical characterization of optical pulse propagation in polarization-sensitive semiconductor optical amplifiers. *IEEE Journal of Quantum Electronics*. 42:1062–1077.

Pitris S, Vagionas C, Kanellos GT, Pleros N, Kisacik R, Tekin T, Broeke R (2015) Monolithically integrated all-optical SOA-based SR Flip-Flop on InP platform. *International Conference on Photonics in Switching (PS)*. 2015:208–210.

Qasaimesh O (2003) Optical gain and saturation characteristics of quantum-dot semiconductor optical amplifier. *IEEE Journal of Quantum Electronics*. 39:794–800.

Qasaimesh O (2013) Broadband gain-clamped linear quantum dash optical amplifiers. *Optical and Quantum Electronics*. 45:1277–1286.

Qin C, Huang X, Zhang X (2012) Theoretical investigation on gain recovery dynamics in step quantum well semiconductor optical amplifiers. *Journal of the Optical Society of America B*. 29:607–613.

Ramaswami R (2002) Optical fiber communication: From transmission to networking. *IEEE Communications Magazine*. 40:138–147.

Razaghi M, Ahmadi V, Connelly MJ (2009) Comprehensive finite-difference time-dependent beam propagation model of counterpropagating picosecond pulses in a semiconductor optical amplifier. *Journal of Lightwave Technology*. 27:3162–3174.

Reithmaier JP, Somers A, Deubert S, Schwertberger R, Kaiser W, Forchel A, Calligaro M, Resneau P, Parillaud O, Bansropun S, Krakowski M, Alizon R, Hadass D, Bilenca A, Dery H, Mikhelashvili V, Eisenstein G, Gioannini M, Montrosset I, Berg TW, van der Poel M, Mørk, J, Tromborg B (2005) InP based lasers and optical amplifiers with wire-/dot-like active regions. *Journal of Physics D: Applied Physics*. 38:2088–2102.

Runge P, Elschner R, Petermann K (2010) Time-domain modeling of ultralong semiconductor optical amplifiers. *IEEE Journal of Quantum Electronics*. 46:484–491.

Schmuck H, Bonk R, Poehlmann W, Haslach C, Kuebart W, Karnick D, Meyer J, Fritzsche D, Weis E, Becker J, Freude W, Pfeiffer T (2013) Demonstration of SOA-assisted open metro-access infrastructure for heterogeneous services. *39th European Conference and Exhibition on Optical Communication (ECOC)*. 2013:1–3.

Schrenk B (2011) Characterization and Design of Multifunction Photonic Devices for Next Generation Fiber-to-the-Home Optical Network Units. PhD diss., Universitat Politècnica de Catalunya.

Serrat C, Masoller C (2006) Modeling spatial effects in multi-longitudinal-mode semiconductor lasers. *Physical Review A*. 73:043812.

Shtaif M, Tromborg B, Eisenstein G (1998) Noise spectra of semiconductor optical amplifiers: Relation between semiclassical and quantum descriptions. *IEEE Journal of Quantum Electronics*. 34:869–878.

Silver M, Phillips AF, Adams AR, Greene PD, Collar AJ (2000) Design and ASE characteristics of 1550-nm polarization-insensitive semiconductor optical amplifiers containing tensile and compressive wells. *IEEE Journal of Quantum Electronics*. 36:118–122.

Simon JC, Doussiere P, Pophillat L, Fernier B (1989) Gain and noise characteristics of a 1.5 μm near-travelling-wave semiconductor laser amplifier. *Electronics Letters*. 25:434–436.

Stabile R, Williams KA (2011) Photonic integrated semiconductor optical amplifier switch circuits. In *Advances in Optical Amplifiers*, edited by P. Urquhart, 205–230. Rijeka, Croatia: InTech.

Stier O, Grundmann M, Bimberg D (1999) Electronic and optical properties of strained quantum dots modeled by 8-band k.p theory. *Physical Review B*. 59:5688–5701.

Sygletos S, Tomkos I, Leuthold J (2008) Technological challenges on the road toward transparent networking. *Journal of Optical Networking*. 7:321–350.

Talli G, Adams MJ (2003) Amplified spontaneous emission in semiconductor optical amplifiers: Modelling and experiments. *Optics Communications*. 218:161–166.

Tauber DA, Spickermann R, Nagarajan R, Reynolds T, Holmes AL, Bowers JE (1994) Inherent bandwidth limits in semiconductor lasers due to distributed microwave effects. *Applied Physics Letters*. 64:1610–1612.

Thylén L (1988) Amplified spontaneous emission and gain characteristics of Fabry-Perot and traveling wave type semiconductor laser amplifiers. *IEEE Journal of Quantum Electronics*. 24:1532–1537.

Tiemeijer LF, Thijs PJA, Van Dongen T, Slootweg RWM, van der Heijden JMM, Binsma JJM, Krijn MPCM (1993) Polarization insensitive multiple quantum well laser amplifiers for the 1300 nm window. *Applied Physics Letters*. 62:826–828.

Tishinin D, Uppal K, Kim I, Dapkus PD (1997) 1.3-μm polarization insensitive amplifiers with integrated-mode transformers. *IEEE Photonics Technology Letters*. 9:1337–1339.

Toptchiyski G, Kindt S, Petermann K, Hilliger E, Diez S, Weber HG (1999) Time-domain modeling of semiconductor optical amplifiers for OTDM applications. *Journal of Lightwave Technology*. 17:2577–2583.

Totović AR, Crnjanski JV, Krstić MM, Gvozdić DM (2011) Application of multi-quantum well RSOA in remodulation of 100 Gb/s downstream RZ signal for 10 Gb/s upstream transmission. *19th Telecommunications Forum (TELFOR)*. 2011:840–843.

Totović AR, Crnjanski JV, Krstić MM, Gvozdić DM (2012) Modelling of carrier dynamics in multi-quantum well semiconductor optical amplifiers. *Physica Scripta*. 2012:014032.

Totović AR, Crnjanski JV, Krstić MM, Gvozdić DM (2014) An analytical solution for stationary distribution of photon density in traveling-wave and reflective SOAs. *Physica Scripta*. 2014:014013.

Totović AR, Crnjanski JV, Krstić MM, Gvozdić DM (2014) An efficient semi-analytical method for modeling of traveling-wave and reflective SOAs. *Journal of Lightwave Technology*. 32:2106–2112.

Totović AR, Crnjanski JV, Krstić MM, Gvozdić DM (2015) Numerical study of the small-signal modulation bandwidth of reflective and traveling-wave SOAs. *Journal of Lightwave Technology*. 33:2758–2764.

Totović AR, Crnjanski JV, Krstić MM, Mašanović ML, Gvozdić DM (2013) A self-consistent numerical method for calculation of steady-state characteristics of traveling-wave and reflective SOAs. *IEEE Journal of Selected Topics in Quantum Electronics*. 19:3000411.

Totović AR, Levajac VG, Gvozdić DM (2016) Electro-optical modulation bandwidth analysis for traveling-wave and reflective semiconductor optical amplifiers in transparency operating regime. *Optical and Quantum Electronics*. 48:262.

Tsai CY, Tsai CY, Lo YH, Spencer RM, Eastman LF (1995) Nonlinear gain coefficients in semiconductor quantum-well lasers: Effects of carrier diffusion, capture, and escape. *IEEE Journal of Selected Topics in Quantum Electronics*. 1:316–330.

Valiente I, Lablonde L, Simon JC, Billès L (1996) Effects of amplified spontaneous emission on gain recovery dynamics of semiconductor optical amplifiers. In *Optical Amplifiers and Their Applications*, edited by R. Jopson, K. Stubkjaer, and M. Suyama, Vol. 5, *OSA Trends in Optics and Photonics Series*. Washington, DC: Optical Society of America.

Veprek RG, Steiger S, Witzigmann B (2007) Ellipticity and the spurious solution problem of k · p envelope equations. *Physical Review B*. 76:165320.

Visser TD, Blok H, Demeulenaere B, Lenstra D (1997) Confinement factors and gain in optical amplifiers. *IEEE Journal of Quantum Electronics*. 33:1763–1766.

Vyrsokinos K, Vagionas C, Fitsios D, Miliou A (2014) Frequency and time domain analysis of all optical memories based on SOA and SOA-MZI switches. *IEEE Optical Interconnects Conference*. 2014: 57–58.

Wang J, Maitra A, Poulton CG, Freude W, Leuthold J (2007) Temporal dynamics of the alpha factor in semiconductor optical amplifiers. *Journal of Lightwave Technology*. 25:891–900.

Willatzen M, Uskov A, Mørk J, Olesen H, Tromborg B, Jauho AP (1991) Nonlinear gain suppression in semiconductor lasers due to carrier heating. *IEEE Photonics Technology Letters*. 3:606–609.

Wolfson D. All-optical signal processing and regeneration. PhD diss., Research Center COM, Technical University of Denmark, 2001.

Wu B, Georges JB, Cutrer DM, Lau KY (1995) On distributed microwave effects in semiconductor lasers and their practical implications. *Applied Physics Letters*. 67:467–469.

Wünstel K, Laube G, Idler W, Daub K, Lach E, Dütting K, Klenk M, Schilling M (1996) High speed and polarization insensitive wavelength converters by MQW optimization, In *Conference Proceedings of IPR'96*, paper IMG6, Boston, MA.

Xia M, Ghafouri-Shiraz H (2015) Theoretical analysis of carrier heating effect in semiconductor optical amplifiers. *Optical and Quantum Electronics*. 47:2141–2153.

Xia M, Ghafouri-Shiraz H (2016) A novel transmission line model for quantum well semiconductor optical amplifiers. *Optical and Quantum Electronics*. 48:52.

Xing W, Yikai S, Xiang L, Leuthold J, Chandrasekhar S (2004) 10-Gb/s RZ-DPSK transmitter using a saturated SOA as a power booster and limiting amplifier. *IEEE Photonics Technology Letters*. 16:1582–1584.

Yacomotti AM, Furfaro L, Hachair X, Pedaci F, Giudici M, Tredicce J, Javaloyes J, Balle S, Viktorov EA, Mandel P (2004) Dynamics of multimode semiconductor lasers. *Physical Review A*. 69:053816.

Yamatoya T, Koyama F (2004) Optical preamplifier using optical modulation of amplified spontaneous emission in saturated semiconductor optical amplifier. *Journal of Lightwave Technology*. 22:1290–1295.

Yariv A, Yeh P. *Photonics: Optical Electronics in Modern Communications*. New York, NY: Oxford University Press, 2007.

Zhang Y, Ruden PP (1999) 1.3 μm polarization-insensitive optical amplifier structure based on coupled quantum wells. *IEEE Journal of Quantum Electronics*. 35:1509–1514.

Zhou E, Zhang X, Huang D (2007) Analysis on dynamic characteristics of semiconductor optical amplifiers with certain facet reflection based on detailed wideband model. *Optics Express*. 15:9096–9106.

Zilkie AJ, Meier J, Mojahedi M, Poole PJ, Barrios P, Poitras D, Rotter TJ, Yang C, Stintz A, Malloy KJ, Smith PWE, Aitchison JS (2007) Carrier dynamics of quantum-dot, quantum-dash, and quantum-well semiconductor optical amplifiers operating at 1.55 μm. *IEEE Journal of Quantum Electronics*. 43:982–991.

Zimmerman DR, Spiekman LH (2004) Amplifiers for the masses: EDFA, EDWA, and SOA amplets for metro and access applications. *Journal of Lightwave Technology*. 22:63–70.

22

Tapered Semiconductor Optical Amplifiers

José-Manuel G. Tijero

Antonio Pérez-Serrano

Gonzalo del Pozo

and

Ignacio Esquivias

22.1 Introduction

In recent years, the pervasive extension of semiconductor-based laser sources has been reaching application domains, such as lidar, material processing, metrology, and frequency doubling, where other laser sources are still prevalent because of the concurrent requirements of high power, high spectral purity, and high-beam quality. Two slightly different semiconductor devices are already in use for some of these applications: tapered laser diodes (Walpole, 1996; Wenzel et al., 2003; Sumpf et al., 2009) and master-oscillator power-amplifiers (MOPAs) (O'Brien et al., 1993; Spreemann et al., 2009). A tapered MOPA consists of either a distributed Bragg reflector laser or a distributed feedback laser acting as the master oscillator (MO) and a tapered semiconductor optical amplifier (SOA) acting as the power amplifier. Both hybrid and integrated MOPAs are of great interest. In a hybrid MOPA, the MO and the SOA are coupled through additional optics (Schwertfeger et al., 2011) with the advantage of separate fabrication of the components but at the expense of a more complex set-up. The integrated MOPAs have the advantages of reduced total size but the drawback of possible optical coupling between sections (Vilera et al., 2015).

The schematic of a typical tapered SOA is shown in Figure 22.1a. It is composed of a straight and narrow index-guided section used to filter the input beam and convert it into a single spatial mode, and a gain-guided tapered section where the beam is amplified while preserving its shape. The tapered SOA of an integrated MOPA does not include an index-guided section since the MO provides a single spatial mode to the tapered section. Cross-sectional views of the index and gain-guided sections are shown in Figure 22.1b. The index-guided section is typically a ridge waveguide (RW) structure in which the etched regions (filled with an isolator) provide lateral optical confinement. In the tapered gain-guided section, the injection area is defined by a proton-implanted region.

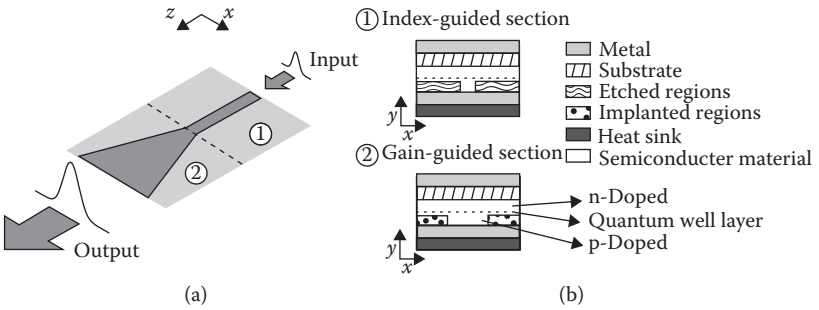

FIGURE 22.1 (a) Schematic planar view of a typical tapered SOA, consisting of a straight and narrow index-guided section and a gain-guided tapered section. (b) Cross-sectional views of the index-guided section (1) and the gain-guided section (2).

The characteristics of the output beam of a tapered SOA are very similar to those of tapered lasers which have been studied in detail by simulations and experiments (Williams et al., 1999; Sujecki et al., 2003; Borruel et al., 2004) and are reviewed in Volume 2 of this book (Chapter 28) (Esquivias et al., 2017). In brief, the single spatial mode of the RW section is launched into the tapered region where it suffers simultaneously diffraction, gain guiding, and index guiding (or antiguiding) due to the carrier and temperature dependencies of the semiconductor refractive index. The full taper angle α_{tap} is usually designed to match the free diffraction angle at $1/e^2$ (Borruel et al., 2008), and therefore it depends on the RW width and the lateral index step. At low power, the beam is strongly astigmatic: the virtual source in the lateral axis (x-axis) is located approximately at a distance from the output facet given by the taper section length divided by the effective index n_{eff}, while the virtual source in the vertical axis (y-axis) is at the output facet. The far-field (FF) pattern is almost Gaussian in both axes and much narrower in the lateral axis. However, when the output power increases, the beam quality degrades due to the combined effects of carrier and thermal lensing, as shown in Section 22.4.

The optimization of the tapered SOA's geometry and epitaxial design is a key point to improve the performance of these devices. The complex interaction between the semiconductor media and the optical field makes it extremely difficult to advance meaningful predictions of the behavior of a specific design by means of simple analytical calculations. Such difficulties together with the complex and costly fabrication process make necessary the use of complete numerical simulation tools to help the analysis and design of tapered SOAs to be used in hybrid or integrated MOPAs. Different numerical models, with different degrees of complexity, have been proposed and used to predict the behavior of tapered SOAs. In the case of the straight SOAs used in communications, the main emphasis has been placed on analyzing the dynamic response and the role of the amplified spontaneous emission in the noise characteristics (Razaghi et al., 2009; Connelly, 2001, and references therein). In contrast, in the case of high-power tapered SOAs the main performance characteristics are the maximum output power and the beam properties, and therefore steady-state models including thermal equations have been employed (Lang et al., 1993; Lai and Lin, 1998; Tijero et al., 2015).

In Section 22.2, we present a review of the different modeling approaches that can be applied to tapered SOAs; in Section 22.3, we explain the implementation of our numerical model; and in Section 22.4 we present as an example the results of the simulations of a 1.5-μm tapered SOA, including the analysis of the influence of some selected design parameters on the device performance. The Section 22.5 summary concludes the chapter.

22.2 Modeling Approaches

There are many options for the modeling approaches needed to simulate tapered SOAs. The proper choice depends on the degree of numerical complexity and on the performance characteristics of interest. In this

section, we review the most common approaches, explain the main differences between them, and refer the interested reader to the most important references for a detailed accounts. We will also use references corresponding to tapered lasers and laser diodes in general, as most of the modeling approaches for high-power SOAs are equally appropriate for high-power semiconductor lasers.

One of the main characteristics of tapered SOAs and lasers compared with other semiconductor devices is the nonuniformity of the photon, carrier, and temperature profiles along the longitudinal (z-axis) and the lateral directions. This leads to the need to solve the coupled equations in at least two dimensions and to use and using some approximation to solve the equations in the vertical direction separately.

22.2.1 Carrier Transport Models

The main role of a carrier transport model is to provide the 2D carrier density distribution along the active region, which is needed to calculate the main material parameters affecting the optical wave propagation (optical gain and losses and refractive index variation), as well as to calculate the local heat sources required by the thermal model. But, in turn, the knowledge of the local photon density and the temperature distribution is needed for solving the electrical equations, and therefore iterative schemes are usually applied (see Section 22.3). The external input is the applied voltage (V_0), rather than the total current (I), which is the usual input in experiments. In the RW section, the current flow spreads out of the nominal contact width. Furthermore, the local current density depends not only on the applied voltage but also on the local temperature and stimulated recombination, and hence on the local photon density, which is strongly dependent on the lateral and longitudinal position. In consequence, the current density J is not uniform, but depends on the position in the x–z plane, $J = J(x, z)$.

Most of the published tapered SOA models make use of the unipolar approximation assuming that the electron (n) and hole (p) densities in the active layer are identical (Lang et al., 1993; Lai and Lin, 1998; Spreemann et al., 2009). Under this approximation, which is also very common in laser diode models, the carrier density in the active layer $N(x, z)$ can be calculated using the simple rate equation:

$$\frac{\mathrm{d}N(x,z)}{\mathrm{d}t} = \frac{J(x,z)}{qd_{\mathrm{act}}} - R(N) - R_{\mathrm{stim}}(N,S) + D_{\mathrm{eff}}\nabla^2_{x,z}N(x,z), \tag{22.1}$$

where q is the elementary charge, d_{act} the active layer thickness, $R(N)$ the carrier recombination rate including nonradiative and spontaneous recombination, and $R_{\mathrm{stim}}(N, S)$ the stimulated recombination rate, which depends on the local photon density $S(x, z)$. Finally, finally, $D_{\mathrm{eff}}\nabla^2_{x,z}N(x, z)$ accounts for carrier diffusion in the longitudinal and lateral directions and is perhaps the most important consideration. In this expression, D_{eff} is an effective diffusion coefficient accounting for both the carrier diffusion and the current spreading. The local current density $J(x, z)$ can be expressed in terms of the applied voltage, the contact (and/or p-layer) resistivity, and the junction voltage $V_J(x, z)$, which in turn depends on the carrier density. Details on this formulation can be found in Lai and Lin (1998).

The unipolar approximation is a simple way to reduce the complexity of the carrier transport model and provides very reasonable results, but the p–n junction is essentially a bipolar device, thus requiring the solution of the complete semiconductor drift–diffusion equations. These equations can be expressed in terms of three unknown variables, the electrostatic potential (ϕ) and the electron (n) and hole (p) concentrations. In the steady state, the equations are (Selberherr, 1984)

$$\nabla\left(\varepsilon_S\nabla\varphi\right) + q\left(p - n + C_i\right) = 0 \tag{22.2}$$

$$\nabla\mathbf{j_n} - q\left(R(n,p) + R_{\mathrm{stim}}(n,p,S)\right) = 0 \tag{22.3}$$

$$\nabla\mathbf{j_p} + q\left(R(n,p) + R_{\mathrm{stim}}(n,p,S)\right) = 0, \tag{22.4}$$

where ε_S is the static dielectric constant, C_i is the charged impurity density (ionized donor density minus ionized acceptor density), and j_n (j_p) is the electron (hole) current density. The current densities can be

expressed as a function of the local variables ϕ, n, p, and temperature (T) using as local parameters the electron and hole mobilities and thermal diffusivities.

The carrier transport models often consider the capture and escape of carriers into and out of the quantum wells (QWs) (Nagarajan et al., 1992). This effect is well known in high-speed lasers, and it also influences the steady-state emission properties. When the carrier capture time is not negligible, there is an accumulation of carriers in the confinement layers that can result in a reduction of the efficiency (Borruel et al., 2003). In the case of unipolar models using rate equations, the carrier capture/escape processes are modeled by solving a second equation for the unconfined carriers. In the case of bipolar models of laser diodes using the complete semiconductor equations, different approaches have been proposed (Borruel et al., 2003; Grote et al., 2005), but as far as we know the importance of these effects in the modeling of SOAs has not been analyzed.

Bipolar carrier transport models require also appropriate boundary conditions at the metal–semiconductor contacts (Selberherr, 1984) and at the abrupt heterojunctions, where thermionic emission or tunneling-assisted thermionic emission should be considered instead of the standard drift–diffusion equations.

22.2.2 Optical Models

All optical models start from Maxwell equations and a description of the material susceptibility in the frequency or time domain, leading to optical wave equations, which have to be solved numerically. There are two main types of models: those solving the equations in the time domain, usually known as traveling-wave models (TWM), and frequency domain models. TWM provide dynamic solutions as well as spectral properties, and are appropriate for pulse propagation, beam filamentation, transient phenomena, and multifrequency devices. Frequency domain models are much simpler to implement and are useful for steady-state studies where the overall behavior of the device can be described in terms of a single frequency.

The beam propagation method (BPM) (Van Roey et al., 1981) is the most commonly used frequency domain method for the field propagation in waveguide optoelectronic and fiber devices, thanks to its low computational time demand. BPM calculates the propagation along the longitudinal direction of the steady-state transverse field, verifying the Helmholtz equation:

$$\nabla^2 \vec{E}(x, y, z) + \tilde{n}^2(x, y, z) k_0^2 \vec{E}(x, y, z) = 0, \tag{22.5}$$

where $\vec{E}(x, y, z)$ is the complex optical field vector, $\tilde{n}(x, y, z)$ is the complex refractive index, and k_0 is the wavenumber in vacuum.

In order to obtain a solution for the Helmholtz equation, the scalar approximation is commonly used in the study of tapered lasers and amplifiers (Sujecki et al., 2003; Lang et al., 1993). This approximation ignores the vectorial nature of the field, assuming continuity of the field and its derivatives through the dielectric interfaces. The approximation implies that the optical polarization remains unchanged along the device. The effective refractive index approximation is used to decrease the computational complexity of the BPM (Buus, 1982). It consists of solving Equation 22.5 for the vertical axis at every lateral position, taking into account the existence of etched regions and considering only a real index vertical profile (passive approximation). This leads to an effective index lateral profile and a vertical distribution of the optical mode $f(y)$. The effective index profile is used for the beam propagation and the function $f(y)$ is usually assumed to be independent of the longitudinal and lateral positions. In this way, the original 3D problem becomes a 2D problem in the x–z plane.

Dynamical TWMs naturally incorporate the spatial effects and the multifrequency character of the field, with the geometry of the device being incorporated through the boundary conditions for the waves. Although TWMs have long been applied to study laser physics (Lugiato and Narducci, 1985), application

to semiconductor media requires a proper description in the time domain of the spectral dependence of the gain and the index changes due to the injected carriers. TWMs are based on making the slowly varying amplitude approximation or paraxial approximation of the electric fields. Under this approximation, the equations for the electric field of the optical wave can be written as

$$-\frac{i}{2k_0}\frac{\partial^2 E_\pm}{\partial x^2} \pm \frac{\partial E_\pm}{\partial z} + \frac{1}{v_g}\frac{\partial E_\pm}{\partial t} = f(E_+, E_-, P_+, P_-), \tag{22.6}$$

where $E_\pm$ are the complex counter propagating electric fields, v_g is the group velocity, and the function f contains different terms describing the relationship of the field with the dielectric polarization ($P_\pm$) that includes gain, internal losses, Bragg couplings, etc. Several approaches have been used to solve Equation 22.6, including finite-difference time-domain (Fischer et al., 1996) and Fourier split-step methods (Spreemann et al., 2009; Pérez-Serrano et al., 2013). Although TWMs have been applied mainly for describing laser dynamics, they have also been applied to tapered SOAs (Balsamo et al., 1996) and for the analysis of coupled cavity effects in tapered MOPAs (Spreemann et al., 2009; Pérez-Serrano et al., 2013).

22.2.3 Thermal Models

The temperature distribution along the complete device is a relevant variable in the simulation of a tapered SOA due to the dependence of the gain and refractive index on the local temperature. The 3D steady-state heat equation is expressed as

$$\nabla(\kappa \nabla T) + w(x, y, z) = 0, \tag{22.7}$$

where κ is the temperature-dependent thermal conductivity and $w(x, y, z)$ the local density of heat sources. This term usually includes Joule, nonradiative recombination, and free-carrier absorption heat sources. A complete description, based on a rigorous thermodynamic approach (Wachutka, 1990), can be found in Bandelow et al. (2005). Two heat sources are usually not included in most of the laser and amplifier models due to the difficulties in the quantification of their local distribution. These are the sources of heat arising from the energy lost by the scattered stimulated photons and by the spontaneously emitted photons that do not leave the device. After a photon recycling process, their energy ends up in heat transferred to the lattice somewhere in the device. To account for this effect, as well as for other uncertainties in the expressions and parameters for the local heat sources, an additional excess power P_{exc} shall be included (Borruel et al., 2002). The amount of this power is calculated from the energy conservation expression:

$$P_{exc} = IV_0 - (P_{out} - P_{in}) - \int w(x, y, z)\mathrm{d}V, \tag{22.8}$$

where P_{out} and P_{in} are the output and input powers, respectively, and the integration extends over the entire device volume. After determining P_{exc}, the corresponding heat source w_{exc} is either distributed uniformly over the whole device or weighted according to the different absorption properties of the epitaxial layers.

Thermal equations should be solved taking into account the boundary conditions imposed by the thermal properties and the geometry of the mount and submount and the heatsink temperature.

22.2.4 Material Properties

22.2.4.1 Material Susceptibility

There are different options to describe the interaction between the gain medium and the optical field. The simplest approach, which is usually employed in rate equation models, is to consider a logarithmic or linear

dependence of the material gain on the carrier density, together with a constant value for the linewidth enhancement factor (LEF) (Lai and Lin, 1998). The gain spectra can be taken as Lorentzian (Spreemann et al., 2009), although the most sophisticated models include a complete solution of the band dispersion equations to calculate the material gain as a function of the local carrier densities, the wavelength, and the temperature. A complete microscopic 8×8 $\mathbf{k}\cdot\mathbf{p}$ model for the semiconductor band structure implies a large computational effort and even a more simplified 4×4 valence band mixing model results in a high computation time when repeated locally. Additionally, most of the input parameters for the complete models are not well known. For these reasons, some modeling approaches perform initial complete or semicomplete band structure calculations and either (1) use a parabolic band model previously fitted to the results of the complete model (Borruel et al., 2004), (2) use curve fits to a more sophisticated model (Mariojouls et al., 2000), or (3) use precalculated look-up tables (Koch et al., 2005).

The refractive index's dependence on the wavelength, carrier density, and temperature can also be calculated using complete microscopic approaches (Koch et al., 2005) and then again using look-up tables to decrease the computational cost. A simpler approach is to neglect the wavelength dependence of the index and to use simple expressions for the carrier and temperature dependencies, i.e.,

$$\delta\tilde{n} = \delta\tilde{n}_T + \delta\tilde{n}_N, \tag{22.9}$$

where $\delta\tilde{n}$ is the variation of the active layer index with respect to its reference value at the heatsink temperature and without injection, $\delta\tilde{n}_T$ is the thermally induced variation, and $\delta\tilde{n}_N$ is the carrier contribution to the variation. $\delta\tilde{n}_T$ is usually considered a linear function of the local temperature increase while $\delta\tilde{n}_N$ can be considered either as dependent on the carrier density (Connelly, 2001; Borruel et al., 2004) or it is calculated from the gain variations using a constant LEF (Lang et al., 1993; Mariojouls et al., 2000).

Full space-time models require a good description of the material complex susceptibility, which has been done in different ways: at microscopic level (Gehrig and Hess, 2001), by using multiple Lorentzians fitted either to experiments or to microscopic calculations (Moloney et al., 1997), and by a convolution integral (Javaloyes and Balle, 2010).

22.2.4.2 Carrier Recombination

The unipolar models typically use a polynomial approximation for the carrier recombination rate in Equation 22.1, which can be given by

$$R(n) = An + Bn^2 + Cn^3, \tag{22.10}$$

where A, B, and C are the coefficients corresponding to nonradiative trap recombination, spontaneous recombination, and Auger recombination, respectively. It is important to remark that even in this simple description, the dependence of the coefficients on temperature, especially the dependence of C, should be taken into account. Some other polynomial approaches have also been employed (Connelly, 2001). The more complete bipolar models use the complete Shockley–Read–Hall (SRH) recombination expression for the nonradiative trap recombination and the electron and hole Auger recombination rates and calculate the spontaneous recombination rate from the complete energy band description by using the same approach used for the optical gain.

22.2.4.3 Internal Losses Coefficient

The internal absorption losses have a dramatic effect on the amplifier performance, and therefore the coefficient accounting for them, α_{in}, is an extremely important parameter for the simulation. It can be taken as a constant value to be estimated from experiments in broad area lasers, or it can be considered the result of two contributions: the scattering losses α_{scat}, and the losses due to different mechanism of photon absorption by free carriers, the so-called free-carrier absorption losses α_{fc}. In the approaches that solve the

electrical equations in the vertical direction (Borruel et al., 2004; Grote et al., 2005), α_{fc} is locally calculated taking into account the carrier and photon distribution by

$$\alpha_{fc}(x,z) = \int_{L_y} \left[\kappa_n n(x,y,z) + \kappa_p p(x,y,z)\right] S(x,y,z)\mathrm{d}y, \tag{22.11}$$

where L_y is the thickness of the epilayer structure, and $\kappa_n(\kappa_p)$ is the electron (hole) free carrier absorption cross section. In most materials, the main contribution to α_{fc} arises from the hole term due to the mechanism of intervalence band absorption.

The most sophisticated amplifier models, especially those solving the complete electro-thermal-optical semiconductor equations, require many additional material parameters such as carrier mobilities, bandgap narrowing coefficients, energy band parameters, thermoelectric powers, thermal conductivities, etc.

22.3 Model Implementation

22.3.1 Overview of Solution Procedure

In this section, we describe the implementation of HAROLD 4.0, the model and code that we have developed for the simulation of tapered SOAs. Our approach is based on a previous model for tapered lasers (Borruel et al., 2004; Sujecki et al., 2003). The original algorithm has been modified slightly and a part of it has been rewritten in order to consider a single pass amplifier instead of a resonant cavity. HAROLD 4.0 solves self-consistently the steady-state partial differential equations describing the electrical, thermal, and optical behavior of a tapered SOA. The simulator includes a 3D electrical solver for the Poisson and continuity equations (Equations 22.2 through 22.4) coupled to a 3D thermal solver for the heat-flow equation (Equation 22.7). The thermal solver uses the local heat sources provided by the electrical solution. On the optical side, a wide-angle finite-difference beam propagation method (WA-FDBPM) (Hadley, 1992), under the effective index approximation, is used to propagate the optical field in the x–z plane. The optical solution is not fully 3D, as the vertical direction and the x–z plane are solved separately, and therefore the complete model is considered as quasi-3D.

Due to the large number of variables and iteration loops involved in the model, an important point is how to initialize the solution. In order to provide a good initial guess to the quasi-3D algorithm, a 1D laser simulator (Harold, 2001) is used for the initialization of the electrical, thermal, and optical variables. Although the 1D laser simulator was not designed for amplifiers, it provides useful initial guess values for the electrothermal variables as well as some inputs for the quasi-3D algorithm such as the applied voltage V_0 and the optical field modal profile in the vertical direction $f(y)$. The 1D simulator requires the electrical, thermal, and optical properties of all the device materials. The user introduces a target bias current and the 1D simulator solves the electrothermal and optical equations for an equivalent broad area laser having the same electrical injection area as the tapered SOA. The 1D simulator provides V_0, as well as an initialization for the vertical distribution of the electrostatic potential, the electron and hole concentrations, and the temperature. The power, wavelength, and lateral profile of the input optical field are provided by the user as inputs for the algorithm. The input optical field is symmetric and therefore only one half of the device is considered in the simulations.

The main flow of the quasi-3D algorithm is shown in Figure 22.2. It includes the following steps: (1) the 1D simulator provides V_0 and $f(y)$, and initializes all unknown 2D variables according to the initial 1D solution for the target current; (2) the initial lateral optical field profile at the first longitudinal slice ($z_i = 1$) is either set by the user or calculated as the fundamental mode of the waveguide in the lateral direction; (3) A 2D electrical solver is applied to the first slice in the $x - y$ plane at $z_i = 1$. It provides a 2D map of the electrical variables (n, p, and φ) and of the Joule (w_{joule}), the nonradiative (w_{nr}), and the free-carrier (w_{fc}) heat sources. It also calculates the complex effective refractive index along the lateral axis

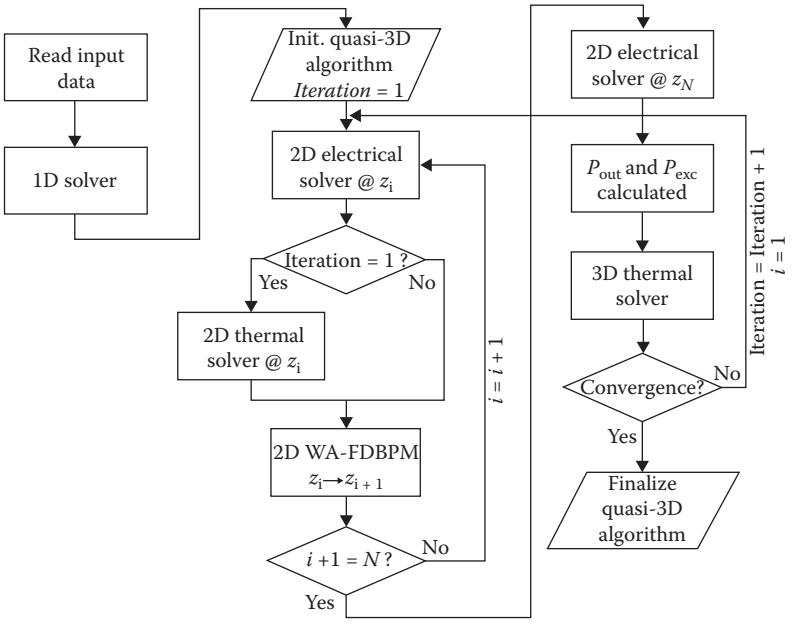

FIGURE 22.2 Main flow of the quasi-3D algorithm HAROLD 4.0 (see text for details).

at $z_i = 1$, thus providing the gain and refractive index variation due to the carriers. (4) The calculated heat sources are used as inputs for a 2D thermal solver applied to the x–y plane at $z_i = 1$. It should be noted that the thermal and electrical meshes are different and therefore some interpolation between the meshes is used. The 2D thermal solver provides a map of the temperature in the x–y plane and the thermally induced refractive index variation. This 2D thermal solver is only applied in the first iteration in order to initialize the thermal solution. (5) The WA-FDBPM is used to propagate the optical field from $z_i = 1$ to $z_i = 2$ using a fine mesh in the x–z plane. It uses the gain and refractive index changes given by the electrothermal solvers in the previous step and takes into account the geometry of the device. (6) Steps (3)–(5) are repeated until the algorithm arrives to the output facet at $z_i = N$. At this point, the output power P_{out} is known and the excess power P_{exc} can be calculated. Then, a 3D thermal solver is applied allowing heat flow between the z-slices. (7) The process described in (3), (5), and (6) is repeated until convergence is reached and a stable optical field, as well as stable temperature, carrier, and current distributions are found.

In the following subsections, the solvers for the electrical, thermal, and optical equations are described in more detail.

22.3.2 Solver for Electrical Equations

The electrical equations are solved in the volume defined by the total thickness of the epitaxial layers, the amplifier length, and the chip width. The input for the equations is taken from material databases according to the epilayer structure. Etched and implanted regions are simulated by assuming negligible carrier mobility. The electrical equations are solved together with two capture–escape continuity equations for electrons and holes at each QW, taking into account the nonequilibrium condition between the confined carriers in the QWs and the unconfined carriers in the barriers. Nonradiative (SRH and Auger) and spontaneous recombination terms are included along the complete device, in addition to the stimulated recombination in the active region. The model also includes free carrier absorption and band gap renormalization with standard dependencies and appropriate parameters.

The material gain and spontaneous recombination rate in the QWs are calculated using the expressions in Coldren and Corzine (1995), considering simple parabolic bands and Lorentzian broadening to decrease the computational effort. The parameters for the gain calculations (energy levels, effective masses, and intraband relaxation time) were previously fitted to yield similar results to those of a more sophisticated gain model that takes into account the valence band mixing. The local material gain (or absorption) and carrier-induced refractive index changes are calculated at the wavelength of the input power for each point of the mesh, taking into account the local temperature and carrier concentrations. They are subsequently used as inputs for the optical solver.

The equations are discretized using a finite difference approach. Nonuniform, separate meshes are taken for the vertical and lateral directions. The denser regions in the vertical and lateral directions correspond to the QW and to the border of the implanted/etched areas, respectively. The lateral mesh depends on the longitudinal position and typically contains around 40 mesh points. We chose 100 μm for the x–y slice separation in the longitudinal direction, after making sure that the results in our structures were similar when decreasing the longitudinal mesh size. The core of the numerical procedure is a Newton–Raphson algorithm, which solves the coupled Equations 22.2 through 22.4 in 1D along the vertical direction. The algorithm considers at each mesh point the influence of the next neighbors in the lateral and longitudinal directions. The 1D solver scans iteratively the lateral direction until convergence, providing a 2D map of the electrical variables at the z-slice i, z_i. The electrical variables are used to calculate the heat sources needed by the thermal solver, while the computed gain (or absorption) and the carrier-induced refractive index changes will be used by the optical solver to propagate the electric field to the slice z_{i+1}. In the resolution of the z_{i+1} slice, the values of the electrical variables previously obtained for z_i and z_{i+2} are considered in order to account for the longitudinal current flow. Finally, when convergence of the whole algorithm is reached, a complete 3D map of the electrical variables (electrostatic potential and electron and hole densities), consistent with the photon and temperature distributions, is produced.

22.3.3 Solver for Optical Equations

As mentioned above, the shape of the field at the amplifier input ($z_i = 1$) is either provided by the user or obtained by solving the Helmholtz equation in the lateral direction making use of the effective index approximation. Then, the WA-FDBPM is applied to propagate the field along a longitudinal optical mesh, which is much denser than the electrothermal mesh. The method uses the modal complex index along the lateral axis provided by the electrothermal solution of the initial slice. The WA-FDBPM uses the (1,1) Padé approximant, allowing the propagation of the field a few degrees around the longitudinal direction (1°–6°). The propagation continues until reaching the next slice of the electrothermal mesh, where the electrical and thermal solvers update the modal complex index. In this way, the tapered section is considered a succession of rectangular slices with increasing width.

To complete the optical solution, perfectly matched layers (PML) (Huang et al., 1996) are used as boundary conditions. The PML method defines a lossy region to which the Helmholtz equation is mapped by an anisotropic complex transformation. The PML attenuates the lateral traveling waves ensuring that the field at the borders of the device in the lateral direction vanishes. Due to the lateral symmetry of the optical field, a zero derivative is applied as the boundary condition at $x = 0$.

22.3.4 Solver for Thermal Equations

The heat flow equation (Equation 22.7) is solved in a larger region and using a different mesh than those of the electrical solver. In addition to the epilayer, the substrate, the metal layers, and the heatsink are also considered in the thermal solution. The boundary conditions for the heat-flow equation in the case of a p-down mounted device are negligible heat flow at the n-metal and lateral chip external interfaces and uniform temperature at the bottom of the heatsink. Etched regions are thermally simulated by introducing the thermal conductivity of the planarization isolator.

As mentioned in Section 22.3.1, during the first iteration of the Quasi-3D algorithm, the 2D heat flow equation is solved at each x–y slice with the local heat sources obtained from the electrical solver. The 2D heat flow equation is discretized with a finite difference method, and the system of equations is solved by using a stabilized biconjugate gradient method. The calculated temperature distribution replaces the initialization values provided by the 1D laser simulator. Once the electro-optical solution process has reached, the output facet and the output power P_{out} has been calculated, the excess power P_{exc} is calculated using Equation 22.8, and the excess power heat source is distributed along the complete device volume. Then, a 3D thermal solver is applied. The 3D thermal solver is based on scanning the 2D solver along the longitudinal direction allowing the longitudinal heat flow between slices until reaching convergence. Successive iterations of the complete algorithm use this 3D thermal solver as indicated in Figure 22.2.

22.4 Simulation Example: 1.5-μm InGaAsP/InP Tapered Amplifier

As an illustrative example, in this section we analyze a typical 1.5-μm InGaAsP/InP tapered amplifier with the HAROLD 4.0 simulation tool. After a summary of the most relevant material, and geometrical and simulation parameters, we present the simulation results of a reference device and based on these results, we illustrate the potential of the simulation tools by analyzing the effect on the device performance of two important design parameters: the taper angle α and the confinement factor Γ. The analysis is presented here only for the sake of illustration, so we will present an overview of some interesting effects without a detailed analysis.

22.4.1 Device Geometry and Simulation Parameters

As a reference device, we have considered an SOA with an InGaAsP/InP multi-QW epitaxial structure similar to that of the MOPA reported in Faugeron et al. (2015). It features an asymmetric cladding structure especially conceived for shifting the broad vertical profile of the optical mode to the n-side of the diode, thus minimizing the overlapping with the highly absorbing p-doped layers. Table 22.1 provides the geometrical parameters of the device as well as a brief summary of the most influential material and device parameters used in the simulation. The taper angle has been selected so as to fit the calculated free diffraction angle assuming an index step $\Delta n_{eff} = 7 \times 10^{-3}$. We have considered a p-side down mounting configuration as more appropriate for the heat management required in a power device. For the Auger recombination

TABLE 22.1 Geometrical Parameters of the Reference SOA and Summary of the Most Relevant Material and Device Parameters Used in the Simulation

Symbol	Parameter	Value	Units
L_{RW}	Length of the ridge waveguide (RW) section	1	mm
W_{RW}	Width of the RW section	3.5	μm
L_{Tap}	Length of the taper section	2	mm
α_{tap}	Taper angle	7	°
Δn_{eff}	Effective index step of the RW section	7×10^{-3}	–
	Mounting configuration (p-up/p-down)	p-Down	–
T_{HS}	Heatsink temperature	18	°C
P_{in}	Input power	20	mW
Γ	Confinement factor	0.037	
α_{scat}	Scattering losses coefficient	0.5	cm^{-1}
$C_n(C_p)$	Electron (hole) Auger recombination coefficient	$8(8) \times 10^{-29}$	$cm^6 s^{-1}$
k_e (k_h)	Electron (hole) free carrier absorption coefficient	$1(30) \times 10^{-18}$	cm^2
n_I	Differential refractive index coefficient	10^{-1}	$cm^{3/2}$

coefficients and the electron and hole free carrier absorption coefficients, we have used judicious values in the range of published values (Joindot and Beylat, 1993; Piprek et al., 2000). We have accounted for the dependence of the refractive index on the carrier density by means of a square root function with a coefficient n_1 (Borruel et al., 2004) such that it results in a value of about 5 for the LEF at the operating wavelength and carrier densities. The value used for the internal scattering losses together with the free-carrier absorption losses calculated using Equation 22.9 yield a total internal loss of approximately 8 cm^{-1} for a broad area laser with the same epitaxial structure.

22.4.2 Analysis of the Reference SOA

Figure 22.3 shows the simulated power–current (P–I) characteristics of the reference SOA together with the evolution of the electrical-to-optical conversion efficiency ($\eta_{E\text{-}O}$). For injection currents above a transparency level ($I \sim 1.3$ A) the device actually amplifies with an increasing conversion efficiency. The output power shows an approximately linear increase in the current range $4 < I < 9.5$ A. For higher injection levels, both the output power and the conversion efficiency start a saturation process.

The simulation provides the means to make a more in-depth analysis revealing details of the behavior of relevant variables inside the SOA. As an example, Figure 22.4 shows 3D plots of several magnitudes in the QW region for a relatively low injection current ($I = 4$ A). In the RW section, due to the index guiding, the profile of the photon density (Figure 22.4a) is narrow and stable, and shows an increase of the maximum along the longitudinal direction revealing the optical gain. The maximum drops and the profile broadens when the tapered region starts, and from there up to the output facet, the photon profile evolves smoothly. In this evolution, the maximum photon density increases and so does the profile width, following the evolution of the width of the tapered section. For this relatively low injection level, the electron density profile (Figure 22.4b) is almost flat inside the tapered section. In the RW section, the electron density profile is broader than the width of the section due to the current spreading (not shown). The maximum electron density in this section is lower than the density in the tapered section and decreases slightly along the longitudinal direction. Both effects are a consequence of a higher stimulated recombination ratio in the RW section. The hole density (not shown) is slightly different but shows a similar profile. The mutual dependence between carrier and photon densities is much more pronounced at high-injection levels as explained below. The temperature profile in the lateral direction (Figure 22.4c) reminds the injection profile showing higher values in the injected region and a fast variation at the edge of the region. In the RW section, the lateral profile shows a small dip at the cavity center, whereas in the tapered section, the temperature decreases smoothly from a maximum at the axis to a minimum at the edges of the injected region. In the noninjected regions, the lateral evolution is smooth and shows a slow decrease toward the edges of the chip. In the longitudinal direction, the temperature increases smoothly from the RW section to the output facet. This increase is slow in the RW section and faster in the taper section (see also Figure 22.5b). At

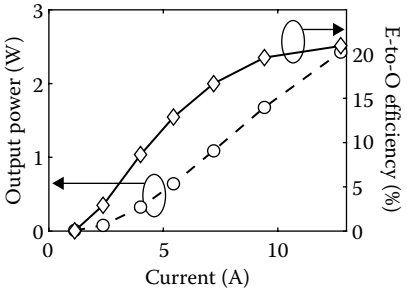

FIGURE 22.3 Power–current characteristics (circles) and electrical-to-optical conversion efficiency (diamonds) of the reference SOA.

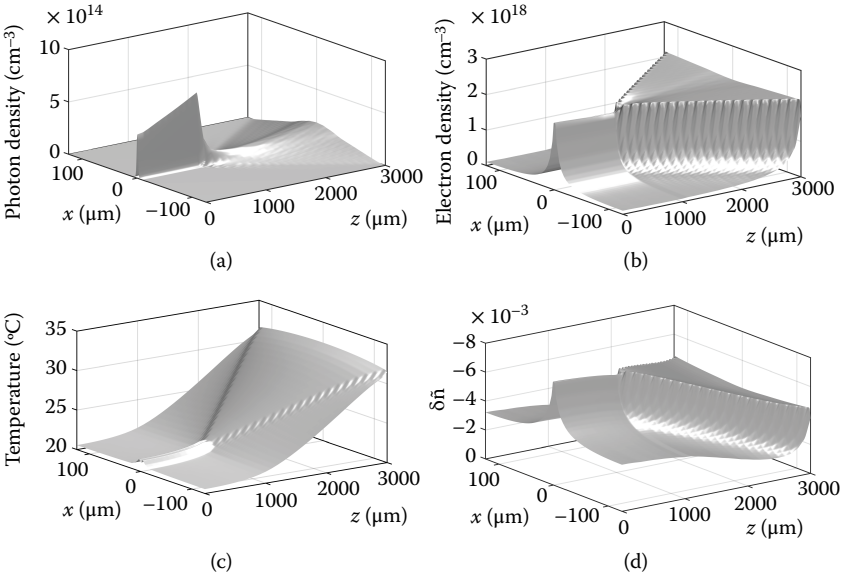

FIGURE 22.4 3D maps of the photon (a) and the averaged electron densities (b), the temperature (c), and the carrier and thermally induced refractive index change (d) in the active region of the reference SOA for an injection $I = 4$ A. The little "ripples" appearing at the edges of the tapered section in some plots are artifacts due to the discretization in the longitudinal direction.

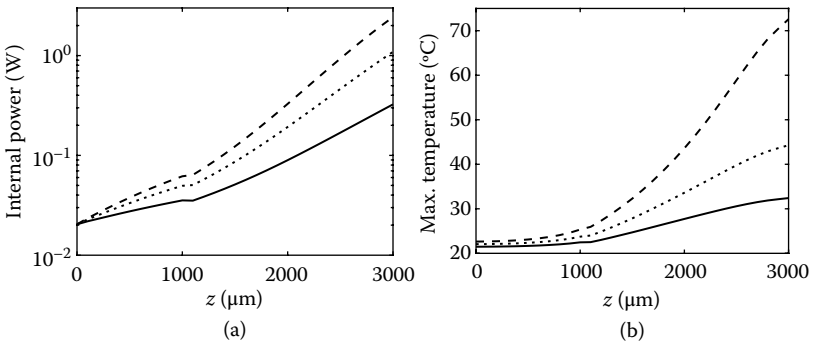

FIGURE 22.5 Evolution along the longitudinal direction of the internal optical power (a) and the maximum QW temperature (b), for different current values. $I = 4$ A (solid), $I = 7.2$ A (dotted), and $I = 12.7$ A (dashed).

this relatively low-injection level, the evolution of the longitudinal temperature profiles are similar in the injected and in the noninjected regions. Finally, Figure 22.4d shows a 3D map of the QW refractive index variation given by Equation 22.9. This variation is a balance between the positive thermal contribution and the negative contribution of the excess carrier density. Therefore the profile is similar to the electron density profile (Figure 22.4b) smoothly modified by the temperature profile (Figure 22.4c). This index variation is the way by which the density of carriers and the local temperature influence the photon density and, hence, the beam profile.

More insight into the evolution of the optical power along the SOA can be provided by plots such as the one in Figure 22.5a, where the internal optical power at each x–y slice is plotted along the longitudinal direction in a logarithmic scale. The evolution of the internal optical power can be described in terms of an effective optical gain g_{eff} by $P(z + \Delta z) = P(z)e^{g_{\text{eff}}\Delta z}$ and therefore g_{eff} is proportional to the slope of the

curves in Figure 22.5a. In this description, g_{eff} corresponds to the difference between the modal gain and all the losses occurring in the beam propagation. For the low-injection level considered previously (4 A, solid line), the effective gain is relatively low and slightly decreasing in the RW section and much higher in the tapered section. This can be explained from the maps of photon and carrier densities in Figure 22.4a and b: for approximately the same carrier density in both sections, the photon density is much higher in the RW section and therefore the gain shows an increasing saturation effect which is absent in the tapered section where the photon density is much lower. In a transition region, just at the beginning of the tapered section, there is a dramatic drop of the gain corresponding to an increase of the losses due to the change in the guiding mechanism from index guiding to gain guiding. This drop is due to the poor overlapping of the mode and the injected region at the beginning of the tapered section since the external part of the mode expands to unpumped and, therefore, absorbing regions. In this device, in which the taper angle (and therefore the angle of the gain region) almost matches the free diffraction angle, the gain recovers soon after the transition. For higher-injection levels, Figure 22.5a shows a qualitatively similar behavior of the gain. In both sections, the gain is higher as corresponding to a higher carrier density and evidences some saturation at the end of each section corresponding to a high photon density in these regions.

To complete the overview picture of the longitudinal evolution of internal variables, Figure 22.5b shows the evolution of the maximum QW temperature for the same low-, intermediate-, and high-injection levels of Figure 22.5a. As expected, the QW temperature evolves similarly for the three injection levels, showing a faster increase in the taper section for the highest injection level.

More local details of the behavior of the photon and carrier densities when the injection increases are provided by Figure 22.6. Figure 22.6a shows the electron and photon density profiles along the lateral direction at the output facet of the device. The mutual dependence between carrier and photons pointed above for low injection is much more apparent at high-injection levels and can be explained as follows: The density of carriers injected at these levels is high on average. In comparison with the outer regions, the number of photons generated by stimulated recombination around the axis ($x = 0$) (where the optical mode reaches the maximum) is higher, and therefore the carrier density locally decreases. This is the well-known spatial hole burning (SHB) effect. Due to its negative dependence on the carrier density, the refractive index locally increases in the places more affected by the SHB effect, giving rise to a more abrupt index profile. In turn, the new index profile contributes to a higher confinement of the optical mode in the axial region in a feedback loop in which the local temperature also plays a role through the thermal dependence of the refractive index. As a consequence, the smooth profile of the optical beam at low injection undergoes a slight degradation when the injection increases as illustrated in Figure 22.6b, where the FF profiles at the three injection levels have been compared.

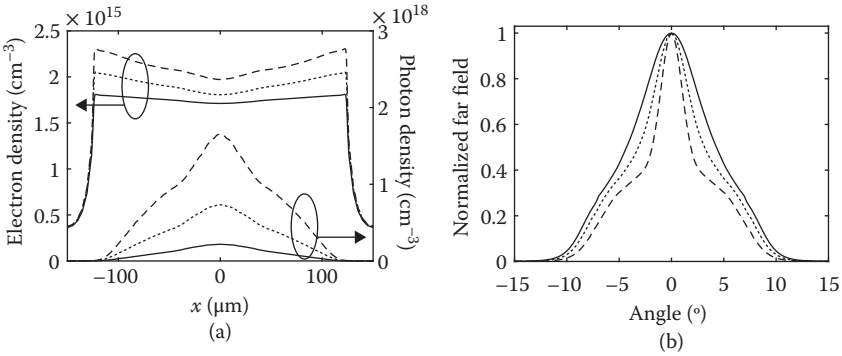

FIGURE 22.6 (a) Photon and electron density lateral profiles at the output facet for three injection levels. (b) The corresponding far field profiles. $I = 4$ A (solid), $I = 7.2$ A (dotted), and $I = 12.7$ A (dashed).

22.4.3 Effect of the Confinement Factor and Taper Angle

The confinement factor and the taper angle are two critical design parameters affecting the performance of a tapered SOA. In order to illustrate the capabilities of the simulation tools for the analysis of the influence of these parameters, we have compared the reference SOA ($\Gamma = 3.7\%$ and $\alpha = 7°$) with two devices: (1) an SOA which epitaxial design has been carefully modified so as to result in a confinement factor $\Gamma = 5.6\%$ without increasing the mode overlapping with the p-doped cladding (high Γ-SOA) and (2) a device with $\alpha = 3°$ and the same RW and tapered section lengths as the reference SOA (3°-SOA). Figure 22.7 shows a comparison of the *P–I* characteristics, and the conversion efficiency of the three devices. In comparison with the reference SOA, the high Γ-SOA has a lower transparency current, a higher slope of the *P–I* characteristics, and a higher conversion efficiency. Therefore, at the highest current its output power and conversion efficiency are significantly higher. This can be qualitatively understood just taking into account the higher mode overlapping with the active region. The 3°-SOA shows also a lower transparency current, a higher slope of the *P–I* characteristics, and a higher conversion efficiency. In this case, the explanation is the higher current density corresponding to the same current as a consequence of the lower area of the device.

Figure 22.8 shows the effective optical gain in the three devices at the highest injection level of around 13 A. Note that the output power of each device is different (see Figure 22.7a). In the RW section, the effective gain of the high Γ-SOA is only slightly higher than the effective gain of the reference SOA in spite of the higher value of Γ. The reason for this is the material gain saturation due to the high photon density in this section that makes the gain almost independent of Γ. The effective gain of the 3°-SOA in this RW section reaches higher values corresponding to the higher carrier injection. In the tapered section, the gain of the high Γ-SOA is clearly superior to that of the reference SOA as can be expected from its higher value of Γ. The difference is more apparent at the beginning of the section, where the photon densities are low, than at the end, where the photon densities (and hence the saturation) become high. The most revealing difference between the gain of the 3°-SOA and the other devices is in the transition region at the beginning of the taper section where the mismatch between the free diffraction angle and the taper angle in the 3°-SOA results in high losses evidenced as a low effective gain in this region.

The improved performance of the high Γ-SOA and the 3°-SOA in terms of output power and conversion efficiency is, however, at the expense of a much faster beam degradation as revealed by the evolution of the FF width and the beam propagation factor (M^2) plotted in Figure 22.9 (see [Esquivias et al., 2017] Chapter 28, Volume 2 of this book). In the case of the high Γ-SOA, the beam quality as revealed by M^2 progressively worsens, reaching high values at relatively low currents. In the case of the 3°-SOA, the degradation takes place at intermediate values of the current whereas the reference SOA keeps a relatively low value of M^2 up to a high-injection level.

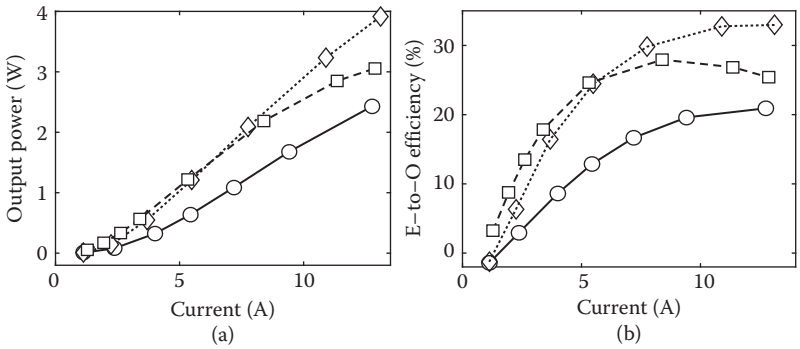

FIGURE 22.7 (a) *P–I* characteristics of the reference SOA (circles), the high Γ-SOA (diamonds), and the 3°-SOA (squares). (b) Their corresponding electrical-to-optical conversion efficiencies.

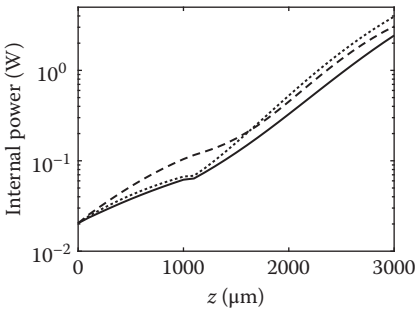

FIGURE 22.8 Evolution along the longitudinal direction of the internal optical power of the three devices at the highest injection ($I = 13$ A), showing the different effective gain (slope of the curves). Reference SOA (solid), high Γ-SOA (dotted), and 3°-SOA (dashed).

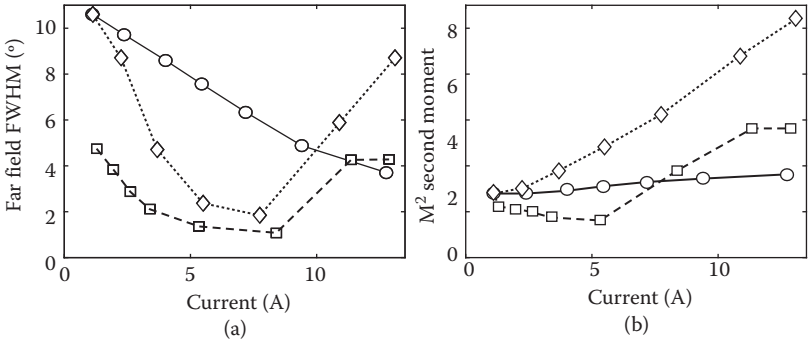

FIGURE 22.9 (a) Far field full width at half-maximum (FWHM) and (b) M^2 dependence on current for the three devices considered. Reference SOA (circles), high Γ-SOA (diamonds), and 3°-SOA (squares).

As mentioned above, more detailed information of the mechanism underlying beam degradation is brought by the plots in Figure 22.10a where the electron and photon density profiles at the output facet of the three devices are plotted for the highest injection level. The mutual dependence between carriers and photons described in Section 22.4.2 for the reference SOA is much more apparent for the high Γ- and the 3°-SOAs and results in deep holes in the axial region of the electron density profiles together with the corresponding narrow peaks in the photon density. As a consequence, the beam quality severely degrades, as revealed, for example, by the FF profiles plotted in Figure 22.10c and d in comparison with the profile of the reference SOA (Figure 22.10b).

The self-focusing is another manifestation of the beam degradation due to the interplay between carriers and photons. Figure 22.11 shows a comparison between the evolution of the beam profiles in the reference (Figure 22.11a and b) and the 3°-SOA (Figure 22.11c and d) for low- (Figure 22.11a and c) and high injection conditions (Figure 22.11b and d). In these plots, the photon density in each slice perpendicular to the longitudinal axis has been normalized to its maximum value in order to visualize the focusing. The white dashed lines show the borders of the injected region. In contrast with the virtually absent focusing of the beam in the reference SOA, Figure 22.11d shows a strong self-focusing in the 3°-SOA at high current. As a consequence, the slightly increasing astigmatism in the reference SOA when the injection increases (not shown) becomes abrupt and then drops down to negative values in the 3°-SOA.

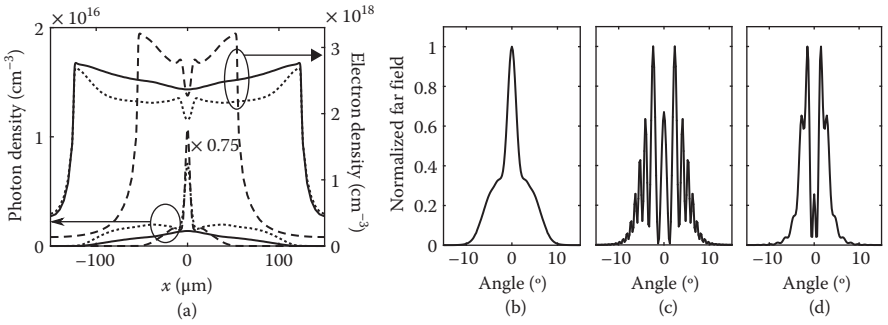

FIGURE 22.10 (a) Photon and electron density lateral profiles at the output facet at the highest injection level ($I = 13$A) for the three devices considered. Reference SOA (solid), high Γ-SOA (dotted), and 3°-SOA (dashed). For clarity, the photon density values of the 3°-SOA device (dashed) have been multiplied by 0.75. (b) through (d) Normalized far field profiles for the reference SOA, the high Γ-SOA, and the 3°-SOA, respectively.

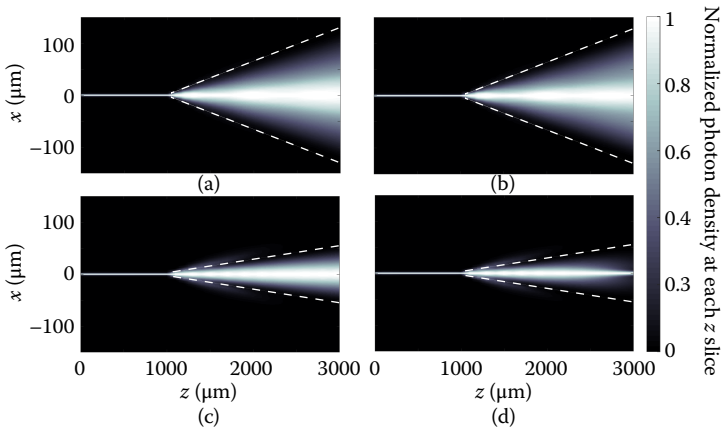

FIGURE 22.11 Maps of the normalized photon density of the reference SOA (top) and the 3°-SOA (bottom) under low-injection (left) and high-injection conditions (right). The white dashed lines show the borders of the injected region. For each value of the longitudinal coordinate z, the photon density was normalized to its maximum along the corresponding lateral x-axis.

22.5 Summary

We have presented an overview of the current state of the art in the modeling of high-power tapered SOAs. We have described the most relevant models used for the simulation of carrier transport, optical field, material properties, and temperature distribution in this type of devices. The particular geometry of tapered amplifiers makes difficult the reduction of the dimensionality of the problem, requiring relatively complex numerical models. The implementation of a steady-state quasi-3D model has been explained in detail, with emphasis on the interaction between the electrical, thermal, and optical solvers. For illustration, the model has been applied to a 1.5-μm tapered SOA, showing the relation between internal carrier and photon distributions and the external measurable characteristics. The influence of the optical confinement factor and the taper angle in the output power and beam quality has also been analyzed.

The main limitation of the steady-state single-frequency models is that they cannot be used to analyze the noise properties of the SOAs, as well as other complex nonlinear phenomena as cross-talk in wavelength division multiplexing applications. Two- or quasi-3D TWMs, coupled to bipolar carrier and thermal equations are the natural evolution of steady-state models to account for dynamical and spectral issues.

Acknowledgments

This work was supported by the European Commission through the FP7-Space project BRITESPACE under grant agreement no. 313200, by Ministerio de Economía y Competitividad of Spain under projects RANGER (TEC2012-38864-C03-02) and COMBINA (TEC2015-65212-C3-2-P), and by the Comunidad de Madrid under program SINFOTON-CM (S2013/MIT-2790). A. Pérez-Serrano acknowledges support from Ayudas a la Formación Posdoctoral 2013 program (FPDI-2013-15740). The authors acknowledge the contribution of L. Borruel, H. Odriozola, S. Sujecki, and E. C. Larkins to the development of the initial model and code for the simulation of tapered lasers.

References

Balsamo, S., Sartori, F., and Montrosset, I. 1996. Dynamic beam propagation method for flared semiconductor power amplifiers. *IEEE J. Quantum Electron.* 2(2):378–384.

Bandelow, U., Gajewski, H., and Hünlich, R. 2005. Fabry–Perot lasers: Thermodynamics-based modeling. In *Optoelectronic Devices. Advanced Simulation and Analysis*. Ed. J. Piprek. 63–85. New York, NY: Springer.

Borruel, L., Arias, J., Romero, B. et al. 2003. Incorporation of carrier capture and escape processes into a self-consistent cw model for Quantum Well lasers. *Microelectron. J.* 34:675–677.

Borruel, L., Odriozola, H., Tijero, J. M. G. et al. 2008. Design strategies to increase the brightness of gain guided tapered lasers. *Opt. Quantum Electron.* 40(2–4):175–189.

Borruel, L., Sujecki, S., Esquivias, I. et al. 2002. Self-consistent electrical, thermal, and optical model of high-brightness tapered lasers. *Proc. SPIE* 4646:355–366.

Borruel, L., Sujecki, S., Moreno, P. et al. 2004. Quasi-3-D simulation of high-brightness tapered lasers. *IEEE J. Quantum Electron.* 40:463–472.

Buus, J. 1982. The effective index method and its application to semiconductor lasers. *IEEE J. Quantum Electron.* 18(7):1083–1089.

Coldren, L. A. and Corzine, S. W. 1995. *Diode Lasers and Photonic Integrated Circuits*, New York, NY: John Wiley & Sons.

Connelly, M. J. 2001. Wideband semiconductor optical amplifier steady-state numerical model. *IEEE J. Quantum Electron.* 37(3):439–447.

Esquivias, I., Pérez-Serrano, A., and Tijero, J. M. G. 2017. High brightness tapered lasers. In: *Handbook of Optoelectronic Device Modeling and Simulation*, vol 2, (Piprek, J., ed) pp.59–80. Boca Raton, FL: Taylor & Francis.

Faugeron, M., Vilera, M., Krakowski, M. et al. 2015. High power three-section integrated master oscillator power amplifier at 1.5 μm. *IEEE Photon. Technol. Lett.* 27:1449–1452.

Fischer, I., Hess, O., Elsäßer, W. et al. 1996. Complex spatio-temporal dynamics in the near-field of a broad-area semiconductor laser. *Europhys. Lett.* 35(8):579–584.

Gehrig, E., and Hess, O. 2001. Spatio-temporal dynamics of light amplification and amplified spontaneous emission in high-power tapered semiconductor laser amplifiers. *IEEE J. Quantum Electron.* 37(10):1345–1355.

Grote, B., Heller, E. K., Scarmozzino, R. et al. 2005. Fabry–Perot lasers: Temperature and many-body effects. In *Optoelectronic Devices. Advanced Simulation and Analysis*. Ed. J. Piprek. 63–85. New York, NY: Springer.

Hadley, G. R. 1992. Wide-angle beam propagation using Padé approximant operators. *Opt. Lett.* 17(20):1426–1428.

Harold™ 2001. *3.0 Reference Manual*. Oxford: Photon Design.

Huang, W. P., Xu, C. L., Lui, W. et al. 1996. The perfectly matched layer (PML) boundary condition for the beam propagation method. *IEEE Photon. Technol. Lett.* 8(5):649–651.

Javaloyes, J. and Balle, S. 2010. Quasiequilibrium time-domain susceptibility of semiconductor quantum wells. *Phys. Rev. A* 81:062505.

Joindot, I. and Beylat, J. L. 1993. Intervalence band absorption coefficient measurements in bulk layer, strained and unstrained multiquantum well 1.55 μm semiconductor lasers. *Electron. Lett.* 29: 604–606.

Koch, S. W., Hader, J., Thränhardt, A. et al. 2005. Gain and absorption: Many-body effects. In *Optoelectronic Devices. Advanced Simulation and Analysis*. Ed. J. Piprek. 63–85. New York, NY: Springer.

Lai, J.-W. and Lin, C.-F. 1998. Carrier diffusion effect in tapered semiconductor-laser amplifier. *IEEE J. Quantum Electron.* 34(7):1247–1256.

Lang, R. J., Hardy, A., Parke, R. et al. 1993. Numerical analysis of flared semiconductor laser amplifiers. *IEEE J. Quantum Electron.* 29:2044–2051.

Lugiato, L. A. and Narducci, L. M. 1985. Single-mode and multimode instabilities in lasers and related optical systems. *Phys. Rev. A* 32(3):1576–1587.

Mariojouls, S., Margott, S., Schmitt, A. et al. 2000. Modeling of the performance of high-brightness tapered lasers. *Proc. SPIE* 3944:395–406.

Moloney, J. V., Indik, R. A., and Ning, C. Z. 1997. Full space-time simulation of high-brightness semiconductor lasers. *IEEE Photon. Technol. Lett.* 9:731–733.

Nagarajan, R., Ishikawa, M., Fukushima, T. et al. 1992. High speed quantum-well lasers and carrier transport effects. *IEEE J. Quantum Electron.* 28:1990–2008.

O'Brien, S., Welch, D. F., Parke, R. A. et al. 1993. Operating characteristics of a high-power monolithically integrated flared amplifier master-oscillator power-amplifier. *IEEE J. Quantum Electron.* 29:2052–2057.

Pérez-Serrano, A., Javaloyes, J., and Balle, S. 2013. Spectral delay algebraic equation approach to broad area laser diodes. *IEEE J. Sel. Top. Quant. Electron.* 19(5):1502808.

Piprek, J., Abraham, P., and Bowers, J. E. 2000. Self-consistent analysis of high-temperature effects on strained-layer multiquantum-well InGaAsP–InP lasers. *IEEE J. Quantum Electron.* 36:366–374.

Razaghi, M., Ahmadi, A., and Connelly, M. J. 2009. Comprehensive finite-difference time-dependent beam propagation model of counter propagating picosecond pulses in a semiconductor optical amplifier. *IEEE /OSA J. Lightwave Technol.* 27(15):3162-3174.

Schwertfeger, S., Klehr, A., Hoffmann, T. et al. 2011. Picosecond pulses with 50 W peak power and reduced ASE background from an all-semiconductor MOPA system. *Appl. Phys. B* 103:603–607.

Selberherr, S. 1984. *Analysis and Simulation of Semiconductor Devices*, Vienna: Springer-Verlag.

Spreemann, M., Lichtner, M., Radziunas, M. et al. 2009. Measurement and simulation of distributed-feedback tapered master-oscillator power-amplifiers. *IEEE J. Quant. Electron.* 45:609–616.

Sujecki, S., Borruel, L., Wykes, J. et al. 2003. Nonlinear properties of tapered laser cavities. *IEEE J. Sel. Top. Quant. Electron.* 9:823–834.

Sumpf, B., Hasler, K.-H., Adamiec, P. et al. 2009. High-brightness quantum well tapered lasers. *IEEE J. Sel. Top. Quant. Electron.* 15(3):1009–1020.

Tijero, J. M. G., Borruel, L., Vilera, M. et al. 2015. Analysis of the performance of tapered semiconductor optical amplifiers: Role of the taper angle. *Opt. Quant. Electron.* 47(6):1437–1442.

Van Roey, J., van der Donk, J., and Lagasse, P. E. 1981. Beam-propagation method: Analysis and assessment. *J. Opt. Soc. Am.* 71:803–810.

Vilera, M., Pérez-Serrano, A., Tijero, J. M. G. et al. 2015. Emission characteristics of a 1.5 μm all semiconductor tapered master oscillator power amplifier. *IEEE Photon. J.* 7(2):1500709.

Wachutka, G. K. 1990. Rigorous thermodynamic treatment of heat generation and conduction in semiconductor device modeling. *IEEE Trans. Comput. Aided Des. Integr. Circuits Syst.* 9:1141–1149.

Walpole, J. N. 1996. Semiconductor amplifiers and lasers with tapered gain regions. *Opt. Quant. Electron.* 28:623–645.

Wenzel, H., Sumpf, B., and Erbert, G. 2003. High-brightness diode lasers. *C. R. Phys.* 4:649–661.

Williams, K. A., Penty, R. V., White, I. H. et al. 1999. Design of high-brightness tapered laser arrays. *IEEE J. Sel. Top. Quant. Electron.* 5:822–831.

23

Quantum-Dot Semiconductor Optical Amplifiers

Benjamin Lingnau
and
Kathy Lüdge

23.1 Introduction

The rapidly increasing need for telecommunications and data-streaming applications within our society still demands a deeper understanding of the physical processes behind this emerging technology. In the last decades, there have been many attempts to optimize the performance of optoelectronic devices by using innovative nanostructured semiconductor gain materials [1,2]. A lot of these innovative devices already have found their way into photonic applications [3,4]. In particular, the demand for faster and more energy-efficient data transfer set the trend to replace the well-established cable-based data transmission with energy efficient optical technologies [5]. As one example, optical amplifiers are needed in optical networks to raise the signal power level and compensate for the inevitable optical losses in glass–fiber connections. Semiconductor-based optical amplifiers (SOAs) are cheap, relatively easy to fabricate, and consume only little energy within an electric circuit. They are structurally similar to semiconductor laser devices, with the difference lying in the absence of an optical cavity (see Chapter 20 SOA Fundamentals).

In this chapter, we describe the modeling of optical amplifiers that contain semiconductor quantum dots (QDs) as active media. Those nearly zero-dimensional QD structures gained a lot of attention as the material of choice for highly energy-efficient and small-footprint optoelectronic devices [6]. The scattering mechanisms and the unique electronic structure of semiconductor QDs have been found to make such devices prime candidates for the implementation of next-generation optoelectronic applications and novel high-speed data transmission schemes. QDs are the final step in miniaturization of the optically active gain material and thus in the confinement of charge carriers below the de Broglie wavelength of electrons (a few nanometers). In addition to the modeling of the quantum-dot semiconductor optical amplifiers (QDSOAs) as active media described within this chapter, other QD-based optical devices such as QD laser and QD

light-emitting diodes are treated separately in a different section of this book. Nevertheless, our microscopically based material model for the QDs can equally be used as the building block in laser devices [7,8].

Our main focus will be the characterization of both the performance and the special nonlinear features of QDSOAs that are induced by the low dimensional and thus highly confined QD gain medium. While linear amplification with a low noise figure is required, to ensure low distortion of the input signal for data transmission [9–11], nonlinear optical applications, such as four-wave-mixing [12–15] and cross-gain modulation [16–18] for wavelength conversion, as well as regenerative amplification, require a nonlinear response of the optical amplifier. QDSOAs generally have a high gain bandwidth due to the growth-induced inhomogeneity in the dot size and material composition. These fluctuations lead to an inhomogeneous broadening of the localized QDs states and consequently allow for a broadband amplification. Additionally, due to the coupling to a charge-carrier reservoir with charge-carrier scattering times in the picosecond range, ultrafast gain recovery [19–24] and nonlinear signal processing are possible [15,16,25]. The comparably slow dephasing time of the microscopic interband polarization in the localized QD states [26–28] allows the possibility to directly observe quantum-mechanical effects, such as Rabi oscillations [29–33] or self-induced transparency [34,35]. This could potentially open up new applications in the signal processing of ultra-short, ultra-strong optical pulses.

The optical amplifier devices we consider in this work are single-pass devices, where the optical signal coupled into one side of the waveguide structure is ideally passing exactly once across the device. Thus, the edge-emitting QDSOAs are longer than typical laser devices, in order to provide a long enough interaction time between optical signal and the active medium. The model used for the numeric simulations is based on a traveling-wave approach for the pulse propagation, using Maxwell's wave equation in the slowly varying amplitude and rotating wave approximation. The polarization of the active medium is modeled using microscopic considerations for the charge-carrier dynamics, i.e., the light–matter interaction is modeled on the basis of Maxwell–Bloch equations, taking into account the microscopic polarization of the QD medium.

The structure of the chapter is as follows. First, a delay-differential equation model for an efficient and accurate description of the electric field propagation through the QDSOA is presented (Section 23.2). Subsequently, the charge-carrier dynamics is described in the framework of microscopically calculated nonlinear charge-carrier scattering rates before our approach for a quantitative modeling of the amplified spontaneous emission (ASE) inside the QDSOA is discussed. In Section 23.3, we present exemplary results on the performance of the QDSOA, focusing on the unique properties of semiconductor QDs as active medium. After a static characterization of a chosen sample device, we discuss the ultrafast gain dynamics of QDSOAs, identifying the main timescales that determine its gain recovery. We then present results on the coherent propagation of strong optical pulses. The long dephasing time of QDs leads to strong signatures of the coherent interaction, leading to modifications in the pulse shape and the gain dynamics due to the appearance of Rabi oscillations. A brief conclusion is provided.

23.2 QD Semiconductor Optical Amplifier Model

QDSOAs differ from conventional devices in the choice of active medium. The charge-carrier dynamics in QDs can be very complex due to the localization of electrons within the QDs embedded in the surrounding quantum-well or bulk material. In this chapter, we, therefore, aim to describe the charge-carrier dynamics and derive a set of coupled differential equations for the electronic states involved. The strong nonlinearity of the resulting equations leads to important differences in the performance of QDSOAs when compared to conventional devices. It also opens up the possibility of novel applications, based on their ultrafast gain recovery for linear applications, or their broad gain spectrum for nonlinear or wavelength conversion applications.

In this section, we derive a QDSOA model, in which we focus on the unique dynamics of the QD gain medium. The wave equation used for the propagation of the light will be similar to conventional SOA

models (see Chapter 20 on SOA fundamentals in this book). In other works, models without spatial resolution have been employed for the description of semiconductor amplifiers [17,36–38]. As soon as strong spatial inhomogeneities arise, such models are, however, bound to fail. On the other hand, numerically solving the partial differential equation for the electric field propagation along the waveguide axis is computationally very expensive[39]. We, therefore, develop a delay-differential equation model that combines spatial resolution and reasonable computation time. The light–matter interaction will be described within a Maxwell–Bloch framework, which couples the light propagation dynamics to the QD active medium.

In the following, we derive the electric field propagation equations and the material equations describing the active medium. Furthermore, we derive Boltzmann-like equations that govern the charge-carrier scattering dynamics within a quantum-dot-in-a-well system. Spontaneous emission will be included in a phenomenological way to yield stochastic differential equations.

23.2.1 Electric Field Propagation: Delay-Differential-Equation Model

In order to calculate the dynamics of the QDSOA device, we must solve the wave equation of the optical field inside the waveguide. Here we concentrate on narrow-area ridge waveguide structures where the propagation along the longitudinal axis (labeled z) dominates, and the transverse mode profile is assumed to be constant. The electric field is thus governed by the one-dimensional wave equation

$$\frac{\partial^2}{\partial t^2}\boldsymbol{\mathcal{E}}(\boldsymbol{r},t) - {c_0}^2\frac{\partial^2}{\partial z^2}\boldsymbol{\mathcal{E}}(\boldsymbol{r},t) = -\frac{1}{\varepsilon_0}\frac{\partial^2}{\partial t^2}\boldsymbol{\mathcal{P}}(\boldsymbol{r},t)\,, \tag{23.1}$$

where $\boldsymbol{\mathcal{E}}$ and $\boldsymbol{\mathcal{P}}$ denote the real electric field and polarization, respectively, and c_0 and ε_0 are the vacuum speed of light and dielectric constant, respectively. The field quantities are expanded in terms of plane waves,

$$\mathcal{E}(z,t) = \frac{1}{2}\left[E^{+}(z,t)e^{ikz} + E^{-}(z,t)e^{-ikz}\right]e^{-i\omega t} + \text{c.c.}\,, \tag{23.2}$$

where we have introduced the slowly varying field amplitudes $E^{\pm}$, describing the forward (+) and backward (−) propagating electric field. The wave number is given by k, and ω is the optical frequency of the reference frame. From Equation 23.1, we can derive the propagation equations for the electric field amplitudes within the slowly varying envelope approximation (SVEA), neglecting all but the lowest order of derivatives. The SVEA limits the description to field envelopes that change on time scales and lengths much larger than the respective optical period and wavelength, respectively. The propagation equation for the slowly varying field envelope is then written as

$$\left(\frac{\partial}{\partial t} \pm v_g\frac{\partial}{\partial z}\right)E_{\pm}(z,t) = \frac{i\omega\Gamma}{2\varepsilon_{\text{bg}}\varepsilon_0}P_{\pm}(z,t) =: S_{\pm}(z,t)\,, \tag{23.3}$$

with the group velocity $v_g \equiv \frac{c_0}{\sqrt{\varepsilon_{\text{bg}}}}$, with the background permittivity ε_{bg}. $P_{\pm}(z,t)$ is the macroscopic slowly varying polarization amplitude. The transverse optical confinement factor Γ is introduced phenomenologically to the above equation. It describes the overlap of the electric field mode with the active medium, integrated over the transverse (x and y) coordinates. We summarize the right-hand side in a general source term $S_{\pm}(z,t)$.

The numerical solution of the above partial differential equation using a finite-difference method requires a spatial discretization into very fine sections of length $v_g\mathrm{d}t$, where $\mathrm{d}t$ is the numerical time-step, in order to ensure numerical stability [41]. For common device lengths on the order of 1 mm, a high number of spatial discretization points is needed. The numerical integration, therefore, becomes very expensive in

terms of computation time and memory requirements [42,43]. A more elegant approach is the formulation of the problem as a delay-differential equation system [40,44], which we do in the following.

The partial differential equation Equation 23.3 can be formally solved by integrating along its characteristic lines, given by

$$z = \pm v_g t + \text{const.} \tag{23.4}$$

Expanding the total derivative $\frac{\mathrm{d}}{\mathrm{d}t} = \frac{\partial z}{\partial t}\frac{\partial}{\partial z} + \frac{\partial}{\partial t}$, we can thus write

$$\frac{\mathrm{d}}{\mathrm{d}t}E_{\pm}(z,t) = \left[\pm v_g \frac{\partial}{\partial z} + \frac{\partial}{\partial t}\right] E_{\pm}(z,t) = S_{\pm}(z,t)\,. \tag{23.5}$$

Now we describe the optical amplifier of length ℓ by a number of Z sections along the propagation axis, such that the distance between two discretization points is given by $\Delta z := \ell/Z$. Integrating Equation 23.5 over the time interval $\Delta t = \frac{\Delta z}{v_g}$ thus yields

$$\begin{aligned} E_{\pm}(z,t) &= E_{\pm}(z \mp \Delta z, t - \Delta t) + \int_{-\Delta t}^{0} \left[\frac{\mathrm{d}}{\mathrm{d}t}E_{\pm}\left(z \pm v_g\tau, t + \tau\right)\right] \mathrm{d}\tau' \\ &= E_{\pm}(z \mp \Delta z, t - \Delta t) + \int_{-\Delta t}^{0} S_{\pm}\left(z \pm v_g\tau, t + \tau\right) \mathrm{d}\tau \\ &\approx E_{\pm}(z \mp \Delta z, t - \Delta t) + \frac{\Delta t}{2}\Big[S_{\pm}(z,t) + S_{\pm}(z \mp \Delta z, t - \Delta t)\Big]. \end{aligned} \tag{23.6}$$

The integral over the source term was approximated by its values at the end points of the integration interval. This approximation is valid for negligible change of $S_{\pm}$ along the integration path, i.e., for a sufficiently small space discretization step. The electric field at time t now depends on the values of $E_{\pm}$, $S_{\pm}$ at time $t - \Delta t$, which introduces a time delay into the equations.

The electric field in each of the spatial sections along the amplifier device thus couples to the time-delayed electric field in the neighboring sections, with the time Δt describing the time needed for the electric field propagation along the length of one section [40,44]. The resulting discretization scheme is illustrated in Figure 23.1. The advantage of this approach is the decoupling of the time and space discretization steps, ensuring numerical stability even for $\Delta z \gg v_g \mathrm{d}t$. The temporal dynamics at each point within the amplifier device is usually much faster than the characteristic timescale over which a propagating pulse changes its shape. Thus, a reduced number of spatial discretization points can be chosen compared to the finite-difference method, which significantly improves the simulation efficiency. The implementation of the delay-differential equations, however, means that the history of the electric fields as well as the source terms must be saved over a time interval Δt.

23.2.2 Quantum-Dot-in-a-Well Material Equations

The amplifier active medium is composed of an ensemble of of semiconductor quantum dots. For InAs quantum dots grown in the Stranski–Krastanov (SK) mode by molecular beam epitaxy (MBE), their areal density is in the order of $2 - 5{\times}10^{10}\ \mathrm{cm}^{-2}$ [45]. The considered QDs are assumed to have two optically active localized states. These are denoted by GS and ES, for the ground and first excited state, respectively, which are located within the bands of the surrounding quantum well, as sketched in Figure 23.2. The resulting energy structure is sketched in Figure 23.3.

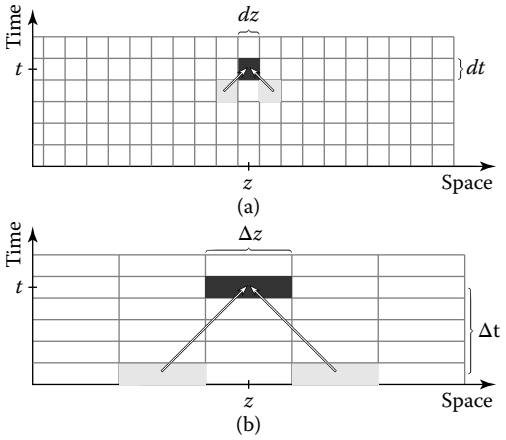

FIGURE 23.1 Electric field propagation schemes: (a) Traditional time-domain traveling-wave integration scheme. The device is discretized into spatial sections with width dz, usually related to the numerical time step dt via the electric field group velocity $\mathrm{d}z = v_g \mathrm{d}t$. The field $E(z, t)$ is then determined from the field in neighboring discretization points at the previous time step $E(z \pm \mathrm{d}z, t - \mathrm{d}t)$. (b) The discretization into fewer spatial sections separated by Δz leads to a coupling to neighboring points with a time delay Δt. The time evolution in each section is still calculated with a time step dt, separating space and time discretization steps. (After J. Javaloyes and S. Balle, *Opt. Express*, 20, 8496–8502, 2012.)

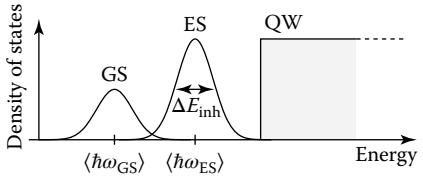

FIGURE 23.2 Sketch of the conduction band density of states of a quantum-dot-in-a-well material system. The QD transitions are assumed to consist of a ground-state (GS) and excited-state (ES) transition, which are inhomogeneously broadened with a full-width-at-half maximum (FWHM) of ΔE_{inh}. The two-dimensional quantum-well (QW) states act as a charge-carrier reservoir for the QD states.

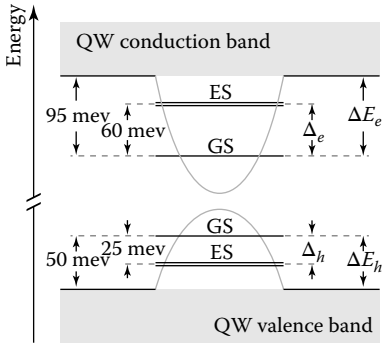

FIGURE 23.3 Energy scheme of the considered dot-in-a-well (DWELL) structure. The QD ground states (GS) lie ΔE_b below the quantum-well (QW) band edge, with an energy spacing of Δ_b between GS and first excited state (ES).

Due to fluctuations in QD size and composition, their emission spectrum is inhomogeneously broadened around the central emission energy of ≈ 950 meV for InAs/InGaAs QDs. Typical inhomogeneous linewidths lie around 30 meV—higher than their homogeneous linewidth [27,46]. An accurate description of the QD medium, therefore, requires a separate treatment of quantum dots in dependence of their respective transition energy. Both the interaction with the optical field as well as the charge-carrier scattering dynamics are influenced by the transition and localization energies. A natural way to deal with the inhomogeneous broadening is, therefore, to distribute the whole QD ensemble into a number of subgroups, characterized by their optical transition energy. This procedure is illustrated in Figure 23.4. We label each subgroup by an index j and its respective mean transition energy $\hbar\omega^j$. We introduce the probability mass function $f(j)$ denoting the fraction of QDs within the jth subgroup. Following a Gaussian distribution with an FWHM of ΔE_{inh}, the distribution function $f(j)$ is then given by

$$f(j) = \frac{1}{\mathcal{N}} \exp\left(-4 \ln 2 \left[\frac{\hbar\omega^j - \langle\hbar\omega\rangle}{\Delta E_{\text{inh}}}\right]^2\right), \tag{23.7}$$

with the normalization constant $\mathcal{N}$ chosen such that $\sum_j f(j) \stackrel{!}{=} 1$, calculated numerically. The inhomogeneous broadening of the optical spectrum is given by the sum of the individual single-particle state broadenings of electrons and holes (subscripts e and h, respectively),

$$\Delta E_{\text{inh}} = \Delta\varepsilon_e + \Delta\varepsilon_h\,, \tag{23.8}$$

where $\Delta\varepsilon_b$, $b \in \{e, h\}$ is the corresponding electron and hole state broadening. Only the total broadening ΔE_{inh} is experimentally readily accessible, e.g., by measurements of the QD luminescence spectra [47]. For the individual state broadening, we assume widths proportional to the localization energy of the given state:

$$\Delta\varepsilon_b = \Delta E_{\text{inh}} \frac{\Delta E_b}{\Delta E_e + \Delta E_h}\,. \tag{23.9}$$

We now proceed by deriving the dynamic equation for each of the QD subgroups within each amplifier section. In addition to the QD subgroup index j, we introduce the state index $m \in \{\text{GS}, \text{ES}\}$, distinguishing the charge carriers in the GS and first ES. The material dynamics are described within the Maxwell–Bloch approach [48], characterizing the QD active medium by their occupation probabilities ρ_m^j and the microscopic polarization amplitudes p_m^j. The microscopic polarization is induced by the electric field and describes the transition probability under emission of a photon, and thus couples the

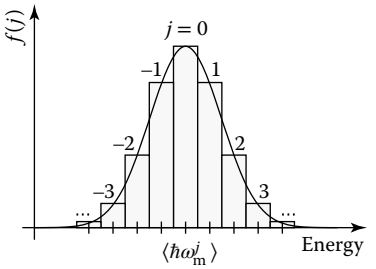

FIGURE 23.4 Illustration of the QD subgroups to model inhomogeneous broadening. The QDs are distributed into j_{max} subgroups, assumed to follow a Gaussian distribution around the mean transition energy $\langle\hbar\omega_m\rangle$. The probability mass function $f(j)$ gives the probability for a QD to be found in the jth subgroup.

charge-carrier equations to the light field. Similar to the electric field, we expand p_m^j in terms of forward and backward propagating amplitudes,

$$p_m^j(z,t) = \left[p_{m,+}^j(z,t)e^{ikz} + p_{m,-}^j(z,t)e^{-ikz}\right] e^{-i\omega t}. \tag{23.10}$$

We assume a coupling of the individual polarization amplitudes $p_{m,\pm}^j$ only to the corresponding co-propagating part of the electric field. This is the rotating wave approximation, neglecting terms oscillating with $e^{\pm 2ikz}$ and $e^{\pm 2i\omega t}$, which would appear in the coupling of counter-propagating polarization and field terms.

The Maxwell–Bloch equations of the QD active medium polarization amplitudes and occupation probabilities then read [49,50]

$$\frac{\mathrm{d}}{\mathrm{d}t}p_{m,\pm}^j(z,t) = -\left[i(\omega_m^j - \omega) + \frac{1}{\tau_2}\right] p_{m,\pm}^j(z,t) - i\frac{\mu_m}{2\hbar}\left(\rho_{e,m}^j(z,t) + \rho_{h,m}^j(z,t) - 1\right) E_\pm(z,t), \tag{23.11}$$

$$\begin{aligned}\frac{\mathrm{d}}{\mathrm{d}t}\rho_{b,m}^j(z,t) = {} & \frac{1}{\hbar}\mathrm{Im}\left[p_{m,+}^j(z,t)\mu_m^* E_+^*(z,t)\right] + \frac{1}{\hbar}\mathrm{Im}\left[p_{m,-}^j(z,t)\mu_m^* E_-^*(z,t)\right] \\ & - W_m\rho_{e,m}^j(z,t)\rho_{h,m}^j(z,t) + \frac{\partial}{\partial t}\rho_{b,m}^j(z,t)\Big|_{\mathrm{sc}}.\end{aligned} \tag{23.12}$$

Here, we again denote the localized QD states by $m \in \{\mathrm{GS}, \mathrm{ES}\}$ and their subgroup index by j. The above equations describe the micoscopic polarization amplitudes in the reference frame of ω, whereas ω_m^j denotes the transition frequency of the respective optical transition. The polarization decays with the time constant τ_2. This dephasing time describes the loss of the quantum-mechanical coherence between different QDs due to scattering processes with other electrons or phonons. In semiconductors, these processes are usually in the order of a few tens of femtoseconds, due to the high density of charge carriers as potential scattering partners. The polarization is driven by the electric field $E_\pm(z,t)$ and the carrier inversion, with the interaction strength given by the transition dipole moment μ_m.

The QD charge-carrier dynamics is given by stimulated recombination induced by the microscopic polarization, and bimolecular spontaneous recombination with a rate W_m. The term $\frac{\partial}{\partial t}\rho_{b,m}^j(z,t)\Big|_{\mathrm{sc}}$ denotes charge-carrier scattering contributions, which we will address in the following section.

The above equations couple to the macroscopic light field via the macroscopic slowly varying polarization amplitudes $P_\pm(z,t)$. These are given by the macroscopic sum over the individual microscopic contributions:

$$P_\pm(z,t) = \frac{2N^{\mathrm{QD}}}{h^{\mathrm{QW}}} 2\sum_{j,m} \nu_m f(j)\mu_m^* p_{m,\pm}^j(z,t)\,, \tag{23.13}$$

where N^{QD} is the areal QD density per quantum-well layer and h^{QW} the layer height. The sum $\sum_{j,m}\nu_m f(j)$ gives the sum over all QD subgroups and confined states, with ν_m the degeneracy (excluding spin) of the mth state and $f(j)$ the distribution function as defined in Equation 23.7. The macroscopic polarization couples back to the electric field equation as a source term, as shown in Equation 23.3:

$$\begin{aligned}\frac{\mathrm{d}}{\mathrm{d}t}E_\pm(z,t) = S_\pm(z,t) &= \frac{i\omega\Gamma}{2\varepsilon_{\mathrm{bg}}\varepsilon_0}P_\pm(z,t) \\ &= \frac{2N^{\mathrm{QD}}}{h^{\mathrm{QW}}}\frac{i\omega\Gamma}{\varepsilon_{\mathrm{bg}}\varepsilon_0}\sum_{j,m}\nu_m f(j)\mu_m^* p_{m,\pm}^j(z,t)\,.\end{aligned} \tag{23.14}$$

It is tempting to identify a small-signal gain $g(z, t, \omega)$, as used in traditional rate equation models, from an earlier equation:

$$g(z, t, \omega) = \frac{i\omega\Gamma}{2\varepsilon_{\mathrm{bg}}\varepsilon_0}\frac{P_{\pm}(z, t)}{E_{\pm}(z, t)}. \tag{23.15}$$

However, the independent dynamics of the polarization would lead to a strongly varying (and even diverging) value of $g(z, t, \omega)$ in time. Nevertheless, in a static limit, by setting $\frac{\partial}{\partial t}p_m^j = 0$, the adiabatic small-signal gain can be calculated from Equation 23.11, which yields

$$g(z, t, \omega) = \frac{\hbar\omega\Gamma}{\varepsilon_0\varepsilon_{\mathrm{bg}}h^{\mathrm{QW}}}2N^{\mathrm{QD}}\sum_{j,m}\nu_m f(j)\frac{\tau_2|\mu_m|^2}{2\hbar^2}\frac{\left[\rho_{e,m}^j(z, t) + \rho_{h,m}^j(z, t) - 1\right]}{1 + [\tau_2(\omega - \omega_m^j)]^2}. \tag{23.16}$$

This expression, however, neglects the dynamics of the polarization, assuming it to follow the incident electric field instanteously. For coherent interactions, such as Rabi oscillations discussed later in this chapter, the above equation, therefore, cannot be applied. Furthermore, Equation 23.16 is strictly valid only for a monochromatic electric field at a given frequency ω. When simulating broadband amplification, such as optical pulses, the full polarization dynamics must, therefore, be taken into account. For slowly varying and near-monochromatic electric field envelopes, such as encountered in lasers, the adiabatic elimination of the polarization equations is a valid and widely used approximation, and Equation 23.16 can be used to calculate the optical gain.

The Maxwell–Bloch equations only describe the optically active QD states. In order to describe the carrier dynamics in the surrounding charge-carrier reservoir, we model the quantum-well charge-carrier density w_b by a rate equation,

$$\frac{\mathrm{d}}{\mathrm{d}t}w_b(z, t) = \eta\frac{J}{e_0} - A^S\sqrt{w_e(z, t)w_h(z, t)} - B^S w_e(z, t)w_h(z, t) + \frac{\partial}{\partial t}w_b(z, t)\Big|_{\mathrm{sc}}, \tag{23.17}$$

with the pump current density J, the electron charge $-e_0$, and a pump current efficiency η accounting for losses in the surrounding semiconductor layers, as well as imperfect carrier injection into the active region, which is not modeled explicitly. Linear and bimolecular recombination rates in the reservoir are given by A^S and B^S, respectively, which are important to describe carrier losses over a wide range of currents. We neglect Auger recombination, as with typical values ($C = 10^{-28}\,\mathrm{cm}^6 \cdot \mathrm{s}^{-1}$) the losses are found to be dominated by A^S and B^S in the current ranges considered in this chapter. The term $\frac{\partial}{\partial t}w_b(z, t)\Big|_{\mathrm{sc}}$ accounts for scattering of charge carriers into the QD states, which is derived in the next section. The above equations are defined for each space discretization point along the amplifier device, allowing for a spatially inhomogeneous distribution of the charge-carrier distribution, as encountered in long amplifier devices [51,52].

23.2.3 QD Charge-Carrier Scattering

QDs differ from conventional quantum-well or bulk gain media in the presence of localized states and thus a strongly modified density of states. Electrically injected charge carriers reach the active region in high-energy states near the bulk material band edges. The optically active QD states must, therefore, be populated by means of scattering processes. While the charge-carrier distributions within the quasi-continuous bulk and quantum-well bands quickly thermalize due to electron–phonon interaction [53,54], an effective scattering of carriers into the QD states by scattering with phonons is limited due to the existence of the "phonon bottleneck"[55]. Instead, at elevated charge-carrier densities, Coulomb-mediated carrier-carrier scattering provides an ultrafast scattering mechanism between the QD states and

the surrounding semiconductor material [56]. In the following, we derive expressions for the Coulomb scattering mechanism.

The starting point for calculating the carrier-carrier scattering is the many-body Hamiltonian in second quantization [49,57],

$$H_{\mathrm{sys}} = H_{\mathrm{kin}} + H_{\mathrm{C}} = \sum_{\substack{a \\ s}} \varepsilon_a a_{as}^{\dagger} a_{as} + \frac{1}{2} \sum_{\substack{abcd \\ ss'}} W_{abcd}\, a_{as}^{\dagger} a_{bs'}^{\dagger} a_{cs'} a_{ds}\,, \tag{23.18}$$

where a_x, $a_x^{\dagger}$ are the electron annihilation and creation operators in the state x with the energy ε_x, respectively. The Hamiltonian consists of the kinetic (free-carrier) contribution H_{kin}, and the Coulomb-interaction Hamiltonian H_{C}, which includes the many-body interaction between the charge carriers in the semiconductor. In the sums, the labels a, b, c, d denote all possible electronic states, with s, s' denoting their spins. The occupation probability for a given state (ν, s) is given by

$$\rho_{\nu s} = \langle a_{\nu s}^{\dagger} a_{\nu s} \rangle\,. \tag{23.19}$$

The screened Coulomb interaction matrix element is given by

$$W_{abcd} = \iint \mathrm{d}^3 r\, \mathrm{d}^3 r'\, \phi_a^*(\boldsymbol{r}) \phi_b^*(\boldsymbol{r}') \frac{{e_0}^2}{4\pi\varepsilon_0 \varepsilon_{\mathrm{bg}}} \frac{e^{-\kappa|\boldsymbol{r}-\boldsymbol{r}'|}}{|\boldsymbol{r}-\boldsymbol{r}'|} \phi_c(\boldsymbol{r}') \phi_d(\boldsymbol{r})\,, \tag{23.20}$$

with the single-particle wave functions $\phi_x(\boldsymbol{r})$, approximated as harmonic oscillator wave functions, which was shown to yield surprisingly accurate results [58]. The vacuum and background permittivity are given by ε_0 and $\varepsilon_{\mathrm{bg}}$, respectively, and $-e_0$ is the electron charge. The screening wave number κ describes the screening of the Coulomb interaction potential by the surrounding charge-carrier plasma, which can be calculated in a self-consistent way [57,59,60]. Here, we implement the screening wave number in the static quasi-equilibrium limit as

$$\kappa = \frac{{e_0}^2}{2\varepsilon_0 \varepsilon_{\mathrm{bg}}} \sum b \frac{\partial w_b}{\partial E_{\mathrm{F},b}^{\mathrm{eq}}} = \frac{{e_0}^2}{2\varepsilon_0 \varepsilon_{\mathrm{bg}}} \sum_b D_b f(E_{b,0}^{\mathrm{QW}}, E_{\mathrm{F},b}^{\mathrm{eq}}, k_B T^{\mathrm{eq}})\,, \tag{23.21}$$

with the quasi-Fermi level $E_{\mathrm{F},b}^{\mathrm{eq}}$, quasi-equilibrium temperature T^{eq}, and 2D density of states D_b of the corresponding electron and hole plasma. Within the quasi-equilibrium approximation, the screening can be expressed by the occupation probability at the band edge, $E_{b,0}^{\mathrm{QW}}$, increasing the screening of the Coulomb interaction with increasing charge-carrier density. The screening becomes very important at elevated charge-carrier densities where the unscreened Coulomb potential would greatly overestimate the interaction between the charge carriers.

An exact numeric solution to Heisenberg's equation of motion within the given problem is generally not possible. The Coulomb interaction Hamiltonian couples the dynamic evolution of n-operator expectation values to $n+2$-operator expectation values, leading to an infinite number of coupled differential equations. It is, therefore, necessary to apply further approximations. We truncate this infinite chain of dynamic equations by factorizing six-operator expectation values into factors of two-operator expectation values, i.e., occupation probabilities. The Coulomb matrix elements thus enter the dynamic equations in up to second order. First-order contributions lead to renormalization effects of the single-particle energies and polarization amplitudes due to the Coulomb interaction with surrounding charge carriers [59,61]. These effects do not lead to a net change in the charge-carrier distribution and are therefore neglected.

By applying the Markov approximation to the resulting equations of motion, the explicit time dependence of four-operator expectation values is discarded. Instead, a quasi-static dependence of these expectation values on the occupation probabilities is assumed, by setting their time derivative to zero in the adiabatic limit. The scattering processes are thus assumed to follow any changes in the charge-carrier

distribution instantaneously. The scattering contribution to the charge-carrier states then yields a Boltzmann-type equation:

$$\frac{\partial}{\partial t}\rho_{\nu\sigma}\Big|_{\mathrm{sc}} = \frac{2\pi}{\hbar}\sum_{\substack{bcd\\ s'}}\mathrm{Re}\left[W_{\nu bcd}\left(W^{*}_{\nu bcd} - W^{*}_{\nu bdc}\right)\right]\delta(\varepsilon_{\nu}+\varepsilon_{b}-\varepsilon_{c}-\varepsilon_{d}) \times\left[(1-\rho_{\nu\sigma})(1-\rho_{bs'})\rho_{cs'}\rho_{d\sigma} - \rho_{\nu\sigma}\rho_{bs'}(1-\rho_{cs'})(1-\rho_{d\sigma})\right], \tag{23.22}$$

which describes the Coulomb scattering in the second-order Born–Markov approximation [23,62–64]. The summation terms in Equation 23.22 describe the simultaneous scattering between states $d \leftrightarrow \nu$ and $c \leftrightarrow b$. The delta function ensures energy conservation, such that the total energy of the final states equals that of the initial states. The Coulomb scattering is thus revealed to be of Auger-type, requiring the simultaneous scattering of two electrons, with no net change in the total charge-carrier energy. The individual scattering processes are proportional to the occupation probabilities in the initial states c, d and proportional to the probability to find vacant final states ν, b, accounting for Pauli blocking. The second term in the sum in Equation 23.22 describes the reverse scattering processes, with electrons scattering out of the states ν, b.

Equation 23.22 can be written in the form of a Boltzmann equation for the occupation probability $\rho(t)$ of any given state in the system,

$$\frac{\partial}{\partial t}\rho(t)\Big|_{\mathrm{sc}} = S^{\mathrm{in}}[1-\rho(t)] - S^{\mathrm{out}}\rho(t), \tag{23.23}$$

combining the summation terms into an in-scattering rate S^{in} and a corresponding out-scattering rate S^{out}. These rates are calculated from the sums in Equation 23.22, which include all possible individual scattering processes. An exact treatment of the scattering dynamics within the second-order Born–Markov approximation would still require the dynamic tracking of the complete charge-carrier distribution, making numerical treatment difficult. Fortunately, the given QD-quantum-well system allows the distinction between qualitatively different scattering processes in order to break up the sums in Equation 23.22 into different parts which can be handled more easily.

For the dot-in-a-well (DWELL) structures considered in this chapter, two general classes of charge-carrier scattering processes can be distinguished: the capture of a quantum-well electron into a confined QD state, and the intradot electron relaxation, each with their respective inverse escape processes. This is illustrated in Figure 23.5a and b, respectively. The accompanying Auger-electron can involve either quantum-well states only, or transitions between quantum-well and other QD states. Note that depending on the involved energy differences, not all of these scattering channels are possible. For example, in the depicted case of the intra-dot relaxation in Figure 23.5b, the Auger transition in the valence band from the quantum well to the GS is not possible, as it would violate energy conservation. The possible scattering processes contributing to the total scattering rate thus strongly depend on the exact energy scheme of the QD-quantum-well system. Note that throughout this work impact ionization and Auger-assisted recombination, i.e., the direct scattering between conduction and valence bands, is not considered.

Following the earlier discussion, the scattering dynamics of the localized QD states are rewritten in the electron–hole picture as

$$\frac{\partial\rho_{b,\mathrm{GS}}}{\partial t}\Big|_{sc} = S^{\mathrm{cap,in}}_{b,\mathrm{GS}}(\{\rho_{\mathrm{QW}}\})(1-\rho_{b,\mathrm{GS}}) - S^{\mathrm{cap,out}}_{b,\mathrm{GS}}(\{\rho_{\mathrm{QW}}\})\rho_{b,\mathrm{GS}} + S^{\mathrm{rel,in}}_{b,\mathrm{GS}}(\{\rho_{\mathrm{QW}}\})\rho_{b,\mathrm{ES}}(1-\rho_{b,\mathrm{GS}}) - S^{\mathrm{rel,out}}_{b,\mathrm{GS}}(\{\rho_{\mathrm{QW}}\})(1-\rho_{b,\mathrm{ES}})\rho_{b,\mathrm{GS}}, \tag{23.24}$$

$$\frac{\partial\rho_{b,\mathrm{ES}}}{\partial t}\Big|_{sc} = S^{\mathrm{cap,in}}_{b,\mathrm{ES}}(\{\rho_{\mathrm{QW}}\})(1-\rho_{b,\mathrm{ES}}) - S^{\mathrm{cap,out}}_{b,\mathrm{ES}}(\{\rho_{\mathrm{QW}}\})\rho_{b,\mathrm{ES}} + S^{\mathrm{rel,in}}_{b,\mathrm{ES}}(\{\rho_{\mathrm{QW}}\})\rho_{b,\mathrm{GS}}(1-\rho_{b,\mathrm{ES}}) - S^{\mathrm{rel,out}}_{b,\mathrm{ES}}(\{\rho_{\mathrm{QW}}\})(1-\rho_{b,\mathrm{GS}})\rho_{b,\mathrm{ES}}. \tag{23.25}$$

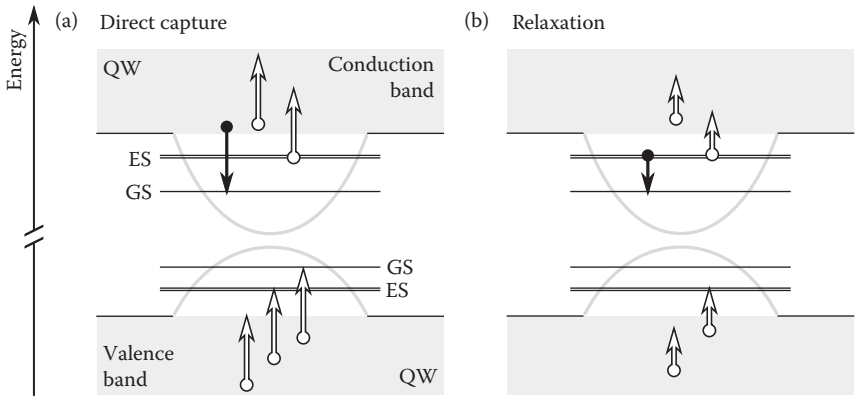

FIGURE 23.5 Possible scattering channels in quantum-dot (QD) quantum-well (QW) systems. (a) Direct capture into the QD ground state (GS). (b) Intradot relaxation from excited state (ES) to GS. The electron scattering process considered is shown by the black arrow, with the white arrows denoting the possible Auger processes. For all processes shown, the corresponding reverse scattering is also possible. Not shown is the direct capture into the QD ES, analogous to (a).

Here, ρ_b denotes either electron or hole occupation probabilities for $b \in \{e, h\}$. The scattering rates $S^{\text{cap,in}}$ denote the direct capture of quantum-well electrons into the QD states, $S^{\text{rel,in}}$ the intradot relaxation between the QD states, with S^{out} the scattering rate of the respective reverse processes. We can relate the relaxation processes of the ES to the corresponding GS terms,

$$S^{\text{rel,in}}_{b,\text{ES}}(\{\rho_{\text{QW}}\}) = -\frac{1}{2} S^{\text{rel,out}}_{b,\text{GS}}(\{\rho_{\text{QW}}\}), \tag{23.26}$$

$$S^{\text{rel,out}}_{b,\text{ES}}(\{\rho_{\text{QW}}\}) = -\frac{1}{2} S^{\text{rel,in}}_{b,\text{GS}}(\{\rho_{\text{QW}}\}), \tag{23.27}$$

with a factor $\frac{1}{2}$ compared to the GS contribution, due to the twofold degeneracy of the ES. All scattering rates in the above equations depend on the whole quantum-well distribution in both bands, denoted by $\{\rho_{\text{QW}}\}$.

Thus far the derived scattering expressions only describe the dynamics of QD states and their interaction with the quantum-well charge carriers. The dynamics of quantum-well carriers can in principle be expressed by Equation 23.22 as well. However, this would require resolving all quantum-well states and tracking their population distribution in time, which greatly increases the dimensionality of the system state. This problem can be resolved by assuming a specific distribution of the carrier population within the quantum well.

The intraband scattering between quantum-well states is typically in the order of $\approx 100\,\text{fs}$ [65–69]. As long as this scattering is faster than the charge-carrier exchange between the quantum well and QDs, the quantum well can be assumed to be in quasi-equilibrium with good accuracy:

$$\rho_{b,\text{QW}}(\varepsilon^{\text{2D}}_{b,\boldsymbol{k}}) \approx f(\varepsilon^{\text{2D}}_{b,\boldsymbol{k}}, E^{\text{eq}}_{\text{F},b}, T^{\text{eq}}) \equiv \left[1 + \exp\left(\frac{\varepsilon^{\text{2D}}_{b,\boldsymbol{k}} - E^{\text{eq}}_{\text{F},b}}{k_{\text{B}} T^{\text{eq}}}\right)\right]^{-1}, \tag{23.28}$$

with the corresponding single-particle energies $\varepsilon^{\text{2D}}_{b,\boldsymbol{k}}$ and the quasi-Fermi level $E^{\text{eq}}_{\text{F},b}$. From this quasi-Fermi distribution the 2D-charge-carrier density w_b in the quantum wells can be calculated by taking the density of states in the quantum well as

$$\mathcal{D}_b(E) = D_b \Theta(E - E^{\text{QW}}_{b,0}) = \frac{m^*_b}{\pi\hbar^2} \Theta(E - E^{\text{QW}}_{b,0}), \tag{23.29}$$

under the assumption that the quantum-well sub-band spacing is large enough that only the lowest sub-band needs to be taken into account. The energy $E_{b,0}^{\mathrm{QW}}$ is the corresponding quantum-well band edge and Θ is the Heaviside function. The quantum-well charge-carrier density can then be written as

$$\begin{aligned} w_b &= \frac{2}{A_{\mathrm{act}}} \sum_{\boldsymbol{k}^{\mathrm{2D}}} \left[1 + \exp\left(\frac{\varepsilon_{b,\boldsymbol{k}}^{\mathrm{2D}} - E_{\mathrm{F},b}^{\mathrm{eq}}}{k_{\mathrm{B}} T^{\mathrm{eq}}} \right) \right]^{-1} \\ &= \int_{-\infty}^{\infty} \mathrm{d}\varepsilon_{b,\boldsymbol{k}}^{\mathrm{2D}} \, \mathcal{D}_b(\varepsilon_{b,\boldsymbol{k}}^{\mathrm{2D}}) \left[1 + \exp\left(\frac{\varepsilon_{b,\boldsymbol{k}}^{\mathrm{2D}} - E_{\mathrm{F},b}^{\mathrm{eq}}}{k_{\mathrm{B}} T^{\mathrm{eq}}} \right) \right]^{-1} \\ &= D_b k_{\mathrm{B}} T^{\mathrm{eq}} \log\left[1 + \exp\left(\frac{E_{\mathrm{F},b}^{\mathrm{eq}} - E_{b,0}^{\mathrm{QW}}}{k_{\mathrm{B}} T^{\mathrm{eq}}} \right) \right], \end{aligned} \tag{23.30}$$

where the sum over all quantum-well $\boldsymbol{k}$-states was expressed as the integral over the charge-carrier energy. A_{act} is the active region in-plane area, with the factor 2 accounting for spin degeneracy. By inverting the above expression, the quasi-Fermi level $E_{\mathrm{F},b}^{\mathrm{eq}}$ can be expressed in terms of the charge-carrier density in the quantum well,

$$E_{\mathrm{F},b}^{\mathrm{eq}} = E_{b,0}^{\mathrm{QW}} + k_{\mathrm{B}} T^{\mathrm{eq}} \log\left[\exp\left(\frac{w_b}{D_b k_{\mathrm{B}} T^{\mathrm{eq}}} \right) - 1 \right]. \tag{23.31}$$

Thus, the quantum-well charge-carrier population can be expressed as a function of the carrier density and the quasi-equilibrium temperature:

$$\rho_{b,\mathrm{QW}}(\varepsilon_{b,\boldsymbol{k}}^{\mathrm{2D}}) \equiv \rho_{b,\mathrm{QW}}(\varepsilon_{b,\boldsymbol{k}}^{\mathrm{2D}}, w_b, T^{\mathrm{eq}}) = \left[1 + \exp\left(\frac{\varepsilon_{b,\boldsymbol{k}}^{\mathrm{2D}} - E_{\mathrm{F},b}^{\mathrm{eq}}(w_b, T^{\mathrm{eq}})}{k_{\mathrm{B}} T^{\mathrm{eq}}} \right) \right]^{-1}. \tag{23.32}$$

By entering this relation into the expressions for the scattering rates Equation 23.22, also the individual scattering rates can be expressed as functions of only the 2D charge-carrier densities w_b and their quasi-equilibrium temperature T^{eq}, eliminating the need to keep track of the microscopic carrier population distribution.

Furthermore, it is now possible to relate the in- and out-scattering rates of a given scattering process to each other [70,71]. The out-scattering contribution in Equation 23.22 is equivalent to the in-scattering contribution under the replacement $\rho \to 1 - \rho$, which for the quantum well in quasi-equilibrium can be expressed as

$$1 - \rho_{\mathrm{QW}}(\varepsilon_{b,\boldsymbol{k}}^{\mathrm{2D}}) = \rho_{\mathrm{QW}}(\varepsilon_{b,\boldsymbol{k}}^{\mathrm{2D}}) \exp\left(\frac{\varepsilon_{b,\boldsymbol{k}}^{\mathrm{2D}} - E_{\mathrm{F},b}^{\mathrm{eq}}(w_b, T^{\mathrm{eq}})}{k_{\mathrm{B}} T^{\mathrm{eq}}} \right). \tag{23.33}$$

For the QD scattering processes the out-scattering rates can thus be written as [72]:

$$S_{b,m}^{\mathrm{cap,out}}(w_e, w_h, T^{\mathrm{eq}}) = S_{b,m}^{\mathrm{cap,in}}(w_e, w_h, T^{\mathrm{eq}}) \exp\left(\frac{\varepsilon_{b,m}^{\mathrm{QD}} - E_{\mathrm{F},b}^{\mathrm{eq}}}{k_{\mathrm{B}} T^{\mathrm{eq}}} \right) \tag{23.34}$$

$$S_b^{\mathrm{rel,out}}(w_e, w_h, T^{\mathrm{eq}}) = S_b^{\mathrm{rel,in}}(w_e, w_h, T^{\mathrm{eq}}) \exp\left(\frac{\varepsilon_{b,\mathrm{GS}}^{\mathrm{QD}} - \varepsilon_{b,\mathrm{ES}}^{\mathrm{QD}}}{k_{\mathrm{B}} T^{\mathrm{eq}}}\right), \tag{23.35}$$

where $\varepsilon_{b,m}^{\mathrm{QD}}$ denotes the energy of the localized QD state, with $m \in \{\mathrm{GS}, \mathrm{ES}\}$ distinguishing between GS and ES. The out-scattering of charge carriers thus becomes more probable at elevated charge-carrier temperatures [73,74]. Note that in the derivation of above expressions, only a quasi-equilibrium within the quantum well must be assumed without making assumptions about the QD occupations. Equations 23.34 and 23.35 are therefore also valid in nonequilibrium situations between QD and quantum well.

The resulting scattering contribution to the dynamics of the QD occupation probability is, therefore, written as

$$\begin{aligned}\frac{\partial \rho_{b,\mathrm{GS}}^{j}(z,t)}{\partial t}\Big|_{\mathrm{sc}} &= S_{b,\mathrm{GS}}^{\mathrm{cap,in}}\left[1-\rho_{b,\mathrm{GS}}^{j}\right] - S_{b,\mathrm{GS}}^{\mathrm{cap,out}}\rho_{b,\mathrm{GS}}^{j} \\ &\quad + S_b^{\mathrm{rel,in}}\rho_{b,\mathrm{ES}}^{j}\left[1-\rho_{b,\mathrm{GS}}^{j}\right] - S_b^{\mathrm{rel,out}}\rho_{b,\mathrm{GS}}^{j}\left[1-\rho_{b,\mathrm{ES}}^{j}\right] \end{aligned} \tag{23.36}$$

$$\begin{aligned}\frac{\partial \rho_{b,\mathrm{ES}}^{j}(z,t)}{\partial t}\Big|_{\mathrm{sc}} &= S_{b,\mathrm{ES}}^{\mathrm{cap,in}}\left[1-\rho_{b,\mathrm{ES}}^{j}\right] - S_{b,\mathrm{ES}}^{\mathrm{cap,out}}\rho_{b,\mathrm{ES}}^{j} \\ &\quad - \frac{1}{2}\left\{S_b^{\mathrm{rel,in}}\rho_{b,\mathrm{ES}}^{j}\left[1-\rho_{b,\mathrm{GS}}^{j}\right] - S_b^{\mathrm{rel,out}}\rho_{b,\mathrm{GS}}^{j}\left[1-\rho_{b,\mathrm{ES}}^{j}\right]\right\}. \end{aligned} \tag{23.37}$$

The scattering contribution to the quantum-well equations can be calculated from charge-carrier number conservation. It is simply given by the total charge-carrier density captured in the QD states:

$$\frac{\partial}{\partial t} w_b(z,t)\Big|_{\mathrm{sc}} = -2N^{\mathrm{QD}} \sum_{j,m} \nu_m f(j) \left(S_{b,m}^{\mathrm{cap,in}}(z,t)\left[1-\rho_{b,m}^{j}(z,t)\right] - S_{b,m}^{\mathrm{cap,out}}(z,t)\rho_{b,m}^{j}(z,t)\right). \tag{23.38}$$

23.2.4 Fit Functions for Scattering Rates

The microscopic calculation of the QD charge-carrier scattering rates requires a summation over all possible electronic states in the DWELL system, and such a calculation is, therefore, quite expensive in terms of computation time. While the scattering rates can be implemented by means of lookup tables, having a simpler analytic expression would be advantageous.

A first look at the scattering rates in dependence of the reservoir densities w_b reveals for the capture rates a quadratic increase at low densities, and a transition to nearly linear increase at higher values of w_b. The relaxation rates, on the other hand, show a linear increase at first and subsequent saturation. This is depicted in Figure 23.6 (circles). Taking these characteristics into account, we fit the scattering rates, using the following functions

$$S_{b,m}^{\mathrm{cap,in}}(w_b) = \frac{A {w_b}^2}{B + w_b} \tag{23.39}$$

$$S_{b,m}^{\mathrm{rel,in}}(w_b) = \frac{C w_b}{D + w_b}. \tag{23.40}$$

The corresponding out-scattering rates are calculated via Equations 23.34 and 23.35. Table 23.1 gives the fitting parameters extracted from the microscopically calculated rates. The comparison shown in Figure 23.6 shows good agreement between the microscopically calculated rates and the fit functions. For high reservoir carrier densities the fits show a slight deviation, especially pronounced in the hole

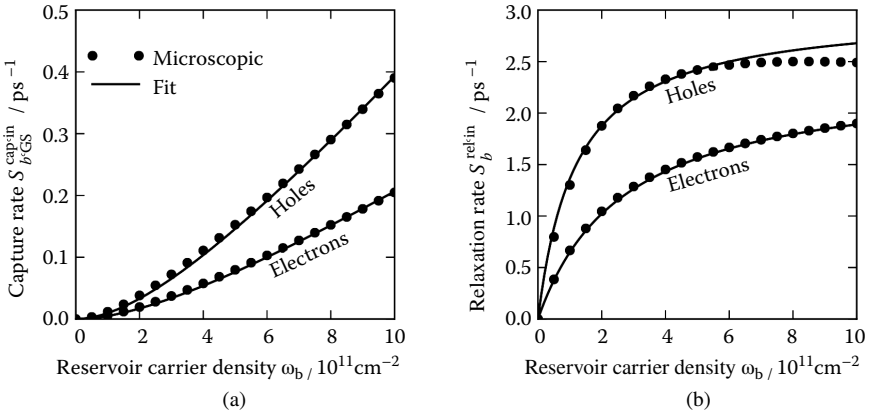

FIGURE 23.6 Fits of the quantum-dot scattering rates. Shown are (a) the ground-state direct-capture and (b) the intradot relaxation rate for electrons and holes, in dependence of the electron reservoir density w_b at $T = 300$ K. The microscopically calculated rates (circles) are shown together with the simple fit functions (lines). The fit parameters are given in Table 23.1.

TABLE 23.1 Fitting Parameters for the Scattering Rates

	Electrons		Holes	
	GS	ES	GS	ES
A (10^{-11}cm^2·ns^{-1})	32	54	60	79
B (10^{11}cm^{-2})	5.6	2.9	5.3	2.1
C (ns^{-1})	2400		3000	
D (10^{11}cm^{-2})	2.7		1.2	

Confinement energies: $\Delta E_e = 95$ meV, $\Delta_e = 60$ meV, $\Delta E_h = 50$ meV, $\Delta_h = 25$ meV.

relaxation rate. These values, however, correspond to very strong electrical pumping. For currents typically used in these devices, the fit functions presented are in very good agreement with the microscopic calculations.

The relatively simple expressions extracted from the fits to the microscopically calculated scattering rates show that the common approach of capture rates which are directly proportional to the reservoir charge-carrier density [17,75] should even yield quantitatively acceptable results. The saturation of the intradot relaxation rates at elevated carrier densities suggests the use of constant relaxation rates when simple QD models are desired. Nevertheless, when the accurate description of dynamics over a large range of operating conditions is required, the microscopic description of the QD scattering should be preferred.

23.2.5 Modeling of Spontaneous Emission

The spontaneous emission created in optical amplifier devices will be subject to stimulated amplification when emitted along the propagation axis. This ASE can reach significant optical power levels and is important for the device characteristics and performance. Apart from adding an optical noise background to the device output, it can often become strong enough to influence the charge-carrier dynamics [76–78]. These effects will deteriorate the device performance and the optical signal quality.

A consistent description of the ASE is important. In general there exist two appropriate modeling approaches: the deterministic description of the ASE power spectral density in the frequency space [17,79]

and the stochastic description in timedomain [43,78]. Here, we will employ the stochastic description, which simplifies the inclusion of time-varying input signals.

We, therefore, phenomenologically add an additional source term on the right-hand side of Equation 23.5, modeling the stochastic spontaneous emission added to the propagating electric field:

$$\frac{\mathrm{d}}{\mathrm{d}t}E_{\pm}(z,t') = S_{\pm}(z,t') + S_{\pm}^{\mathrm{sp}}(z,t')\,. \tag{23.41}$$

The electric field propagation along the one space-discretization section is again determined by integration of Equation 23.41 over the interval Δz:

$$E_{\pm}(z,t) \approx E_{\pm}(z \mp \Delta z, t-\Delta t) + \frac{\Delta t}{2}\left[S_{\pm}(z,t) + S_{\pm}(z \mp \Delta z, t-\Delta t)\right] + \int_{-\Delta t}^{0} S_{\pm}^{\mathrm{sp}}\Big(z \pm v_g\tau, t+\tau\Big)\mathrm{d}\tau\,. \tag{23.42}$$

The spontaneous emission source term must account for all optical transitions in the inhomogeneously broadened QD ensemble. Let $\eta_m^j(z,t)$ describe the spontaneous emission contribution of the jth subgroup of the mth localized state. We write for the electric field spontaneously added to the propagating field along Δz:

$$\int_{-\Delta t}^{0} S_{\pm}^{\mathrm{sp}}\Big(z \pm v_g\tau, t+\tau\Big)\mathrm{d}\tau \equiv \sum_{m,j}\eta_m^j(z,t)\,. \tag{23.43}$$

The spontaneous emission of an optical transition has a finite linewidth given by its homogeneous broadening. The homogeneous linewidth of a given transition is directly linked to the dephasing time τ_2 of the microscopic polarization, with the linewidth simply given by $2\tau_2^{-1}$. In order to correctly implement the spectral properties of the ASE, the spontaneously emitted field $\eta_m^j(z,t)$ must, therefore, have the correct linewidth and center frequency. It is thus not possible to describe the spontaneous emission by white noise, which would produce a flat noise spectrum; it must instead be modeled using colored noise. We implement this colored noise by two-dimensional Ornstein–Uhlenbeck processes [80], which describe quantities which are driven by white noise but relax with a given rate γ toward zero. This relaxation rate leads to a finite "memory" of the process, which translates into a finite spectral width around a center frequency. The time evolution of each of the respective noise signals is modeled by the following stochastic differential equation:

$$\frac{\mathrm{d}}{\mathrm{d}t}\eta_m^j(z,t) = -(i\omega_m^j + \gamma)\eta_m^j(z,t) + \sqrt{D_{\mathrm{sp},m}^j(z,t)}\,\tilde{\xi}_m^j(z,t)\,, \tag{23.44}$$

where $\tilde{\xi}(z,t)$ is a complex Gaussian white noise process, which is δ-correlated both in z and t. The relaxation rate of η_m^j is given by γ, and its center frequency by ω_m^j. The noise signal then fulfills the following properties [80]:

$$\langle \mathrm{Re}\,\eta_m^j(z,t)\rangle = \langle \mathrm{Im}\,\eta_m^j(z,t)\rangle = 0 \tag{23.45}$$

$$\langle |\eta_m^j(z,t)|^2\rangle = \frac{D_{\mathrm{sp},m}^j(z,t)}{\gamma} \tag{23.46}$$

$$\langle \eta_m^j(z,t)\eta_m^{j\,*}(z',t+\tau)\rangle \approx \frac{D_{\mathrm{sp},m}^j(z,t)}{\gamma}e^{-\gamma|\tau|}e^{i\omega_m^j\tau}\delta_{z,z'}\,. \tag{23.47}$$

Equation 23.47 is valid only under the assumption of a slowly varying noise amplitude $\partial_t D_{\mathrm{sp}}(z,t) \ll \gamma$, such that within one correlation time γ^{-1} the spontaneous emission amplitude can be assumed as constant. We can use the Wiener–Khinchin-theorem [81] this relation can be used to calculate the power spectrum $\mathcal{S}_{\eta_m^j}(z,\omega)$ of $\eta_m^j(z,t)$:

$$\mathcal{S}_{\eta_m^j}(z,\omega) = \frac{1}{2\pi}\int_{-\infty}^{\infty} \langle \eta_m^j(z,t)\eta_m^{j\,*}(z,t+\tau)\rangle e^{-i\omega\tau}\mathrm{d}\tau \tag{23.48}$$

$$= \frac{D_{\mathrm{sp},m}^j(z)}{\pi}\frac{1}{(\omega_m^j-\omega)^2+\gamma^2}\,, \tag{23.49}$$

which yields a Lorentzian line shape with a FWHM of 2γ. We thus identify $\gamma = (\tau_2)^{-1}$, such that the noise linewidth equals the homogeneous linewidth of the QD transitions.

Using the noise correlation properties, the average power that is added to the electric field by the noise can be calculated. Combining Equations 23.42 and 23.43 and summarizing the deterministic source terms in a combined variable, $\widetilde{S}_{\pm}^{\mathrm{stim}}$, yields for the electric field:

$$E_{\pm}(z,t) = E_{\pm}(z\mp\Delta z, t-\Delta t) + \widetilde{S}_{\pm}^{\mathrm{stim}}(z,t) + \sum_{m,j}\eta_m^j(z,t) \tag{23.50}$$

$$\left\langle \left|E_{\pm}(z,t)\right|^2\right\rangle = \left|E_{\pm}(z\mp\Delta z,t-\Delta t) + \widetilde{S}_{\pm}^{\mathrm{stim}}(z,t)\right|^2 + \sum_{m,j}\left\langle\left|\eta_m^j(z,t)\right|^2\right\rangle$$

$$= \left|E_{\pm}(z\mp\Delta z,t-\Delta t) + \widetilde{S}_{\pm}^{\mathrm{stim}}(z,t)\right|^2 + \sum_{m,j}\tau_2 D_{\mathrm{sp},m}^j(z,t)\,, \tag{23.51}$$

where we have used the zero mean property, $\langle\eta_m^j\rangle = 0$. On average, the spontaneous emission thus increases the squared modulus of the electric field along one space discretization step during the propagation time Δt by $\sum_{m,j}\tau_2 D_{\mathrm{sp},m}^j(z,t)$. Or, written in terms of a time derivative,

$$\frac{\partial}{\partial t}|E_{\pm}(z,t)|^2\Big|_{\mathrm{sp}} = \frac{\tau_2}{\Delta t}\sum_{m,j} D_{\mathrm{sp},m}^j(z,t)\,. \tag{23.52}$$

In the photon picture, the average change of the electric field energy density due to the spontaneous emission can be calculated:

$$\frac{\partial}{\partial t}u(z,t)\Big|_{\mathrm{sp}} = \frac{\varepsilon_{\mathrm{bg}}\varepsilon_0}{2}\frac{\partial}{\partial t}|E_{\pm}(z,t)|^2\Big|_{\mathrm{sp}}$$

$$= \beta\frac{2N^{\mathrm{QD}}\Gamma}{h^{\mathrm{QW}}}\sum_{m,j}\nu_m f(j)\hbar\omega_m^j W_m \varrho_{\mathrm{e},m}^j(z,t)\varrho_{\mathrm{h},m}^j(z,t)\,. \tag{23.53}$$

Here we model spontaneous emission by bimolecular recombination processes, given by the sum over all QD states. The spontaneous emission ratio β gives the fraction of photons spontaneously emitted into the waveguide mode. Comparing Equations 23.52 and 23.53 yields for the individual noise strengths

$$D_{\mathrm{sp},m}^j(z,t) = \frac{\Delta t}{\tau_2}\frac{2\beta\Gamma\hbar\omega_m^j 2N^{\mathrm{QD}}}{\varepsilon_{\mathrm{bg}}\varepsilon_0 h^{\mathrm{QW}}}\nu_m f(j)\frac{1}{2}\left[R_{\mathrm{sp},m}^j(z,t) + R_{\mathrm{sp},m}^j(z\mp\Delta z, t-\Delta t)\right]\,, \tag{23.54}$$

where the average of the spontaneous emission rate at the endpoints of the integration interval $[z, z \mp \Delta z]$ was taken, defined by

$$R^j_{\mathrm{sp},m}(z,t) := W_m \varrho^j_{\mathrm{e},m}(z,t)\varrho^j_{\mathrm{h},m}(z,t)\,. \tag{23.55}$$

The spontaneous emission noise thus depends on the optical frequency and on the occupation of the individual QD subgroups. The resulting propagation equation for the electric field is thus given by

$$E_\pm(z,t) \approx E_\pm(z \mp \Delta z, t-\Delta t) + \frac{\Delta t}{2}\left[S_\pm(z,t) + S_\pm(z \mp \Delta z, t-\Delta t)\right] + \sum_{m,j} \eta^j_m(z,t)\,. \tag{23.56}$$

23.3 Application Examples

The QDSOA model derived in the previous section will now be applied to an exemplary device. We implement Equations 23.11 through 23.17, which describe the active medium dynamics, along with Equation 23.56 to describe the electric field propagation including spontaneous emission noise. The charge-carrier scattering is described within the full microscopic framework as described in Equations 23.36 through 23.38, with the individual scattering rates depending on the reservoir carrier densities as well as the device temperature.

In this section we will at first investigate the static characteristics of the amplifier, focusing on the unique properties of the QD active medium. We thus calculate the pump-current dependent-gain spectra for the sample device, along with ASE spectra. Our modeling approach allows for a characterization over a large range of pump currents, accounting for the changing carrier dynamics by the nonlinear scattering rates. We analyze the performance of the QDSOA for optical signals centered on either the GS or ES energies, exploiting the broad gain spectrum due to the different localized states. Subsequently, we characterize the dynamic gain recovery after perturbation of the gain medium by a strong pulse. The gain recovery dynamics provide an important insight into the ultrafast amplification capabilities of an amplifier. Furthermore, we show how the internal charge-carrier dynamics imprint their signature onto the gain dynamics. The last part of this section addresses the phenomenon of coherent pulse-shaping by Rabi oscillations in QDSOAs, enabled by the comparably long dephasing time of the interband polarization. The interaction of ultrashort pulses with the QD gain medium, therefore, leads to strong modifications of the pulse shape. These modifications differ from classical descriptions and can be very complex due to the individual dynamics of QDs within the inhomogeneous ensemble.

23.3.1 Static Characterization of the QDSOA

In linear amplification applications, the device performance of SOAs is generally limited by two competing effects. On the one hand, the maximum achievable optical output power is limited by the charge carriers available for stimulated emission. The gain of the amplifier will, therefore, decrease when the optical power becomes too large. This effect is known as gain saturation. On the other hand, a too small optical signal will significantly reduce the signal-to-noise ratio, as the spontaneous emission background will dominate the output. Noise effects thus play an important role in the amplification of optical data signals [82,83]. A strong noise background will negatively impact the signal quality by distorting the corresponding optical output, and potentially corrupting the transmitted data stream. It is, therefore, important to investigate the ASE and gain of a given amplifier device to assess its suitability in a given application.

We implement the previously derived QD amplifier model to simulate the static characteristics of a specific device. We solve the delay-differential equation system using the simple forward-Euler method. The Gaussian white noise for implementing the spontaneous emission is generated by the Box–Muller algorithm [84]. For each spatial section of the amplifier device, we save a history array containing $\Delta t/\mathrm{d}t$

entries (up to Δt before the current time t) of the electric field $E_{\pm}(z,t)$, the field source term $S_{\pm}(z,t)$, and the spontaneous emission rate $R^{j}_{\mathrm{sp},m}(z,t)$.

The modeled amplifier is a 3-mm-long DWELL structure, consisting of ten 5-nm-thick InGaAs quantum wells, each embedding a density of $3 \times 10^{10}\,\mathrm{cm}^{-2}$ InAs QDs with a shallow-etched, 4-μ-wide ridge waveguide. Refer to Figure 23.3 for an illustration of the modeled energy structure. The device parameters that will be used here and in the following sections are given in Table 23.2, unless otherwise noted.

Additional phenomenological dependencies of the dephasing time and the device temperature on the applied pump current are included to account for heating effects as well as carrier-induced dephasing. We assume a temperature that increases linearly with the applied current,

$$T_{\ell}(j) = 295\,\mathrm{K} + \frac{j}{14}\frac{\mathrm{K}}{\mathrm{mA}}\,. \tag{23.57}$$

The increase in temperature significantly alters the detailed balance relationship, Equations 23.34 and 23.35, which determines the out-scattering rates out of the localized QD states. This, in turn, determines the quasi-equilibrium distribution that is reached in the steady state. Furthermore, the dephasing time of the QD interband polarization is known to decrease under strong excitation and with temperature [27,28]. We thus introduce a current-dependent dephasing time,

$$\tau_2(j) = \frac{\tau_2^0}{1 + \frac{j}{300\,\mathrm{mA}}}\,, \tag{23.58}$$

TABLE 23.2 Model Parameters Used in the Simulations, unless Otherwise Stated.

Symbol	Value	Meaning
N^{QD}	$3 \times 10^{10}\,\mathrm{cm}^{-2}$	QD density per layer
a_L	10	Number of layers
h^{QW}	5 nm	QW layer height
w_{wg}	4μ	Waveguide width
n_{bg}	3.77	Background index
ΔE_{inh}	30 meV	QD inhomogeneous broadening FWHM
η	0.4	Current injection efficiency
A^S	$0.7\,\mathrm{ns}^{-1}$	QW linear recombination rate
B^S	$50\,\mathrm{nm}^2\,\mathrm{ns}^{-1}$	QW bimolecular recombination rate
W_m	$1\,\mathrm{ns}^{-1}$	QD spontaneous recombination rate
β	3.5×10^{-4}	Spontaneous emission ratio
$\langle\hbar\omega_{\mathrm{GS}}\rangle$	963 meV (1288 nm)	QD GS center emission
$\langle\hbar\omega_{\mathrm{ES}}\rangle$	1048 meV (1183 nm)	QD ES center emission
μ_m	$0.6\,\mathrm{nm}\,e_0$	QD transition dipole moment
τ_2	$200\,\mathrm{fs} \times \left(1 + \frac{j}{300\,\mathrm{mA}}\right)^{-1}$	QD polarization dephasing time
T_{ℓ}	$295\,\mathrm{K} + \frac{j}{14}\frac{\mathrm{K}}{\mathrm{mA}}$	Lattice temperature
Γ	0.045	Geometric confinement factor
$\Delta E_e(\Delta E_h)$	95 meV (50 meV)	Electron (hole) QD GS localization energy
$\Delta_e(\Delta_h)$	60 meV (25 meV)	Electron (hole) QD GS–ES energy spacing
Z	31	Number of space discretization steps
$\mathrm{d}t$	1 fs	Numeric time step

QW, quantum well; QD, quantum dot; GS, ground state; ES, excited state; FWHM, full-width half maximum.

where τ_2^0 denotes the corresponding dephasing time at $j = 0$. The above effects lead to broadening and subsequent decrease of the optical gain at high pump currents, as frequently observed in experiments [85]. Note that the dephasing time can in principle be calculated from microscopic scattering processes similar to the formalism presented in Section 23.2.3. A rigorous treatment of these effects, however, requires microscopic approaches that go beyond the employed Born–Markov approximation [86–90], which are beyond the scope of this chapter.

With the above additions, we calculate the key characteristics of the amplifier device, starting with the small-signal optical gain spectrum. The small-signal gain $G(\omega)$ is calculated from the stationary QD distribution (i.e., without a disturbing optical signal) via

$$G(\omega) = \exp\left[\frac{2}{v_g}\int_0^{\ell} g\,(z, t, \omega)\,\mathrm{d}z\right], \tag{23.59}$$

with the instantaneous amplitude gain

$$g(z, t, \omega) = \frac{\hbar\omega\Gamma}{\varepsilon_0\varepsilon_{\mathrm{bg}}h^{\mathrm{QW}}}2N^{\mathrm{QD}}\sum_{j,m}\nu_m f(j)\frac{\tau_2|\mu_m|^2}{2\hbar^2}\frac{\left[\rho^j_{e,m}(z,t)+\rho^j_{h,m}(z,t)-1\right]}{1+[\tau_2(\omega-\omega^j_m)]^2} \tag{23.60}$$

determined from the steady-state solution to Equation 23.11. The resulting spectra are shown in Figure 23.7a, clearly showing the GS gain peak around 1300 nm, which saturates and decreases for higher pump currents, at which the ES gain becomes dominant. We plot the optical gain at the GS and ES transitions, at $\lambda = 1288$ nm and $\lambda = 1183$ nm, respectively, under the dependence of the pump current, shown in Figure 23.7b.

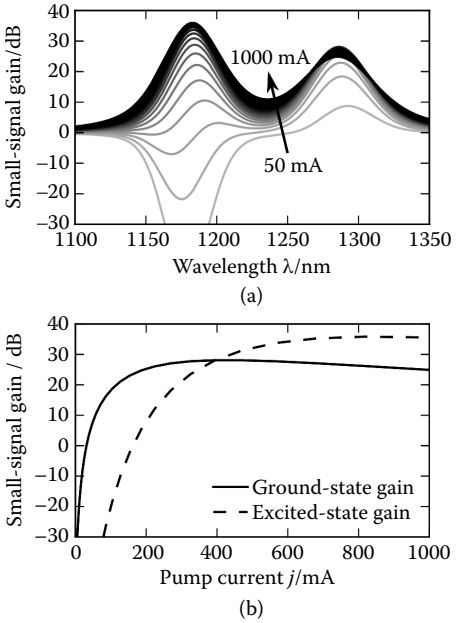

FIGURE 23.7 (a) Static gain spectra of the quantum dot semiconductor optical amplifier device for increasing pump currents up to $j = 1000$ mA in steps of 50 mA. (b) Small-signal gain at the ground (solid) and excited state (dashed) wavelengths ($\lambda_{\mathrm{GS}} = 1288$ nm, $\lambda_{\mathrm{ES}} = 1183$ nm) under the dependence of the pump current.

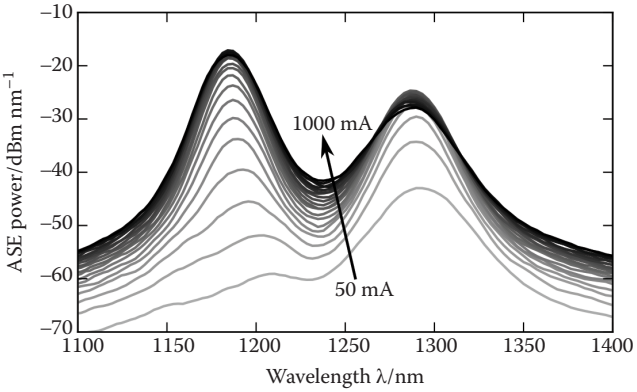

FIGURE 23.8 Simulated amplified spontaneous emission (ASE) spectra for increasing pump currents up to $j = 1000$ mA in steps of 50 mA.

Additionally, we can calculate the ASE spectra, shown in Figure 23.8. These are calculated by direct integration of the dynamic equations and subsequent Fourier transform of the electric field time series at the output facets. The resulting spectra can be used for a direct quantitative comparison with experimental data. The output power at the corresponding end facets is related to the electric field via

$$P_{\pm}^{\text{out}} = A_{\text{beam}} \frac{\varepsilon_0 n_{\text{bg}} c_0}{2} |E_{\pm}^{\text{out}}|^2 , \tag{23.61}$$

where $A_{\text{beam}} = \frac{a_L h^{\text{QW}} w_{\text{wg}}}{\Gamma}$ is the beam area in the waveguide and $E_{\pm}^{\text{out}} = \left\{E_+(\ell), E_-(0)\right\}$ denotes the forward- and back-propagating electric fields at their respective end facets. The ASE spectra mimic the qualitative behavior of the gain spectra, with clearly distinguishable GS and ES peaks and a saturation for strong pump currents (see Figure 23.8, where increasing gray levels indicate higher pump current). In addition, an initial blueshift of the emission peaks is visible especially for the ES emission. This is due to state filling, i.e., the shift of the quasi-Fermi levels toward higher energies with increasing carrier densities. At low currents, only the lowest energy states are occupied by charge carriers, and only with increasing current can the higher lying energy states be filled. In the model, this is accounted for by the detailed balance relation between the in- and out-scattering rates (Equations 23.34 and 23.35), which ensures the relaxation toward a quasi-Fermi distribution in the steady state. The quasi-Fermi level shifts toward higher energies with increasing reservoir carrier density, thus leading to a higher occupation in higher energy states.

When an optical signal of significant power is amplified by the gain medium, its charge-carrier distribution can be substantially perturbed. This leads to a power-dependent response of the device and thus induces nonlinearities. In order to quantify this response, we simulate the amplifier under the injection of a constant optical input signal with varying power. As we have seen previously, the existence of localized QD states makes it possible for the amplifier to work on GS and ES wavelengths. We will, therefore, investigate the device performance under amplification of signals at either of the two corresponding wavelengths. We put in an electric field at the input facet as

$$E_+(0, t) = E_{\text{in}}^m e^{-i(\langle\omega^m\rangle - \omega)t} , \tag{23.62}$$

with the frequency detuning $(\langle\omega^m\rangle - \omega)$ $(m \in \{\text{GS}, \text{ES}\})$ of the input signal relative to the carrier frequency chosen to yield signals centered on the energy of either QD state. After the propagation of the signal through

the amplifier device and after a steady state is reached, we can simply evaluate the power-dependent device gain by the power ratio

$$G = \frac{|E_+(\ell, t)|^2}{|E_+(0, t)|^2} \,. \tag{23.63}$$

Figure 23.9a shows the GS gain in dependence on the achievable optical output power for different pump currents. The small-signal gain, i.e., at low input powers, shows the behavior that we have seen before in Figure 23.7, with a saturation and subsequent decrease of the gain for increasing current. In the linear amplification regime, for lower optical power, the gain is flat. Under these small-signal conditions, the optical power is not strong enough to perturb the gain medium appreciably. Once the optical power becomes large enough, the nonlinear or gain saturation regime is reached [10,11,79]. In Figure 23.9, the onset of the GS saturation regime increases from 18 dBm output power at $j = 200$ mA to 25 dBm at $j = 1000$ mA. Here, the number of charge carriers injected into the optically active QD states is not sufficient to replenish the QD states that are depleted by the signal, and the optical gain thus gradually decreases.

A general trend toward higher achievable output power with increasing current and corresponding shift of the nonlinear regime toward higher optical power can be observed both in the GS and ES (see Figure 23.9a and b). This is a direct consequence of the increased in-scattering rates and the higher reservoir charge-carrier density [10]. The faster and more efficient refilling of the QD states after depletion by the optical signal shifts the saturation regime toward higher power. The ES shows a transition to the nonlinear gain regime at lower optical power than the GS, as shown in Figure 23.9b. This can be understood by the weaker confinement of the QD ES relative to the reservoir, which increases the sensitivity of the ES occupation to changes in the reservoir charge-carrier density. Nevertheless, the ES allows a high gain and a sufficiently high saturation power to allow for its application in optical communication networks. Furthermore, the ultra-broad gain bandwidth of QDSOAs could be exploited for a simultaneous amplification of data signals with wide wavelength spacing. The low cross-talk between the GS and ES transitions makes an error-free amplification of two suitable data signals possible, as was recently shown [91].

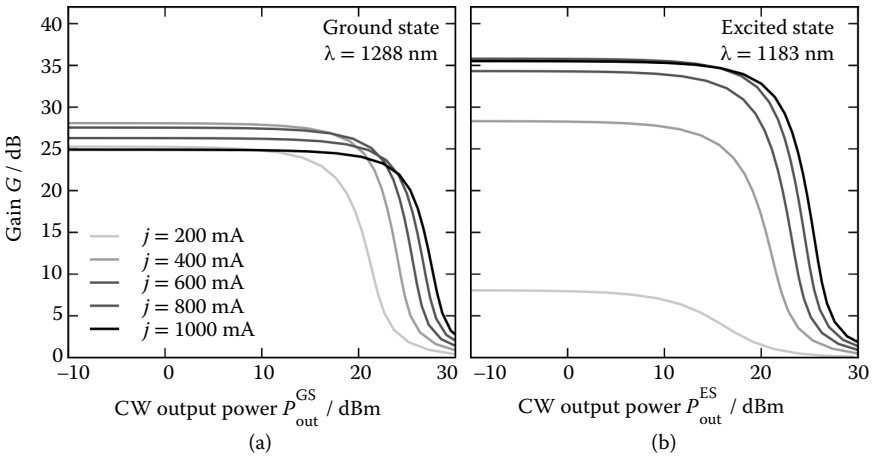

FIGURE 23.9 Optical gain G of the quantum-dot amplifier in dependence of the optical output power P_{out}^{m} for different pump currents j. Shown is the response to optical signals centered on (a) the ground state, and (b) the excited-state wavelength.

23.3.2 Gain Recovery Dynamics in QDSOAs

We now wish to characterize the dynamic performance of the modeled QD semiconductor amplifier. When optical amplifiers are used in optical data signal transmission, e.g., for propagation loss compensation, their dynamics must be fast enough to follow the signal symbol rate in order to minimize patterning effects and reduce transmission errors, as detailed in Chapter 25 on patterning effects. In experimental setups the gain recovery dynamics can be characterized by observing the time evolution of the optical gain after a perturbation of the active medium. This is commonly done in a pump-probe setup [19,92–94]. The principle is as follows: A strong and temporally narrow optical pump pulse is injected into the waveguide and depletes charge carriers during its amplification. A weaker probe pulse injected with a time delay $\Delta t_{\mathrm{p-p}}$ with respect to the pump pulse then experiences a different gain, depending on the perturbation of the carrier distribution after this delay time. By repeating the measurement for a range of $\Delta t_{\mathrm{p-p}}$ and measuring the probe pulse intensity, the time evolution of the gain after propagation of the pump pulse can be extracted experimentally.

The gain-recovery dynamics is obtained from the QDSOA model by simulating the amplifier in a pump-probe experiment. The perturbation of the gain medium is induced by a strong Gaussian pump pulse injected into the input facet at $z = 0$:

$$E_{+}(0,t) = E_{\mathrm{in}} \exp\left[-4\ln 2\left(\frac{t-t_0}{\Delta_{\mathrm{FWHM}}}\right)^2\right] e^{-i\delta\omega t}, \tag{23.64}$$

with an input amplitude E_{in}, arrival time t_0, and pulse width Δ_{FWHM}. We additionally allow for a detuning $\delta\omega$ of the pump pulse with respect to the chosen optical reference frequency which we can use to tune the pump wavelength. In order to probe the gain after the pump pulse has passed the active medium, the probe pulse does not have to be modeled explicitly. Instead, we can directly calculate the gain that the probe would experience along the device:

$$G(\Delta t_{\mathrm{p-p}}, \omega) = \exp\left[\frac{2}{v_g}\int_0^{\ell} g\left(z, t_0 + \Delta t_{\mathrm{p-p}} + \frac{z}{v_g}, \omega\right) \mathrm{d}z\right]. \tag{23.65}$$

Here, we used the instantaneous amplitude gain, as defined in Equation 23.60, integrated along the device in a copropagating frame with a delay time $\Delta t_{\mathrm{p-p}}$ relative to the pump pulse. Note that in pump-probe experiments the temporal resolution is limited by the temporal width of the probe pulse. Measuring the integrated probe pulse power averages the extracted gain over the pulse profile.

As an example, we simulate the amplifier under the influence of a pump pulse with a width of $\Delta_{\mathrm{FWHM}} =$ 300 fs and a pulse energy of 1 pJ, centered on the GS gain peak. In Figure 23.10a the resulting gain recovery curves are shown in dependence of the pump current. Here, we show the gain difference ΔG with respect to the unperturbed case. A strong initial reduction in gain can be observed due to the depletion of charge carriers by the pump pulse, with a subsequent recovery toward the unperturbed value on a picosecond timescale. This fast recovery is the signature of the charge-carrier refilling by carrier scattering, which as a consequence is strongly current-dependent and mimics the current dependence of the scattering rates. Pump-probe gain recovery measurements can, therefore, be used to extract effective charge-carrier scattering timescales of the active QD medium [95]. In addition to the GS performance, we take a look at the dynamics of the ES gain in Figure 23.10b. Here, for $j = 100$ mA, the pump-pulse induces an initial increase of the gain, as seen in the initially increasing light gray curve. At this current, the ES is below transparency, and the pump pulse is absorbed, which increases the inversion and thus the gain. For higher pump currents (increasing gray levels in Figure 23.10) the dynamics follows the same trends as the GS, albeit with a slower recovery. Here again the less efficient carrier refilling of the ES becomes apparent. The intricate scattering

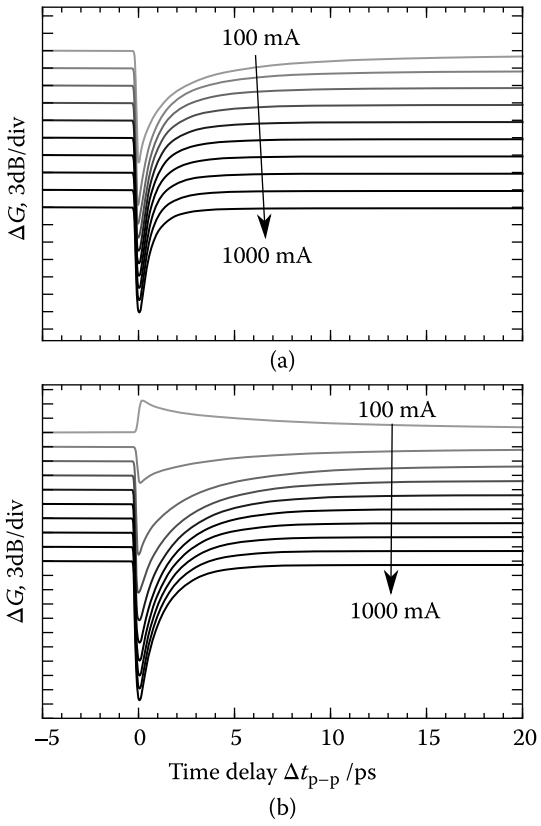

FIGURE 23.10 Gain recovery after perturbation with a strong pump pulse at $\Delta t_{\mathrm{p-p}} = 0$. (a) Ground-state gain after excitation at the ground-state wavelength centered at $\lambda = 1288$ nm, and (b) excited-state gain after excitation at the excited-state wavelength centered at $\lambda = 1183$ nm. The current was increased from $j = 100$ mA to $j = 1000$ mA in steps of 100 mA. Shown is the gain difference with respect to the unperturbed case, with individual curves shifted vertically by 3 dB for improved readability.

dynamics between the different QD and reservoir states in the active medium, therefore, directly affects the performance of QD optical amplifiers, emphasizing the importance of its accurate modeling, as described in Section 23.2.3.

With the QDSOA model at hand, we can take a closer look at the dynamics of the QD gain medium. The gain recovery can be seen to consist of three main components, i.e., it can be fitted very accurately by a triexponential recovery, as shown in Figure 23.11a. Here, we do not show the fit for $t \lesssim 0.1$ ps as for small times the pulse is still interacting with the medium, which the fit cannot describe. We can attribute the three time constants to the intradot relaxation, being the fastest component, the charge-carrier capture from the reservoir, and a slow recovery of the whole system, governed mainly by the reservoir carrier lifetime. An experimental determination of the individual timescales, however, is usually difficult due to their narrow separation. This is already evident from the three effective timescales that determine the gain recovery. In principle, we would expect at least seven different timescales: GS and ES capture rates and intradot relaxation for both electrons and holes, along with the recovery of the reservoir. The three extracted timescales must, therefore, be interpreted as effective values.

Our model also allows us to analyze the charge-carrier dynamics within the gain medium directly, which is not possible within the experimental setup. We thus evaluate the variation of the carrier occupation in

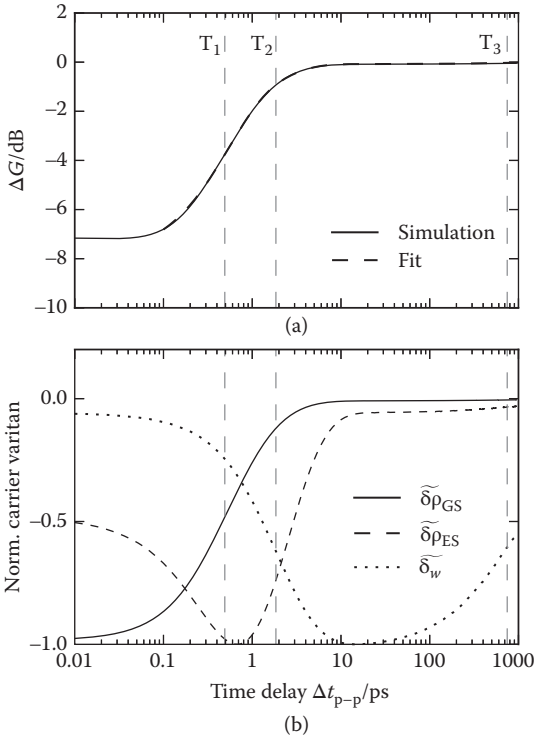

FIGURE 23.11 (a) Fit to the gain recovery after a perturbation of the ground state at $j = 500\,\text{mA}$. The three characteristic timescales, $\tau_1 = 0.49\,\text{ps}$, $\tau_2 = 1.8\,\text{ps}$, $\tau_3 = 750\,\text{ps}$, correspond to the intradot relaxation, charge-carrier capture, and reservoir refilling, respectively. (b) Time evolution of the normalized carrier variations with respect to their respective steady-state values in the GS, ES, and reservoir states.

the QD GS and ES as well as in the reservoir states at the output facet, by defining a normalized carrier variation,

$$\widetilde{\delta\rho}_m(t) = \frac{\sum_b \left[\rho_{b,m}(t) - \rho^0_{b,m}\right]}{\max\left|\sum_b \left[\rho_{b,m}(t) - \rho^0_{b,m}\right]\right|}, \tag{23.66}$$

where ρ^0_m denotes the corresponding QD occupation in the unperturbed steady state. A similar expression for the reservoir density variation, $\widetilde{\delta w}$, can be written down. During the perturbation the normalized variations reach their minimum value of -1 and during recovery slowly grow back to a value of zero. The variations of the GS, ES, and reservoir carriers are plotted in Figure 23.11b, as solid, dashed, and dotted lines, respectively. We can clearly observe the three qualitative steps in the recovery of the gain medium we discussed earlier. The GS occupation is minimal right after the pulse has passed the device. On a timescale close to τ_1, the GS starts a fast recovery under a reduction of the ES occupation, illustrating the intradot relaxation from the ES states to the GS. These relaxation processes dominate the ultrafast gain recovery of QDSOAs. The ES then starts to recover with a timescale $\approx \tau_2$ due to charge-carrier capture from the reservoir, which is subsequently depleted. The timescale τ_3 then constitutes the recovery time of the reservoir, which equilibrates the whole system again.

For the modeled device, the two fast timescales of the GS gain recovery decrease from $\tau_1 = 1.4\,\text{ps}$, $\tau_2 = 7.5\,\text{ps}$ at a current of 100 mA to $\tau_1 = 0.43\,\text{ps}$, $\tau_2 = 1.2\,\text{ps}$ at $j = 1000\,\text{mA}$ (not shown here). Together

with the increasing saturation power at higher currents, a high operating current could be seen as optimal for high-power ultrafast applications. However, the saturation and decrease of the optical gain at elevated pump currents limits the range of possible operating conditions.

23.3.3 Rabi Oscillations in QD Semiconductor Amplifiers

When the quantum-mechanic phase is maintained over macroscopically accessible timescales, coherent effects can induce phenomena that significantly differ from classical predictions. The precondition for this is a sufficiently long dephasing time of the quantum-mechanic coherence. The comparably long lifetime of the interband polarization in semiconductor QDs makes them promising candidates for applications in quantum-optics [96]. Recently, coherent pulse propagation in macroscopic semiconductor devices has been observed in quantum-cascade lasers [97] and quantum-dash [30] and QD semiconductor amplifiers [32], relying on ultrashort, strong optical pulses. It is important to note that in the experiments using optical amplifiers, the measurements were performed at room temperature, opening up possible future quantum-coherent applications using uncooled devices.

In this section, we present a theoretical description of Rabi oscillations induced by ultrashort pulses in a QDSOA at room temperature [32]. Rabi oscillations denote a periodic exchange of energy between the optical field and the active medium, which leads to characteristic modifications of the optical pulse traveling through the amplifier device. The principle of Rabi oscillations can be derived from the dynamic equation for a single QD subgroup:

$$\frac{\partial}{\partial t}p_m^j(z,t) = -\left[i(\omega_m^j-\omega)+\frac{1}{\tau_2}\right]p_m^j - i\frac{\mu_m}{2\hbar}\left(\rho_{e,m}^j+\rho_{h,m}^j-1\right)E(z,t)\,, \tag{23.67}$$

$$\frac{\partial}{\partial t}\rho_{b,m}^j(z,t) = \frac{1}{\hbar}\mathrm{Im}\left[p_m^j\mu_m^*E^*(z,t)\right] - W_m\rho_{e,m}^j\rho_{h,m}^j + \frac{\partial}{\partial t}\rho_{b,m}^j\Big|_{\mathrm{sc}}\,. \tag{23.68}$$

We reduce the above equations by introducing the inversion $d = (\rho_{e,m}^j+\rho_{h,m}^j-1)$ and neglecting losses. We also limit ourselves to a resonant excitation, i.e., $\omega = \omega_m^j$:

$$\frac{\partial}{\partial t}p_m^j(z,t) = -i\frac{\mu_m}{2\hbar}d(z,t)E(z,t)\,, \tag{23.69}$$

$$\frac{\partial}{\partial t}d(z,t) = \frac{2}{\hbar}\mathrm{Im}\left[\mu_m^*E^*(z,t)p_m^j(z,t)\right]. \tag{23.70}$$

For an initial inversion of d_0 and zero polarization, the above equations have the solution

$$p_m^j(z,t) = -\frac{i}{2}\sin\Theta(z,t), \tag{23.71}$$

$$d(z,t) = d_0\cos\Theta(z,t), \tag{23.72}$$

with the pulse area defined as

$$\Theta(z,t) = \int_{-\infty}^{t}\frac{\mu_{\mathrm{GS}}}{2\hbar}\left|E(z,t')\right|\mathrm{d}t'. \tag{23.73}$$

Equation 23.72 shows that, with a proper choice of the pulse area, it is possible, e.g., to invert the charge-carrier distribution by choosing $\Theta=\pi$. When choosing $\Theta = n2\pi, n\in\mathbb{N}$, i.e., integer multiples of 2π, the system returns to its initial state after the exciting pulse has passed through. This important property shows

that the coherent interaction between the optical field and the active material is a reversible process, as long as the polarization dephasing time is much larger than the pulse width. In most cases, however, this condition is not strictly fulfilled, leading to an additional damping of the Rabi oscillations[48].

We now apply our QD amplifier model to the amplification of strong optical pulses. We use the same pulse width of 300 f s as in the previous section, but with higher input amplitudes and we evaluate the output pulse shape as well as the integrated optical gain, as defined in Equation 23.65. For different input pulse areas Θ, the field amplitude at the output facet is shown in Figure 23.12a. At a small pulse area $\Theta = 0.1\pi$ (23 f J pulse energy, light gray line) the pulse retains its Gaussian shape during propagation. For increasing pulse energies (darker lines in Figure 23.12), a pronounced shoulder at the leading edge of the pulse appears and the pulse shape noticeable diverts from its original Gaussian envelope. For $\Theta = 2\pi$ a pronounced dip in amplitude is visible, and a second dip appears for $\Theta = 5\pi$ (black line), where a complex pulse shape is obtained. A look into the dynamics of the optical gain, shown in Figure 23.12b, reveals a strong decrease in gain after injection of the optical pulse, as already seen in the previous section. For strong pulses, the gain exhibits oscillations and intermittently becomes negative, i.e., absorbing (see black line in Figure 23.12). This is a clear indication of the occurrence of Rabi oscillations, i.e., the coherent interaction between the microscopic polarization and the inversion. For an incoherent interaction, i.e., neglecting the coherent dynamics of the polarization, the optical gain cannot be reduced below transparency in optically pumped media. The coherent dynamics thus imprints a clear signature onto the QD amplifier behavior, which can differ strongly from conventional expectations.

We take a closer look at the dynamics of the amplifier under the amplification of strong pulses in Figure 23.13. The dynamics of the microscopic polarization and the carrier occupation across the inhomogeneously broadened QD GS at the output facet are visualized as gray scale values in Figure 23.13b and c, respectively. The optical pulse can be seen to induce a complex response of the gain medium. The QD

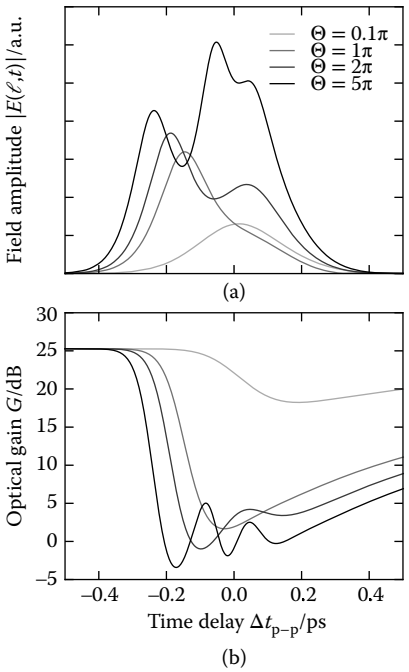

FIGURE 23.12 Rabi oscillations in the QD semiconductor optical amplifier. (a) Output electric field amplitudes for different input pulse areas $\Theta \in \{0.1\pi, 1\pi, 2\pi, 5\pi\}$, corresponding to pulse energies of 0.023, 2.3, 9.4, 58 pJ, respectively. (b) Integrated optical gain in dependence of the time delay $\Delta t_{\mathrm{p-p}}$. The pump current was set to $j = 200$ mA.

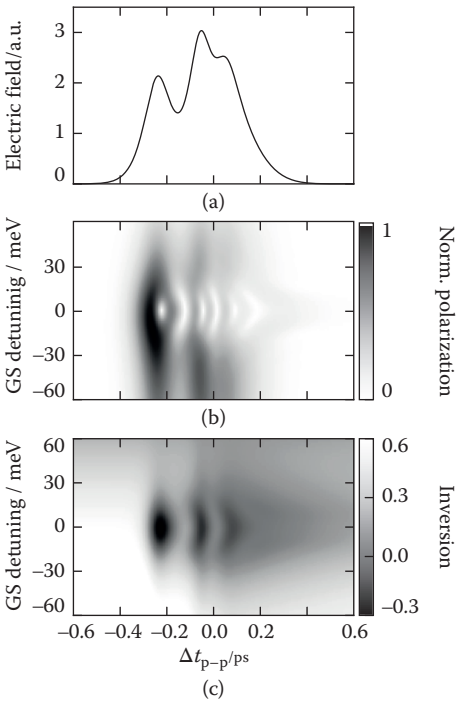

FIGURE 23.13 Quantum-dot (QD) ground-state dynamics for an input pulse area $\Theta = 5\pi$. (a) Output electric field amplitude. (b) Time evolution of the microscopic polarization amplitude p_m^j in dependence of the QD GS transition energy. The color code denotes the normalized polarization amplitude. (c) QD ground-state carrier dynamics in dependence of the QD GS transition energy. The color code denotes the QD subgroup inversion. The pump current was set to $j = 200$ mA.

subgroups within the ensemble which are resonant to the pulse (detuning of 0 meV), exhibit pronounced Rabi oscillations visible in both the polarization and inversion. The outer subgroups show this behavior to a lesser extent but with a different temporal profile. The resulting macroscopic polarization that drives the pulse is a superposition of the individual microscopic polarization amplitudes across the whole QD ensemble (see Equation 23.13). The response of the gain medium to such strong optical pulses can, therefore, be very complex and go beyond what a simple two-level system would predict. This underlines the importance of taking both homogeneous as well as inhomogeneous effects into account when modeling light–matter interaction in QD devices in the high-power and ultrafast regime.

23.4 Conclusion

In this chapter, we have presented a model for QDSOAs that takes into account the intricate scattering dynamics between the localized QD states and the surrounding carrier reservoir states. The Coulomb scattering, which dominates the carrier dynamics, can be microscopically calculated to yield Boltzmann-like terms describing the charge-carrier scattering, which can be implemented numerically in terms of lookup tables, or approximated by simplified fit functions. The description of the electric field propagation along the device is modeled using a delay-differential equation approach, which allows a separation of numeric time step and spatial discretization length for an efficient integration algorithm.

The complex charge-carrier dynamics determine both the static and dynamic behavior of QDSOAs and is responsible for their ultrafast gain recovery. An accurate modeling of these dynamics is, therefore, necessary for a quantitatively accurate description of these optoelectronic devices. The simulations of an

exemplary QDSOA device show that the signature of the internal charge-carrier dynamics can be directly seen in dynamic gain recovery measurements. The strong pump-current dependence of the scattering timescales lead to the existence of optimal operating conditions when either high gain or ultrafast gain recovery is desired. The long dephasing time of QDs compared to other semiconductor materials leads to a macroscopically accessible measurement of quantum-coherence manifesting itself in the break-up of ultrashort strong optical pulses, even at room temperature. The induced Rabi oscillations lead to a complex response of the QD gain medium which requires a detailed modeling of the polarization dynamics across the inhomogeneously broadened QD ensemble. The thoroughly nonclassical response of the QD medium to ultrashort pulses due to long-lived coherence might pave the way to novel quantum-optical devices using semiconductor QDs as the medium of choice.

References

1. P. Harrison, *Quantum Wells, Wires and Dots: Theoretical and Computational Physics of Semiconductor Nanostructures*. Chichester, UK: John Wiley & Sons (2005).
2. K. Lüdge, *Nonlinear Laser Dynamic—From Quantum Dots to Cryptography*. Weinheim: Wiley-VCH (2012).
3. D. Bimberg, Quantum dot based nanophotonics and nanoelectronics, *Electron. Lett*., 44 (2008), p. 168.
4. J. J. Coleman, The development of the semiconductor laser diode after the first demonstration in 1962, *Semicond. Sci. Technol*., 27 (2012), p. 090207.
5. D. Bimberg, D. Arsenijevic, G. Larisch, H. Li, J. A. Lott, P. Moser, H. Schmeckebier, and P. Wolf, Green nanophotonics for future datacom and Ethernet networks, *Proc. SPIE*., 9134 (2014), pp. 913402–913913.
6. T. D. Steiner, *Semiconductor Nanostructures for Optoelectronic Applications, Semiconductor Materials and Devices Library*. Norwood, MA: Artech House (2004).
7. B. Lingnau, Nonlinear and Nonequilibrium Dynamics of Quantum-Dot Optoelectronic Devices, PhD thesis, Technical University of Berlin (2015).
8. B. Lingnau, W. W. Chow, E. Schöll, and K. Lüdge, Feedback and injection locking instabilities in quantum-dot lasers: A microscopically based bifurcation analysis, *New J. Phys*., 15 (2013), p. 093031.
9. T. Akiyama, N. Hatori, Y. Nakata, H. Ebe, and M. Sugawara, Pattern-effect-free amplification and cross-gain modulation achieved by using ultrafast gain nonlinearity in quantum-dot semiconductor optical amplifiers, *Phys. Stat. Sol. B*, 238 (2003), pp. 301–304.
10. T. W. Berg, J. Mørk, and J. M. Hvam, Gain dynamics and saturation in semiconductor quantum dot amplifiers, *New J. Phys*., 6 (2004), p. 178.
11. A. V. Uskov, E. P. O'Reilly, M. Lämmlin, N. N. Ledentsov, and D. Bimberg, On gain saturation in quantum dot semiconductor optical amplifiers, *Opt. Commun*., 248 (2005), p. 211.
12. T. Akiyama, H. Kuwatsuka, N. Hatori, Y. Nakata, H. Ebe, and M. Sugawara, Symmetric highly efficient (~0dB) wavelength conversion based on four-wave mixing in quantum dot optical amplifiers, *IEEE Photon. Technol. Lett*., 14 (2002), pp. 1139–1141.
13. N. Majer, K. Lüdge, and E. Schöll, Maxwell-Bloch approach to four-wave mixing in quantum dot semiconductor optical amplifiers, In *IEEE Proceedings of the 11th International Conference on Numerical Simulation of Optical Devices (NUSOD)*, edited by J. Piprek, pp. 153–154. Rome (2011).
14. O. Qasaimeh, Theory of four-wave mixing wavelength conversion in quantum dot semiconductor optical amplifiers, *IEEE Photon. Technol. Lett*., 16 (2004), pp. 993–995.
15. H. Schmeckebier, C. Meuer, D. Arsenijevic, G. Fiol, C. Schmidt-Langhorst, C. Schubert, G. Eisenstein, and D. Bimberg, Wide-range wavelength conversion of 40-Gb/s NRZ-DPSK signals using a 1.3-μm quantum-dot semiconductor optical amplifier, *IEEE Photon. Technol. Lett*., 24 (2012), pp. 1163–1165.

16. G. Contestabile, A. Maruta, S. Sekiguchi, K. Morito, M. Sugawara, and K. Kitayama, Cross-gain modulation in quantum-dot SOA at 1550 nm, *IEEE J. Quant. Electron*., 46 (2010), pp. 1696–1703.
17. J. Kim, M. Laemmlin, C. Meuer, D. Bimberg, and G. Eisenstein, Theoretical and experimental study of high-speed small-signal cross-gain modulation of quantum-dot semiconductor optical amplifiers, *IEEE J. Quant. Electron*., 45 (2009), pp. 240–248.
18. C. Meuer, H. Schmeckebier, G. Fiol, D. Arsenijevic, J. Kim, G. Eisenstein, and D. Bimberg, Cross-gain modulation and four-wave mixing for wavelength conversion in undoped and p-doped 1.3-μm quantum dot semiconductor optical amplifiers, *IEEE Photon. J.*, 2 (2010), pp. 141–151.
19. P. Borri, W. Langbein, J. M. Hvam, F. Heinrichsdorff, M. H. Mao, and D. Bimberg, Ultrafast gain dynamics in InAs–InGaAs quantum-dot amplifiers, *IEEE Photon. Technol. Lett*., 12 (2000), 594–596.
20. S. Dommers, V. V. Temnov, U. Woggon, J. Gomis, J. Martinez-Pastor, M. Lämmlin, and D. Bimberg, Complete ground state gain recovery after ultrashort double pulses in quantum dot based semiconductor optical amplifier, *Appl. Phys. Lett*., 90 (2007), p. 033508.
21. M. Lämmlin, GaAs-Based Semiconductor Optical Amplifiers with Quantum Dots as an Active Medium, PhD thesis, Technical University of Berlin (2006).
22. N. Majer, S. Dommers-Völkel, J. Gomis-Bresco, U. Woggon, K. Lüdge, and E. Schöll, Impact of carrier-carrier scattering and carrier heating on pulse train dynamics of quantum dot semiconductor optical amplifiers, *Appl. Phys. Lett*., 99 (2011), p. 131102.
23. N. Majer, K. Lüdge, and E. Schöll, Cascading enables ultrafast gain recovery dynamics of quantum dot semiconductor optical amplifiers, *Phys. Rev. B*., 82 (2010), p. 235301.
24. M. van der Poel, E. Gehrig, O. Hess, D. Birkedal, and J. M. Hvam, Ultrafast gain dynamics in quantum-dot amplifiers: Theoretical analysis and experimental investigations, *IEEE J. Quant. Electron*., 41 (2005), pp. 1115–1123.
25. C. Meuer, C. Schmidt-Langhorst, R. Bonk, H. Schmeckebier, D. Arsenijevic, G. Fiol, A. Galperin, J. Leuthold, C. Schubert, and D. Bimberg, 80 Gb/s wavelength conversion using a quantum-dot semiconductor optical amplifier and optical filtering, *Opt. Express*, 19 (2011), pp. 5134–5142.
26. P. Borri, W. Langbein, S. Schneider, U. Woggon, R. L. Sellin, D. Ouyang, and D. Bimberg, Ultralong dephasing time in InGaAs quantum dots, *Phys. Rev. Lett*., 87 (2001), p. 157401.
27. P. Borri, W. Langbein, S. Schneider, U. Woggon, R. L. Sellin, D. Ouyang, and D. Bimberg, Exciton relaxation and dephasing in quantum-dot amplifiers from room to cryogenic temperature, *IEEE J. Sel. Top. Quantum Electron*., 8 (2002), pp. 984–991.
28. T. Koprucki, A. Wilms, A. Knorr, and U. Bandelow, Modeling of quantum dot lasers with microscopic treatment of Coulomb effects, *Opt. Quant. Electron*., 42 (2011), pp. 777–783.
29. P. Borri, W. Langbein, S. Schneider, U. Woggon, R. L. Sellin, D. Ouyang, and D. Bimberg, Rabi oscillations in the excitonic ground-state transition of InGaAs quantum dots, *Phys. Rev. B*, 66 (2002), p. 081306(R).
30. A. Capua, O. Karni, G. Eisenstein, and J. P. Reithmaier, Rabi oscillations in a room-temperature quantum dash semiconductor optical amplifier, *Phys. Rev. B*, 90 (2014), p. 045305.
31. H. Kamada, H. Gotoh, J. Temmyo, H. Ando, and T. Takagahara, Exciton Rabi oscillation in single isolated quantum dots, *Phys. Stat. Sol. A*, 190 (2002), pp. 485–490.
32. M. Kolarczik, N. Owschimikow, J. Korn, B. Lingnau, Y. Kaptan, D. Bimberg, E. Schöll, K. Lüdge, and U. Woggon, Quantum coherence induces pulse shape modification in a semiconductor optical amplifier at room temperature, *Nature Commun*., 4 (2013), p. 2953.
33. T. H. Stievater, X. Li, D. G. Steel, D. Gammon, D. S. Katzer, D. Park, C. Piermarocchi, and L. J. Sham, Rabi oscillations of excitons in single quantum dots, *Phys. Rev. Lett*., 87 (2001), p. 133603.
34. A. Icsevgi and W. E. Lamb, Propagation of light pulses in a laser amplifier, *Phys. Rev*., 185 (1969), pp. 517–545.
35. S. Schneider, P. Borri, W. Langbein, U. Woggon, J. Förstner, A. Knorr, R. L. Sellin, D. Ouyang, and D. Bimberg, Self-induced transparency in InGaAs quantum-dot waveguides, *Appl. Phys. Lett*., 83 (2003), pp. 3668–3670.

36. T. W. Berg and J. Mørk, Quantum dot amplifiers with high output power and low noise, *Appl. Phys. Lett*., 82 (2003), pp. 3083–3085.
37. T. Erneux, E. A. Viktorov, P. Mandel, T. Piwonski, G. Huyet, and J. Houlihan, The fast recovery dynamics of a quantum dot semiconductor optical amplifier, *Appl. Phys. Lett*., 94 (2009), p. 113501.
38. S. B. Kuntze, A. J. Zilkie, L. Pavel, and J. S. Aitchison, Nonlinear state-space model of semiconductor optical amplifiers with gain compression for system design and analysis, *J. Lightwave Technol*., 26 (2008), pp. 2274–2281.
39. M. Radziunas and H. J. Wünsche, Dynamics of multi-section DFB semiconductor laser: Traveling wave and mode approximation models, *Proc. SPIE*, 4646 (2002), p. 27.
40. J. Javaloyes and S. Balle, Multimode dynamics in bidirectional laser cavities by folding space into time delay, *Opt. Express*, 20 (2012), pp. 8496–8502.
41. W. H. Press, B. P. Flannery, S. A. Teukolsky, and W. T. Vettering, *Numerical Recipes*, 3rd ed. Cambridge: Cambridge University Press (2007).
42. M. Radziunas, Numerical bifurcation analysis of the traveling wave model of multisection semiconductor lasers, *Physica D*, 213 (2006), pp. 98–112.
43. M. Rossetti, P. Bardella, and I. Montrosset, Time-domain travelling-wave model for quantum dot passively mode-locked lasers, *IEEE J. Quant. Electron*., 47 (2011), p. 139.
44. M. Rossetti, P. Bardella, and I. Montrosset, Modeling passive mode-locking in quantum dot lasers: A comparison between a finite- difference traveling-wave model and a delayed differential equation approach, *IEEE J. Quant. Electron*., 47 (2011), p. 569.
45. H. Y. Liu, M. Hopkinson, C. N. Harrison, M. J. Steer, R. Frith, I. R. Sellers, D. J. Mowbray, and M. S. Skolnick, Optimizing the growth of 1.3 μm InAs/InGaAs dots-in-a-well structure, *J. Appl. Phys*., 93 (2003).
46. Q. T. Vu, H. Haug, and S. W. Koch, Relaxation and dephasing quantum kinetics for a quantum dot in an optically excited quantum well, *Phys. Rev. B*, 73 (2006), p. 205317.
47. W. Lei, M. Offer, A. Lorke, C. Notthoff, C. Meier, O. Wibbelhoff, and A. D. Wieck, Probing the band structure of InAs/GaAs quantum dots by capacitance-voltage and photoluminescence spectroscopy, *Appl. Phys. Lett*., 92 (2008), p. 193111.
48. M. O. Scully, *Quantum Optics*. Cambridge: Cambridge University Press (1997).
49. W. W. Chow and S. W. Koch, *Semiconductor-Laser Fundamentals*, Berlin: Springer (1999).
50. H. Haug and S. W. Koch, *Quantum Theory of the Optical and Electronic Properties of Semiconductors*, 2nd ed. Singapore: World Scientific (2004).
51. W. C. W. Fang, C. G. Bethea, Y. K. Chen, and S. L. Chuang, Longitudinal spatial in homogeneities in high-power semiconductor lasers, *IEEE J. Sel. Top. Quantum Electron*., 1 (1995), pp. 117–128.
52. J. N. Fehr, M. A. Dupertuis, T. P. Hessler, L. Kappei, D. Marti, F. Salleras, M. S. Nomura, B. Deveaud, J.-Y. Emery, and B. Dagens, Hot phonons and Auger related carrier heating in semiconductor optical amplifiers, *IEEE J. Quant. Electron*., 38 (2002), p. 674.
53. P. Sotirelis and K. Hess, Electron capture in GaAs quantum wells, *Phys. Rev. B*, 49 (1994), pp. 7543–7547.
54. M. Vallone, Quantum well electron scattering rates through longitudinal optic-phonon dynamical screened interaction: An analytic approach, *J. Appl. Phys*., 114 (2013), p. 053704.
55. R. Heitz, H. Born, F. Guffarth, O. Stier, A. Schliwa, A. Hoffmann, and D. Bimberg, Existence of a phonon bottleneck for excitons in quantum dots, *Phys. Rev. B*, 64 (2001), p. 241305(R).
56. K. Schuh, P. Gartner, and F. Jahnke, Combined influence of carrier-phonon and coulomb scattering on the quantum-dot population dynamics, *Phys. Rev. B*, 87 (2013), p. 035301.
57. G. D. Mahan, *Many-Particle Physics*. New York, NY: Plenum (1990).
58. A. Wojs, P. Hawrylak, S. Fafard, and L. Jacak, Electronic structure and magneto-optics of self-assembled quantum dots, *Phys. Rev. B*, 54 (1996), p. 5604.
59. H. Haug and S. W. Koch, Semiconductor laser theory with many-body effects, *Phys. Rev. A*, 39 (1989), p. 1887.

60. H. Haug and S. Schmitt-Rink, Electron theory of the optical properties of laser-excited semiconductors, *Prog. Quant. Electron*., 9 (1984), p. 3.
61. W. W. Chow and S. W. Koch, Theory of semiconductor quantum-dot laser dynamics, *IEEE J. Quant. Electron*., 41 (2005), pp. 495–505.
62. H. Haug and A. P. Jauho, *Quantum Kinetics in Transport and Optics of Semiconductors*. Berlin: Springer (1996).
63. E. Malic, K. J. Ahn, M. J. P. Bormann, P. Hövel, E. Schöll, A. Knorr, M. Kuntz, and D. Bimberg, Theory of relaxation oscillations in semiconductor quantum dot lasers, *Appl. Phys. Lett*., 89 (2006), p. 101107.
64. T. R. Nielsen, P. Gartner, and F. Jahnke, Many-body theory of carrier capture and relaxation in semiconductor quantum-dot lasers, *Phys. Rev. B*, 69 (2004), p. 235314.
65. L. Bányai, Q. T. Vu, B. Mieck, and H. Haug, Ultrafast quantum kinetics of time-dependent RPA-screened Coulomb scattering, *Phys. Rev. Lett*., 81 (1998), pp. 882–885.
66. R. Binder, D. Scott, A. E. Paul, M. Lindberg, K. Henneberger, and S. W. Koch, Carrier-carrier scattering and optical dephasing in highly excited semiconductors, *Phys. Rev. B*, 45 (1992), p. 1107.
67. F. X. Camescasse, A. Alexandrou, D. Hulin, L. Bányai, D. B. Tran Thoai, and H. Haug, Ultrafast electron redistribution through Coulomb scattering in undoped GaAs: Experiment and theory, *Phys. Rev. Lett*., 77 (1996), pp. 5429–5432.
68. M. G. Kane, Nonequilibrium carrier-carrier scattering in two-dimensional carrier systems, *Phys. Rev. B*, 54 (1996), pp. 16345–16348.
69. D. B. Tran Thoai and H. Haug, Coulomb quantum kinetics in pulse-excited semiconductors, *Z. Phys. B*, 91 (1992), pp. 199–207.
70. E. Schöll, *Nonequilibrium Phase Transitions in Semiconductors*. Berlin: Springer (1987).
71. K. Lüdge and E. Schöll, Quantum-dot lasers—Desynchronized nonlinear dynamics of electrons and holes, *IEEE J. Quant. Electron*., 45 (2009), pp. 1396–1403.
72. K. Lüdge, Modeling quantum dot based laser devices. In *Nonlinear Laser Dynamics–From Quantum Dots to Cryptography*, Chapter 1, pp. 3–34. Weinheim: Wiley-VCH (2012).
73. M. Rossetti, A. Fiore, G. Sek, C. Zinoni, and L. Li, Modeling the temperature characteristics of InAs/GaAs quantum dot lasers, *J. Appl. Phys*., 106 (2009), p. 023105.
74. J. Urayama, T. B. Norris, H. Jiang, J. Singh, and P. Bhattacharya, Temperature-dependent carrier dynamics in self-assembled InGaAs quantum dots, *Appl. Phys. Lett*., 80 (2002), pp. 2162–2164.
75. T. Erneux, E. A. Viktorov, and P. Mandel, Time scales and relaxation dynamics in quantum-dot lasers, *Phys. Rev. A*, 76 (2007), p. 023819.
76. P. Baveja, D. Maywar, A. Kaplan, and G. P. Agrawal, Self-phase modulation in semiconductor optical amplifiers: Impact of amplified spontaneous emission, *IEEE J. Quant. Electron*., 46 (2010), pp. 1396–1403.
77. T. W. Berg and J. Mørk, Saturation and noise properties of quantum-dot optical amplifiers, *IEEE J. Quant. Electron*., 40 (2004), pp. 1527–1539.
78. A. M. de Melo and K. Petermann, On the amplified spontaneous emission noise modeling of semiconductor optical amplifiers, *Opt. Commun*., 281 (2008), pp. 4598–4605.
79. C. Meuer, J. Kim, M. Lämmlin, S. Liebich, A. Capua, G. Eisenstein, A. R. Kovsh, S. S. Mikhrin, I. L. Krestnikov, and D. Bimberg, Static gain saturation in quantum dot semiconductor optical amplifiers, *Opt. Express*, 16 (2008), p. 8269.
80. C. W. Gardiner, *Handbook of Stochastic Methods*. New York, NY: Springer (1985).
81. N. Wiener, Generalized harmonic analysis, *Acta Math.*, 55 (1930), pp. 117–258.
82. R. Bonk, T. Vallaitis, J. Guetlein, C. Meuer, H. Schmeckebier, D. Bimberg, C. Koos, and J. Leuthold, The input power dynamic range of a semiconductor optical amplifier and its relevance for access network applications, *IEEE Photon. J*., 3 (2011), pp. 1039–1053.

83. S. Wilkinson, B. Lingnau, J. Korn, E. Schöll, and K. Lüdge, Influence of noise on the signal properties of quantum-dot semiconductor optical amplifiers, *IEEE J. Sel. Top. Quantum Electron*., 19 (2013), p. 1900106.
84. G. E. P. Box and M. E. Muller, A note on the generation of random normal deviates, *Ann. Math. Statist*., 29 (1958), pp. 610–611.
85. H. Shahid, D. Childs, B. J. Stevens, and R. A. Hogg, Negative differential gain due to many body effects in self-assembled quantum dot lasers, *Appl. Phys. Lett*., 99 (2011), p. 061104.
86. E. Goldmann, M. Lorke, T. Frauenheim, and F. Jahnke, Negative differential gain in quantum dot systems: Interplay of structural properties and many-body effects, *Appl. Phys. Lett*., 104 (2014), p. 242108.
87. S. W. Koch, T. Meier, F. Jahnke, and P. Thomas, Microscopic theory of optical dephasing in semiconductors, *Appl. Phys. A*, 71 (2000), pp. 511–517.
88. M. Lorke, T. R. Nielsen, J. Seebeck, P. Gartner, and F. Jahnke, Influence of carrier-carrier and carrier-phonon correlations on optical absorption and gain in quantum-dot systems, *Phys. Rev. B*, 73 (2006), p. 085324.
89. H. H. Nilsson, J. Z. Zhang, and I. Galbraith, Homogeneous broadening in quantum dots due to Auger scattering with wetting layer carriers, *Phys. Rev. B*, 72 (2005), p. 205331.
90. H. Tahara, Y. Ogawa, F. Minami, K. Akahane, and M. Sasaki, Long-time correlation in non-Markovian dephasing of an exciton-phonon system in InAs quantum dots, *Phys. Rev. Lett*., 112 (2014), p. 147404.
91. H. Schmeckebier, B. Lingnau, S. König, K. Lüdge, C. Meuer, A. Zeghuzi, D. Arsenijevic, M. Stubenrauch, R. Bonk, C. Koos, C. Schubert, T. Pfeiffer, and D. Bimberg, Ultra-broadband bidirectional dual-band quantum-dot semiconductor optical amplifier. In *Optical Fiber Communication Conference and Exposition* (2015), p. Tu3I.7.
92. A. Girndt, A. Knorr, M. Hofmann, and S. W. Koch, Theoretical analysis of ultrafast pump-probe experiments in semiconductor amplifiers, *Appl. Phys. Lett*., 66 (1995), p. 550.
93. E. P. Ippen and C. V. Shank, Techniques for measurement, edited by S. L. Shapiro, In *Ultrashort Light Pulses: Picosecond Techniques and Applications*, pp. 83–122. Berlin: Springer (1977).
94. J. M. A. Mecozzi and J. Mørk, Theory of heterodyne pump-probe experiments with femtosecond pulses, *J. Opt. Soc. Am. B*, 13 (1996), pp. 2437–2452.
95. P. Borri, S. Schneider, W. Langbein, and D. Bimberg, Ultrafast carrier dynamics in InGaAs quantum dot materials and devices, *J. Opt. A: Pure Appl. Opt*., 8 (2006), p. S33.
96. T. Brandes, Coherent and collective quantum optical effects in mesoscopic systems, *Phys. Rep*., 408 (2005), pp. 315–474.
97. H. Choi, V. M. Gkortsas, L. Diehl, D. Bour, S. Corzine, J. Zhu, G. Höfler, F. Capasso, F. X. Kärtner, and T. B. Norris, Ultrafast Rabi flopping and coherent pulse propagation in a quantum cascade laser, *Nature Photon*., 4 (2010), pp. 706–710.

24

Wave Mixing Effects in Semiconductor Optical Amplifiers

Simeon N. Kaunga-Nyirenda
Michal Dlubek
Jun Jun Lim
Steve Bull
Andrew Phillips
Slawomir Sujecki
and
Eric Larkins

24.1 Introduction

The growing demand for telecommunications services continues to push optical transmission rates beyond 10 G-symbols/s and to use more efficient modulation formats (e.g., quadrature phase shift keying [QPSK], differential QPSK [DQPSK]) to cope with the ever-increasing demand for bandwidth. The growing demand for bandwidth is also driving a move to perform high bandwidth signal processing functions directly in the optical domain. All-optical signal processing generally requires nonlinear optical functionality. Semiconductor optical amplifiers (SOAs) are attractive for such functions because of their strong nonlinear optical response. Optical signal processing applications that employ SOAs include wavelength conversion, phase conjugation, optical switching, Boolean logic functions, all-optical recovery, and all-optical demultiplexing. SOAs offer large bandwidth, ease of integration, compactness, low power consumption, electrical pumping/control, and potentially low cost. Interest in SOAs continues to grow as photonic integrated circuit (PIC) integration densities continue to increase, with applications in signal leveling and signal regeneration or integration with electronics as optical interconnects for high-speed cross-chip communications. SOAs are also useful in electrically reconfigurable optical switching/routing networks (Williams et al., 2008). For these applications, however, SOAs may introduce nonlinear signal impairments that adversely affect system performance, and these impairments must be managed.

This chapter focuses on the numerical modeling and simulation of carrier plasma–induced nonlinear optical phenomena in SOAs. The chapter starts with a brief description of nonlinear processes in SOAs and their applications. We then discuss SOA modeling, paying particular attention to challenges encountered in the modeling and simulation of nonlinear effects. An efficient optical model based on a one-dimensional (1D) bidirectional traveling wave algorithm is then presented. The optical model is coupled to the semiconductor material through light–matter interactions. The electrical properties are simulated using a simplified 1D (unipolar) electrical model, which only takes into account the dynamics of the total carrier density in the active medium. The unipolar model assumes flat quasi-Fermi levels and charge neutrality in order to remove the additional computational complexity associated with the use of a self-consistent bipolar electrical model with band bending (due to charge imbalance in the well). Nevertheless, while a bipolar model will certainly improve the overall accuracy of the model, the focus of this work was the development and demonstration of an efficient model for the nonlinear optical response. For this purpose, the simplicity of the unipolar model is an advantage.

The material polarization is represented by an effective susceptibility that self-consistently includes the carrier-induced perturbations of the net optical gain and refractive index spectra, both of which are functions of the optical field. No particular functional dependence on the optical field is assumed. This allows a general representation of the light–matter interaction under quasi-equilibrium conditions, which is applicable for all optical intensity levels. The most widely used power series expansion of the polarization is usually implemented with a single nonlinear term, which is only applicable when the optical intensity is sufficiently weak. The gain and spontaneous emission spectra are calculated using the band structure details of the semiconductor. These spectra were appropriately broadened to account for the spectral broadening of the carrier energies in the bands due to carrier lifetime dependent dephasing and various scattering events. The refractive index spectrum is obtained from the broadened gain spectrum using a nonlinear Kramers–Kronig transformation.

The need to perform simulations in the time domain poses a particular challenge for the inclusion of the frequency-dependent complex material polarization (i.e., gain and refractive index dispersion) and spontaneous emission spectra. We use recursive digital filter functions to accurately represent the spectrally dependent material quantities in the time-domain simulation. This method captures the asymmetric nature of the spectral material response and can also be used to incorporate frequency responses obtained from experimental measurements as well as complicated responses that cannot easily be represented analytically. The use of spatiotemporal filter coefficients ensures that physical effects such as spatial-hole burning and spectral changes in the gain caused by band-filling and bandgap renormalization effects are correctly included. A further advantage of the recursive filter method is that the filter coefficients can be obtained offline from the main simulation engine and tabulated, improving the computational efficiency and minimizing the resources required by the simulations. The refractive index spectra are also represented more accurately than approaches using a constant linewidth enhancement factor (at best a small-signal representation of the Kramers–Kronig relation, which ignores the spectral dependence of the index changes).

The chapter concludes with a case study exploring carrier density modulation (CDM) caused by optical wave beating in SOAs. We use the time-domain model developed to obtain an understanding of wave mixing processes in SOAs and the dependence of CDM on different operating parameters. The simulation results are compared with experimental results from a commercial buried heterostructure (BH) 1550 nm InGaAs multiple quantum well (MQW)-SOA made by the Centre for Integrated Photonics (SOA-NL-OEC-1550).

24.2 Review of Nonlinear Phenomena in SOAs and Applications

Nonlinear optical processes occur when the complex dielectric response of the material depends on the strength of the optical field passing through the medium (Boyd, 2007). When an optical wave interacts

with the semiconductor gain medium, there is a shift in the carriers of the gain medium, resulting in a field-induced dipole moment that becomes the source of an electromagnetic field at the microscopic level. This interaction between the optical field and the material is through the induced macroscopic material polarization (the polarization term in the wave equation; see Section 24.4.1). This macroscopic polarization is the sum of the distinct microscopic polarizations

$$P(\vec{r}, t) = \frac{2}{V_k} \sum_k d_{cv}(k) p(k, \vec{r}, t), \tag{24.1}$$

where V_k is the normalized volume, $d_{cv}(k)$ is the optical dipole matrix element, and p is the interband polarization. k, $\vec{r}$, and t are the electron wave vector, position vector, and time, respectively. The random high-speed temporal fluctuations of the microscopic dipole elements are eliminated by spatial averaging over the incoherent dipole ensemble. Only coherent (i.e., externally driven) fluctuations remain and their response can be described with a macroscopic polarization (Jackson, 1975). This induced macroscopic polarization, $\tilde{P}^{\pm}$, is a frequency-dependent quantity that is a function of the total optical field, $\tilde{E}$, interacting with the medium via the time-varying carrier distributions. In the frequency domain, the polarization is related to the total electric field by

$$\tilde{P}^{\pm}(\omega, N, \tilde{E}) = \varepsilon_0 \chi_{\text{eff}}(\omega, N, \tilde{E}) \tilde{E}^{\pm}, \tag{24.2}$$

where $\tilde{P}(\omega)$ and $\tilde{E}(\omega)$ are the Fourier transforms of $P(t)$ and $E(t)$, respectively, and ω is the angular frequency. N is the total carrier density in the active region. The effective susceptibility, χ_{eff} takes into account all processes, both linear and nonlinear. No particular functional dependence on the optical field is assumed in Equation 24.2. When the optical field is small, the polarization can be expanded into a power series of the optical field and the effective susceptibility is

$$\chi_{\text{eff}} = \sum_n \chi^{(n+1)} \tilde{E}^n \; : \; n = 0, 1, 2 \ldots \tag{24.3}$$

At low optical intensities, the optical properties of the material tend to behave in a linear manner. However, as the optical intensity increases, the strong nonlinear response, which results from the interaction between strong optical signals and the gain medium, can manifest itself as self- and cross-gain modulation (SGM/XGM), self-, and cross-phase modulation (SPM/XPM), and wave mixing. SOAs are optoelectronic devices whose behavior is governed by the material properties of the amplifying medium and the light propagation through it. These are strongly coupled and influenced by the operating conditions, e.g., input power levels, pumping current and form of the input. The nonlinear processes arise because of the dynamics of the excited carrier populations (and their distributions in real and momentum space) as the material interacts with the optical radiation. These nonlinear phenomena are detrimental to applications that rely on device linearity but can be exploited for optical signal processing and other applications requiring all-optical functionality.

CDM, carrier heating (CH), and spectral hole burning (SHB) are the most important processes giving rise to nonlinear optical phenomena in semiconductor devices.

24.2.1 Carrier Density Modulation

CDM is a coherent interband process that results from the dependence of the stimulated carrier recombination rate on the optical intensity. Stimulated emission and absorption processes, and to some extent the (amplified) spontaneous emission process, modify the total carrier densities in the gain medium, leading to changes in the total gain spectrum and the refractive index of the semiconductor material. A strong optical input signal will increase the stimulated emission rate and decrease the carrier density in the active

material. This reduces the gain and perturbs the refractive index, which affect the propagation of both the perturbing signal and other co-/counterpropagating signals. This is the basis for effects such as SGM, XGM, SPM and XGM. When at least two waves distinguishable in frequency, polarization, or wave vector propagate through the SOA, wave beating can excite the material by modulating the carrier density. This modulation in turn creates dynamic gain and index gratings, which are responsible for creating new frequency components.

24.2.2 Carrier Heating

Carrier heating (CH) results from modulation of the carrier energy distributions in the valence and/or conduction bands (sub-bands for quantum wells [QWs] and wires). CH is caused by processes that increase the temperatures of the carrier distributions relative to the lattice temperature, including carrier injection, stimulated emission, and free carrier absorption (FCA). Carrier injection adds high energy ("hot") carriers to the carrier plasma, while stimulated emission removes "cold" carriers close to the band edge. FCA transfers energy from photons to carriers, moving them to higher energies within the bands. Such carriers quickly thermalize and transfer energy to other carriers by carrier–carrier scattering, thereby increasing the plasma energy density or temperature (Uskov et al., 1994).

24.2.3 Spectral Hole Burning

SHB is also a form of modulation of the energy distributions of the carriers within the valence and/or conduction bands (or sub-bands for QWs and wires). While CH perturbs the entire carrier plasma, the plasma can usually still be described with a quasi-equilibrium distribution with an increased plasma temperature. SHB, on the other hand, is an energetically localized perturbation of the plasma, which cannot be described with a quasi-equilibrium distribution. SHB occurs when carriers in the states supporting stimulated recombination are consumed faster than they are replenished by intraband scattering. This creates a spectral hole in the intraband carrier distribution relative to the corresponding thermal carrier distribution.

In contrast to CDM, CH, and SHB are intraband processes. SHB is due to changes in the carrier distribution away from Fermi–Dirac distributions and is responsible for gain saturation. (The gain compression coefficient, frequently used to describe gain saturation at high power, is a manifestation of SHB.) CH results in a Fermi–Dirac distribution that has a higher temperature than that of the lattice. CDM, CH, and SBH all create perturbations that result in the modulation of the gain/absorption and refractive index spectra, whose dynamics also create spatiotemporal index and gain gratings that can diffract waves propagating in the medium to generate new frequency components. Although the gain and index gratings caused by CDM are larger, CH and SHB contribute to the nonlinear optical response. CDM dominates up to frequencies limited by the carrier replenishment rate. CH and SHB are important at higher frequencies, but CDM remains important.

24.2.4 Other Nonlinear Effects

Other processes, e.g., optical Kerr effect, two-photon absorption (TPA), and second harmonic generation (SHG), also contribute to the nonlinear optical response, but their contribution is smaller compared to that of CDM and CH, and are neglected in this work. The inclusion of the Kerr effect in simulations is complicated by the lack of causality. TPA is a multiphoton process that is resonantly enhanced for photon energies of the order of half the bandgap of the semiconductor material. Instantaneous coherent processes like the optical Kerr effect, TPA and SHG are not discussed further here, but are important for some applications (e.g., all-optical gates) at high optical power densities. The reader is referred to Boyd (2007) or other texts on nonlinear optics for more information.

24.2.5 Summary of Important Nonlinear Applications

Optical nonlinearities cause signal impairments in linear applications, but have been exploited to great benefit in the field of functional photonics. SOA nonlinearities are used for all-optical signal processing to eliminate the need for optical–electrical–optical (OEO) conversion in communication networks. Processing tasks such as demultiplexing, clock recovery, regeneration, and routing can be undertaken entirely in the optical domain at higher speeds than are possible with electronics (Manning et al., 1997). One of the key applications of nonlinear processes in SOAs is wavelength conversion.

Wavelength converters increase the flexibility and performance of all-optical networks based on wavelength division multiplexing (WDM) (Kovačević and Acampora, 1995). All-optical wavelength converters are essential for coping with increasing data rates. They increase the network performance by reducing the effects of lightpath blocking due to the wavelength continuity constraints in optical packet and optical circuit switching networks. Of the different approaches to all-optical wavelength conversion, SOA-based wavelength converters have attracted the greatest interest because of their compactness, easy integration, and strong nonlinear response. Different approaches have been used for SOA-based wavelength conversion, including XGM, XPM, and four-wave mixing (FWM). FWM is the most flexible approach because it has a large extinction ratio and retains the phase information of the carrier signal, making it bitrate independent and intrinsically transparent to modulation format (a useful attribute in optical networks). FWM-based SOA wavelength converters also have the potential for processing ultrahigh speed analog and digital signals using ultrafast processes like SHB and CH. Spectral inversion also occurs during the FWM-conversion process. FWM-converted signals with inverted spectral distribution have been used for dispersion compensation by positioning a nonlinear SOA at the center of the link (Yanhua et al., 2003).

Another important application of nonlinear processes in SOA is optical performance monitoring in optical networks. The increasing complexity of optical networks and the emergence of new types of traffic and data protocols have rendered digital signal monitoring in the electronic domain impractical (Dlubek, 2008). As a result, optical signal monitoring methods that measure the analogue parameters in the optical domain are required for transparent optical networks. Optical sampling using FWM in SOAs has been used to generate signal histograms for bit error rate (BER) estimation (Dlubek, 2008).

24.3 Challenges in Modeling Nonlinear Effects

SOA modeling is a sophisticated subject due to the number and complexity of processes that take place simultaneously in the device. The dynamic nature of optical nonlinearities requires the use of time-domain models. Time-domain simulations are needed to determine the carrier densities (i.e., drift-diffusion, generation/recombination effects, etc.), whereas the calculation of the complex index needs to be done in the frequency domain. Optical propagation can be done in the frequency domain, but spatiotemporal carrier density (and complex index) variations make time-domain models more tractable.

The challenge for time-domain simulations is the inclusion of the frequency-dependent complex material polarization (gain and refractive index dispersion). Several attempts have been made to include dispersion in time-domain simulations: single-pole Lorentzian filter (Pratt and Carroll, 2000), finite impulse filter (FIR) theory (Jones et al., 1995; Toptchiyski et al., 1999), a first-order (Durhuus et al., 1992) and a second-order (Das et al., 2000) Taylor series expansion about the gain peak wavelength with constant coefficients. The second-order Taylor series expansion and the Lorentzian profile are both inadequate for the asymmetric material gain spectrum. Furthermore, the use of constant filter coefficients is inadequate for representing carrier-induced shifts in the gain spectrum. Other approaches include the spectrum slicing technique (SSM) (Park et al., 2005) and effective Bloch equations (EBE). The SSM method can handle the asymmetric gain spectrum, but is not suited to modeling nonlinear interactions (Park et al., 2005). The EBE fits the gain and refractive index spectra using a series of Lorentzians. A single Lorentzian

is used in Ning et al. (1997), which is only useful for signals with a very narrow spectrum. Accurate implementation for high bandwidth signals requires the inclusion of more Lorentzian terms, making the model computationally intensive.

24.4 Improved Modeling of Nonlinear Phenomena in SOAs

The theoretical model described here is applied to an MQW SOA fabricated with a BH (Figure 24.1). The operation of the SOA depends on the interaction of the optical waves with the material. Processes such as optical gain, optical absorption, and changes in the refractive index must be appropriately coupled to the optical model in order to develop numerical models that accurately represent the operation of the actual device. This section describes the different components of a coupled optoelectronic simulation tool for nonlinear SOAs.

24.4.1 Optical Model

The optical field propagation in the SOA active region is described by Maxwell's equations

$$\nabla \times \nabla \times \vec{\mathbf{E}} + \frac{n^2}{c^2}\frac{\partial^2 \vec{\mathbf{E}}}{\partial t^2} = -\frac{1}{\varepsilon_0 c^2}\left(\frac{\partial^2 \vec{\mathbf{P}}}{\partial t^2} + \frac{\partial \vec{\mathbf{j}}}{\partial t}\right), \tag{24.4}$$

where n is the refractive index of the unexcited material (background index), c is the speed of light in vacuum, ε_0 is the free-space permittivity, $\vec{\mathbf{P}}(x, y, z, t)$ is the macroscopic polarization of the medium, and $\vec{\mathbf{j}}(x, y, z, t)$ is the current density. It is assumed that the SOA is designed to support only the fundamental mode with a transverse field distribution $U(x, y)$, which is assumed to be wavelength independent and normalized such that $\int\int |U(x, y)|^2 \, dxdy = 1$. For simplicity, all effective and modal parameters (e.g., the transverse confinement factor) are assumed to have been obtained at this point, so that only the longitudinal spatial direction needs to be considered. The strong waveguiding of the BHs further confines the optical field in the transverse directions beyond the vertical confinement of the separate confinement heterostructure (SCH) (Agrawal and Dutta, 1986).

The variation of the injection current with respect to time is very small compared to that of the optical fields, so it is justifiable to assume

$$\frac{\partial j}{\partial t} = \frac{\partial (\sigma E)}{\partial t} \approx 0. \tag{24.5}$$

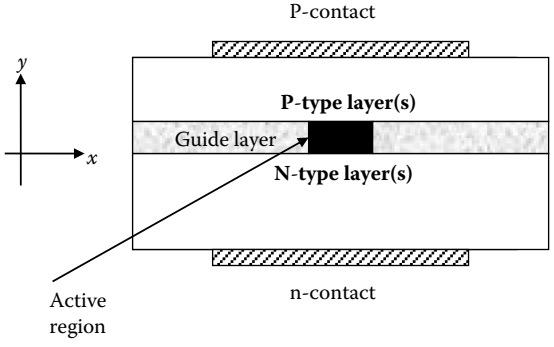

FIGURE 24.1 Schematic of a buried heterostructure (BH) semiconductor optical amplifier (SOA).

An alternative way of looking at this assumption is that optical fields are not usually generated directly by free currents and charges (Liu, 2005). Under these assumptions, the wave equations take the same form as those in a medium free of sources. The assumption in Equation 24.5 is plausible at optical frequencies, but this term may contribute in nonlinear optical beat-frequency devices, e.g., microwave and terahertz (THz) devices. This assumption is also not *a priori* valid for plasmonic devices (i.e., metals). For a straight and symmetric waveguide, the fields can be assumed to remain linearly polarized during propagation through the device. For a single polarization component, this implies that $\nabla \cdot \vec{\mathbf{E}} = \nabla \cdot \vec{\mathbf{P}} = 0$ and the left-hand side of Equation 24.1 is $\nabla \times \nabla \times \vec{\mathbf{E}} = \nabla\left(\nabla \cdot \vec{\mathbf{E}}\right) - \nabla^2\vec{\mathbf{E}} = -\nabla^2\vec{\mathbf{E}}$, so the scalar wave equation can be used.

Zero facet reflectivities are the target in traveling-wave SOAs. However, facets with antireflection (AR) coatings still exhibit residual reflectivities, which can result in the formation of an optical cavity with longitudinal resonances. Only real amplitude reflection coefficients are considered in this work. Although any wave reflected at the facet may initially be small, it will be amplified as it back-propagates along the waveguide such that it is not negligible compared to the forward field. Thus, reflected fields contribute to carrier depletion, gain compression, and refractive index change in the active medium. This affects the amplification, pulse shape, and phase of the output field. Reflected fields can also give rise to delayed replicas or echoes of the bits, which act as noise. Fields generated by ASE may also be nonnegligible compared to forward travelling fields. In the general case, the total optical field is comprised of both backward and forward propagating fields. Counterpropagating fields are also used deliberately in some applications relying on XGM and/or XPM.

Dropping the vector nature and using the slowly varying envelope approximation, the total optical field in the active region can be written as

$$E(x,y,z,t) = \frac{1}{2}U(x,y)\left\{\psi^{+}(z,t)\exp\left[i\left(\omega t - kz\right)\right] + \psi^{-}(z,t)\exp\left[i\left(\omega t + kz\right)\right] + c.c.\right\}. \tag{24.6}$$

Taking into account that multiple signals may be input into the SOA, this can be rewritten as

$$E(x,y,z,t) = U(x,y)\sum_{q}\left\{\psi_q^{+}(z,t)\exp\left[i\left(\omega_q t - k_q z\right)\right] + \psi_q^{-}(z,t)\exp\left[i\left(\omega_q t + k_q z\right)\right] + c.c.\right\}, \tag{24.7}$$

where $\lambda_q = \frac{c}{f_q}$ is the center wavelength of the qth signal and $\omega_q = 2\pi f_q$. From Equations 24.6 and 24.7, the total forward and backward slowly varying components are

$$\psi^{+}(z,t) = \sum_{q}\psi_q^{+}(z,t)\exp\left\{i\left[\left(\omega_q - \omega_{\text{ref}}\right)t - \left(k_q - k_{\text{ref}}\right)z\right]\right\} + c.c. \tag{24.8}$$

$$\psi^{-}(z,t) = \sum_{q}\psi_q^{-}(z,t)\exp\left\{i\left[\left(\omega_q - \omega_{\text{ref}}\right)t + \left(k_q - k_{\text{ref}}\right)z\right]\right\} + c.c., \tag{24.9}$$

where $k_{\text{ref}} = \frac{n\omega_{\text{ref}}}{c}$ is the optical propagation constant in the longitudinal direction and ω_{ref} is a reference frequency for the baseband transformation of all the signals propagating through the active medium. $\psi^{+}(z,t)$ and $\psi^{-}(z,t)$ are the forward and backward propagating complex envelopes of the optical field. The induced polarization can be written in a similar form as the field

$$\mathrm{P}(x,y,z,t) = \frac{1}{2}U(x,y)\left\{P^{+}(z,t)\exp\left[i\left(\omega t - kz\right)\right] + P^{-}(z,t)\exp\left[i\left(\omega t + kz\right)\right] + c.c\right\}, \tag{24.10}$$

where $P^{+}(z,t)$ and $P^{-}(z,t)$ are the slowly varying forward and backward propagating complex polarizations. Substitution of Equations 24.7 and 24.10 into the scalar version of the wave Equation 24.4 and

applying the slowly varying envelope approximation (SVEA) and paraxial approximation leads to the following propagation equations

$$\frac{n}{c}\frac{\partial \psi^{\pm}}{\partial t} \pm \frac{\partial \psi^{\pm}}{\partial z} = i\frac{\Gamma_{xy} k_{\text{ref}}}{2\varepsilon_0 n^2} P^{\pm} + \psi^{\pm}_{\text{sp}}(z,t), \tag{24.11}$$

which are subject to the boundary conditions

$$\psi^{+}(0,t) = \sqrt{R_1}\psi^{-}(0,t) + \sqrt{1-R_1}\psi_{\text{in1}}(0,t) \tag{24.12}$$

$$\psi^{-}(L,t) = \sqrt{R_2}\psi^{+}(L,t) + \sqrt{1-R_2}\psi_{\text{in2}}(L,t), \tag{24.13}$$

where $\psi_{\text{in1}}(0,t)$ and $\psi_{\text{in2}}(L,t)$ are optical inputs injected through the end facets. These facets have power reflectivities R_1 and R_{21}, respectively. The last term in Equation 24.11 is the local spontaneous noise contribution to the total propagating field. For simplicity, k_{ref} is referred to as k from here onward.

The transverse confinement factor, Γ_{xy}, in 24.11 is given by

$$\Gamma_{xy} = \frac{\int_{-w/2}^{w/2}\int_{-d/2}^{d/2} \left|U(x,y)\right|^2 \mathrm{d}y\mathrm{d}x}{\int_{-\infty}^{\infty}\int_{-\infty}^{\infty} \left|U(x,y)\right|^2 \mathrm{d}y\mathrm{d}x}, \tag{24.14}$$

where w and d are the active region width and thickness, respectively.

24.4.2 Electrical Model

The carrier dynamics are calculated using a simplified 1D carrier density model based on the evolution of the total carrier density in the active region (White et al., 1998)

$$\frac{\partial N(z,t)}{\partial t} = \frac{\eta J(z,t)}{ed} - \gamma_{\text{nr}}(N)N - \frac{i\Gamma_{xy}}{4\hbar}\left\{ \left(\psi^{+}\right)\left(P^{+}\right)^{*} + \left(\psi^{-}\right)\left(P^{-}\right)^{*} - c.c. \right\}, \tag{24.15}$$

where J is the total injected current density, e is the electron charge, γ_{nr} represents nonradiative recombination (generally carrier dependent), and η is the current injection efficiency. Carrier diffusion effects have been neglected in Equation 24.15 since the longitudinal electrical mesh spacing is larger than the carrier diffusion length. Thus, the total current density is only due to the external source from the electrodes. The current density from the external source is determined as in Dai et al. (1997)

$$J_{ext}(z,t) = \frac{V_{bias} - V_{jcn}(z,t)}{r_{\text{s}}}, \tag{24.16}$$

where r_{s} is the series resistance (in units of Ωm^{-2}) of the p- and n-layers on either side of the active region and the p- and n-contact resistance. V_{jcn} is the voltage drop across the active layer (p–n junction) and relates to the difference between the two quasi-Fermi levels as

$$V_{jcn}(z,t) = \frac{E_{\text{F}n}(z,t) - E_{\text{F}p}(z,t)}{e}, \tag{24.17}$$

where $E_{\text{F}n}$ and $E_{\text{F}p}$ are the electron and hole quasi-Fermi levels, respectively. The quasi-Fermi levels are calculated within the gain model under the commonly used assumption of charge neutrality. While charge neutrality is a valid assumption in bulk material, it may not be a valid assumption for QWs, especially at

high current pumping levels. A significant charge imbalance in the QW may strongly affect the optical properties of the surrounding optical guiding layers (SCH layers) and the entire waveguide due to the carriers injected into the region (Tolstikhin, 2000). Nevertheless, charge neutrality is assumed in order to use the unipolar model to simplify the analysis, which should be acceptable for moderate injection currents. $E_{\mathrm{F}n}$ and $E_{\mathrm{F}p}$ are estimated using the Joyce–Dixon approximation (Joyce and Dixon, 1977)

$$E_{\mathrm{F}n,p} = k_{\mathrm{B}}T\left[\ln\left(\frac{N}{N_{c,v}}\right) + \frac{1}{2}\left(\frac{N}{N_{c,v}}\right) + \frac{1}{24}\left(\frac{N}{N_{c,v}}\right)^2 - 0.0000347\left(\frac{N}{N_{c,v}}\right)^3\right], \tag{24.18}$$

where N_c and N_v are the effective densities of states for electrons and holes, k_{B} is the Boltzmann constant, and T is the temperature. The nonradiative processes considered in Equation 24.15 are Shockley–Read–Hall (SRH) and Auger recombination. The recombination rates are calculated under the charge neutrality condition.

24.4.3 Light–Matter Interactions

The interaction between light and the semiconductor gain medium is represented by the material (interband) polarization through an effective susceptibility (Equation 24.2). A general description of the polarization that is applicable for all levels of optical intensity is necessary. The effective susceptibility consists of the carrier-dependent changes in net gain and refractive index, both of which are functions of the optical field

$$\chi_{\mathrm{eff}}\left(\omega, N, \tilde{E}\right) = -\frac{1}{k}\left\{i\left[g_{net}\left(\omega, N, \tilde{E}\right) - \left(\frac{1-\Gamma_{xy}}{\Gamma_{xy}}\right)\alpha_{conf}\right] + k\Delta n\left(\omega, N, \tilde{E}\right)\right\}, \tag{24.19}$$

where α_{conf} represents the optical losses in the confinement regions. α_{conf} is needed because $1-\Gamma_{xy}$ of the optical energy is located in the confinement layers outside the gain material. Equation 24.19 allows the induced nonlinear polarization to be described in a general fashion, without any assumptions based on its functional dependence on the optical field. This approach is more straightforward and physically robust than the common truncated series expansion of the polarization based on Equation 24.3. With this representation, the band structure is taken account of through the determination of the gain and refractive index changes.

To complete the analysis, a model is required for the material gain, spontaneous emission, and refractive index spectra. A parabolic model is used for the conduction band, while the valence band structure is calculated using a four-band **k·p**-model (Vurgaftman et al., 2001). The gain and spontaneous emission rates are obtained using Equations 24.20 and 24.21, respectively (Zory, 1993),

$$g(\hbar\omega) = \frac{1}{\hbar\omega}\frac{\bar{n}_{\mathrm{g}}\pi e^2\hbar}{n^2 c\varepsilon_0 m_0^2}\sum_{ic=iv}\left|M_{\mathrm{T}}\right|^2\rho_{\mathrm{red}}^{mD}\left(f_n - f_p\right) \tag{24.20}$$

$$R_{\mathrm{sp}}(\hbar\omega) = \frac{1}{\hbar\omega}\frac{\pi e^2\hbar}{n^2\varepsilon_0 m_0^2}\sum_{ic=iv}\left|M_{\mathrm{avg}}\right|^2\rho_{\mathrm{red}}^{mD}f_n\left(1-f_p\right) \tag{24.21}$$

$$\left|M_{\mathrm{avg}}\right|^2 = \frac{1}{3}\sum_{\substack{\text{all 3}\\ \text{polarizations}}}\left|M_{\mathrm{T}}\right|^2. \tag{24.22}$$

$f_{n,p}(E)$ is a Fermi–Dirac distribution function and gives the occupational probability of the electron of energy state E. ρ_{red}^{mD} is the reduced density of states, with $m = 2$ for QW material, and $m = 3$ for bulk.

$|M_T|^2$ is the transition matrix element and determines the probability and hence strength of interaction between the states at energy E_e and E_h in the presence of an electromagnetic field.

Carrier lifetime dependent dephasing and intraband scattering processes (carrier–carrier, carrier–phonon, etc.) broaden the range of energy states that may participate in the optical transitions. This energy broadening is taken into account phenomenologically by directly broadening the optical spectra (Zory, 1993). Instead of broadening the gain spectrum directly, the spontaneous emission spectrum was broadened using a hyperbolic secant lineshape function (Lim et al., 2007)

$$L\left(E_{eh} - \hbar\omega\right) = \frac{\tau_{in}}{\hbar\pi} \sec h\left(\frac{E_{eh} - \hbar\omega}{\hbar/\tau_{in}}\right), \tag{24.23}$$

where τ_{in} is the intraband relaxation time mainly due to scattering processes, and E_{eh} is the transition energy. The gain spectrum is obtained from the broadened spontaneous emission spectrum, $R_{sp,broad}(\hbar\omega)$, through

$$g(\hbar\omega) = \frac{1}{(\hbar\omega)^2} \frac{3\pi^2\hbar^3c^2}{2\bar{n}^2} R_{sp,broad}(\hbar\omega) \left[1 - \exp\left(\frac{\hbar\omega - \Delta E_F}{k_B T}\right)\right]. \tag{24.24}$$

The form of Equation 24.24 ensures that the gain passes through zero exactly at the quasi-Fermi level separation ΔE_F.

Gain compression due to SHB is included phenomenologically by introducing a constant gain compression factor, ε_{shb}

$$g(\hbar\omega) = \frac{g(N,T)}{1 + \varepsilon_{shb} S(\hbar\omega)}, \tag{24.25}$$

where $S(\hbar\omega)$ is the density of photons with energy $\hbar\omega$.

The carrier-induced changes in the refractive index spectrum are calculated from the changes in the gain/absorption spectrum through the nonlinear Kramers–Kronig relations (Hutchings et al., 1992) to ensure that the absorption and index changes are self-consistent. This is expressed as

$$\Delta n(\hbar\omega;\xi) = -\frac{c}{2\pi\omega} \int_{-\infty}^{\infty} \frac{\Delta g(\hbar\omega\prime;\xi)}{\omega' - \omega} d\omega', \tag{24.26}$$

where ξ is the external excitation, e.g., an electromagnetic field or temperature. This form is appropriate for different nonlinear processes, e.g., self-action effects (nonlinear refraction) and cascaded processes (Boyd, 2007). In this work, the carrier-induced changes in the gain/absorption spectrum only include band-filling effects and bandgap renormalization, but CH and SHB effects can also be included.

24.4.4 Inclusion of Material Dispersion in the Time-Domain Model

The challenge for time-domain simulations is the inclusion of the frequency-dependent complex material polarization (i.e., gain and refractive index dispersion). In this work, recursive digital filters are used to accurately represent the spectrally dependent material quantities in the time-domain model (Kaunga-Nyirenda et al., 2010). The most general linear digital filter takes a sequence of input points and produces a sequence of output points by the following difference equation (Smith, 2002):

$$y[n] = a_0 x[n] + a_1 x[n-1] + a_2 x[n-2] + \cdots + b_1 y[n-1] + b_2 y[n-2] + \ldots, \tag{24.27}$$

where n is the time index, and $x[]$ and $y[]$ represent the input and output, respectively. The a's and b's that define the filter are called recursive coefficients, with $b_0 \equiv 1$ corresponding to the sample being calculated.

Digital filtering allows the computation of long convolution integrals of two functions in the time domain for discretely sampled signals. The optimization of the filter coefficients involves the fast Fourier transform. Hence, it can be argued that the overhead incurred in obtaining the filter coefficients at every spatial point and time step is much larger than Fourier transforming the field and multiplying by the frequency dependent quantities directly, followed by inverse Fourier transforming back into the time domain. This computational overhead is, however, avoided by obtaining the filter coefficients offline from the main simulation and storing them in tables. For a given set of parameters (e.g., carrier density and temperature), the gain and refractive index changes can be calculated and the filter coefficients obtained for each case and stored in tables. The filter coefficients can then be retrieved during simulation with negligible additional computational burden. This approach is not possible with the direct energy–time transformation approach, which must be done during the simulation.

Figure 24.2 shows the fitted gain and refractive index spectra for an eight-pole filter after applying the filter to an impulse input and taking the Fourier transform of the resulting impulse response. A good fit is observed between the filter response and the desired response. The number of poles is dictated by the index spectrum, which has a sharp turning point and is less smooth than the gain spectrum. The number of poles for the filters for both spectra has to be the same for ease of implementation in the field update equation. Therefore, the number of poles chosen was one that gave a satisfactory fit for the index spectral profile, i.e., 8 (Figure 24.2).

This method accurately captures the asymmetric spectral response of the material polarization (Figure 24.2) and can be used to incorporate frequency responses from experimental measurements as well as complicated responses, not easily represented analytically. The use of spatiotemporal filter coefficients allows correct inclusion of spatial-hole burning and shifts of the gain spectrum due to band-filling and bandgap renormalization.

24.4.5 Numerical Implementation

The optical propagation (Equation 24.11) and carrier density (Equation 24.15) are coupled through the material Equations 24.19 through 24.21. These two equations are solved self-consistently by dividing the active region into small enough (shorter than the diffusion length) sections, such that quantities can be considered constant within each section. The field propagation equations are marched in time using the Lax differencing scheme, which allows use of a larger time step than is allowed by the explicit differencing scheme. The stability condition of the Lax differencing scheme is given by the Courant condition $(c\Delta t/n\Delta z) \leq 1$ (Press et al., 2002). The carrier density equation is integrated using a fourth-order Runga–Kutta method. All carrier-dependent quantities are estimated at the midpoint of each section, while the optical fields are evaluated at the section boundaries (Kaunga-Nyirenda et al., 2010). This ensures that the photons traveling to the right and to the left in a particular section both interact with the same carrier-related quantities (Wong and Carroll, 1987).

24.5 Case Study: FWM

FWM studies in nonlinear media have focused largely on the optical characteristics of mixing processes and experimental observations in the optical domain (Agrawal, 1988; Mukai and Saitoh, 1990; Uskov et al., 1994; Darwish et al., 1996; Gong et al., 2004), with emphasis mainly on the issue of conversion efficiency (Mukai and Saitoh, 1990). Very little attention has been paid to the characteristics of wave mixing in the electrical domain. Electrical measurements have been reported before for semiconductor laser diodes (SLDs) and a simplified model based on frequency modulation was presented in Nietzke et al. (1989). Although the operational characteristics of SLDs and SOAs are different, the material physics is the same, so that CDM and resulting wave mixing have their origins in the same physical processes. The carrier density is usually clamped to its threshold value in SLDs, limiting the modulation depth. On the other hand,

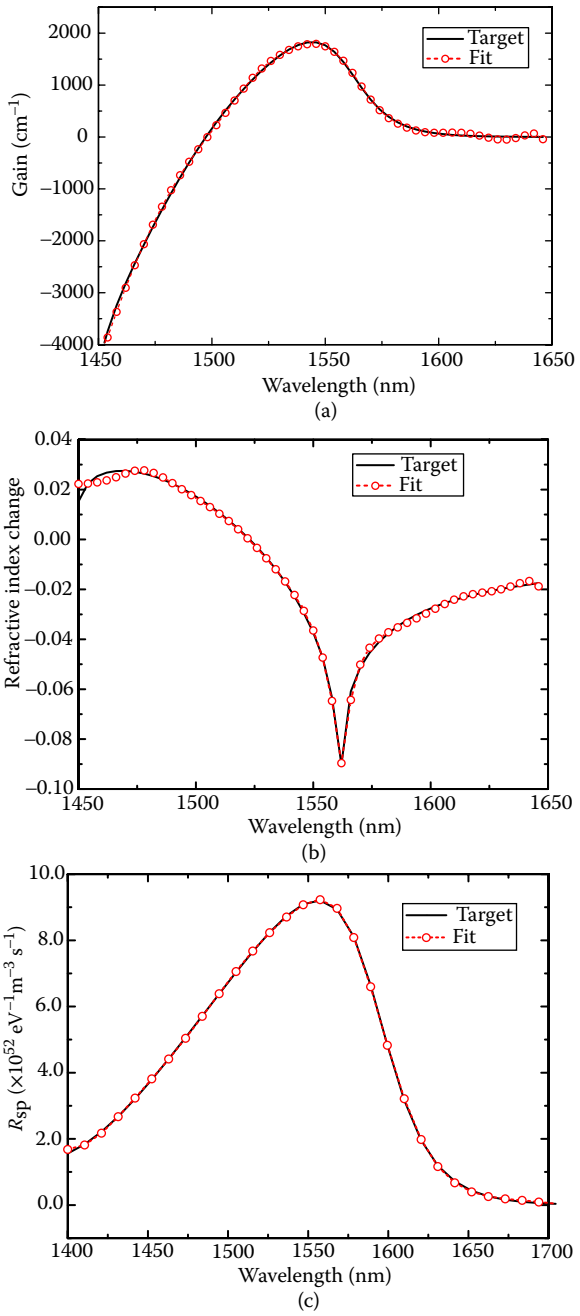

FIGURE 24.2 Fits for (a) gain spectrum, (b) refractive index change, and (c) spontaneous emission rate using recursive filters. The solid lines are the spectral quantity to be fitted, while the dotted lines are fits using the recursive filter. Number of poles for the filter is 8. Fits are obtained from the impulse responses of the filters.

large carrier density excursions are common in SOAs. In SLDs, the presence of strong optical feedback (i.e., large reflections at the facets) complicates the carrier density dynamics by introducing relaxation oscillations (Nietzke et al., 1989). A proper understanding of the characteristics of CDM is, therefore, likely to be stronger and clearer with SOAs (Dlubek et al., 2010). The model developed in Section 24.4 is used to study

the characteristics of CDM over different operating conditions. No *a priori* assumptions are made about the existence or form of the CDM—it is obtained directly from the physics.

24.5.1 CDM Characteristics

The CDM characteristics in wave mixing in SOAs are studied using the model developed earlier. The input to the SOA is of the form

$$E_{\text{in}}(0,t) = \left\{ \psi_{\text{p}}(0,t) + \psi_{\text{s}}(0,t) \exp\left(-j\Omega t\right) \right\} \exp\left(-j\omega_{\text{ref}} t\right), \tag{24.28}$$

where $\Omega = 2\pi f_{\text{d}}$ and $f_{\text{d}} = \left| f_{\text{p}} - f_{\text{s}} \right|$ is the detuning frequency between the inputs (referred to as pump and probe). The pump and probe laser frequencies are $f_{\text{p}} = \omega_{\text{p}}/2\pi$ and $f_{\text{s}} = \omega_{\text{s}}/2\pi$, respectively. The time dependence of the pump and probe slowly varying fields is a general form and allows the use of modulated input signals. The input (Equation 24.28) enters through the boundary conditions (Equations 24.12 and 24.13).

The parameters used in the simulations are given in Table 24.1.

Indium gallium arsenide (InGaAs) was used as the active material for the quantum wells. The barrier material was strained InGaAs (−0.67% strain) (Kelly et al., 1996). This matches the material system for the device used in the experiments reported in Dlubek et al. (2010). The indium composition in the InGaAs active material was taken to be 0.62. This reproduced the device characteristics as reported in its data sheet and Kelly et al. (1996). This device has a nonlinear geometry, (Figure 24.3) so an effective length with a

TABLE 24.1 Simulation Parameters Used in the Study of Wave Mixing

Symbol	Description	Value (Units)
L	SOA length	1.1 mm (Lealman, 2009)
W	SOA width	1.3 μm (Lealman, 2009)
D	SOA thickness	0.1 μm (Lealman, 2009)
Δz	Longitudinal grid spacing	10 μm
Γ_{xy}	Optical confinement factor	0.18 (Lealman, 2009)
R_1	Input facet reflectivity	0.05% (Kelly et al., 1996)
R_2	Output facet reflectivity	0.05% (Kelly et al., 1996)
α_{int}	Internal loss	2.0 cm^{-1}
A	Linear gain coefficient	2.0×10^{-20} m^2
N_0	Carrier density at transparency	1.7521×10^{24} m^{-3}
τ_{s}	Effective carrier lifetime	0.7 ns
α_{LWEF}	Linewidth enhancement factor	−3
A	Linear radiative recombination coefficient	1.0×10^{7} s^{-1}
B	Bimolecular recombination coefficient	5.6×10^{-16} m^3s^{-1}
C	Auger recombination coefficient	3.0×10^{-41} m^6s^{-1}
$\bar{n}_{\text{g}}$	Group index of refraction for the mode	3.6
n	Index of refraction of active region	3.3
H	Current injection efficiency	0.7
ε_{shb}	Gain compression factor	5.0×10^{-17} cm^3
τ_{in}	Intraband relaxation time	0.2 ps

Source: Agrawal, G.P., *Journal of the Optical Society of America B*, 5, 147–159, 1988.
Note: Some phenomenological parameters (carrier density at transparency, linear gain coefficient, effective carrier lifetime, linewidth enhancement factor, internal loss) are required as input to Agrawal's truncated series approximation (TSA) model.

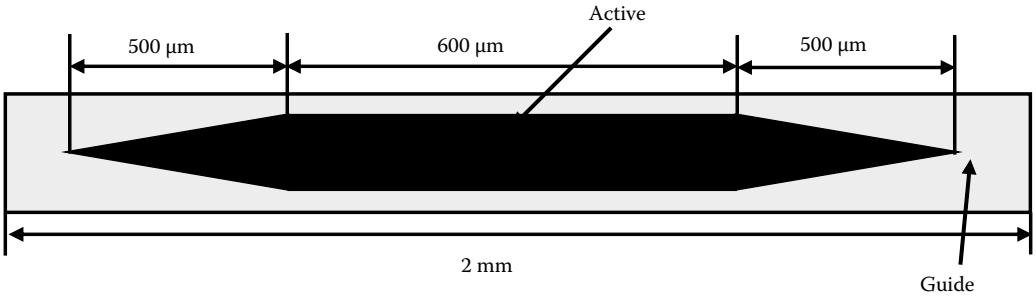

FIGURE 24.3 Sketch of the nonlinear geometry of a large spot semiconductor optical amplifier (SOA).

confinement factor equal to that of the untapered region was used in the simulations. All simulations were performed at 300 K. The carrier temperature was assumed to remain constant and equal to that of the lattice.

The CDM amplitude is obtained from the solution of the carrier density equation. A measurable quantity related to this is the variation in the injection current or voltage across the device, since the temporal fluctuations in the stimulated recombination rate result in temporal fluctuations in the current to resupply the carriers. The time series for the CDM amplitude is obtained at any spatial point along the longitudinal propagation direction as

$$\Delta N(z,t) = N(z,t) - N_{SS}(z), \tag{24.29}$$

where N_{SS} is the carrier density determined by the carrier injection, nonradiative recombination, and the amplified spontaneous emission (ASE) rates in the absence of external optical injection. The spectrum of the CDM amplitude is obtained by taking the discrete Fourier transform of Equation 24.29. Modulation of the carrier density results in modulation of the quasi-Fermi levels—and hence of the voltage drop across the active region (Equation 24.17). The spectrum of the injection current comes from DFT of Equation 24.16, while that of the voltage from Equation 24.17.

Simulated input and output optical spectra (from discrete Fourier transforms of the optical wave time series), and carrier density spectra (from discrete Fourier transform of Equation 24.29) are shown in Figure 24.4. The detuning of the two input signals was 2 GHz and the bias voltage was adjusted so that the current was 150 mA. The CW input optical fields had power levels of −0.7 and −0.8 dBm, respectively. The reference frequency was taken as the average of the pump and probe frequencies. An identical CDM spectra to Figure 24.4c was obtained when the reference frequency coincided with the pump frequency, confirming that the CDM spectra do not depend on the choice of the reference frequency used for the slowly varying envelope approximation. For the rest of the results presented below, the reference frequency coincided with the frequency of the pump. Figure 24.4 shows that the carrier density pulsates at the detuning frequency (beat frequency) of the pump and probe. The central peak in the carrier density spectrum is the static carrier density. The carrier population pulsations observed in Figure 24.4 are consistent with the experimental results (Nietzke et al., 1989).

The earlier simulations were repeated but with one of the optical input signals increased from −0.8 dBm to +4.7 dBm. Smaller secondary peaks are now also observed in Figure 24.4c at the multiples of the detuning frequency and these are enhanced as one of the input powers is increased (Figure 24.5).

The higher-order components (small secondary peaks at multiples of the detuning frequency) in Figure 24.5 are due to beating between the newly generated FWM products and the input beams or to higher-order harmonics in the CDM due to the nonlinearity of the carrier equation. Nonlinearities in the carrier equation are caused by the carrier density-dependent carrier lifetime and the saturation of the stimulated recombination rate. The peaks at the detuning frequency disappeared in the carrier density

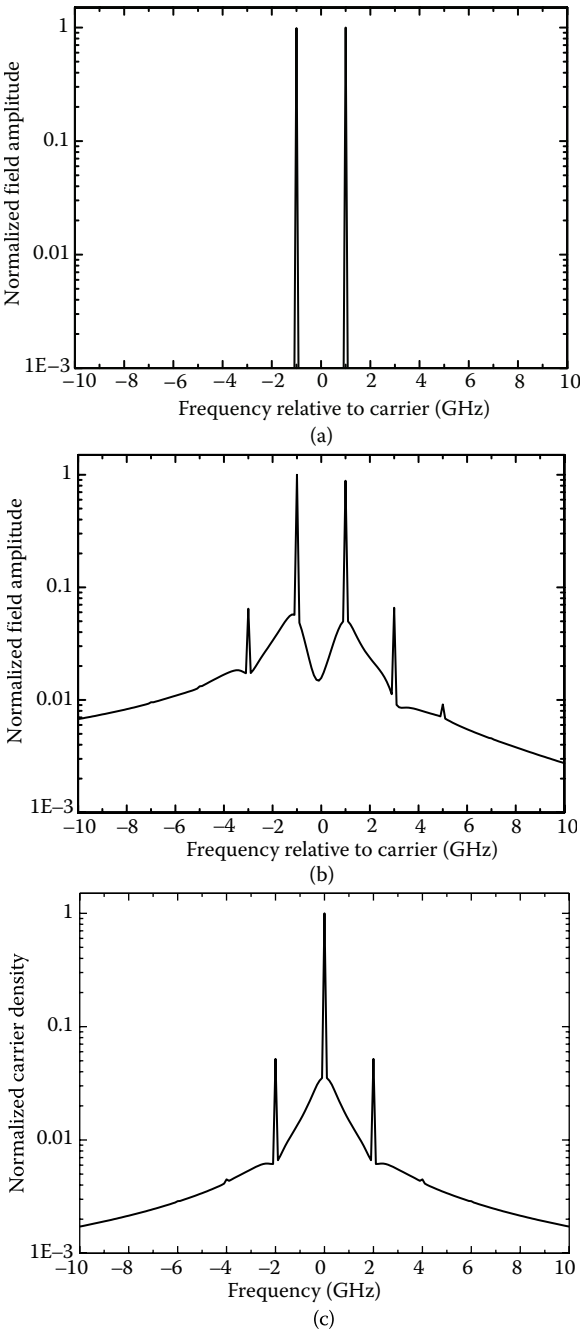

FIGURE 24.4 Simulated spectra (a), input optical field (b), output optical field, and (c) carrier density. Parameters: detuning 2 GHz, pump power −0.7 dBm, probe power −0.8 dBm, bias current 150 mA.

spectrum when one of the input signals was set to zero, confirming that the CDM is caused by the interaction of the input waves. This is consistent with the experimental results reported in (Dlubek et al., 2010). In addition to the primary peak, a weaker peak was observed in the measured CDM spectrum at twice the detuning frequency. This second harmonic had a bandwidth larger than the primary harmonic by a factor

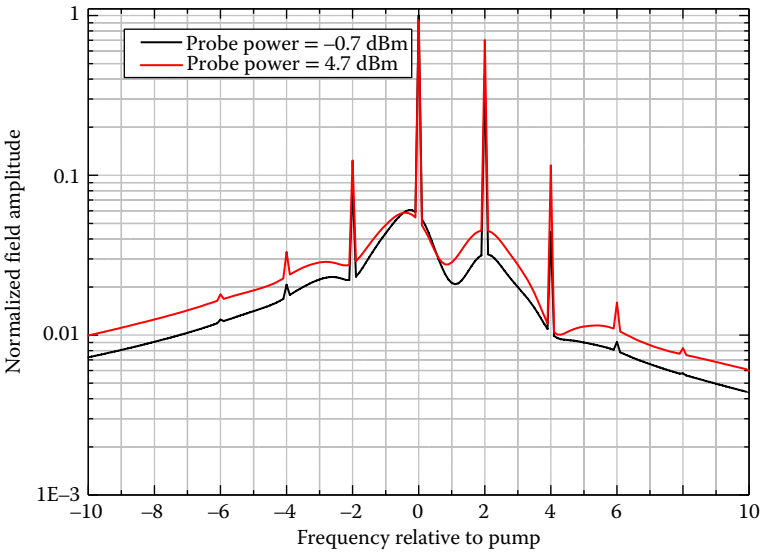

FIGURE 24.5 Optical spectra for the same parameters as in Figure 24.4 for two different probe powers. The pump signal is aligned to the reference signal, chosen around the gain peak.

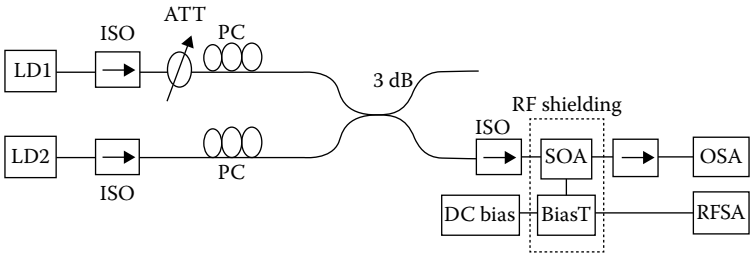

FIGURE 24.6 Carrier density modulation (CDM) measurement setup. ISO, isolator; ATT, variable optical attenuator; PC, polarization controller; 3 dB–50:50 coupler; OSA, optical spectrum analyzer; RFSA, radio frequency spectrum analyzer (From Dlubek, M.P. et al., *Optics Communications*, 283, 1481–1484, 2010).

of 1.5, indicating that it is the result of beating between the original waves and a new wave, which is itself broadened compared to the input waves.

24.5.2 Experimental Procedure for Measuring CDM

The experimental setup is shown in Figure 24.6 (Dlubek et al., 2010). The SOA used in the experiment was a nonlinear SOA from Centre of Integrated Photonics (CIP) (SOA-NL-OEC-1550 operating in 1550 nm region) with an active region consisting of InGaAs unstrained quantum wells and InGaAs barriers (Kelly et al., 1996). Two standard telecommunications diode lasers, LD1 and LD2, both a nominal wavelength of 1547.02 nm, were used as probe and pump, respectively. The frequency detuning between the two lasers was obtained by temperature tuning, so that it did not exceed 3 GHz (the bandwidth of the radio frequency (RF) spectrum analyzer). An optical spectrum analyzer was used to monitor the frequency detuning. A BiasT connector was used to uncouple the constant bias current to the SOA from the RF component from the device. Polarization controllers were used to adjust the polarization states of the interacting waves. Further experimental details are reported in Dlubek et al. (2010).

Before measuring the CDM spectrum, the reference beating spectrum of the two lasers (LD1 and LD2) was measured by heterodyning them on a standard 10 Gb/s photodetector. The 3 dB bandwidth of the heterodyne spectrum was ~40 MHz, suggesting that the laser linewidths were ~20 MHz. The spectral shape was approximately Lorentzian, as expected (Dlubek et al., 2010).

24.5.3 Dependence on Operating Conditions

The strength of interband effects depends on the rate of carrier replenishment into the active region. Thus, the CDM amplitude should decrease as the frequency detuning increases, since the carrier density cannot follow the fast oscillations of the stimulated emission rate. This was tested by simulating the FWM in the SOA for detuning frequencies up to 1 THz (by varying f_d in Equation 24.28), with all other parameters the same as in earlier simulations. Figure 24.7 shows the CDM spectra for different detunings. The peak at 2 GHz is a second harmonic for the 1 GHz detuning.

To obtain a clearer view of the frequency dependence of the CDM amplitude, the information in Figure 24.7 is extracted by obtaining the amplitude of the first harmonic (indicated against the detuning in Figure 24.7b) and plotting it against the detuning frequency (log scale), as shown in Figure 24.8. The CDM amplitude decreases sharply as the detuning frequency increases. The CDM amplitude at 1 THz is almost three orders of magnitude smaller than the value for a few GHz. The stimulated emission rate fluctuates at a much faster rate than the carriers injected into the active region. As a result, the carrier density cannot respond and the modulation efficiency decreases as the frequency detuning increases. Bream (2006) has also shown that the contribution of CDM to the refractive index perturbation is still significant even at frequencies well above the modulation bandwidths of the QW carrier distributions. As observed in Figure 24.8, although CDM continues to decrease with increasing detuning, it still contributes significantly to very fast nonlinear optical processes (even for detuning up to 1 THz) (Bream, 2006). Dynamic CH and SHB have not been taken into account in the model. It is interesting to note the similarity in the dependence of the CDM amplitude on detuning frequency and the dependence of amplitude of the conjugate signal on the detuning frequency observed in Figure 24.5a of Uskov et al. (1994). However, it is also worth noting that above 1 THz (~4 meV), acoustic phonon scattering should become relevant, while longitudinal optical (LO) phonon scattering should also be important above 9 THz. Thus, care is needed when extrapolating results to 1 THz and beyond, as other carrier scattering mechanisms can be resonantly excited.

Figure 24.9 shows the variation of the normalized CDM amplitude with bias current. The CDM in each case were normalized with respect to their maximum amplitude. As expected, the CDM amplitude increases with bias current. The detuning was adjusted to 1.23 GHz to match the experiments. In Agrawal's seminal paper on FWM (Agrawal, 1988), the carrier density rate equation is expressed as a power series involving the harmonics of the frequency detuning. The truncated series approximation (TSA1) curve in Figure 24.9 was calculated using Agrawal's model, where the power series is truncated at the first harmonic (Agrawal, 1988). The simulated and the experimental results both show that the CDM amplitude saturates as the bias current is increased further. Furthermore, a comparison of the experimental and simulated curves shows that the CDM approaches saturation at a faster rate in the experimental measurements than is observed in simulations. The CDM from measurements and truncated series assumption show the largest amplitude at 0 mA (experiment) and very close to 0 mA (TSA1).

The qualitative behavior is similar in both experiment and simulation. The model predicts the behavior of CDM better than the TSA1 in the gain region. At 0 mA, the rate of absorption is at its maximum and the net gain is equal to the absorption coefficient. The SOA behaves like an unbiased diode with an internal field and hence acts as a square-law detector. As the bias current increases from 0 mA toward transparency at around 35 mA, the rate of absorption decreases while the rate of emission increases. This results in an overall decrease in the net absorption and explains why the CDM amplitude decreases as the current increases from 0 mA toward transparency. Above transparency, the net gain increases. This leads to an increased rate of stimulated emission relative to absorption, which results in an increase in the CDM amplitude, saturating at about 150 mA. This is consistent with the measured gain-current dependence

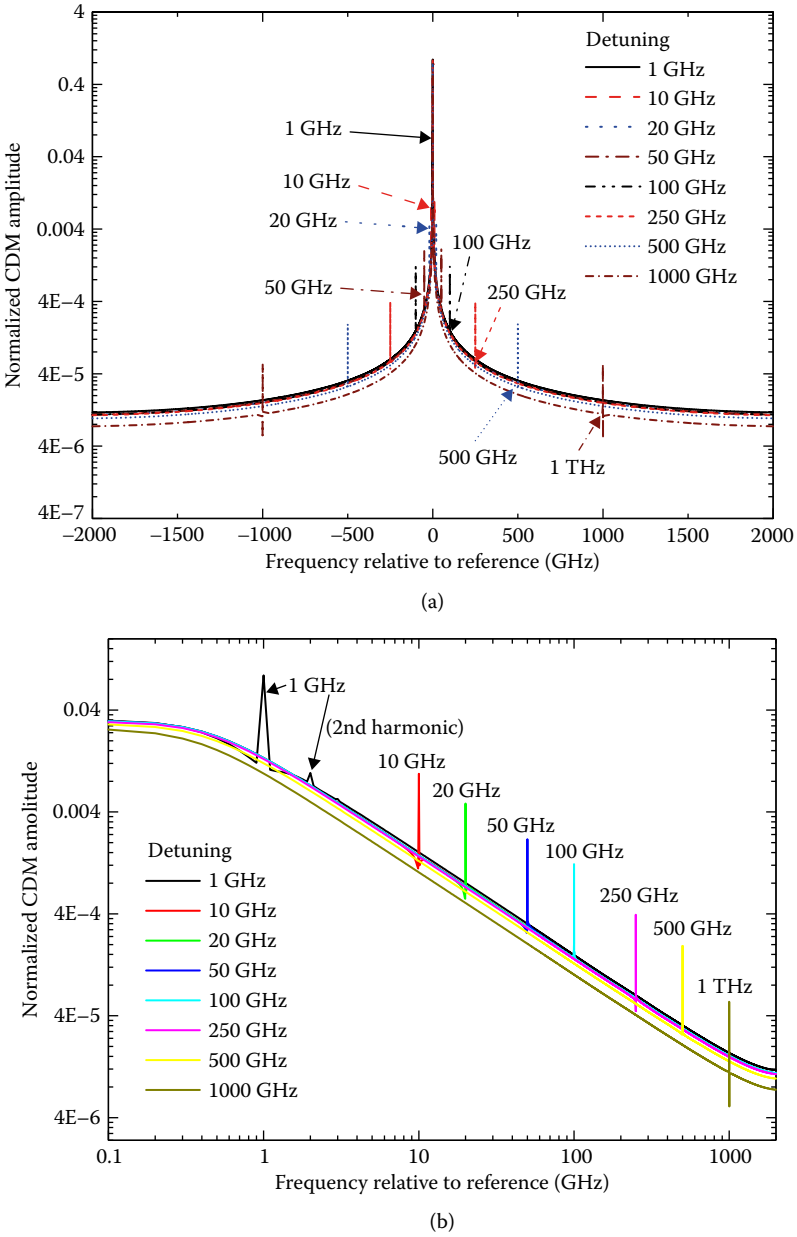

FIGURE 24.7 Normalized CDM amplitude for different detunings (a) full spectra and (b) positive spectra (log scale).

shown in Figure 24.10. The discrepancy between simulations and experiments in the absorption region and low bias current above transparency (0–50 mA) in Figure 24.9 can be attributed to the use of the unipolar model and the effects of ASE. The I–V characteristics of a diode appear most nonlinear near zero bias. The unipolar model is based on the linear approximation of the current injection (Equations 24.16 and 24.17), which does not include the nonlinear I–V characteristics, hence in the deviation for currents between zero and transparency. Spontaneous emission, and the subsequent ASE, have not been included in the propagating field. The effects of ASE on carrier dynamics are more pronounced at low (electrical)

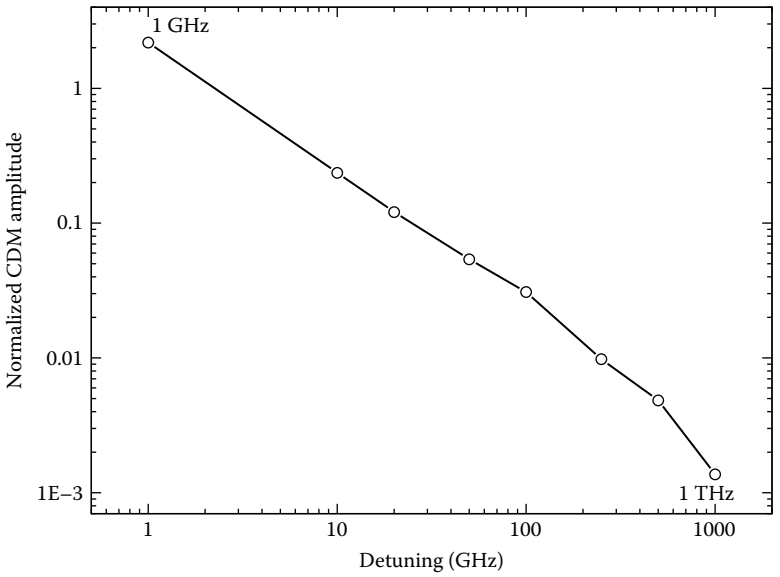

FIGURE 24.8 Normalized CDM amplitude at the first harmonic for different detunings (frequency in log scale).

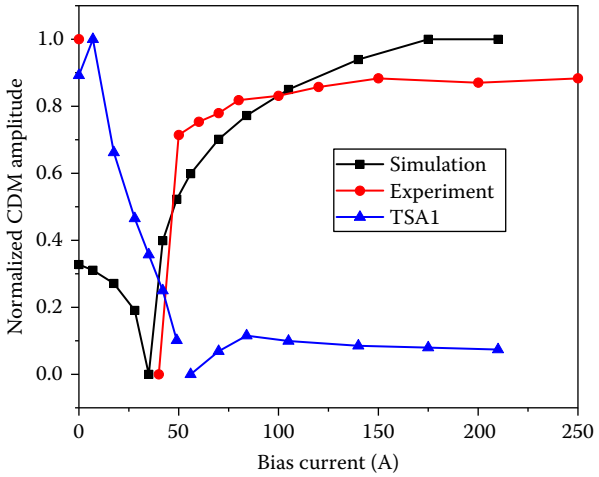

FIGURE 24.9 Normalized CDM amplitude at the first harmonic for different bias current, detuning 1.23 GHz, pump power −0.8 dBm, probe power −0.7 dBm. Truncated series approximation (TSA1) based on Agrawal's model (Agrawal, 1988), truncated at the first harmonic.

bias and optical input power level, since the rate of spontaneous emission can be comparable to the rate of stimulated emission.

The absence of experimental data points between 0 and approximately 50 mA in Figure 24.9 can be attributed to the low level of CDM, such that its amplitude was below the noise level. Although there is significant CDM in the absorption regime, it is not useful for many applications (apart from heterodyne detection, as discussed in Section 24.5.2) and both experiments and simulations confirm that there are no detectable/measurable optical mixing products.

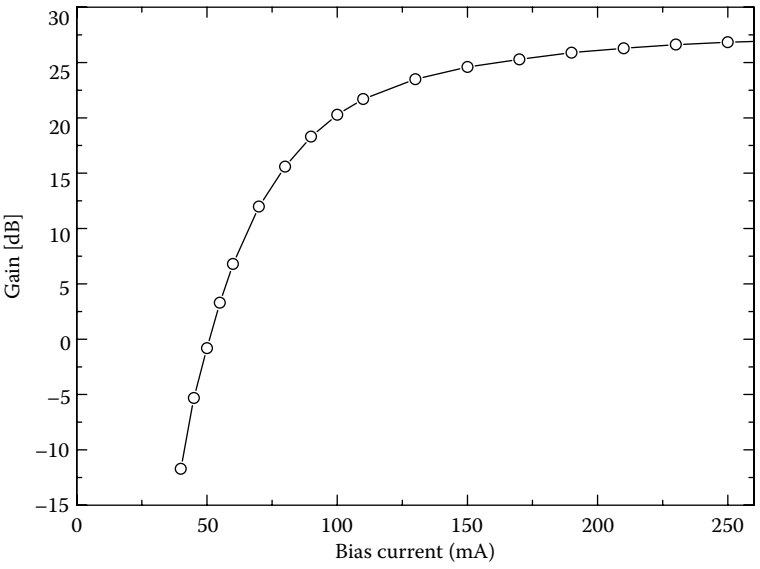

FIGURE 24.10 Measured small signal gain. Dependence on bias current for input power −28 dBm.

The effectiveness of CDM is expected to increase with input power, as the interaction between the different signals should be enhanced. As the optical power intensity increases in the active region, carrier depletion, and gain saturation effects should ultimately prevent any further increase in the CDM amplitude. (Signal distortion due to clipping as the carrier density approaches its transparency value should also create more signal components in the frequency spectrum.) Figure 24.11a and b show the simulated and measured CDM amplitude dependence on pump power for two probe powers (−0.8 dBm and +4.7 dBm). The detuning between the pump and probe was 1.23 GHz and the bias voltage was adjusted to give a bias current of 150 mA. The CDM amplitude increased with input power up to a point. The figures also reveal that the largest CDM is produced when the pump and probe signals have approximately equal power. This is a key result that cannot be determined from previous works, which rely on the assumption that the pump power is much larger than the probe power.

There is good qualitative agreement between simulation and experiment. However, there is some discrepancy in the amplitude of the CDM obtained using simulations and experiment, as shown in Figures 24.9 and 24.11. Apart from the limitations of the unipolar electrical and 1D traveling wave optical models, some of these differences are due to errors in the material parameters of the SOA, as these were not provided by the manufacturer. This discrepancy may also result from a lack of knowledge of the device's parasitic impedances and layer resistivities, which will also affect the RF signal measured at the device terminals (after the BiasT in Figure 24.6).

The normalized CDM amplitude is generally higher for the lower probe power (−0.8 dBm), as shown in Figure 24.12, where the dependence of the simulated CDM amplitude on the pump power is plotted for two probe powers (−0.8 dBm, +4.7 dBm). The other parameters are the same as those used in the simulations for Figure 24.11. When one beam is much weaker than the other, the CDM amplitude decreases as the beating is reduced due to carrier depletion and gain saturation by the strong beam.

24.6 Summary and Conclusions

We have developed a suitable time-domain model to investigate dynamic nonlinear optical effects in SOAs. The model takes into account the most important interband processes and minimizes the number of phenomenological parameters. This simulation tool was used to show how wave mixing processes manifest

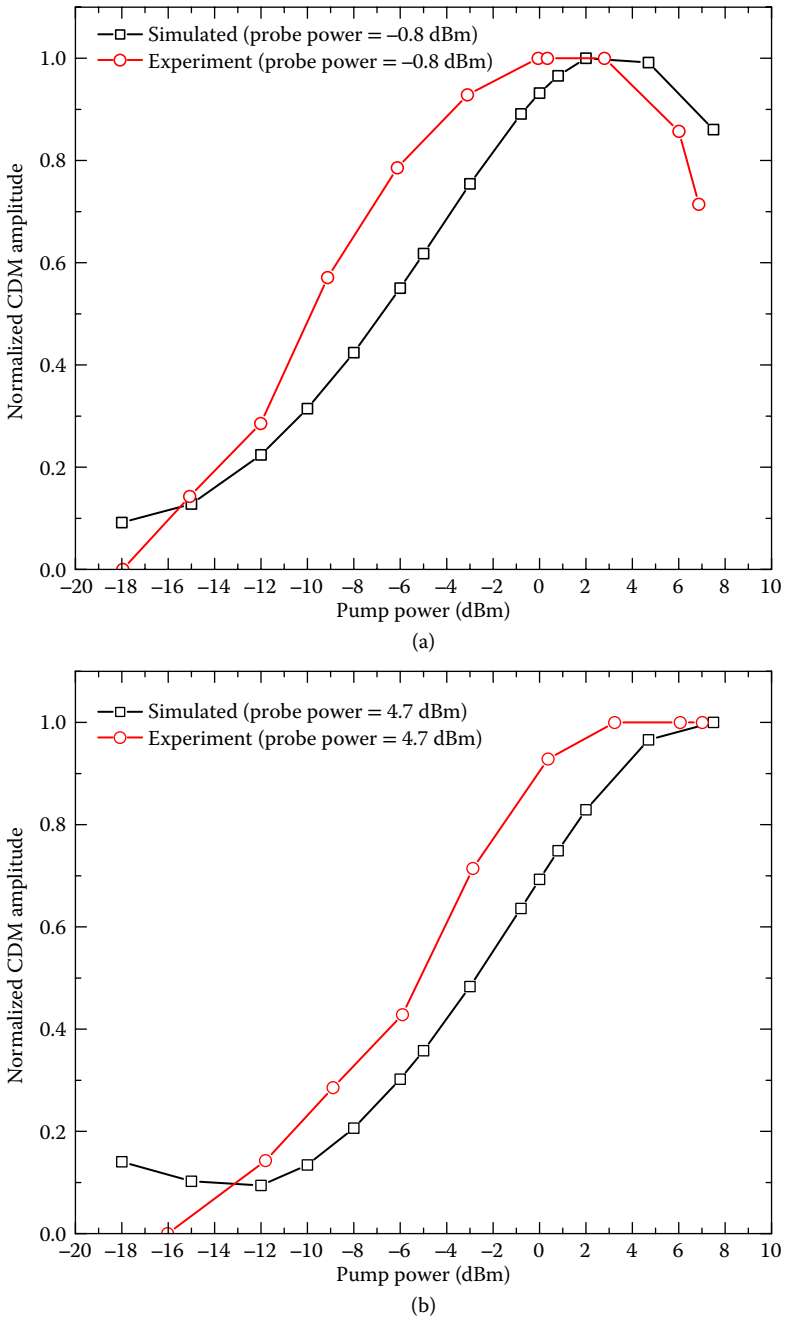

FIGURE 24.11 Normalized CDM amplitude dependence on pump power for different probe power levels: (a) probe power −0.8 dBm and (b) probe power +4.7 dBm. Detuning 1.23 GHz, bias current 150 mA.

themselves in SOAs, and discuss their impact on existing and potential applications. This is key to understanding and modeling nonlinear optical signal impairments. Furthermore, the knowledge obtained from these studies can be used in the design of new devices and/or for optimizing existing ones that rely on similar nonlinear optical effects, e.g., high-density PICs. The nonlinear phenomena are also accessible

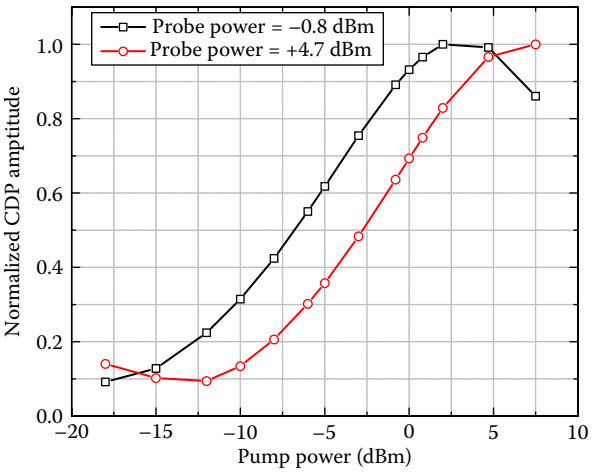

FIGURE 24.12 Simulated CDM amplitude (normalized) for two probe levels as in Figure 24.11a and b.

through electrical measurements, as well as through FWM and SHG measurements, providing additional opportunities for the validation of the simulation tool.

Other key outcomes of this work are the general description of the nonlinear polarization and the demonstration of the inclusion of nonlinear optical effects using the recursive filter functions. These can be used in more advanced tools, such as those with higher dimensionality (2D or 3D), those with a dynamic bipolar electrical model, and those with more accurate time domain-optical models (e.g., which properly include the spectral effects in the propagation and waveguiding). Finally, the general description of the nonlinear polarization means this approach can be readily adapted to include other contributions to the nonlinear polarization.

Acknowledgments

S.N. Kaunga-Nyirenda would like to thank the Commonwealth Scholarship Commission (United Kingdom) for financial support. This work was also supported in part by the Higher Education Funding Council of England (HEFCE) with a HERMES Fellowship and the UK Engineering and Physical Sciences Research Council (EPRSC) under grant GR/T09309/01. The authors are also grateful to the CIP for useful information and discussion about the SOA. The authors would also like to thank Prof. M. Wale (Oclaro) and Prof. K. Williams (TU Eindhoven) for useful discussions on the simulation requirements for active devices in PICs.

References

Agrawal, G.P. (1988) Population pulsations and nondegenerate four-wave mixing in semiconductor lasers and amplifiers. *Journal of the Optical Society of America B*, **5**, 147–159.

Agrawal, G.P. and Dutta, N.K. (1986) *Long-Wavelength Semiconductor Lasers*. New York, NY: Van Nostrand Reinhold.

Boyd, R.W. (2007) *Nonlinear Optics*. Cambridge, MA: Academic Press.

Bream, P.J. (2006) *Nonequilibrium Carrier Dynamics and Gain in Semiconductor Quantum Wells*. Nottingham: School of Electrical and Electronic Engineering.

Dai, Z., Michalzik, R., Unger, P., and Ebeling, K.J. (1997) Numerical simulation of broad-area high-power semiconductor laser amplifiers. *IEEE Journal of Quantum Electronics*, **33**, 2240–2254.

Darwish, A.M., Ippen, E.P., Le, H.Q., Donnelly, J.P., and Groves, S.H. (1996) Optimization of four-wave conversion efficiency in the presence of nonlinear loss. *Applied Physics Letters*, **69**, 737–739.

Das, N.K., Yamayoshi, Y., and Kawagushi, H. (2000) Analysis of basic four-wave mixing characteristics in a semiconductor optical amplifier by finite-difference beam propagation method. *IEEE Journal of Quantum Electronics*, **36**, 1184–1192.

Dlubek, M.P. (2008) *Optical Performance Monitoring for Amplified Spontaneous Emission Related Issues in Transparent Optical Networks*. Nottingham: School of Electrical and Electronic Engineering.

Dlubek, M.P., Kaunga-Nyirenda, S.N., Phillips, A.J., Sujecki, S., Harrison, I., and Larkins, E.C. (2010) Experimental verification of the existence of optically induced carrier pulsations in SOAs. *Optics Communications*, **283**, 1481–1484.

Durhuus, T., Mikkelsenm, B., and Stubkjaer, K.E. (1992) Detailed dynamic model for semiconductor optical amplifiers and their crosstalk and intermodulation distortion. *Journal of Lightwave Technology*, **10**, 1056–1064.

Gong, P.-M., Hsieh, J.-T., Lee, S.-L., and Wu, I. (2004) Theoretical analysis of wavelength conversion based on four-wave mixing in light-holding SOAs. *IEEE Journal of Quantum Electronics*, **40**, 31–40.

Hutchings, D.C., Sheik-bahae, M., Hagan, D.J., and Stryland, E.W. (1992) Kramers-Kronig relations in nonlinear optics. *Optical and Quantum Electronics*, **24**, 1–30.

Jackson, J.D. (1975) *Classical Electrodynamics*. New York, NY: John Wiley & Sons.

Jones, D.J., Zhang, L.M., Carroll, J.E., and Marcenac, D.D. (1995) Dynamics of monolithic passively mode-locked semiconductor lasers. *IEEE Journal of Quantum Electronics*, **31**, 1051–1058.

Joyce, W.B., and Dixon, R.W. (1977) Analytic approximations for the Fermi energy of an ideal Fermi gas. *Applied Physics Letters*, **31**, 354–356.

Kaunga-Nyirenda, S.N., Dlubek, M.P., Phillips, A.J., Lim, J.J., Larkins, E.C., and Sujecki, S. (2010) Theoretical investigation of the role of optically induced carrier pulsations in wave mixing in semiconductor optical amplifiers. *Journal of Optical Society of America B*, **27**, 168–178.

Kelly, A.E., Lealman, I.F., Rivers, L.J., Perrin, S.D., and Silver, M. (1996) Polarisation insensitive, 25 dB gain semiconductor laser amplifier without antireflection coatings. *Electronics Letters*, **32**, 1835–1836.

Kovačević, M., and Acampora, A. (1995) Benefits of wavelength translation in all-optical clear-channel networks. *IEEE Journal of Selected Areas in Communications*, **14**, 868–880.

Lealman, I.F. (2009) Centre for Integrated Photonics (CIP), B55, Adastral Park (Private Communication).

Lim, J.J., MacKenzie, R., Sujecki, S., Sadeghi, M., Wang, S.M., Wei, Y.Q., Gustavsson, J.S., Larsson, A., Melanen, P., Sipilä, P., Uusimaa, P., George, A.A., Smowton, P.M., and Larkins, E.C. (2007) Simulation of double quantum well GaInNAs laser diodes. *IET Optoelectronics*, **1**, 259–265.

Lim, J.J., Sujecki, S., Lang, L., Zhang, Z., Paboeuf, D., Pauliat, G., Lucas-Leclin, G., Georges, P., MacKenzie, R.C.I., Bream, P., Bull, S., Hasler, K.-H., Sumpf, B., Wenzel, H., Erbert, G., Thestrup, B., Petersen, P.M., Michel, N., Krakowski, M., and Larkins, E.C. (2009) Design and simulation of next-generation high-power, high-brightness laser diodes. *IEEE Journal of Selected Topics in Quantum Electronics*, **15**, 993–1008.

Liu, J. (2005) *Photonic Devices*. Cambridge: Cambridge University Press.

Manning, R.J., Ellis, A.D., Poustie, A.J., and Blow, K.J. (1997) Semiconductor laser amplifiers for ultrafast all-optical signal processing. *Journal of the Optical Society of America B*, **14**, 3204–3216.

Mukai, T., and Saitoh, T. (1990) Detuning characterisitcs and conversion efficiency of nearly degenerate four-wave mixing in a 1.5-μm travelling-wave semiconductor laser amplifier. *IEEE Journal of Quantum Electronics*, **26**, 865–875.

Nietzke, R., Panknin, P., Elsasser, W., and Gobel, E.O. (1989) Four-wave mixing in GaAs/AlGaAs semiconductor lasers. *IEEE Journal of Quantum Electronics*, **25**, 1399–1406.

Ning, C.Z., Indik, R.A., and Moloney, J.V. (1997) Effective Bloch equations for semiconductor lasers and amplifiers. *IEEE Journal of Quantum Electronics*, **33**, 1543–1550.

Park, J., Li, X., and Huang, W.P. (2005) Comparative study of mixed frequency-time-domain models of semiconductor optical amplifiers. *IEE Proceedings in Optoelectronics*, **152**, 151–159.

Pratt, E.M., and Carroll, J.E. (2000) Gain modelling and particle balance in semiconductor lasers. *IEE Proceedings in Optoelectronics*, **147**, 77–82.

Press, W.H., Teukolsky, S.A., Vetterling, W.T., and Flannery, B.P. (2002) *Numerical Recipes in C++: The Art of Scientific Computing*. Cambridge: Cambridge University Press.

Smith, S.W. (2002) *Digital Signal Processing: A Practical Guide for Engineers and Scientists*. Poway, CA: California Technical Publishing.

Tolstikhin, V.I. (2000) Carrier charge imbalance and optical properties of separate confinement heterostructure quantum well lasers. *Journal of Applied Physics*, **87**, 7342–7348.

Toptchiyski, G., Kindt, S., Petermann, K., Hillinger, E., Diez, S., and Weber, H.G. (1999) Time-domain modeling of semiconductor optical amplifiers for OTDM applications. *Journal of Lightwave Technology*, **17**, 2577–2583.

Uskov, A., Mork, J., and Mark, J. (1994) Wave mixing in semiconductor laser amplifiers due to carrier heating and spectral-hole burning. *IEEE Journal of Quantum Electronics*, **30**, 1769–1781.

Vurgaftman, I., Meyer, J.R., and Ram-Mohan, L.R. (2001) Band parameters for III–V compound semiconductors and their alloys. *Applied Physics Review*, **89**, 5815–5875.

White, J.K., Moloney, J.V., Gavrielides, A., Kovanis, V., Hohl, A., and Kalmus, R. (1998) Multilongitudinal-mode dynamics in a semiconductor laser subject to optical injection. *IEEE Journal of Quantum Electronics*, **34**, 1469–1473.

Williams, K.A., Aw, E.T., Wang, H., Penty, R.V., and White, I.H. (2008) Physical layer modelling of semiconductor optical amplifier based terabit/second switch fabrics. *International Conference of Numerical Simulation of Optoelectronic Devices*, Nottingham, United Kingdom.

Wong, Y.L., and Carroll, J.E. (1987) A Travelling-wave rate equation analysis for semiconductor lasers. *Solid-State Electronics*, **30**, 13–19.

Yanhua, H., Bandyopadhyay, S., Spencer, P.S., and Shore, K.A. (2003) Polarization-independent optical spectral inversion without frequency shift using a single semiconductor optical amplifier. *IEEE Journal of Quantum Electronics*, **39**, 1123–1128.

Zory, P.S., Jr. (ed.) (1993) *Quantum Well Lasers*. Cambridge, MA: Academic Press.

25

Semiconductor Optical Amplifier Dynamics and Pattern Effects

Zoe V. Rizou
and
Kyriakos E. Zoiros

25.1 Introduction

Since their advent in the second half of the 1980s (O'Mahony, 1988), semiconductor optical amplifiers (SOAs) have evolved technologically to the point that they have become key elements for the development of optical communications circuits, systems, and networks. Due to their attractive features of low power consumption, compactness, broad gain bandwidth, and ability for integration with affordable cost, the multifunctional potential of SOAs has been exploited in data amplification (Zimmerman and Spiekman, 2004) and processing (Mørk et al., 2003) in the optical domain and, more recently, for data encoding as well (Udvary and Berceli, 2010).

Motivated by the widespread employment of SOAs and the concomitant need to assist their design and support the implementation of the diverse applications they are destined to serve, the purpose of this chapter is to present in a concise and comprehensible manner the basic processes which govern the dynamic behavior of SOAs. Furthermore, it aims at describing how these processes can theoretically be taken into account in order to model their impact on the SOA response. It is concerned with the significant phenomenon of the pattern effect which manifests when the SOA gain is modulated, either optically by a single data pulse train or electrically by digital information superimposed on the SOA current. More specifically, the chapter topics which are addressed with regard to the SOA dynamics are outlined as follows:

Section 25.2: SOA Dynamics Background—Types, physical origin, conditions for manifestation, and qualitative impact on SOA response.
Section 25.3: SOA Model Formulation—SOA gain dynamics modeling theoretical formulation and numerical/closed form solutions.
Section 25.4: SOA Model Simplification—Ways of simplification and implications.
Section 25.5: SOA Optical Gain Modulation—Characterization and implications.
Section 25.6: Pattern Effect I—Direct Optical Amplification: Performance limitations and methods for mitigation.

Section 25.7: SOA Electrical Gain Modulation—Characterization and implications.
Section 25.8: Pattern Effect II—Direct Current Modulation: Performance limitations and methods for mitigation.

25.2 SOA Dynamics Background

Figure 25.1a depicts the standard configuration of an SOA (Mørk et al., 2003). Light is coupled via one of the facets into an intrinsic region of semiconductor material, which is sandwiched between a hole-dominant, that is, p-doped, and electron-dominant, that is, n-doped, cladding layer of higher bandgap energy and slightly lower refractive index. This structure allows confinement of a large number of free carriers in a small active volume, which hence exhibit a large density. By forward biasing the heterojunction through the injection of an electric current being below the lasing threshold point, the population of the carriers can be sufficiently inverted so that optical gain is established at a rate that prevails absorption. Then when signal photons of suitable energy travel through the active area, they stimulate radiative recombinations of electrons and holes and are coherently (i.e., with the same polarization, frequency, and phase) amplified as they propagate along the formed waveguide and exit from the other side of the device. In order to avoid unwanted back reflections and oscillations inside the cavity, the reflectivity of the SOA facets is reduced to very low values of less than 1×10^{-5} using antireflection coatings, tilted waveguides and tapered waveguides (Connelly, 2002). These technological means allow us to achieve a single-pass controllable amplification as high as 30 dB and with ripples-free parabolic-like spectrum profile, which can extend from 1300 to 1600 nm by changing the chemical composition of III–V group semiconductor materials. In particular, in this chapter we consider InGaAsP/InP-based SOAs, which operate in the 1550 nm telecommunications window where the attenuation of signals transmitted via optical fibers is lowest.

When a lightwave beam of optical frequency ν is injected into an SOA with a photon energy, hν, being larger than the bandgap energy, $E_g = E_c\text{-}E_v$, which, as shown in Figure 25.1b, separates the conduction and valence bands having energy at their bottom and top E_c and E_v, respectively, it triggers through band-to-band transitions stimulated emission and depletes the pumped carriers (Diez, 2000; Vacondio, 2011).

The reduction in the density of the excited carriers has then two consequences. First, the produced gain is reduced up to the point where it becomes saturated. Second, a set of dynamic processes tend to

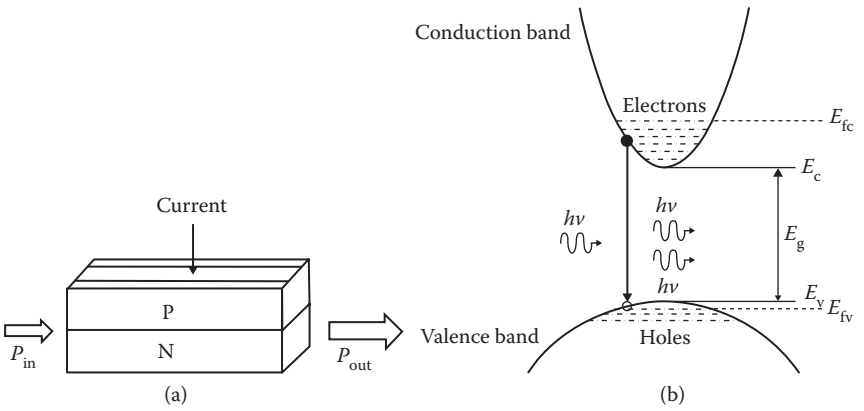

FIGURE 25.1 (a) Schematic representation of typical semiconductor optical amplifier (SOA) structure. (b) Simplified band diagram of semiconductor material. E_g, bandgap energy given by the difference between the energy at the bottom of the conduction band, E_c, and the energy at the top of the valence band, E_v; E_{fc}, quasi-Fermi level in the conduction band, and E_{fv}, quasi-Fermi level in the valence band.

bring the SOA gain back to its original level. These processes, which govern the SOA gain recovery, can be categorized in two cases of transitions (Occhi, 2002):

- Intraband transitions, which affect the distribution of carriers in the energy bands but leave the overall carrier concentrations unchanged. Varying the carrier density affects this distribution, which is further modified by spectral hole burning (SHB), free carrier absorption (FCA), carrier heating (CH), and carrier cooling.
- Interband transitions, which are related to the exchange of carriers between the energy bands and hence result in changes in the carrier density. These transitions are determined by electrical pumping, stimulated emission, absorption, spontaneous emission, nonradiative recombinations and two-photon absorption (TPA).

As electrons need not change band but are rearranged within the latter, the time constants of intraband transitions are much shorter than those of interband transitions. For this reason, the former are referred to as ultrafast effects. Given the time constants of these effects, they tend to be important compared with interband dynamics when the spectrum of the input signal is very wide, as in short pulse amplification, or when many channels are amplified in the context of wavelength division multiplexing (WDM) (Vacondio, 2011).

The SOA gain dynamics are directly coupled with those of free carriers (Occhi, 2002). Figure 25.2 qualitatively illustrates the temporal evolution of the free carrier distribution (energy versus density) in the conduction band (CB) of an SOA, which operates in the gain regime (Hall et al., 1994) subject to an ultrashort optical pulse that belongs to a time-varying signal (Occhi, 2002; Mørk et al., 2003; Wang, 2008). Prior to the pulse arrival, the carrier density within the CB is in quasi-equilibrium (Saleh and Teich, 1991), which occurs when the relaxation times for transitions within an energy band are much shorter than the relaxation time versus the other energy band. In this situation, the carrier distribution within the considered band is graphically shown in Figure 25.2a and is described by the product of the density of states, which is increased away from the band edge ($E = E_c$) at a rate that depends on the effective masses of electrons, with the probability that a given energy level, $E > E_c$, is occupied by an electron (Diez, 2000; Connelly, 2002). This probability is described by the Fermi function, $1/\left[\exp\left((E\text{-}E_{fc})/k_B T\right) + 1\right]$, where E_{fc} is the quasi-Fermi level, T is the temperature of the medium at thermal equilibrium and k_B is Boltzmann's constant (so that $k_B T$ defines the thermal energy, which equals 26 meV at $T = 300$ K). The position of the quasi-Fermi levels in the conduction and valence bands, E_{fc} and E_{fv}, respectively, is determined by the pumping rate (current injection), and if the latter is sufficiently large so that their separation exceeds the bandgap energy then the semiconductor medium provides gain and hence acts as an amplifier (Diez, 2000). Such a condition can be satisfied only if the quasi-Fermi levels lie, as shown in Figure 25.1, inside the conduction and valence bands, respectively, which for a semiconductor happens only under strong biasing (Vacondio, 2011). Note here that since the electrons and holes in the SOA are interrelated because of charge neutrality, it is sufficient to refer only to the conduction band (Schubert, 2004).

The natural quasi-equilibrium state is altered when pulses of duration in a subpicosecond timescale enter the SOA. This happens due to intraband effects which manifest according to the following phenomena: First, the induced stimulated emission responsible for signal amplification causes carriers to recombine around a narrow range of energies defined by pulse photon energy. This opens a hole in the carrier distribution, which is referred to as "SHB" and provokes a deviation from the normal Fermi distribution (Figure 25.2b). As a consequence, a localized reduction in the number of carriers at the transition energies occurs, while the total (electron/hole) carrier density within the band is reduced by the stimulated emission. For high-input pulse energies (>1 pJ) (Tang and Shore, 1998) TPA may also take place where, as the name implies, two photons are simultaneously absorbed and an electron is transferred from the valence band to a high energy level in the conduction band due to the high photon density in the active region (Hall et al., 1994; Mørk et al., 2003). In addition, a free carrier absorbs a photon and moves to a higher energy within the same band, according to the so-called FCA (Hall et al., 1994). After these effects have manifested on a timescale practically of few tens of femtoseconds (fs) (Diez, 2000) and the optical pulse has left

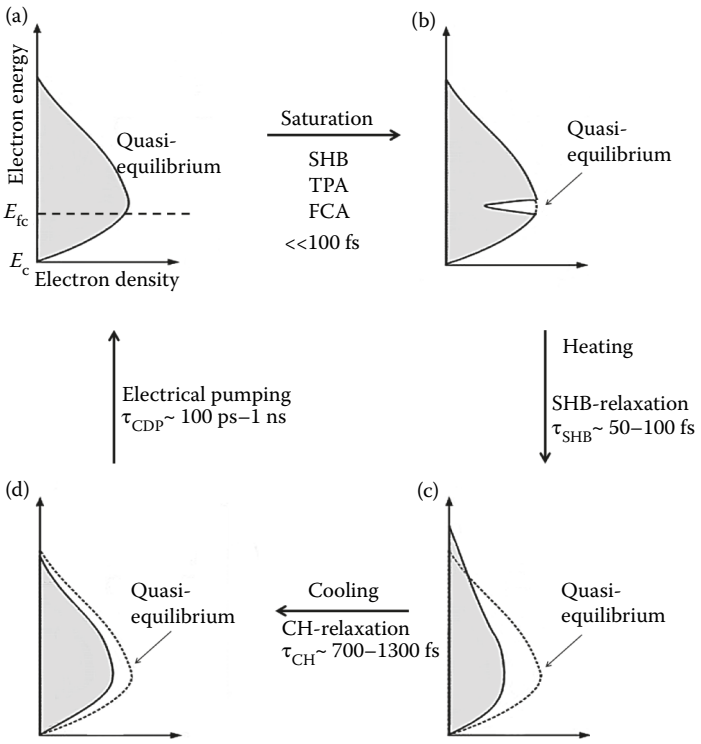

FIGURE 25.2 Evolution of carrier distribution induced in the conduction band (CB) of SOA by an ultrashort strong optical pulse. The shaded areas under the solid lines are proportional to the total carrier concentration in the CB (Wiesenfeld, 1996). The quasi-equilibrium is described by a Fermi distribution of quasi-Fermi level E_{fc}, which exceeds the minimum energy of the CB, E_c, in accordance with Figure 25.1b. SHB, spectral hole burning; CH, carrier heating; FCA, free carrier absorption; TPA, two-photon absorption, which occurs only for high pulse energies. The time constants values are typical for bulk SOAs, and may vary by more than a factor of two. (From Diez S, 2000, All-optical signal processing by gain-transparent semiconductor switches. PhD dissertation, Technical University of Berlin.)

the SOA, the Fermi distribution is restored via a process known as carrier–carrier scattering (Mørk et al., 2003), and the time required for this to happen is determined by the constant τ_{SHB}, which is known as SHB relaxation time, with values typically several tens of femtoseconds (50–100 fs). Since this parameter is finite, the governing SHB essentially sets the timescale during which the quasi-equilibrium Fermi distribution is established among the carriers in a band. Additionally, free carriers at energy levels lower than the average carrier density in the band are removed by stimulated emission or are transferred to higher levels due to the contribution of FCA and (possibly) TPA. As a result, the average carrier temperature is elevated and becomes higher than before the pulse arrival (Hall et al., 1994; Mørk et al., 2003). This transient increase of the electron and hole temperatures is called "CH" and impacts the carrier distribution (Figure 25.2c). The characteristic time, τ_{CH}, required for carriers to release their excess energy through phonon emission and cool down to the lattice temperature is of the order of several hundred femtoseconds (700–1300 fs). After this temperature relaxation time has elapsed, the starting Fermi distribution has been reestablished (Figure 25.2d), but the carrier density is still reduced compared to the stationary state (Figure 25.2a). Then the interband effect of carrier density pulsation (CDP) takes the lead and lasts between some hundreds of picoseconds and a few nanoseconds, depending on the dimensions and material of the active region as well as the SOA operating conditions. During this interval, which is defined by the respective time constant, τ_{CDP}, the carrier density, which had been decaying due to the stimulated emission, is increased again toward its original level owing to the resupply of electrons to the SOA via electrical pumping and the

refilling of the respective bands. Finally, the carrier distribution is recovered to the quasi-equilibrium state (Figure 25.2a).

The distinctive evolution of the above processes can be conveniently viewed on the temporal profile of the SOA gain response, which is coupled to the carrier density. In practice, the SOA intraband and interband gain dynamics temporal characteristics and their dependence on operating parameters are directly disclosed by means of the pump-probe technique (Hall et al., 1994). This is a time-domain measurement technique where the SOA gain is perturbed by a strong optical pulse called "pump" and sampled at different delays, τ_{delay}, by a weak pulse called "probe," as illustrated in Figure 25.3a. The strong pump pulse drives the SOA under test into nonlinearity. The weak probe pulse cannot affect but instead experiences the altered SOA properties (Vallaitis, 2010). In order to capture the full extent of the SOA gain dynamics, the pulse repetition rate is of the order of several tens of MHz so that only one pump pulse at a time travels through the SOA and the gain of the latter is fully recovered before the arrival of the next pulse. Furthermore, ultrashort, that is, femtosecond-wide (Mørk et al., 2003) optical pulses are employed because their width determines the measurement's temporal resolution, which must be as high as possible to be able to extract the maximum information. A typical outcome of such measurement is graphically shown in Figure 25.3b, where the probe transmission has been plotted against the pump–probe delay, which is varied between a few ps to a few hundreds of ps (positive delay means that the pump precedes the probe pulse) [Occhi, 2002; Mørk et al., 2003; Wang, 2008; Vacondio, 2011]. The probe transmission is proportional to the SOA gain, so the curve monitors the SOA gain dynamic behavior.

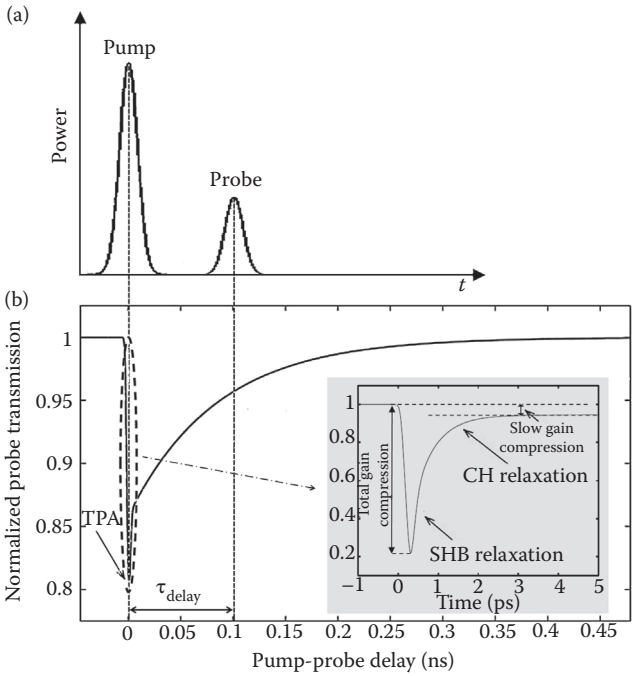

FIGURE 25.3 (a) Pump-probe technique. (From Vallaitis T., *Ultrafast Nonlinear Silicon Waveguides and Quantum Dot Semiconductor Optical Amplifiers*, Germany: Univ Karlsruhe, 2010.) (b) SOA typical evolution of (normalized) probe transmission as a function of pump–probe delay. The depicted curve does not represent exactly the defined SOA gain but rather its convolution with the pump and probe pulses. The timescale of the intraband gain dynamics is depicted in the zoomed-in inset. (From Occhi L, *Semiconductor optical amplifiers made of ridge waveguide bulk InGaAsP/InP: Experimental characterisation and numerical modelling of gain, phase, and noise, PhD dissertation*, Swiss Federal Institute of Technology in Zurich, 2002)

Initially, the pump pulse compresses the gain by an amount defined by the ratio of the unsaturated to the minimum level of the probe transmission, which occurs at the point where the carrier depletion is maximized by the pump peak power (Occhi, 2002). This gain compression is governed by SHB and (if enough photons are present in the SOA) TPA (Hall et al., 1994). Due to the finite resolution of the employed measurement technique (Hall et al., 1994), these ultrafast physical mechanisms are interpreted as instantaneous and thus overlap at zero time delay in the probe transmission (Schreieck, 2001). Afterward, the gain recovers within the interval required for the probe transmission to rise from 10% to 90% of the asymptotically approached maximum level. This recovery occurs according to the following separate processes. More specifically, in the first hundred femtoseconds timescale after the lowest compressed gain point SHB becomes the dominant nonlinear effect. Then CH takes over for a timescale of ~1 ps, which reestablishes the Fermi carrier distribution in the two energy bands. In the last time regime, the interband effects become pronounced and lead to slow gain compression defined by the unsaturated probe level, which is restored due to the applied electrical pumping, divided by the long-lasting probe transmission level (Occhi, 2002).

The impact of different SOA and signal operating conditions on the aforementioned gain dynamics has been investigated and assessed through experimental observations and numerical simulations. From the interpretation and analysis of the results obtained from both approaches, the following conclusions have been drawn (Occhi, 2002):

1. Both total and slow gain compression increase with the pump energy. For the total gain compression, this happens because the lattice temperature in the active region is elevated with higher pump energy. For the slow gain compression on the other hand, this variation is attributed to the reduction of the free carrier density as a by-product of the increased stimulated emission. Moreover, when the pulse energy is increased, it takes longer time for the gain compression associated with the intraband effects to recover.
2. The magnitudes of the two defined types of gain compression are affected differently by the width of the pump pulses. More specifically, the narrower the pump pulses, the larger the compression associated with the intraband effects. In contrast, the slow gain compression becomes smaller, even for input pulse energies higher than the SOA input saturation energy, for which the SOA gain is dropped by 3 dB against the small-signal gain. However, this is not possible for wider pulses, for example in the 100 ps range, since then the slow gain compression is much larger due to the much higher contribution of the interband effects to the SOA saturation.
3. Both gain compressions increase with current density because of the corresponding increase in gain. However, the fast gain recovery time behaves differently from the recovery time resulting from interband mechanisms. In fact, the former becomes longer for higher bias currents, while the latter is decreased.
4. The total gain compression is practically the same for all investigated device lengths in the case of an input energy equal to the SOA input saturation energy. The increase of the input energy beyond this point causes a larger gain reduction in longer SOAs, since their gain is higher compared to the shorter ones, and accordingly results in higher total gain compression. On the contrary, the fast gain recovery time is not influenced by the SOA longitudinal dimension. This finding does not hold too for the recovery time associated with the interband dynamics, since it decreases appreciably with the increase of the SOA length (Girardin et al., 1998).

25.3 SOA Model Formulation

Many theoretical treatments have been conducted aiming at explaining the operation, understanding the dynamics, predicting the behavior, evaluating the performance, and optimizing the working conditions of SOAs. For this purpose, both analytical and numerical models of different complexity level have been formulated. The more elaborate ones provide a thorough insight into what happens inside the SOA. This is done by microscopically describing the propagation of optical pulses and the change of the SOA carrier

dynamics due to interaction with light. This approach provides extensive information at the expense of increased hardware and software resources. On the other hand, it is also practically desirable to maintain a good balance between mathematics and computer power. This can be achieved by viewing and treating the physical processes that manifest within an SOA from a phenomenological perspective (Toptchiyski, 2002).

The theoretical description of the operation of an SOA that is driven by a strong, ultrafast data pulse stream should be as realistic as possible while simultaneously being characterized by versatility and computational efficiency. In this effort, it is necessary to set the valid framework within which this task will be accomplished, which is based on the following key points. First, for SOA applications in which the employed pulse widths are below the critical value of 10 ps the influence of the intraband carrier processes on nonlinear gain compression is significant and must be included in the description of the SOA saturation under pulsed operation (Borri et al., 1999). Moreover, of the possible relevant phenomena, the effect of TPA can be disregarded because it becomes significant for pulses that are hundreds of femtoseconds wide and have energy larger than 1 pJ (Tang and Shore, 1998). In fact, in most cases of interest the width and energy of pulses launched into an SOA >0.1 ps and <1 pJ, respectively. For this reason, the main effects whose contribution is taken into account are CH and SHB. Second, the SOA small-signal gain, internal loss, and saturation energy are treated as wavelength independent parameters, since usually the spectral width of picosecond optical pulses is at least two orders of magnitude smaller than the gain bandwidth (Ning et al., 1997). The wavelength dependence of these SOA parameters must be taken into account when SOAs are employed for multichannel amplification (Jennen et al., 2001) or for nonlinear optical signal processing purposes, where more than one signal propagates and/or interacts within the active medium (Gutiérrez-Castrejón et al., 2000). The modeling approach that is usually adopted in this case is to approximate the spectral profile of the material gain coefficient per unit length with a parabolic function of wavelength, where the peak of the latter is a linear function of the carrier density (O'Mahony, 1988). The scope of this chapter, however, concerns single signal amplification and SOA linear applications, so high-order polynomial approximations of the gain spectrum would only increase the complexity of SOA modeling without offering essential information for the SOA performance. In addition to this reasoning, the central wavelength of the input signal launched into the SOA is assumed to be set at the peak of the SOA gain spectrum (in the vicinity of 1550 nm), which renders the modal gain (defined in Equation 25.2) independent of the wavelength. Third, the gain and group-velocity dispersion are neglected for pulse widths in the picosecond range and SOAs that are several hundreds of micrometers long (Agrawal and Olsson, 1989a; Tang and Shore, 1998). Fourth, the polarization of the input light is linear and preserved during propagation through the SOA, which is treated as a polarization independent element since the polarization sensitivity of practical devices is below 0.5 dB (Morito et al., 2003). Fifth, the residual facet reflectivities are practically negligible and cannot cause gain ripples, as enabled by the relevant technological evolution in the design and fabrication of SOAs devices (Zimmerman and Spiekman, 2004). Sixth, the SOA has the form of a traveling wave amplifier whose active region dimensions allow the support of only a single wave-guide, while it behaves as an isotropic device, which means that the susceptibility tensor is scalar (Gutiérrez-Castrejón et al., 2000).

The SOA response to an optical beam of electrical field $\vec{\mathrm{E}}$ that propagates along the SOA largest dimension (that is, its length), which defines the z-axis in a Cartesian system of coordinates, is described by the carrier density rate equation (Tang and Shore, 1998)

$$\frac{\partial N}{\partial \tau} = \frac{I}{qV} - \frac{N}{\tau_{\text{carrier}}} - \frac{1}{\Gamma \sigma \hbar \omega} \frac{g \left|\vec{\mathrm{E}}\right|^2}{1 + \varepsilon \left|\vec{\mathrm{E}}\right|^2}, \tag{25.1}$$

where $N = N(z, \tau)$ is the carrier density, I is the injection current, q is the electron charge, $V = wdL$ is the volume of the active region whose characteristic geometries have a cross section (wd) of the order of 1 μm^2 and a length (L) of 0.5 to 2 mm, τ_{carrier} is the carrier lifetime that is linked to the total recombination rate of carriers as specified in Gutiérrez-Castrejón and Duelk (2007), Γ is the confinement factor that accounts

for the transverse character of the optical waves and the spread of the optical mode outside the active region of the amplifier (Agrawal and Olsson, 1989a), σ is the mode cross section ($= wd/\Gamma$), $\hbar$ is the reduced Planck's constant, ω is the angular frequency of the electromagnetic radiation, and ε is the gain compression factor, described right below in Equation 25.13. The parameter $g = g(z, \tau)$ stands for the modal gain that is assumed to vary linearly with N as

$$g = \Gamma a_N \left(N - N_{\text{tr}}\right), \tag{25.2}$$

where a_N is the SOA differential gain and N_{tr} is the carrier density at transparency. Since, from Equation 25.2, $N = g/\Gamma a_N + N_{\text{tr}}$, Equation 25.1 can be transformed, after some algebraic manipulations, into the following gain equation

$$\frac{\partial g}{\partial \tau} = \frac{g_{\text{ss}} - g}{\tau_{\text{carrier}}} - \frac{g\left|\vec{\text{E}}\right|^2}{U_{\text{sat}}\left(1 + \varepsilon\left|\vec{\text{E}}\right|^2\right)}, \tag{25.3}$$

where $g_{\text{ss}} = \Gamma a_N N_{tr}(I/I_{tr} - 1) = \frac{\ln(G_{\text{ss}})}{L}$ is the coefficient of the nominal SOA small-signal power gain, G_{ss}, per unit length, $I_{\text{tr}} = qVN_{\text{tr}}/\tau_{\text{carrier}}$ is the injected current required for transparency, and $U_{\text{sat}} = \hbar\omega\sigma/a_N$ is the SOA intrinsic saturation energy, which for typical values $d = 250$ nm, $w = 2$ μm, $\Gamma = 0.48$ and $a_N = 3.3 \times 10^{-20}$ m^2 at an operating wavelength $\lambda = 1550$ nm is approximately 1 pJ. Alternatively, $U_{\text{sat}} = P_{\text{sat}}\tau_{\text{carrier}}$, where P_{sat} is the saturation power of the SOA material, which in steady-state operation mode is approximately 0.7 times the SOA output saturation power (Connelly, 2002).

The dynamical evolution of an input light whose polarization is linear and maintained as it traverses the SOA obeys Maxwell's wave equation

$$\nabla^2\vec{\text{E}} - \frac{1}{c^2}\left(n_b^2 + \chi\right)\frac{\partial^2\vec{\text{E}}}{\partial\tau^2} = 0 \tag{25.4}$$

where c is the speed of light in vacuum, and $n_{\text{b}}^2 \approx 1 + \mathfrak{R}\left\{\chi_0\right\}$ is the background refractive index, with $\mathfrak{R}\left\{\chi_0\right\}$ denoting the real part of the medium susceptibility in the absence of external pumping by current injection so that it accounts for material absorption (Schubert, 2004), while

$$\chi = -\frac{\bar{n}\,c}{\omega\Gamma}g\left(\frac{\imath}{1 + \varepsilon\left|\vec{\text{E}}\right|^2} + \alpha_{\text{CDP}} + \alpha_{\text{CH}}\frac{\varepsilon\left|\vec{\text{E}}\right|^2}{1 + \varepsilon\left|\vec{\text{E}}\right|^2}\right) \tag{25.5}$$

is the susceptibility parameter (Gutiérrez-Castrejón et al., 2000), which represents the contribution of the charge carriers inside the active region, where $\bar{n}$ is the effective mode index, $\imath = \sqrt{-1}$ is the imaginary number, and the parameters α_{CDP} and α_{CH} are described below in Equation 25.22.

The electrical field of the linearly polarized light that is inserted in the SOA and propagates along its longitudinal axis, z, is $E(x, y, z, \tau) = \hat{x}\frac{1}{2}\text{F}(x, y)\text{A}(z, \tau)\exp\left[\imath(\beta z - \omega\tau)\right]$, where $\hat{x}$ is the polarization unit vector, $\text{F}(x, y)$ is the transverse mode distribution, $A(z, \tau)$ is the complex envelope of the optical pulse and $\beta = \bar{n}\omega/c$ represents the propagation constant. According to the procedure in Tang and Shore (1998) and Gutiérrez-Castrejón et al. (2000), which is based on the slowly varying envelope approximation and the integration over the transverse dimensions, an equation that describes the propagation of the optical pulse in the SOA can be obtained from Equations 25.4 and 25.5

$$\frac{\partial\text{A}(z, \tau)}{\partial z} + \frac{1}{\upsilon_{\text{SOA}}}\frac{\partial\text{A}(z, \tau)}{\partial\tau} = \frac{1}{2}\frac{g\text{A}(z,\ \tau)}{1 + \varepsilon\left|\text{A}\right|^2} - \frac{\imath}{2}\left[\alpha_{\text{CDP}}g - \alpha_{\text{CH}}\frac{\varepsilon g\left|\text{A}\right|^2}{1 + \varepsilon\left|\text{A}\right|^2}\right]\text{A}(z, \tau). \tag{25.6}$$

This equation has actually been derived from semiclassical density-matrix equations by adiabatical approximation of the interband polarization dynamics (Mørk and Mecozzi, 1996).

The time measured in a static reference (laboratory) coordinate system, τ, is transformed into the local time t measured in a reference frame moving with the pulse at the group velocity inside the amplifier, υ_{SOA}:

$$t = \tau - \frac{z}{\upsilon_{SOA}}. \tag{25.7}$$

Thus, in this moving coordinate system, the pulse is centered on $t = 0$ at every plane along the amplifier. According to Equation 25.7, the transformation of a general function $f(z, \tau)$ to $f(z, t)$ leads to the following expressions for the time and spatial derivatives (Jennen et al., 2001):

$$\frac{\partial f(z,\tau)}{\partial \tau} = \frac{\partial f(z,t)}{\partial t} \cdot \frac{\partial t}{\partial \tau} = \frac{\partial f(z,t)}{\partial t} \tag{25.8}$$

$$\frac{\partial f(z,\tau)}{\partial z} = \frac{\partial f(z,t)}{\partial z} + \frac{\partial f(z,t)}{\partial t} \cdot \frac{\partial t}{\partial z} = \frac{\partial f(z,t)}{\partial z} - \frac{1}{\upsilon_{SOA}} \cdot \frac{\partial f(z,t)}{\partial t}. \tag{25.9}$$

Separating further "A" into amplitude and phase terms,

$$A = \sqrt{\text{Const} \times P}\exp(\iota\varphi) \Rightarrow P = |A|^2 \Big/ \text{Const}. \tag{25.10}$$

"Const" is a normalization coefficient that relates the units between amplitude and power so that $A(z, t)$ is expressed in units of $W^{1/2}$, while $P = P(z, t)$ and $\varphi = \varphi(z, t)$ are the power and the phase of the traveling optical pulse, respectively. Applying Equations 25.8 and 25.9 together in Equation 25.6 and replacing in Equations 25.3 and 25.6 the squared modulus of the total electrical field, $|\vec{A}|^2 = \vec{E} \cdot \vec{E}^* = |A|^2$, where the symbol $*$ denotes the complex conjugate, the following set of partial coupled differential equations that govern the power, P, gain, g, and phase, φ, evolution of a strong optical signal that propagates and is amplified in an SOA is obtained (Tang and Shore, 1998)

$$\frac{\partial P(z,t)}{\partial z} = \frac{g(z,t)}{1 + \varepsilon P(z,t)} P(z,t) \tag{25.11}$$

$$\frac{\partial g(z,t)}{\partial t} = \frac{g_{ss} - g(z,t)}{\tau_{carrier}} - \frac{g(z,t)}{1 + \varepsilon P(z,t)} \frac{P(z,t)}{U_{sat}} \tag{25.12}$$

$$\frac{\partial \varphi(z,t)}{\partial z} = -\frac{1}{2}\left[\alpha_{CDP} g(z,t) - \alpha_{CH} \frac{\varepsilon g(z,t) P(z,t)}{1 + \varepsilon P(z,t)}\right] \tag{25.13}$$

The term $\varepsilon = \varepsilon_{CH} + \varepsilon_{SHB}$ combines the contribution to the SOA gain compression from CH and SHB when these two effects are considered instantaneous. This assumption holds when the width of the launched optical pulses exceeds 1 ps, and is therefore valid under most practical situations encountered in optical communications. In this case, the impact of CH and SHB on the gain compression is taken into account through the term $1 + \varepsilon P$, where the factor εP is connected to a stationary carrier density above transparency, at which the SOA gain is unity and hence leaves intact a signal that passes through (Occhi, 2002; Wang, 2008).

Equations 25.11 and 25.12 form a system with unknowns the power and gain of the signal that perturbs the SOA nonlinear optical properties. This system cannot be solved in closed form, but only numerically. For this purpose, and in order to account for the spatial and temporal dependence denoted by the variables (z, t), L is divided into discrete segments, each of length $\Delta z = \frac{L}{m}$, as shown in Figure 25.4, while the pulses are sliced over their period, τ_{period}, at uniform intervals $\Delta t = \frac{\tau_{period}}{k}$, where k is a non-zero integer so that their profile can be reconstructed at the output. Now, since the driving signal propagates through one amplifier segment during the sampling time, the space and time infinitesimal elements are linked to each

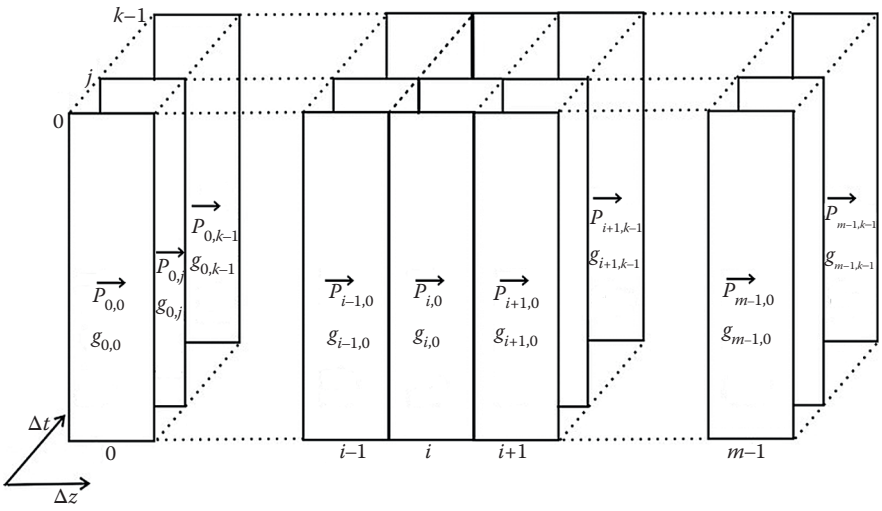

FIGURE 25.4 Dividing the SOA into discrete longitudinal (i) sections and calculating in each one of them the value of the signal power (P) and gain (g) for each sample of the pulse (j) based on the knowledge of the preceding value. This stepwise process is repeated in the formed spatio-temporal grid in an iterative manner until all required values are calculated.

other through $\Delta z = \upsilon_{\mathrm{SOA}} \Delta t$ (Toptchiyski, 2002). The direct expansion gives

$$\Delta t = \frac{\Delta z}{\upsilon_{\mathrm{SOA}}} = \frac{L}{m \cdot \upsilon_{\mathrm{SOA}}} = \frac{\tau_{\mathrm{transit}}}{m} = \frac{\tau_{\mathrm{period}}}{k} \Rightarrow \frac{k}{m} = \frac{\tau_{\mathrm{period}}}{\tau_{\mathrm{transit}}}, \tag{25.14}$$

which means that the number k cannot be chosen independently from m. For example, if $\tau_{\mathrm{period}} = 100$ ps and $\tau_{\mathrm{transit}} = \frac{L}{\upsilon_{\mathrm{SOA}}} = 12$ ps, the specific ratio equals 100:12. This means that the combination of k and m, or their selection, in order to satisfy this requirement, is not unique. Still, this task can be facilitated by taking into account that the number of the longitudinal sections must be larger than 10 (Wong and Blow, 2003). Otherwise, the SOA gain dynamics induced by the input lightwave signal are erroneously quantified. Thus, if $m = 120$, which is a more than sufficient value, then $k = 1000$. This pair allows obtaining a fairly accurate solution of the above equations with the use of simple first-order Euler differentiation. The latter is an efficient arithmetic method when studying in the time domain the nonlinear interactions between picosecond optical pulses whose envelope has a piecewise varying nature, as is the case for a Gaussian shape, and semiconductor active waveguide devices, provided that the sampling rate is high enough (Chi et al., 2001). More precisely, for each discrete space, i, and time section, j, the solution is expressed by

$$P_{\mathrm{i+1},j} = P_{i,j} + \Delta z \frac{\mathrm{d}P}{\mathrm{d}z}\Big|_{i,j}, \quad \text{for} \quad i = 0, 1, 2, \ldots, m-1 \quad \text{and} \quad j = 0, 1, 2, \ldots, k-1 \tag{25.15}$$

$$g_{i,j+1} = g_{i,j} + \Delta t \frac{\mathrm{d}g}{\mathrm{d}t}\Big|_{i,j}, \quad \text{for} \quad i = 0, 1, 2, \ldots, m-1 \quad \text{and} \quad j = 0, 1, 2, \ldots, k-1. \tag{25.16}$$

In other words, for an incoming signal traveling in the longitudinal direction measured from the left facet of the SOA, the knowledge of the values of $P(z, t)$ and $g(z, t)$ as well as of their derivatives (denoted by $|_{i,j}$) at a given step (i, j) of the algorithm, together with the fact that Equations 25.11 and 25.12 are essentially coupled in terms of the power and gain, allows us to calculate the next values $P(z + \Delta z, t)$ and $g(z, t + \Delta t)$ required at steps $(i + 1, j)$ and $(i, j + 1)$, respectively. This process is depicted in Figure 25.4 and is repeated

in an iterative manner until all values are calculated in the spatio-temporal grid $i\,(\Delta z)\times j\,(\Delta t)$. For this purpose, it is necessary to define and apply the appropriate boundary and initial conditions. The setting of the boundary condition is straightforward since the profile of the launched optical power is expressed in analytical form depending on the particular pulse data format and shape. For example, for a return-to-zero on-off keying signal, the power of each temporal sample at the SOA input facet is given by (Pauer et al., 2001) $P_{0,j} = P(t) = \sum_n \{C_n\}\, p\,(j\Delta t - n\tau_{\text{period}})$, where n is the number of bits contained in the data sequence length, the code $\{C_n\}$ is either "1" or "0" with equal probability ½, and $p(t)$ is the pulse shape. For Gaussian pulses (Agrawal and Olsson, 1989a), for example, $p(t) = P_{\text{peak}} \exp\left[-4\ln 2(t - \tau_{\text{period}}/2)^2/\tau_{\text{FWHM}}^2\right]$, where P_{peak} is the peak power and τ_{FWHM} is the full-width at half-maximum (FWHM), which occupies some fraction of the operating period that defines the duty cycle (Pauer et al., 2001). The setting of the initial condition, on the other hand, is more elaborate, since it requires considering the flow of the SOA gain dynamics change by the continuously arriving optical pulses (Tang et al., 2000). More specifically, in each distance segment of the SOA, the first temporal segment in the leading edge of the first arriving pulse experiences an unsaturated, small-signal gain, so that $g_{i,0}\,|_1 = g_{\text{ss}}$. Then, by induction, in each distance segment, the first temporal segment in the leading edge of the following pulse, which reaches the SOA after τ_{period}, sees an initial, recovered gain given by $g_{i,0}\,|_n = g_{\text{ss}} + \left(g_{i,k-1}\,|_{n-1} - g_{\text{ss}}\right) \exp\left(-\frac{\tau_{\text{period}}}{\tau_{\text{carrier}}}\right)$, where $g_{i,k-1}\,|_{n-1}$ is the gain perturbed by the last temporal segment in the trailing edge of the preceding pulse at the same distance segment.

Apart from this arithmetic procedure, other more elaborate techniques can also be employed for numerically solving modified-type nonlinear Schrödinger equations as Equation 25.6, such as the well-known fourth-order Runge-Kutta, or the finite-difference beam propagation method (FDBPM), where the central-difference approximation is applied in the time domain and trapezoidal integration is executed over the spatial section in an iterative manner (Razaghi et al., 2009). This method has enabled us to accurately acquire information for the SOA characteristics, which include the pulse shape, spectrum, and chirp, in the presence of the main ultrafast nonlinear phenomena that critically affect the SOA gain dynamics (Hosseini et al., 2011).

25.4 SOA Model Simplification

The model deployed for simulating the operation of an SOA has been formulated on the basis of the partial coupled differential Equations 25.11 through 25.13. These constitute a system which, due to the existence of the temporal and longitudinal variables, t and z, respectively, is two-dimensional (2D) so that its solution is rather cumbersome from a computational standpoint. However, if the SOA is treated as a "black box" characterized by its impulse response to any arbitrary input optical signal, the dependence on the spatial variable can be dropped and the problem can be reduced to a one-dimensional (1D) one described by an ordinary differential equation in which time is the only independent variable, enabling us to greatly simplify the computational complexity (Cassioli et al., 2000). This reduction is realized starting from the local changes of the carrier density distribution, which occur due to the interaction between the propagating field and the semiconductor material. These changes are the result of the intraband (CH and SHB) and interband (CDP) effects, while nonlinear processes with characteristic times shorter than SHB, such as TPA, are ignored because their effect is comparatively not significant. The gain and the refractive index of the semiconductor depend on these locally perturbed densities, so each local density distribution is associated with a distinct term that contributes to the total gain. The gain then can be expanded to the sum of the respective contributions of the three different physical processes considered. The temporal evolution of the three quantities is described by equal number of rate equations, which in turn depend on the photon density profile and therefore are coupled to the equation that describes the propagation of the field along the waveguide. The key thus for reducing the order of the modeling system to 1D is the integration of both sides of the partial differential equations over the

entire SOA length. This transformation leads to the following compact expression for the total device gain (Cassioli et al., 2000)

$$G(t) = \exp[\mathrm{h}(t)], \tag{25.17}$$

where at each point of the pulse profile, $\mathrm{h}(z,t) = \int_0^z \frac{g(z',t)}{1+\varepsilon P(z',t)} dz'$ represents the power gain integrated over the length of the SOA, which hence is treated as a spatially concentrated device. This dimensionless coefficient incorporates the contribution of each mechanism that affects the SOA gain:

$$\mathrm{h}(t) = \mathrm{h}_{\mathrm{CDP}}(t) + \mathrm{h}_{\mathrm{CH}}(t) + \mathrm{h}_{\mathrm{SHB}}(t). \tag{25.18}$$

More specifically, $\mathrm{h}_{\mathrm{CDP}}$ represents the gain associated with the interband effects and its temporal evolution is described by the following first-order ordinary differential equation

$$\frac{\mathrm{dh}_{\mathrm{CDP}}}{\mathrm{d}t} = -\frac{\mathrm{h}_{\mathrm{CDP}}}{\tau_{\mathrm{carrier}}} - \frac{1}{P_{\mathrm{sat}}\tau_{\mathrm{carrier}}}[G(t)-1]P(t) + \frac{\ln G_{\mathrm{ss}}}{\tau_{\mathrm{carrier}}}. \tag{25.19}$$

h_{CH} is the gain associated with CH, which means that it describes the gain variation due to the mechanisms that heat up the carrier distribution in the conduction band, such as FCA and TPA, as well as due to changes of the carrier density. The relevant rate equation has the form

$$\frac{\mathrm{dh}_{\mathrm{CH}}}{\mathrm{d}t} = -\frac{\mathrm{h}_{\mathrm{CH}}}{\tau_{\mathrm{CH}}} - \frac{\varepsilon_{\mathrm{CH}}}{\tau_{\mathrm{CH}}}[G(t)-1]P(t) \tag{25.20}$$

where $\varepsilon_{\mathrm{CH}}$ is the CH nonlinear gain compression factor. The first term on the right-hand side characterizes the relaxation to the lattice temperature once the exciting pulse has left the SOA and before the arrival of the next pulse. The second term combines all the effects that heat-up the carrier distribution. The typical values of τ_{CH} for InGaAsP/InP-based SOAs with gain peak around 1.55 μm lie between 0.5 and 1 ps, while $\varepsilon_{\mathrm{CH}}$ is between 0.28×10^{-23} and 4.4×10^{-23} m^3 (Occhi, 2002).

Finally, the rate equation for the SHB contribution is

$$\frac{\mathrm{dh}_{\mathrm{SHB}}}{\mathrm{d}t} = -\frac{\mathrm{h}_{\mathrm{SHB}}}{\tau_{\mathrm{SHB}}} - \frac{\varepsilon_{\mathrm{SHB}}}{\tau_{\mathrm{SHB}}}[G(t)-1]P(t) - \frac{\mathrm{dh}_{\mathrm{CH}}}{\mathrm{d}t} - \frac{\mathrm{dh}_{\mathrm{CDP}}}{\mathrm{d}t}, \tag{25.21}$$

where $\varepsilon_{\mathrm{SHB}}$ is the SHB nonlinear gain compression factor. Reported values of τ_{SHB} in the conduction band for InGaAsP/InP-based SOAs with maximum gain centered around 1.55 μm are between 30 and 250 fs, while $\varepsilon_{\mathrm{SHB}}$ has been found to be between 0.14×10^{-23} and 1.7×10^{-23} m^3 (Occhi, 2002).

The above dynamic processes affect not only the gain properties but also the refractive index of the SOA within the active region (Wiesenfeld, 1996). This happens because the free carriers contribute substantially to the SOA optical susceptibility, which is complex in nature. The imaginary part of this parameter is related to the gain of the SOA, and the real part is related to the refractive index (Eiselt et al., 1995). The gain and refractive index variations are not independent but coupled via the Kramers–Kronig relationship, according to which the refractive index modulation can be calculated from the gain variation (Hutchings et al., 1992). However, this calculation requires us to integrate over the whole wavelength spectrum the gain coefficient, which means that the latter must be known for a wide range of optical frequencies. Furthermore, the specific integral must be solved numerically, which increases the model computational time significantly. A more convenient manner to describe the refractive index behavior relies on the alpha factor, also known as the Henry factor (Henry, 1982), which links the changes of the active layer refractive index to those of the gain when the carrier density is varied. The important benefit offered by the employment of this factor is that the refractive index dynamics are given directly by the gain dynamics

and hence are quantified much faster than with the Kramers–Kronig relations. Moreover, the adoption of the alpha-factor approach is practically realizable since it links the gain and the phase variations associated with the changes of the refractive index, where both are directly measurable. The phase of the optical field at the SOA output can be expressed as a linear function of the same variables which describe the optical gain:

$$\varphi(t) = -0.5\,[\alpha_{CDP} h_{CDP}(t) + \alpha_{CH}\, h_{CH}(t) + \alpha_{SHB}\, h_{SHB}(t)], \tag{25.22}$$

where α_{CDP} , α_{CH}, and α_{SHB} are the phase-amplitude coupling coefficients of CDP, CH, and SHB, respectively. Among these alpha factors, α_{CDP} is the traditional linewidth enhancement factor related to CDP, with typical values 3–12 (Agrawal and Olsson, 1989a). α_{CH} is the alpha factor associated with CH and varies especially near the band edge, where the depletion of cooler carriers takes place (Giller et al., 2006). However, usually signal photon energies influence carriers well inside the band and so, α_{CH} can be approximated by a constant with indicative values ranging between 1 and 4.5, as reported in the literature. Finally, α_{SHB} is the alpha factor linked to SHB and is nearly zero because SHB happens symmetrically around the central wavelength (Mecozzi and Mørk, 1997). Thus, the Kramers–Krönig integral over the whole spectrum is nearly zero and the change of the refractive index is very small near the peak wavelength.

Every phase variation at the SOA output is always accompanied by a certain amount of chirp (Agrawal and Olsson, 1989a). This is the instantaneous frequency deviation relative to the optical beam frequency, $\Delta\nu$, which is provoked because the phase, φ, of the amplified signal is not constant in time. Mathematically, it is given by

$$\Delta\nu(t) = -\frac{1}{2\pi}\frac{\partial\varphi}{\partial t}. \tag{25.23}$$

The set of rate Equations 25.19 through 25.21 for the h_j (j = CDP, CH, SHB) functions is numerically solved for a given optical power to the SOA input, $P(t)$, which is the only excitation of the system. Then, Equations 25.17, 25.22 and 25.23 give the overall power gain, phase variation, and chirp that the input signal experiences through the SOA, respectively. In this manner, results have been obtained for the temporal, spectral, and chirp profile of the amplified pulses (Hussain et al., 2010).

Equations 25.11 through 25.13 can be further combined and reduced for optical pulses going into the SOA, whose width exceeds the critical limit of 10 ps, above which the influence of the CH and the SHB effects is not significant (Borri et al., 1999). This means that in this case it is not necessary to take into account these intraband processes. Then, by following the algebraic steps detailed in Mecozzi and Mørk (1997), but setting, ε to null and $h_{CDP} \equiv h(t)$, the differential equation for the SOA response is simplified to the well-known form that holds when the SOA gain saturation is caused only by the depletion of the carrier density due to stimulated emission (Agrawal and Olsson, 1989a)

$$\frac{dh(t)}{dt} = \frac{\ln(G_{ss}) - h(t)}{\tau_{carrier}} - \frac{P(t)}{U_{sat}}\left\{\exp\left[h(t)\right] - 1\right\}. \tag{25.24}$$

This equation can be solved analytically, provided that the width of the launched optical pulses is much shorter than the SOA carrier lifetime. This condition holds in practice, since in real SOA devices, the values of the latter parameter are typically of the order of 100 ps and above. Thus, closed-form expressions can be obtained for the variation of the SOA gain in the rapid saturation and slow recovery regions. These expressions allow us to explicitly describe the pulse profile at the SOA output when this element is driven by multiple pulses of alternating binary content, as it happens in real optical networks that are based on optical time division multiplexing (OTDM) (Hamilton et al., 2002).

25.5 SOA Optical Gain Modulation

The influence of critical parameters, which include the SOA small-signal gain and carrier lifetime as well as the FWHM and energy of the input pulses, on the SOA output characteristics has been investigated and evaluated for the case where the change of the SOA gain dynamics is provoked by a 10-Gb/s data-modulated signal onto itself in the context of straightforward amplification (Zoiros et al., 2007). The results reveal that due to the continuous arrival of pulses, which cause the SOA saturation properties to be more strongly modified than for a single pulse, the requirements for the SOA small-signal gain and the input pulse energy are more stringent than those for the isolated pulse amplification studied elsewhere (Agrawal and Olsson, 1989a), while those for the FWHM and carrier lifetime are also tight but to a lesser extent. For example, Figure 25.5 shows that the SOA small-signal gain must be an order of magnitude lower than that for a single pulse or else the output pulse deviates from its normal symmetrical form (Zoiros et al., 2007). Moreover, Figure 25.6 shows that the pulse energy, U_{in}, must be a small fraction of the SOA saturation energy, U_{sat} (Zoiros et al., 2007). These trends together suggest that the SOA must be biased to operate in the low-saturation regime in order to preserve the shape of the input signal at the SOA exit. This condition essentially determines the dynamic range of the inserted optical signal, which is allowed for distortionless pulse amplification, and its validity is further supported by evidence given in Section 25.6. In contrast, when the focus is on the chirp and how it can be tailored in order to be exploited for pulse compression (Agrawal and Olsson, 1989b; Zoiros et al., 2005), the investigation that was conducted reveals that the

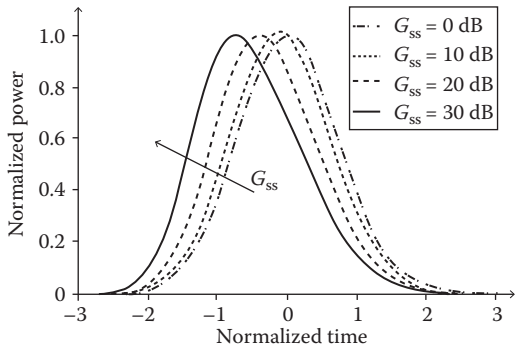

FIGURE 25.5 Shape of amplified pulses versus SOA small-signal gain, G_{ss}. The arrow indicates the G_{ss} direction of increase.

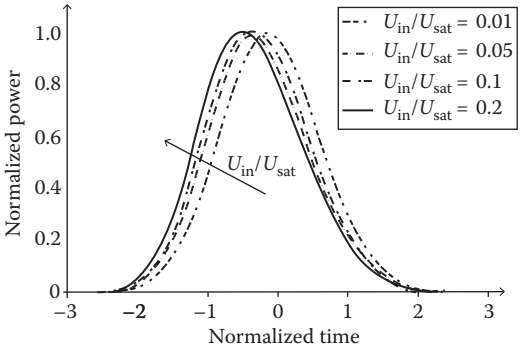

FIGURE 25.6 Shape of amplified pulses versus input pulse energy U_{in}, normalized to SOA saturation energy U_{sat}. The arrow indicates the U_{in}/U_{sat} direction of increase.

SOA small-signal gain and the energy of the incoming pulses must be increased to such extent so that together they heavily saturate the SOA. Then, the reduction of the instantaneous phase shift (Ueno et al., 2002) and of the accompanying chirp due to the alternating bit pulses and the concomitant inability of the SOA to timely recover between them can be efficiently mitigated. In this case, the chirp acquires the form shown in Figure 25.7, which is the required one for the intended purpose (Agrawal and Olsson, 1989a; Zoiros et al., 2007). In fact, the linearly increasing part of the chirp curve in the time domain is situated in the center of the pulse where most of its power is contained, while the chirp magnitude is sufficiently enhanced. Therefore, if the SOA is operated according to these conditions, then it can be ensured that the amplified optical pulses exhibit an appropriate power and chirp profile.

On the other hand, if the FWHM is such that its difference from the pulses repetition interval is smaller than the SOA gain recovery time, then the strain imposed on the SOA gain dynamics is heavier. This happens because the SOA responds more slowly to the rapidly varying logical content of the wider pulses, which worsens the pattern effect described in the next section (Kim et al., 2007). In this demanding case, Equation 25.24 must obligatorily be solved by a numerical approach. This can be done in a stepwise manner by sampling the optical pulse over its period at discrete temporal intervals, approximating the time derivative by a finite difference and applying the appropriate initial conditions to account for the different gain at the beginning of each new bit depending on how it has been perturbed during the previous one (Botsiaris et al., 2007). The knowledge then of $h(t)$ allows us to calculate the electric field of the amplified data, $E_{SOA}(t) = E_{data}(t) \exp\left[\frac{1}{2}\left(1 - j\alpha_{CDP}\right) h(t)\right]$, where, according to Equation 25.10, $|E_{SOA}(t)|^2 = P_{SOA}(t)$ and $|E_{data}(t)|^2 = P(t)$ (Agrawal and Olsson, 1989a), as well as the chirp from $\Delta\nu(t) = -(1/4\pi)\left[\alpha_{CDP} dh(t)/dt dt\right]$, where the derivative of $h(t)$ is directly taken from the right-hand of Equation 25.24. With this approach, the changes that are incurred on the amplified pulse trains and eye diagrams for different SOA saturation conditions can be correctly captured, as verified by comparison to experiments. For this purpose, the degree of pattern effect is modified by altering the maximum launched signal power and the SOA small-signal gain. Figure 25.8 depicts the amplified pulse patterns when the peak power of the marks successively drives the SOA into the low, medium, and deep saturation region, respectively. As the input peak power is progressively doubled, the peak amplitude fluctuations become more pronounced to an extent that depends on whether the marks are preceded either by one or more spaces or by other marks (Zoiros et al., 2008). In contrast, as the input peak power is decreased, these variations are smoothed and the associated pattern effect de-escalates. Similarly, when the SOA small-signal gain is halved, the peak amplitudes become less uneven, as illustrated by comparing Figure 25.9 to Figure 25.8c. The accurate reproduction of the form of the pattern effect which manifests on RZ pulses (Zoiros et al., 2009, 2010a,b), together with the good qualitative matching between the left- and right-hand sides of these figures, designates that the experimental trend for the SOA response is properly modeled. This also holds

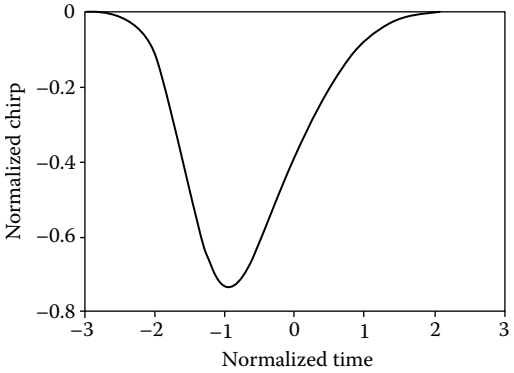

FIGURE 25.7 Profile of SOA output chirp for heavily saturated SOA.

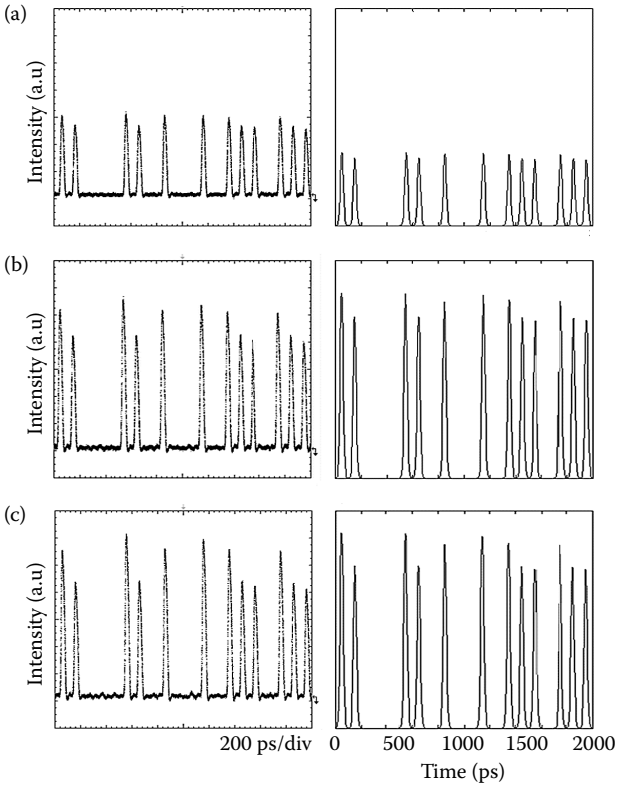

FIGURE 25.8 Experimental (left) and theoretical (right) amplified data pulse trains for (a) low, (b) medium, and (c) deep SOA saturation.

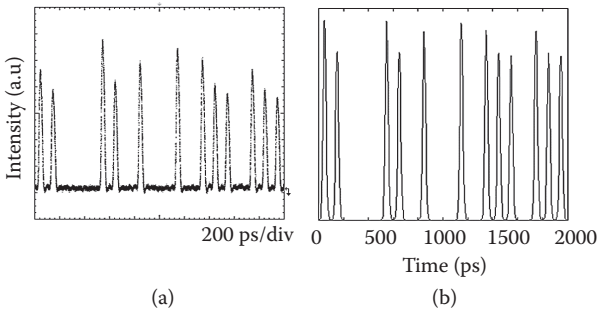

FIGURE 25.9 Experimental (a) and theoretical (b) amplified data pulse trains for halved SOA small-signal gain compared to Figure 25.8(c).

for the respective eye diagrams shown in Figure 25.10. In this case, the asymmetric subenvelopes that occur for a high-input peak power in Figure 25.10c gradually disappear as this parameter is decreased, in Figure 25.10a and b, and the eye diagrams become more uniform, which is an improvement that can be monitored too in the simulated pseudo-eye diagrams obtained as detailed in Gutiérrez-Castrejón et al. (2001).

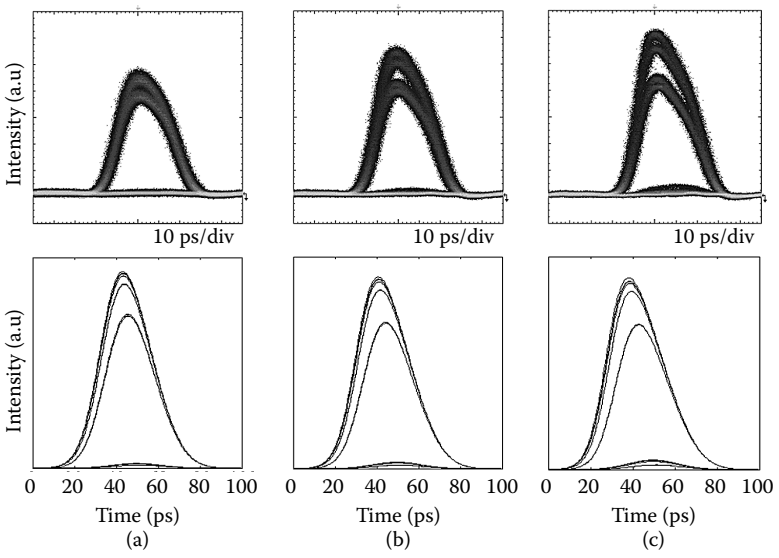

FIGURE 25.10 Experimental (top) and theoretical (bottom) eye diagrams at SOA output for (a) low, (b) medium, and (c) deep SOA saturation.

25.6 Pattern Effect I: Direct Optical Amplification

The distinctive properties of SOAs have revived interest for direct signal amplification purposes, which have traditionally been the primary target of SOAs (Connelly, 2002). As shown in Figure 25.11, the intention is to exploit SOAs as booster amplifiers to enhance the signal power before being launched into an optical link (Kim et al., 2003) as in-line amplifiers to compensate for transmission losses along the link (Boscolo et al., 2006) and as preamplifiers so that the received signal has sufficient power and can be correctly detected (Mynbaev and Scheiner, 2001; Singh, 2011).

In these applications, the profile of the output signal should ideally be an amplified replica of the input signal. In practice, the combination of the power and duration of the input data signal can be such that the SOA is heavily saturated. Concurrently, the SOA gain recovery time is finite with typical values of the order of few hundreds of picoseconds. Thus, in most practical cases, it exceeds the pulses repetition period, which scales inversely with the data rate. Under these driving conditions, the SOA gain is not perturbed in a regular fashion but according to the binary content of each bit slot. As can be schematically seen in Figure 25.12, if the SOA is excited by a train of distinguishable pulses, that is, "1" and "0," whose period, τ_{period}, is such that they arrive faster than the interval available for carrier replenishment, $\tau_{recovery}$, then the gain variation is not uniform since it is dropped for a "1" and partially recovered for a "0" (Manning et al., 1997). This mode of operation has a negative impact on the SOA response, as it can be highlighted by means of the following representative scenarios which concern two "1"s which are separated by a "0." First, in case of a row of marks, the "1" which follows immediately after the "1" that has initially been inserted in the SOA and hence modified its optical properties from a higher level, suffers a reduced gain and this continues to happen for every subsequent "1" with respect to the preceding "1" until an equilibrium is reached or the sequence is broken by a "0." Second, in case of multiple "0"s, which allow the gain to rise substantially, the leading "1" experiences a higher gain than the trailing "1," given that the latter is preceded by only one "0," while it encounters a comparatively lower gain if there are continuous "1"s that prevent the gain from completely recovering. In either case, the amplified output suffers from peak-to-peak amplitude fluctuations, as can characteristically be seen in Figure 25.13.

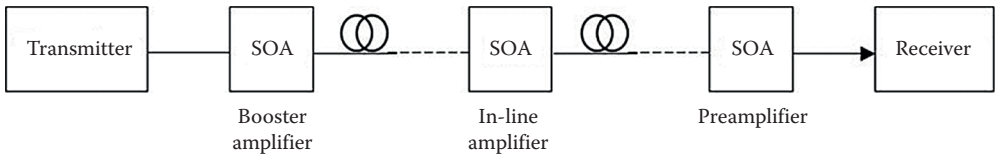

FIGURE 25.11 SOA direct amplification applications.

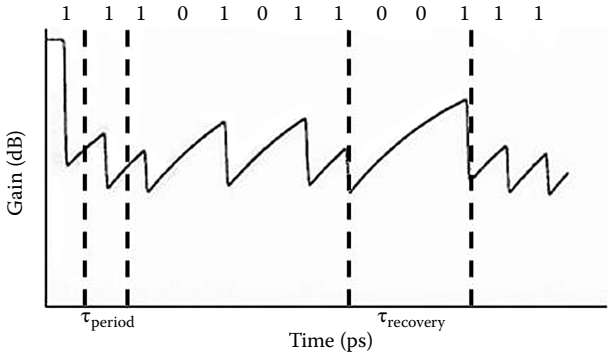

FIGURE 25.12 Evolution of SOA gain in response to data train input.

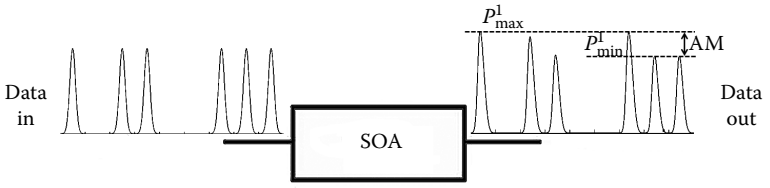

FIGURE 25.13 Data amplification in SOA and pattern-dependent output distortion, with amplitude modulation (AM) definition.

This undesirable phenomenon is called "pattern effect" (Manning et al., 1997) and constitutes a major obstacle in the effort to employ conventional SOAs in their classical role. This happens due to the significant deterioration of several metrics that characterize the quality of the amplified signal, which include the amplitude modulation (AM), the extinction ratio (ER), and the input power dynamic range (IPDR). The AM is defined as AM (dB) $= 10\log\left(P^1_{\max}/P^1_{\min}\right)$, where $P^1_{\max}$ and $P^1_{\min}$ are the maximum and minimum peak power of the marks in the amplified data stream, respectively (Figure 25.13). The AM quantifies the degree of uniformity of the marks and should be as low as possible but it is considered acceptable for lightwave telecommunications systems if it is lower than 1 dB (Zoiros et al., 2008). The ER is defined as $\mathrm{ER}\,(dB) = 10\log\left(P^1_{\mathrm{avg}}/P^0_{\mathrm{avg}}\right)$, where P^1_{avg} and P^0_{avg} are the average power of the marks and spaces in the amplified data stream, respectively (Figure 25.16). The ER quantifies how distinct the marks are from the spaces and it should be as high as possible but it is considered acceptable if it is well over 10 dB (Hinton et al., 2008). Finally, the IPDR is defined as the range where the Q-factor, which in the thermal noise limit, where the amplitude fluctuations due to the pattern effect act as noise variance on the marks, is defined as $Q = P^1_{\mathrm{avg}}/\sigma^1_{\mathrm{std}}$, with σ^1_{std} being the standard deviation of the peak powers of the marks, is over six (Agrawal, 2002). The negative impact of the SOA pattern effect on these metrics has been investigated and evaluated and the main outcome is compiled and presented in the following in Figures 25.14 and 25.15 (Rizou et al., 2015a). In Figure 25.14, the SOA output suffers from intense peak amplitude fluctuations

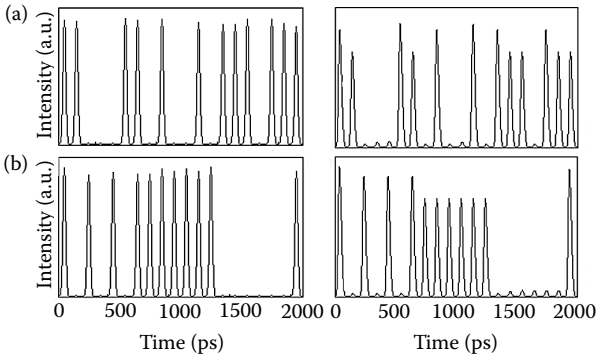

FIGURE 25.14 (a) SOA input data pattern with initial AM = 0.35 dB (left) and corresponding output (right). (b) SOA input data pattern which contains a string of consecutive "0"s (left) and corresponding output (right).

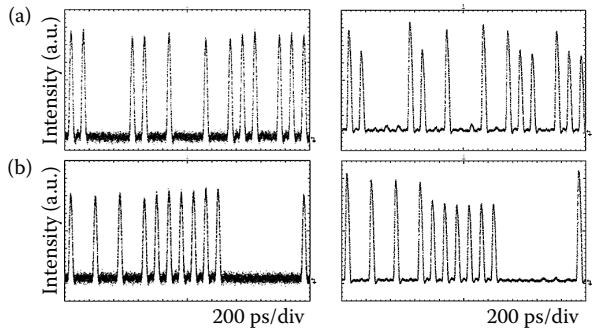

FIGURE 25.15 Corresponding experimental patterns of Figure 25.14.

both when the framed input data waveform has an initial AM = 0.35 dB (Figure 25.14a, left) or contains a string of consecutive "0"s (Figure 25.14b, left). In both cases, the AM level at the SOA exit is intolerable, as it amounts to AM = 1.3 dB (Figure 25.14, right). This behavior is comparable to the experimental one in Figure 25.15 with regard to pulse profile and amplitude wandering. Moreover, in Figure 25.16, the eye diagram at the SOA output is degenerated into secondary traces whose borders deviate from the principal one both in magnitude and shape, while the baseline defined by the spaces is less than 11 dB away from the average level of the marks (Rizou et al., 2013).

In Figure 25.17, on the other hand, the part of the chirp at the SOA output which is negative at the leading edge of each mark, that is, 'red chirp' (Agrawal and Olsson, 1989a), suffers from strong peak-to-peak excursions similar to those observed at the corresponding pulse positions, while the part of the chirp which is positive at the trailing edge of each mark, that is, 'blue chirp', exhibits a much weaker dependence than its red chirp counterpart. Physically, this happens because the red chirp is related to carrier depletion and gain compression, while the blue chirp is linked to carrier regeneration and gain recovery (Girault et al., 2008). This means that the magnitude of the induced chirp is proportional to the rate of change of the carrier concentration and subsequently of the gain. For this reason, it would be rationally expectable that the pattern effect due to the irregular gain variation would be imposed on both types of chirp. However, as can be seen in Figure 25.17, this holds almost exclusively for the red chirp, which exhibits strong peak fluctuations. For the blue chirp, in contrast, an increase in the peaks occurs only for successive "1"s, since then the carrier recombination rate is enhanced due to the weaker carrier depletion, but still this increase is so small that it is hardly noticed. This pronounced discrepancy in the pattern dependence is attributed to

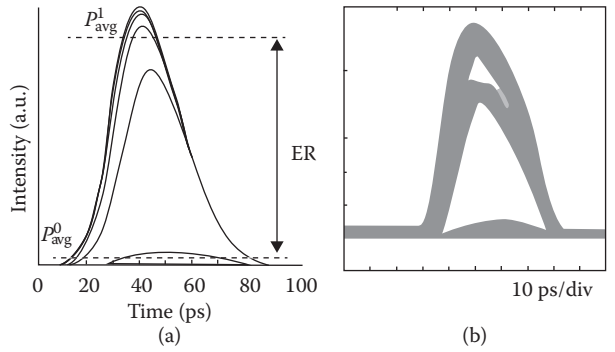

FIGURE 25.16 Theoretical (a) and experimental (b) eye diagrams at SOA output, with extinction ratio (ER) definition.

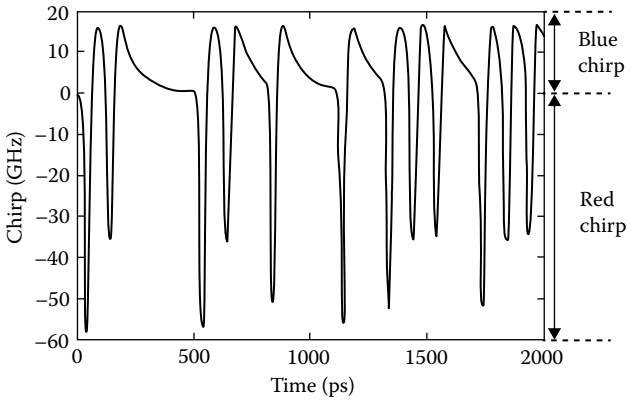

FIGURE 25.17 Chirp variation at SOA output.

the different timescale on which the two chirp phenomena take place. In fact, the carrier depletion and the accompanying phase increase in the leading edge of the pulse is somewhat faster compared to the much slower carrier replenishment and the concomitant phase decrease in its trailing edge, which gives rise to an approximately constant amount of blue chirp. Therefore, the explanation of the pattern effect can also be given in the frequency domain through the red chirp. For this purpose, its form in Figure 25.17 is correlated (Wang et al., 2007) with the corresponding gain change in Figure 25.18.

More specifically, the rising edge of the first "1" at the left-most edge of the pattern window acquires the largest red chirp among all the marks owing to the fact that, for the same energy, its gain is dropped from the maximum possible level, that is, that of the unsaturated state, and as a by-product the incurred gain difference is highest. Similarly, the next largest peak is that of the third "1," since it is preceded by a run of three "0"s. In contrast, the lower the carrier density, or equivalently the greater the extent of gain compression, the slower the additional carriers are depleted, thereby resulting in decreased gain variation and accordingly less red chirp, as it is the case for consecutive "1"s where the SOA cannot fully recover in between them. Finally, in Figure 25.19, the Q-factor is permissible only in saturation region A, where the SOA gain (inset) is reduced up to just 3 dB (Rizou et al., 2013). Thus, the IPDR cannot be extended to regions B and C, since the SOA pattern effect is aggravated as the gain is decreased by more than 3 and 6 dB, respectively. This limitation deteriorates the optical signal-to-noise ratio (OSNR), impedes the maximization of the output power and results in closer amplifier spacings. In order to combat all these pattern-induced

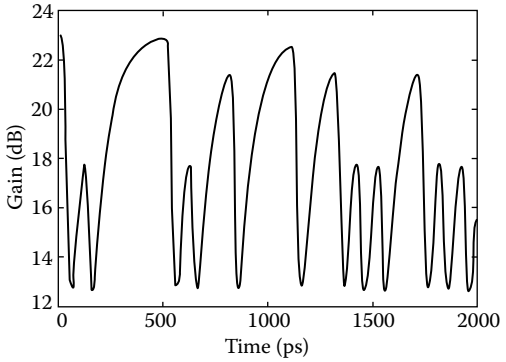

FIGURE 25.18 Instantaneous SOA gain variation.

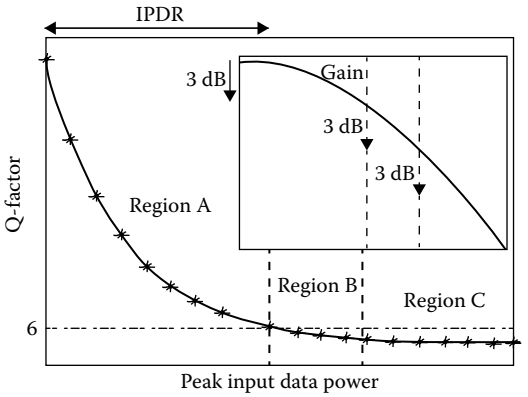

FIGURE 25.19 Variation of Q-factor and corresponding SOA gain (inset) versus peak input data power. The horizontal dotted line denotes the lower limit set for the Q-factor. Defined SOA saturation regions: A = low, B = medium, and C = deep.

performance degradations and restore the quality of the amplified signal, various methods have been proposed and employed. These methods involve intervening on the SOA design, material, and structure and applying sophisticated line coding and interferometric and filtering configurations (see relevant references in Rizou et al., 2013). However, this is a special subject that should be separately addressed elsewhere.

25.7 SOA Electrical Gain Modulation

In addition to straightforward amplification and all-optical signal processing, there has recently been intense research interest in SOAs for use as external modulators. The motivation behind this activity is to be able to provide both data amplification and modulation so as to overcome limitations imposed by other optical modulators (Udvary and Berceli, 2010) while enabling the implementation of various applications (see relevant references in Zoiros et al., 2015). The basic configuration that is exploited for this purpose is shown in Figure 25.20 (Rizou et al., 2015b). The SOA bias current, which is fixed at some point where the *P–I* curve is linear (Udvary and Berceli, 2010), is modulated by an electrical data signal. This modulation alters the SOA gain analogously, which is perceived by a lightwave beam of constant power over time (CW). In this manner, the SOA current modulation is mapped on the CW signal, which thus carries the original information that has now been converted into optical form. According to this physical process, an

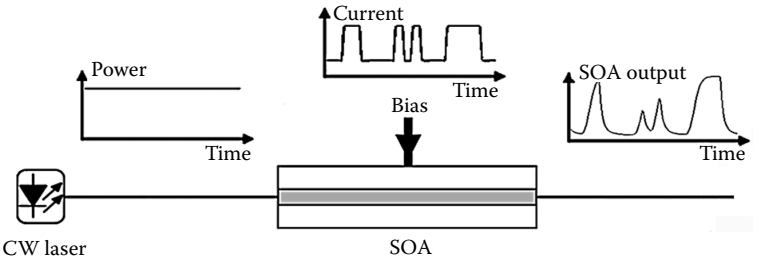

FIGURE 25.20 Basic configuration of directly modulated SOA.

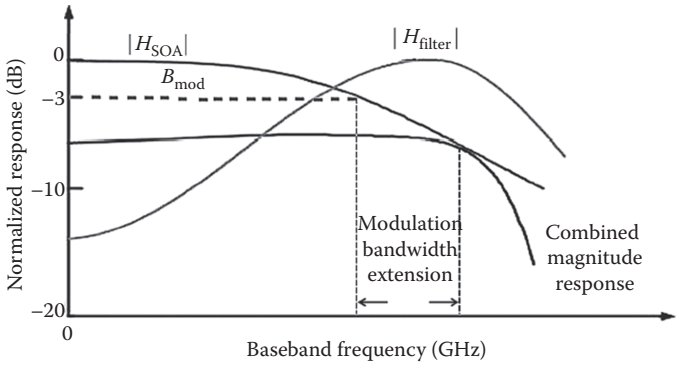

FIGURE 25.21 Schematic description of SOA electrical response characteristic $|H_{SOA}|$, transfer function of a filter $|H_{filter}|$ and the combined magnitude response.

exact copy of the applied electrical signal should be transferred at the SOA output. However, this does not happen when the SOA modulation bandwidth, B_{mod}, is smaller than the bandwidth that corresponds to the rate and format of the applied excitation, B_{exc}. More specifically, due to the SOA finite differential carrier lifetime, τ_d, B_{mod} is limited to the order of 1 GHz. In fact, the small-signal frequency response analysis procedure, where the SOA rate equations are linearized and solved analytically by assuming that there are only small perturbations around an operating point (König, 2014), reveals that B_{mod} scales inversely with τ_d according to $B_{mod} = 1/(2\pi\tau_d)$ and the SOA electrical response exhibits the low-pass filter characteristic qualitatively shown in Figure 25.21 (Wang, 2008). On the other hand, the latter parameter depends on the data format (Agrawal, 2002), and for non-return-to-zero (NRZ) pulses is $B_{exc} = B_{rep}/2$, where B_{rep} is the repetition rate. Thus, if B_{rep} is increased so that B_{exc} exceeds B_{mod}, the performance of the directly modulated SOA becomes progressively pattern-dependent and eventually poor.

25.8 Pattern Effect II: Direct Current Modulation

The characteristics of the encoded pulse stream are degraded as the rate of SOA direct modulation is increased due to the concomitant aggravation of the associated pattern effect. In fact, Figure 25.22 shows that with a five-fold increase from 1 Gb/s to 5 Gb/s the amplitude deviations between marks, between spaces, and between marks and spaces are intensified (compare left- to right-hand side). Moreover, the pseudo-eye diagram becomes asymmetrical due to the long rise and fall times and tends to close (compare left to right-hand side of Figure 25.23). Finally, the chirp suffers from analogous peak amplitude fluctuations and transient distortions (compare left to right-hand side of Figure 25.24). Nevertheless, these impairments can be mitigated and the SOA be directly modulated at an extended data rate than that enabled

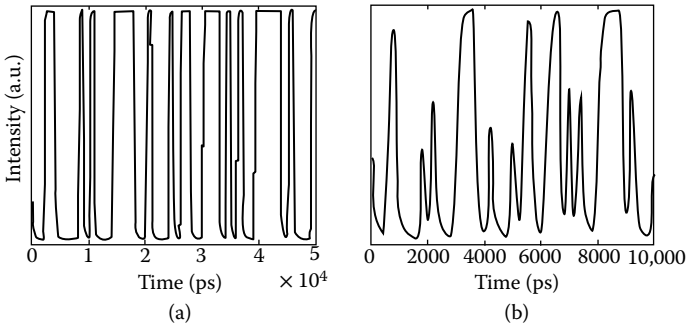

FIGURE 25.22 Encoded data pattern at directly modulated SOA output for (a) 1 Gb/s, (b) 5 Gb/s.

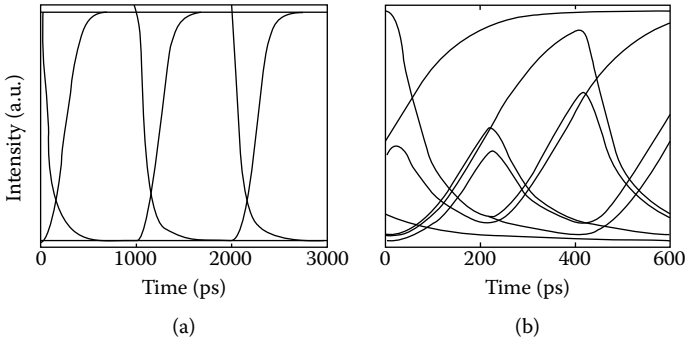

FIGURE 25.23 Pseudo-eye diagram of encoded signal at directly modulated SOA output for (a) 1 Gb/s, (b) 5 Gb/s.

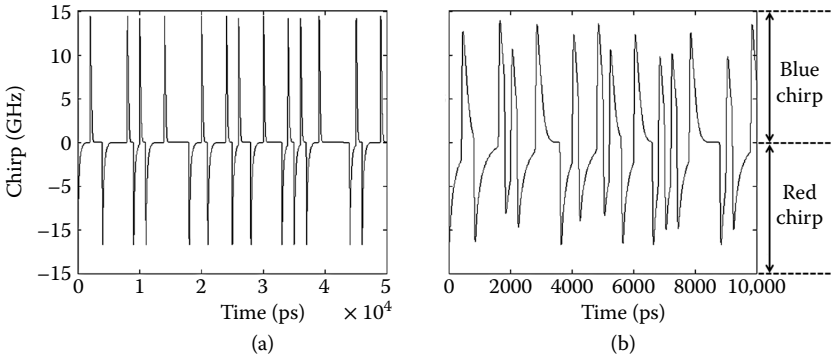

FIGURE 25.24 Chirp of encoded signal at directly modulated SOA output for (a) 1 Gb/s, (b) 5 Gb/s.

by its limited modulation bandwidth by means of post optical notch filtering. This technique can be implemented with different technologies (see relevant references in Zoiros and Morel, 2014), which have in common the fact that they produce a filter characteristic whose slope is in the opposite direction to that of the SOA, as seen in Figure 25.21. This counteracts the SOA response and so the combined transfer function becomes independent of the direct modulation frequency for a wider range than for the SOA only. In this manner, the quality characteristics of the encoded signal at the directly modulated SOA output can be significantly improved so that they are appropriate for supporting the target applications.

References

Agrawal GP (2002) *Fiber-Optic Communication Systems*. New York, NY: Wiley.

Agrawal GP and Olsson NA (1989a) Self-phase modulation and spectral broadening of optical pulses in semiconductor laser amplifiers. *IEEE J Quantum Electron*. 25:2297–2306.

Agrawal GP and Olsson NA (1989b) Amplification and compression of weak picosecond optical pulses by using semiconductor-laser amplifiers. *Opt Lett*. 14:500–502.

Borri P et al. (1999) Measurement and calculation of the critical pulsewidth for gain saturation in semiconductor optical amplifiers. *Opt Commun*. 164:51–55.

Boscolo S, Bhamber R, Turitsyn SK, Mezentsev VK, and Grigoryan VS (2006) RZ-DPSK transmission at 80 Gbit/s channel rate using in-line semiconductor optical amplifiers. *Opt Commun*. 266:656–659.

Botsiaris C, Zoiros KE, Chasioti R, and Koukourlis CS (2007) Q-factor assessment of SOA-based ultrafast nonlinear interferometer. *Opt Commun*. 278:291–302.

Cassioli D, Scotti S, and Mecozzi A (2000) A time-domain computer simulator of the nonlinear response of semiconductor optical amplifiers. *IEEE J Quantum Electron.* 36:1072–1080.

Chi JWD, Chao L, and Rao MK (2001) Time-domain large-signal investigation on nonlinear interactions between an optical pulse and semiconductor waveguides. *IEEE J Quantum Electron.* 37:1329–1336.

Connelly MJ (2002) *Semiconductor Optical Amplifiers*. Dordrecht: Kluwer Academic Publishers.

Diez S (2000) All-optical signal processing by gain-transparent semiconductor switches. PhD dissertation, Technical University of Berlin.

Eiselt M, Pieper W, and Weber HG (1995) SLALOM: Semiconductor laser amplifier in a loop mirror. *J Lightwave Technol*. 13:2099–2112.

Giller R, Manning RJ, and Cotter D (2006) Gain and phase recovery of optically excited semiconductor optical amplifiers. *IEEE Photon Technol Lett*. 18:1061–1063.

Girardin F, Guekos G, and Houbavlis A (1998) Gain recovery of bulk semiconductor optical amplifiers. *IEEE Photon Technol Lett.* 10:784–786.

Girault G et al. (2008) Analysis of bit rate dependence up to 80 Gbit/s of a simple wavelength converter based on XPM in a SOA and a shifted filtering. *Opt Commun*. 281:5731–5738.

Gutiérrez-Castrejón R and Duelk M (2007) Modeling and simulation of semiconductor optical amplifier dynamics for telecommunication applications. In: *Computer Physics Research Trends* (Bianco SJ, ed.), pp. 89–124. New York, NY: Nova Science Publishers.

Gutiérrez-Castrejón R, Occhi L, Schares L, and Guekos G (2001) Recovery dynamics of cross-modulated beam phase in semiconductor amplifiers and applications to all-optical signal processing. *Opt Commun*. 195:167–177.

Gutiérrez-Castrejón R, Schares L, Occhi L, and Guekos G (2000) Modeling and measurement of longitudinal gain dynamics in saturated semiconductor optical amplifiers of different length. *IEEE J Quantum Electron*. 36:1476–1484.

Hall KL, Lenz G, Darwish AM, and Ippen EP (1994) Subpicosecond gain and index nonlinearities in InGaAsP diode lasers. *Opt Commun*. 111:589–612.

Hamilton SA, Robinson BS, Murphy TE, Savage SJ, and Ippen EP (2002) 100 Gb/s optical time-division multiplexed networks. *J Lightwave Technol*. 20:2086–2100.

Henry CH (1982) Theory of the linewidth of semiconductor lasers. *IEEE J Quantum Electron*. 18:259–264.

Hinton K, Raskutti G, Farrell PM, and Tucker RS (2008) Switching energy and device size limits on digital photonic signal processing technologies. *IEEE J Sel Top Quantum Electron*. 14:938–945.

Hosseini SR, Razaghi M, and Das NK (2011) Analysis of ultrafast nonlinear phenomena's influences on output optical pulses and four-wave mixing characteristics in semiconductor optical amplifiers. *Opt Quant Electron*. 42:729–737.

Hussain K, Pradhan R, and Datta PK (2010) Patterning characteristics and its alleviation in high bit-rate amplification of bulk semiconductor optical amplifier. *Opt Quant Electron*. 42:29–43.

Hutchings DC, Sheik-Bahae M, Hagan DJ, and Van Stryland EW (1992) Kramers–Kronig relations in nonlinear optics. *Opt Quant Electron*. 24:1–30.

Jennen J, De Waardt H, and Acket G (2001) Modeling and performance analysis of WDM transmission links employing semiconductor optical amplifiers. *J Lightwave Technol.* 19:1116–1124.

Kim NY, Tang X, Cartledge JC, and Atieh AK (2007) Design and performance of an all-optical wavelength converter based on a semiconductor optical amplifier and delay interferometer. *J Lightwave Technol.* 25:3730–3738.

Kim Y et al. (2003) Transmission performance of 10-Gb/s 1550-nm transmitters using semiconductor optical amplifiers as booster amplifiers. *J Lightwave Technol.* 21:476–481.

König S (2014) *Semiconductor Optical Amplifiers and mm-Wave Wireless Links for Converged Access Networks*. Karlsruhe Series in Photon & Communication (Leuthold J, Freude W, Koos C, eds.), Vol. 14. Karlsruhe: University of Karlsruhe.

Manning RJ, Ellis AD, Poustie AJ, and Blow KJ (1997) Semiconductor laser amplifiers for ultrafast all-optical signal processing. *J Opt Soc Am B*. 14:3204–3216.

Mecozzi A and Mørk J (1997) Saturation effects in nondegenerate four-wave mixing between short optical pulses in semiconductor laser amplifiers. *IEEE J Sel Top Quantum Electron.* 3:1190–1207.

Morito K, Ekawa M, Watanabe T, and Kotaki Y (2003) High-output-power polarization-insensitive semiconductor optical amplifier. *J Lightwave Technol*. 21:176–181.

Mørk J and Mecozzi A (1996) Theory of the ultrafast response of active semiconductor waveguides. *J Opt Soc Am B*. 13:1803–1816.

Mørk J, Nielsen ML, and Berg TW (2003) The dynamics of semiconductor optical amplifiers: Modeling and applications. *Opt Photon News*. 14:42–48.

Mynbaev DK and Scheiner LL (2001) *Fiber-Optic Communications Technology*. New Jersey, NJ: Prentice-Hall.

Ning CZ, Indik RA, and Moloney JV (1997) Effective Bloch equations for semiconductor lasers and amplifiers. *IEEE J Quantum Electron*. 33:1543–1550.

Occhi L (2002) Semiconductor optical amplifiers made of ridge waveguide bulk InGaAsP/InP: Experimental characterisation and numerical modelling of gain, phase, and noise. PhD dissertation, Swiss Federal Institute of Technology, Zurich.

O'Mahony MJ (1988) Semiconductor laser optical amplifiers for use in future fiber systems. *J Lightwave Technol*. 6:531–544.

Pauer M, Winzer PJ, and Leeb WR (2001) Bit error probability reduction in direct detection optical receivers using RZ coding. *J Lightwave Technol*. 19:1255–1262.

Razaghi M, Ahmadi V, and Connelly MJ (2009) Comprehensive finite difference time-dependent beam propagation model of counter-propagation picosecond pulses in a semiconductor optical amplifier. *J Lightwave Technol*. 27:3162–3174.

Rizou ZV, Zoiros KE, Hatziefremidis A, and Connelly MJ (2013) Design analysis and performance optimization of a Lyot filter for semiconductor optical amplifier pattern effect suppression. *IEEE J Sel Top Quantum Electron*. 19:1–9.

Rizou ZV, Zoiros KE, Hatziefremidis A, and Connelly MJ (2015a) Performance tolerance analysis of birefringent fiber loop for semiconductor optical amplifier pattern effect suppression. *Appl Phys B*. 119:247–257.

Rizou ZV, Zoiros KE, and Houbavlis T (2015b) Operating speed extension of SOA external modulator using microring resonator. *Proceedings of 36th Progress in Electromagnetics Research Symposium*, Prague, Czech Republic, July 6–9.

Saleh BEA and Teich MC (1991) *Fundamentals of Photonics*. New York, NY: John Wiley & Sons.

Schreieck RP (2001) Ultrafast dynamics in InGaAsP/InP optical amplifiers and mode locked laser diodes. PhD dissertation, Swiss Federal Institute of Technology in Zurich.

Schubert C (2004) Interferometric gates for all-optical signal processing. PhD dissertation, Technical University of Berlin.

Singh S (2011) An approach to enhance the receiver sensitivity with SOA for optical communication systems. *Opt Commun*. 284:828–832.

Tang JM and Shore KA (1998) Strong picosecond optical pulse propagation in semiconductor optical amplifiers at transparency. *IEEE J Quant Electron.* 34:1263–1269.

Tang JM, Spencer PS, Rees P, and Shore KA (2000) Ultrafast optical packet switching using low optical pulse energies in a self-synchronization scheme. *J Lightwave Technol.* 18:1757–1764.

Toptchiyski GO (2002) Analysis of all-optical interferometric switches based on semiconductor optical amplifiers. PhD dissertation, Technical University of Berlin.

Udvary E and Berceli T (2010) Improvements in the linearity of semiconductor optical amplifiers as external modulators. *IEEE Trans Microw Theory Tech*. 58:3161–3166.

Ueno Y, Nakamura S, and Tajima K (2002) Nonlinear phase shifts induced by semiconductor optical amplifiers with control pulses at repetition frequencies in the 40–160-GHz range for use in ultrahigh-speed all-optical signal processing. *J Opt Soc Am B*. 19:2573–2589.

Vacondio F (2011) On the benefits of phase shift keying to optical telecommunication systems. PhD dissertation, Laval University of Canada.

Vallaitis T. (2010) *Ultrafast Nonlinear Silicon Waveguides and Quantum Dot Semiconductor Optical Amplifiers*. Karlsruhe Series in Photon & Communication (Leuthold J, Freude W, eds.), Vol. 7. Karlsruhe: University of Karlsruhe.

Wang J (2008) *Pattern Effect Mitigation Techniques for All-Optical Wavelength Converters Based on Semiconductor Optical Amplifiers. Karlsruhe Series in Photon & Communication* (Leuthold J and Freude W, eds.), Vol. 3. Germany: Univ Karlsruhe.

Wang J et al. (2007) Pattern effect removal technique for semiconductor optical amplifier based wavelength conversion. *IEEE Photon Technol Lett.* 19:1955–1957.

Wiesenfeld JM (1996) Gain dynamics and associated nonlinearities in semiconductor optical amplifiers. In: *Current Trends in Optical Amplifiers and Their Applications* (Lee TP, ed.), pp. 179–222. Singapore: World Scientific.

Wong WM and Blow KJ (2003) Travelling-wave model of semiconductor optical amplifier based non-linear loop mirror. *Opt Commun*. 215:169–184.

Zimmerman DR and Spiekman LH (2004) Amplifiers for the masses: EDFA, EDWA, and SOA amplest for metro and access applications. *J Lightwave Technol*. 22:63–70.

Zoiros KE, Chasioti R, Koukourlis CS, and Houbavlis T (2007) On the output characteristics of a semiconductor optical amplifier driven by an ultrafast optical time division multiplexing pulse train. *Optik*. 118:134–146.

Zoiros KE, Houbavlis T, and Moyssidis M (2005) Complete theoretical analysis of actively mode-locked fiber ring laser with external optical modulation of a semiconductor optical amplifier. *Opt Commun*. 254:310–329.

Zoiros KE, Janer CL, and Connelly MJ (2010a) Semiconductor optical amplifier pattern effect suppression for return-to-zero data using an optical delay interferometer. *Opt Eng*. 49:085005-085005-4. doi:10.1117/1.3481137.

Zoiros KE and Morel P (2014) Enhanced performance of semiconductor optical amplifier at high direct modulation speed with birefringent fiber loop. *AIP Adv.* 4:077107. doi:10.1063/1.4889869.

Zoiros KE, Morel P, Hamze M (2015) Performance improvement of directly modulated semiconductor optical amplifier with filter-assisted birefringent fiber loop. *Microw Opt Technol Lett.* 57:2247–2251.

Zoiros KE, O'Riordan C, and Connelly MJ (2009) Semiconductor optical amplifier pattern effect suppression using Lyot filter. *Electron Lett*. 45:1187–1189.

Zoiros KE, O'Riordan C, and Connelly MJ (2010b) Semiconductor optical amplifier pattern effect suppression using a birefringent fiber loop. *IEEE Photon Technol Lett*. 22:221–223.

Zoiros KE, Siarkos T, and Koukourlis CS (2008) Theoretical analysis of pattern effect suppression in semiconductor optical amplifier utilizing optical delay interferometer. *Opt Commun*. 281:3648–3657.

Index

C

D

E

F

G

H

I

J

K

L

M

N

O

P

Q

R

S

T

X

Z